A thesis submitted to the School of Environmental Sciences at the University of East Anglia in partial fulfilment of the requirements for the degree of Doctor of Philosophy

The role of sea ice in the carbon uptake by polar oceans

Elise Sayana Droste
100248506

PhD
University of East Anglia
School of Environmental Sciences
May 2023

ABSTRACT

The Southern and Arctic Oceans are key in the regulation of our climate on Earth. They absorb carbon dioxide (CO_2) from the atmosphere, thereby buffering the global impact of anthropogenic CO_2 emissions. The formation and melt of sea ice in the polar oceans significantly influences the sea-air CO_2 exchange by restricting direct gas exchange across the sea-air interface, by modifying the marine carbonate chemistry, and by affecting biology. The variability of sea ice and the CO_2 sink of polar oceans are therefore tightly linked. The atmospheric CO_2 sink of polar oceans is highly variable in time and space. However, the processes that drive this variability are still poorly understood due to sparse spatial and temporal data coverage, especially in perennially sea ice covered regions, in winter, and at temporal resolutions high enough to capture small-scale, rapid processes.

This research studies how sea ice and other factors drive the variability in sea-air CO_2 flux and the surface water carbonate chemistry on different time-scales. It uses observational carbonate chemistry data collected along the Weddell Sea coastline, the West Antarctic Peninsula coastline, and the centre of the Central Arctic Ocean, thereby covering a wide range of conditions and sea ice regimes. Findings show that the sea-air CO_2 flux can be highly variable on semi-diurnal time-scales when tidal currents are strong, that wintertime processes are important to understand interannual variability in CO_2 uptake by the polar ocean, and that small-scale processes, such as storms, can affect the surface layer carbonate chemistry in the seasonal transition from summer to winter. An ever-improving understanding of the processes discussed in this research is key to developing predictions of how the role of sea ice in atmospheric CO_2 uptake by polar oceans, and the CO_2 uptake itself, may change in a rapidly changing global climate.

Access Condition and Agreement

Each deposit in UEA Digital Repository is protected by copyright and other intellectual property rights, and duplication or sale of all or part of any of the Data Collections is not permitted, except that material may be duplicated by you for your research use or for educational purposes in electronic or print form. You must obtain permission from the copyright holder, usually the author, for any other use. Exceptions only apply where a deposit may be explicitly provided under a stated licence, such as a Creative Commons licence or Open Government licence.

Electronic or print copies may not be offered, whether for sale or otherwise to anyone, unless explicitly stated under a Creative Commons or Open Government license. Unauthorised reproduction, editing or reformatting for resale purposes is explicitly prohibited (except where approved by the copyright holder themselves) and UEA reserves the right to take immediate 'take down' action on behalf of the copyright and/or rights holder if this Access condition of the UEA Digital Repository is breached. Any material in this database has been supplied on the understanding that it is copyright material and that no quotation from the material may be published without proper acknowledgement.

TABLE OF CONTENTS

LIST OF FIGURES

LIST OF TABLES

ACKNOWLEDGEMENTS

This PhD project has been possible thanks to the funding from the UK Natural Environment Research Council (NERC) through the EnvEast Doctoral Training Partnership (NE/L002582/1). This included three additional months of funding due to delays related to the COVID-19 pandemic. The PhD research done within the framework of the Multidisciplinary drifting Observatory for the Study of Arctic Climate (MOSAiC) was possible thanks to funding from the UK Department for Business, Energy and Industrial Strategy through the UK Arctic Office. Work done for the PS117 expedition was supported by the Processes Influencing Carbon Cycling: Observations of the Lower limb of the Antarctic Overturning (PICCOLO; NE/P021395/1).

There are many factors that play a role in making a PhD experience a good one. Not least important - or arguably one of the most important - are the supervisors. One of the luckiest draws I had in my PhD was my supervisory team. I could not have asked for a better one: Dorothee Bakker, Bastien Queste, Mario Hoppema, Hugh Venables, and Giorgio Dall'Olmo. Giorgio, thank you for your enthusiasm and for early on instilling in me the importance of the question: *why is it important?* Hugh, thank you for our insightful discussions on all topics Rothera and Ryder Bay-related, as well as balancing those with beautiful imagery of wildlife (in the Southern Ocean and along the Norfolk coast!). Mario, thank you for your massive support in my field-, lab-, and scientific work, including for hosting me at the AWI for a number of months where I could analyse my samples. Your guidance and trust have been significant for what I was able to get out of this PhD experience. Bastien, thank you helping me out with data when I had no way of moving foward, and for your advice and tips on starting a career in academia over coffees, especially at the start of my PhD. Dorothee, thank you for always thinking along with - if not ahead of - me, for your relentless efforts that made it possible for me to go on the PS117 and the MOSAiC expeditions, for helping me take opportunities to enhance my skills and my science, for your encouragement, for your confidence and trust in me, and, most of all, for being a wonderful person.

For my PhD research, more than 2000 seawater samples have been analysed at the University of East Anglia (UEA) and at the Alfred Wegener Institute (AWI) combined. I could not have done this without the kind support and help from the laboratory and technical staff at UEA and at AWI. Thank you, Andy MacDonald, Marcos Cobas-Garcia (also for helping me out with the crate shipment back from PS117), and Nicholas Garrard at UEA, and Marcel Machnik and Laura Wischnewski at AWI. A very special

thank you goes to Gareth Lee, who has taught me everything I know about VINDTAs, their quirks, how to help them work, and how to love them. This part will only make sense to anyone who has ever analysed seawater samples on VINDTAs. Gareth, thank you so much for your never-ending patience in teaching me how to do the analyses, always being on stand-by when they threw a tantrum and I did not know how to make them behave (even late in the evening or when I was in Germany!), and for analysing *so many* of the samples with me. Besides technical and mental support in the lab, you have also bared with me through the most complicated arrangement of shipments of sampling bottles across the globe. The bulk of my PhD research is based on the data from those samples, and that makes your support in my work fundamental to everything that is in it.

I have been lucky enough to have participated in two expeditions during my PhD. The first one was to the Weddell Sea on PS117. I want to thank Karen Heywood and Tom Bell as PI and co-PI of PICCOLO for supporting my work during PS117. Thanks to the logistics team of the AWI for making this expedition possible. Thanks to the captain and crew of R.V. *Polarstern*, the amazing team of scientists on board PS117, and chief scientist, Olaf Boebel, who made this journey wonderful and unforgettable. It was an experience that became a source of motivation for the rest of my PhD research, and continuing my career in this field.

The second expedition I was able to participate on was Leg 5 of the MOSAiC expedition to the Central Arctic Ocean. I again thank the captain and crew of R.V. *Polarstern*, scientists, and chief scientist, Markus Rex, for another intense, yet remarkable experience. Also thanks to the logistics team on board (a.k.a. the polar bear guards), for keeping us safe when we were sticking our instruments in the ice and water, or testing the salinity of platelet ice. Markus, my participation on the MOSAiC expedition is thanks to you. MOSAiC has become a really fun, engaging, and extremely insightful part of my PhD experience, and I am sure for many years to come. I cannot thank you enough. Henry Burgess, thank you for your support through the UK Arctic Office, which made it possible for me to participate in MOSAiC.

Through MOSAiC, I have been able to collaborate with many more scientists during my PhD than I had ever anticipated. To thank every person who made a difference to me and my work would require a chapter's worth of text, so instead I extend my most profound gratitude to everyone on board Leg 5 and to those with whom I have discussed about the exciting data coming from this endeavour. I would, however, like to mention a few names. As coordinators of Team ECO (of which I am a member), Allison Fong, Rolf Gradinger, and Clara Hoppe have done/are still doing a fantastic job at steering and supporting the activities and achievements of Team ECO. Allison, on Leg 5 you have impressed me with your leadership and maintaining the high motivation within and outside our team. Thank you for facilitating the collection of the numerous DIC / TA samples during Leg 5! It is an honour to be a part of Team ECO and I am grateful to all ECO members, as well as the members of Team BGC, on board Leg 5, for our work and time together. Daiki Nomura, Alison Webb, Emelia Chamberlain, Salar Karam, and Jakob Allerholt, working with you on board and post-expedition has been one of the biggest joys in my work. Thank you for your friendship. Salar, Jakob, and Nik Schaaf, I will never forget you visiting me in the lab on board, keeping me company during late hours of work, bringing me cake, and making me laugh even when I felt completely exhausted. Nik, thank you for encouraging me to become the scientist I aspire to be.

The MOSAiC expedition found itself in the uncomfortable start of the COVID-19-pandemic. When countries and ports were shutting down and people had to stay at home, the MOSAiC consortium still managed to achieve its objective to complete a full annual cycle alongside an ice floe in the Arctic Ocean due to major efforts by the organisational team. On a personal basis, my participation on Leg 5 (the final leg) was made possible thanks to the time and effort dedicated by Alistair Grant at UEA to make it possible for me to safely go on international field work at a time when uncertainties around COVID-19 were high and international travel was restricted. Thank you. Also many thanks to Kevin Hiscock and Dorothee, who continued to support my participation on MOSAiC throughout the pandemic.

Working from home during the various lock-downs was challenging, because of a less-favourable working environment, but mostly because it was significantly less motivating and enjoyable when I did not have any of my fabulous office mates around me. As I have been in office 01.37K for a while, I have many lovely office mates to thank for their company, conversations, emotional/mental support, and expressive rants: Chata Seguro, Seth Thomas, David Buchanan, Maria Zamyatina, Yanhui Lui (Alice), Norfazrin Mohn Hanif, Geoff Lee, and Gianfranco Anastasi (the "original" 01.37K office); and Karina Adcock, Yuanxu Dong, Ruth Matthews, Reuben Gilbertson, Eliza Karlowska, Lizzie Archer, Cat Acheson, and Aparna Anitha Reghunathan. Yuanxu, I loved our conversations about science, life, and work-life balance. I will miss sharing an office with you. Ruth, thank you for being my lab and office-buddy. Your positivity has helped me through many tough days and made many good days even better. I am so happy we continue to have our coffee chats! Krisztina Sarkozi, thank you for successfully taking on the role of all my office-mates combined at home during the lock-downs.

In ways that they might not know, my PhD experience was augmented by Alex Baker, Johannes Laube, Emma Leedham-Elvidge, and Andy Hind. Alex, thank you for our conversations and many laughs. It is your fault that I came to UEA and decided to enjoy being there. I will miss standing in your office door and distracting you from whatever you want to be distracted from. Johannes, thank you for all the opportunities you gave me while working with you, which gave me confidence to start a PhD, and the many pieces of wisdom that I continue to ask you for. I have learnt a lot from you academically and non-academically, and I am grateful that we keep in touch. Emma, working with you and being friends with you has had so many positive influences in my life, and much of the good work-life balance that I was able to achieve is credited to you. Andy, I greatly enjoyed working with you and our fun conversations. Thanks for teaching me how to be resourceful at UEA.

As the length of the acknowledgements so far indicates (I am not done yet), I have had tremendous support from an academic/workplace perspective. From the perspective of everything not associated to academia, the support from friends has been equally enormous, keeping me happy throughout the PhD. The time with friends (pub) reminded me that there is much more life outside than inside the PhD. Denis Sergeev, thank you for your Python-godliness from which many of us have benefited, as well as for keeping me physically healthy with Athlean-X and mentally healthy with our conversations. Marina Azaneu, thank you for inviting me along in your crazy adventures, our wine evenings, and our talks, from which I have drawn a lot of strength. Montsa Gasset Arrando, thank you for your kindness, our dinners, and our catch-ups on life that always left me happier than I was before. Jack Rogers, thank you for all our coffees and laughs. I always appreciated you asking me about my spectrophotometer. Nine Douwes Dekker, thank you for all the laughter you bring into the world (it needs it) and inspiring me to try to do the same. Daniel Kloek, thank you for coming back into my life and for promising to read my entire thesis (I am unsure you knew what you were signing up for). Felipe Lobos, thank you for our meet-ups when we attempt to solve our own, as well as the world's, problems. Martijn van den Eijnden, thank you for our long and soulful chats. Damien Ringeisen, thank you for our wholesome conversations. Marlene Meister, thank you for being sunshine and inspiring me to be truthful to myself. Mircea van der Plas, thank you for your unwavering confidence in me, for supporting me through this journey, and for your patience with me in the beginning when I was definitely working too much. Amy Vis, thank you for being there for me my entire life (-5 years), unconditionally supporting me through the good and challenging times, and for being someone I can look up to. Lucija Kerečin, thank you for making every time I talk to you seem like we talk every day, for your amazing support in whatever I choose to do, and for inspiring me to chase what I love doing. To all my friends: I would not have wanted to do this PhD without you. James Christie, thank you for being the reason why I was able to still have work-free weekends until the very end, for cooking for me every evening during the last month so I could get my work done, for all the giggles, and for bringing me back into the moment. Also thank you for the many hours you spent on making the most beautiful maps that are included in my thesis.

And finally, I want to thank my family. To my Opa (who passed away while I was at sea) and my Oma: Dank jullie wel voor al jullie steun en liefde. To mum and dad: I am who I am and where I am today thanks to everything you have done for me. Thanks for continuing to be amazing examples of parents, scientists, and people, that I can strive towards to. To my dearest sister: Hester, thank you for being a source of inspiration in everything I do, for picking me up when I am down, and for lifting me even higher when I am up.

CHAPTER 1 |

Introduction

Contents

1.1 Opening remarks

Very little compares to the sight of a glistening expanse of sea ice. Although it seems overwhelmingly white, sea ice reveals a rich palette of colours, once the eyes adjust. Although seemingly hostile, sea ice supports a rich ecosystem, if we look for it. And although it seems passive, sea ice is constantly in motion and transformation, if we watch it long enough. Underneath, a kilometres-deep, dynamic ocean shelters from the harsh atmospheric conditions of the high-latitudes. This salty world supports us by taking up heat and carbon from our atmosphere, by providing us with food, and quite simply by instilling calmness and serenity with the sounds of its crashing waves and its profound beauty. Technological advances are enabling us to explore the ocean in ways that were never possible before. However, it continues to hold many mysteries worth exploring. One of these mysteries is the impact of the transient states of seawater between its solid and liquid form on our Earth's system, which continues to fascinate me.

In this PhD research, I ventured into some of the unknowns of the polar oceans' carbonate chemistry, how this is affected by sea ice, and what this means for its carbon dioxide (CO_2) exchange with the atmosphere. My hope is to convey some of my fascination for this epic, yet rapidly changing world, to the reader.

1.2 Motivation

The global ocean is a net sink for atmospheric CO_2, annually absorbing 26 % of total anthropogenic CO_2 emissions (Friedlingstein et al., 2022). Subsequent export of carbon to deep and bottom ocean layers where it circulates around the globe is a natural and important CO_2 sequestration process. It can take tens of thousands of years before this carbon will be ventilated to the atmosphere again. The polar oceans remove a significant amount of CO_2 from the atmosphere. To frame the role of polar oceans in terms of how well they can offset the direct atmospheric CO_2 increase by anthropogenic emissions, their contribution is often reported in percentage of the total anthropogenic CO_2 uptake by the global ocean (e.g. DeVries, 2014; Frölicher et al., 2015; Gruber et al., 2009). The Southern Ocean south of 35°S[1] is responsible for about 40 % of global ocean anthropogenic CO_2 uptake (DeVries, 2014; Frölicher et al., 2015). The contribution of the Arctic Ocean is about 6 %[2] (Yasunaka et al., 2018). Even though the Southern

---

[1] As the northern boundary of the Southern Ocean is unofficial, different latidutinal values have been used in the literature, complicating intercomparisons among studies. In more recent years, the latitude of 35°S has more commonly and consistently been used (see e.g., DeVries, 2014; Landschützer et al., 2015). In this work, I continue to use this definition of the Southern Ocean, and will clearly state when comparisons are made to studies that use a different definition.

[2] In the work by Yasunaka et al. (2018), the contribution of the Arctic Ocean is reported as 12 % of the *total* ocean net CO_2 uptake. To report the Arctic Ocean CO_2 uptake in terms of ocean anthropogenic CO_2 uptake (consistent with the Southern Ocean estimate), I first calculated the amount of the Arctic Ocean CO_2 uptake in Pg C yr^{-1} as estimated by Yasunaka et al. (0.18 Pg C yr^{-1}) relative to the estimate for the Southern Ocean by DeVries (2014); 1.1Pg C yr^{-1}), which is 16 % (0.18/1.1 Pg C yr^{-1}). If the contribution of the Southern Ocean to global ocean anthropogenic CO_2 uptake is 40 % (DeVries, 2014), then the contribution of the Arctic Ocean is about 6 % (16 % of 40 % = (0.16 x 0.40) x 100).

and Arctic Oceans together cover only about 30 %[3] of the global ocean surface area, combined they are responsible for almost 50 % of the global ocean anthropogenic CO_2 uptake.

The ocean absorbs CO_2 when the partial pressure of CO_2 (pCO_2) at the water surface is lower than in the atmosphere. Surface ocean pCO_2 is a function of complex combinations of physical and biogeochemical processes. The relatively low mean marine pCO_2 in the polar regions is generally driven by low temperatures that increase seawater CO_2 solubility, and by biological CO_2 drawdown supported by nutrient-rich polar waters (Takahashi, 2002). However, mean values veil considerably high temporal variability ranging from semi-diurnal (e.g., Droste et al., 2022) to decadal time scales (e.g., Landschützer et al., 2015). Atmospheric and ocean circulation are tightly coupled and their feedbacks (e.g., wind-induced mixing, Ekman transport, heat exchange) are important for understanding developments in the polar ocean carbonate chemistry over time. For large parts of the year, sea ice is sandwiched between these two spheres, where it exerts significant local influences on the seawater and atmosphere.

Sea ice modulates sea-air fluxes (Fransson et al., 2011; Fransson et al., 2013; Loose and Schlosser, 2011; Mo et al., 2022), and exchanges CO_2 with the atmosphere (Delille et al., 2014; Geilfus et al., 2012; Geilfus et al., 2013; Kotovitch et al., 2016; Semiletov et al., 2004; Zemmelink et al., 2006). It also exchanges carbon with seawater through brine rejection (Delille et al., 2014; Lake and Lewis, 1970; Rysgaard et al., 2007) and stores buffering capacity in the form of calcium carbonate (Dieckmann et al., 2008; Fransson et al., 2011), which upon release and dissolution during melt enhances CO_2 uptake by the seawater (Rysgaard et al., 2013). The timing of sea ice formation and retreat affects water column mixing (Venables and Meredith, 2014), carbon and nutrient cycling within the ocean interior, and the onset of phytoplankton blooms that consume CO_2 during photosynthesis (Henley et al., 2017; Janout et al., 2016; Rozema et al., 2017; Venables et al., 2013). Sea ice forms its own ecosystem, supporting sympagic (ice-associated) organisms that have adapted to its extreme conditions (Boetius et al., 2015; van Leeuwe et al., 2018). These micro-organism communities support carbon and nutrient cycling within the sea ice and at the seawater interface (Bowman, 2015; Geilfus et al., 2012; Jones et al., 2022; Papadimitriou et al., 2012). "Seeding" seawater in early spring with previously sea ice-trapped microorganisms makes sea ice an important mode of transport for organisms and a preconditioner for springtime biological CO_2 drawdown (van Leeuwe et al., 2022). In addition to CO_2 uptake by the seawater, which is heavily influenced by sea ice formation and melt, the sea ice itself also contributes to the polar ocean net CO_2 sink by an additional uptake equal to 17-42 % of the polar ocean CO_2 sink (south of 50°S and north of 62°N; Delille et al., 2014; Rysgaard et al., 2011). In summary, sea ice is a unique ecosystem and an interactive matrix with complex sea-ice-air interactions that regulate the capacity of the ocean to take up CO_2 from

---

[3] The Southern Ocean south of 35°S relates to 26 % of the total global ocean surface area (Chelton et al., 1990). Following the area used by Yasunaka et al. (2018), the Arctic Ocean north of 65°N (excluding the Greenland Sea, Norwegian Sea, and Baffin Bay) covers 10.7 x 10^6 km^2. Using a global ocean area of 361 x 10^6 km^2, this relates to about 3 % of the total global ocean surface area.

the atmosphere. The variability in the surface marine carbonate system is profoundly linked to variability in sea ice extent and duration.

Throughout the seasons, sea ice covers between 3-15 million km^2 of the Southern Ocean and between 6-15 million km^2 of the Arctic Ocean (Parkinson, 2014). Arctic sea ice extent is declining at an alarming rate (Cavalieri and Parkinson, 2012; Notz and Stroeve, 2016), which is driven by anthropogenic CO_2 emissions, the effects of which are reinforced by climate feedback mechanisms (Dai et al., 2019). Its regime is shifting towards later onset of annual sea ice formation and shorter sea ice seasons (Markus et al., 2009; Stammerjohn et al., 2012). Trends have become apparent in all seasons (Stroeve and Notz, 2018). The effects of climate change on Antarctic sea ice extent are more spatially variable than in the Arctic (Stammerjohn and Maksym, 2017) due to asymmetric geography and the orography of the Antarctic continent affecting regional wind, climate, and ocean circulation patterns (Turner et al., 2015). Since the 1980's, Antarctic sea ice extent had even been showing an increasing mean trend (Parkinson and Cavalieri, 2012). However, it masked the opposing signs of regional trends, such as a declining sea ice extent in the Bellingshausen Sea and increasing trends in the Weddell Sea and Ross Sea (Turner et al., 2015). In 2016, the Antarctic sea ice extent suffered an unexpected Southern Ocean-wide reduction, likely caused by a combination of long-term ocean warming and transitions in large scale atmospheric circulation (Eayrs et al., 2021).

By affecting ocean circulation (Våge et al., 2018; Wang and Danilov, 2022), heat exchange (Haumann et al., 2020), marine primary productivity (Arrigo et al., 2008b), ecosystems (Ducklow et al., 2013), marine biogeochemistry (Barber et al., 2015; Lannuzel et al., 2020), and ice-air CO_2 flux (Delille et al., 2014; Rysgaard et al., 2011) changing seasonal and annual sea ice conditions will have cascading impacts on the marine carbonate system (Yamamoto-Kawai et al., 2009) and the polar ocean CO_2 sink (Bates and Mathis, 2009; Bates et al., 2006; Cai et al., 2010; Metzl, 2019; Parmentier et al., 2013). Understanding the relationships between sea ice and the marine carbonate system is an important step in improving models that predict our future climate in a rapidly changing world.

Motivation

Polar oceans play a **regulatory role on global climate** by significantly contributing to the global anthropogenic CO_2 uptake. Their capacity for net uptake depends on a balance between processes leading to CO_2 uptake and release. These processes are directly or indirectly related to **sea ice**. Global climate change is affecting sea ice extent and regimes, consequences of which are expected to **feed back into climate change**.

1.3 Sea ice as an interactive medium

The seasonal CO_2 flux model in ice covered seas by Rysgaard et al. (2011), illustrated in Fig. 1.1, conceptualises how carbon fluxes between the ocean, ice, and atmosphere are affected by biogeochemical processes that change during sea ice growth and melt. When sea ice forms, brine rejection expels CO_2 and dissolved inorganic carbon ions along with salt from the ice matrix, enriching water under the ice (Miller et al., 2011; Rysgaard et al., 2007). Depending on sea ice porosity, the CO_2-enriched brine trapped near the top of the sea ice is able to release CO_2 to the atmosphere (Delille et al., 2014; Nomura et al., 2006; Papadimitriou et al., 2003; Semiletov et al., 2004). When the temperature of sea ice decreases below a critical temperature as a function of salinity (e.g., -5 °C for sea ice with salinity of 5; Golden et al., 1998), its permeability decreases, such that connection with the atmosphere is blocked, diminishing ice-air flux (Loose and Schlosser, 2011). Calcium carbonate crystals, called ikaite, have been observed to form within the sea ice matrix as a result of supersaturation of minerals within the brine (Dieckmann et al., 2008; Fransson et al., 2011; Nomura et al., 2013b). Its formation produces CO_2, which contributes to brine supersaturation and potentially outgassing to the atmosphere (Geilfus et al., 2013). Ikaite represents a storage of alkalinity and unless ice permeability is high enough for brine gravity drainage, it will remain trapped until sea ice starts to melt in early spring.

Upon ice melt, physical, chemical, and biological processes rapidly create a sink for atmospheric CO_2 (Geilfus et al., 2012; Papadimitriou et al., 2012, ; Fig. 1.1). Within the sea ice, dilution of trapped brine by meltwater decreases its pCO_2 below atmospheric pCO_2 values. Chemical CO_2 consumption in the dissolution of ikaite within the brine further decreases its pCO_2 (Geilfus et al., 2012). Furthermore, sympagic photosynthetic organisms also contribute to decreasing sea ice pCO_2 when enough light is available for photosynthesis. The melted sea ice - a product of freshwater and diluted brine - decreases the seawater pCO_2 by dilution and release of ikaite minerals that have not dissolved yet (Fransson et al., 2013; Geilfus et al., 2016). Pelagic phytoplankton blooms further increase the capacity of the seawater to take up CO_2 from the atmosphere (Bakker et al., 2008; Fransson et al., 2013). The net result is a dramatic decrease in pCO_2 in the ocean surface layer during ice melt. Net respiration and water column mixing with carbon-rich subsurface water increase seawater pCO_2 in the surface layer again in autumn, followed by the onset of freeze-up (Fig. 1.1).

Snow cover adds another layer of complexity to the system. Its insulating properties can reduce the effect of atmospheric cooling on sea ice temperature, thereby maintaining a sea ice porosity still enables ice-air CO_2 exchange, including in winter. At the same time, snow can also dampen ice-air fluxes by forming a physical barrier (Nomura et al., 2018). Both snow and sea ice house a microorganism community, including bacteria that contribute to carbon cycling through respiration, even in winter (Fransson et al., 2013). Biological productivity in snow and its interfaces with the ice and atmosphere can also turn snow layers into ephemeral atmospheric CO_2 sinks (Zemmelink et al., 2006). Snow melt on top of sea ice has also been shown to create a net CO_2 sink (Nomura et al., 2013a). Other processes that add complexity to the sea-ice-air CO_2 flux model include water column mixing, melt pond formation, and meltwater lens formation (Fig. 1.1).

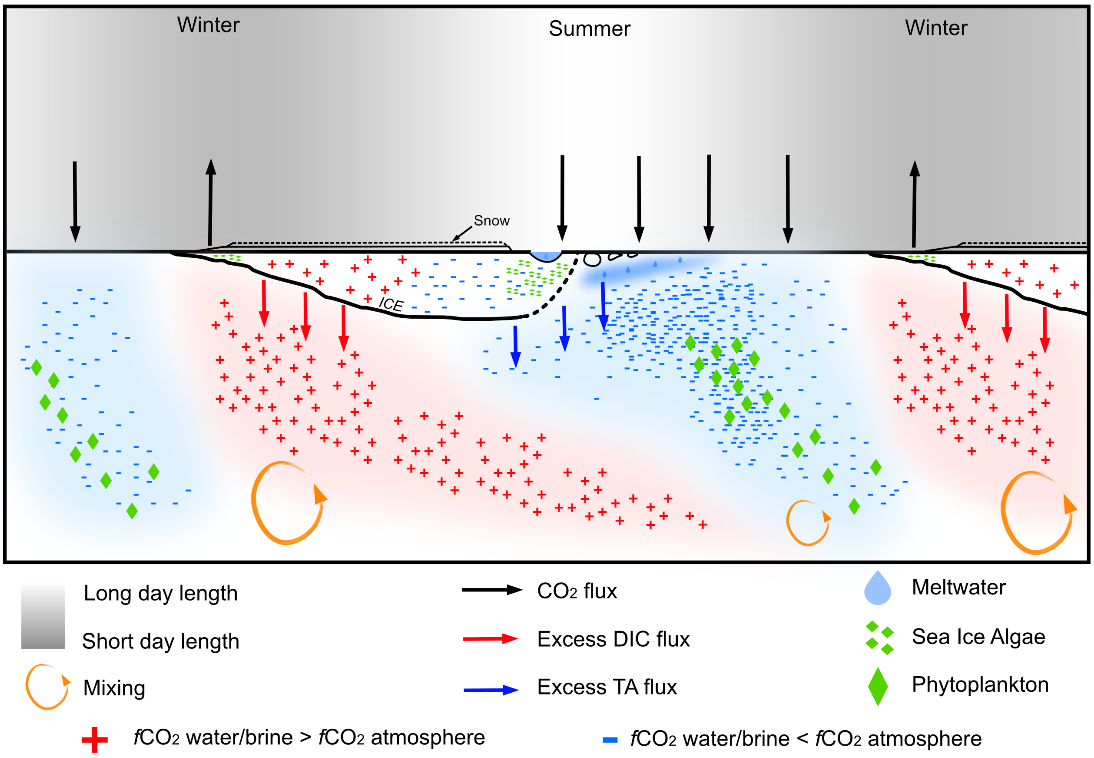

Figure 1.1: Conceptual model of how carbon fluxes vary seasonally in sea ice-covered oceans. Figure modified from Rysgaard et al. (2011). Credit: James Christie.

Overall, experimental, observational, and modelling studies suggest that sea ice can be a source of CO_2 to the atmosphere during growth and a sink during melt. Moreover, sea ice functions as a carbon pump by depositing most of its dissolved inorganic carbon into seawater during brine rejection and gravity drainage, which sinks to deeper waters. This is followed by forming an atmospheric CO_2 sink in the melting season by enhancing the ocean surface layer with alkalinity (Rysgaard et al., 2007). However, the role of sea ice on the marine carbonate system and ocean-ice-atmosphere CO_2 exchange remains a topic shrouded by large uncertainties. As long as sea ice-driven processes remain unconstrained, they cannot accurately be represented in ocean-climate models that estimate carbon budgets and predict future climates. Surface ocean pCO_2 in sea ice-covered regions is spatially highly variable due to variable freshwater input, mixing, biological processes, and sea ice conditions (Fransson et al., 2009). Temporally, significant multi-year variability exists in the CO_2 uptake by the Southern Ocean, which is sensitive to changes in global and regional atmospheric circulation (Hauck et al., 2020; Landschützer et al., 2015). Relatively rapid and small-scale events, such as storms, as well as mesoscale features, such as eddies, also contribute to the spatial and temporal variability of the system (Fransson et al., 2017; Jones et al., 2017a; Mathis et al., 2012; Nicholson et al., 2022). It has therefore been difficult to upscale findings by local, process-based studies within a highly dynamic and heterogeneous system to larger regions. Global ocean biogeochemical models are used to estimate ocean carbon sinks and global carbon budgets (Friedlingstein et al., 2022; Hauck et al., 2020). The fact that they struggle to capture the strong seasonal variability in pCO_2 in the polar oceans indicates that there are major gaps in our understanding of processes driving this variability, and how they may change in the future.

Uncertainties are challenging to reduce, because data with resolutions high enough to constrain seasonal and sub-seasonal processes are scarce in terms of both spatial and temporal coverage. While sea ice poses a major theoretical challenge in understanding the CO_2 sink in polar oceans, it is also literally the logistical obstacle to solving its theoretical counterpart. Sea ice-covered waters can only be traversed with large ice-breakers, which are expensive to operate. Even the most sophisticated ice-breaking research vessels struggle with thick sea ice cover. The result is that ship-based data collected over the last decades have a strong bias to the summertime when - although weather conditions and sea state are still challenging - sea ice-covered regions are easier to navigate. Observational datasets for polar oceans therefore have a distinct lack of data in the wintertime (Gerland et al., 2019; Takahashi et al., 2009). These biases have strong implications for our understanding of seasonality and carbon budgets.

Autonomous vehicles with sensors that collect year-round profiles of the upper ocean are addressing the seasonal (i.e. winter) and spatial data gaps. Datasets they produce can reveal possible over- or underestimations of CO_2 fluxes in ship-based obvervational data products due to the lack of wintertime representation in data collection (e.g., Bushinsky et al., 2019; Gray et al., 2018). For example, estimates using year-round float data suggest that the Southern Ocean CO_2 sink is significantly lower (i.e. less uptake) than estimates based on ship-based data only, as data products based on the latter underestimated outgassing in the wintertime (Bushinsky et al., 2019; Gray et al., 2018). Ideally, pCO_2 would be measured directly by sensors mounted on deep-profiling autonomous vehicles. However, because of technical reasons, pH is the only carbonate system component that is directly measured on biogeochemical floats. Other carbonate system components, such as alkalinity, are estimated from empirical relationships, which are then used to determine pCO_2 (Gray et al., 2018). The resulting uncertainties in pCO_2 estimates are therefore higher compared to direct ship-based measurements, to such an extent that they overlap (Williams et al., 2017). Therefore, even though sensor-based data collected autonomously are a key development in oceanography, *in situ* observations with higher accuracy are required to calibrate sensors and validate their output.

As a result of the uncertainties in the polar ocean carbon cycle, there is no consensus yet on how the polar ocean CO_2 sink will change in the future. For example, on the one hand, some studies hypothesise that the Arctic Ocean CO_2 sink will strengthen with decreasing sea ice extent, mostly driven by enhanced biological CO_2 uptake as more light availability can support primary production (Anderson and Kaltin, 2001; Arrigo et al., 2008b; Bates and Mathis, 2009; Fransson et al., 2013). On the other hand, simultaneously changing factors that oppose CO_2-decreasing processes, such as warmer seawater temperatures and stratification, could lead to a less efficient CO_2 sink (Cai et al., 2010; Else et al., 2013). Acquiring observational data covering different seasons and large spatial scales in high latitude oceans is a high priority within the polar community to constrain uncertainties around the role of sea ice on the sea-air gas exchange and seawater properties.

Problem statement

The sea-air CO_2 exchange in polar oceans has many modes of temporal variability associated to sea ice cover and its regime. The logistical challenges imposed by sea ice cover and the harsh environmental conditions of the high latitudes have resulted in a **low spatial and temporal data coverage**. Regions with low data coverage include perennially sea ice-covered regions and Antarctic coastlines. Temporally, there is a **paucity of data in winter and of continuous year-round observations**, as well as high frequency measurements. Data acquisition biased on ease of access is an **impediment to developing our understanding of processes** that are important to represent in climate and ocean models to predict the effect of **rapidly changing sea ice extent and regimes** on global carbon budgets.

1.4 Approach and scope

The focus of this thesis is on the surface marine carbonate system in seasonally and perennially sea ice-covered regions. The CO_2 exchange that occurs between sea ice and the atmosphere due to ice-air pCO_2 gradients (Delille et al., 2014; Geilfus et al., 2012; Geilfus et al., 2013; Miller et al., 2011; Nomura et al., 2013a; Zemmelink et al., 2006) is not addressed.

I have produced three separate pieces of research (Chapters 3, 4, and 5), with the following overarching research questions:

Overarching research questions

RQ 1: How do tides affect the marine carbonate system in a Weddell Sea coastal polynya and how does the variability affect local sea-air CO_2 fluxes?

RQ 2: How does variability in sea ice cover drive interannual variability in the marine carbonate system and CO_2 sink along the West Antarctic Peninsula?

RQ 3: What are the drivers of changes in upper ocean carbonate chemistry in the Central Arctic Ocean at the onset of annual freeze-up?

The common theme among these research topics is the *variability* within the surface carbonate system and sea-air CO_2 exchange in polar oceans, covering semi-diurnal (Chapter 3), seasonal (Chapter 5), and interannual variability (Chapter 4). Analyses are based on a set of valuable commodities within polar science: observational *in situ* data based on seawater samples in hard-to-reach regions of polar oceans, at either a frequency that is able to resolve rapid and small-scale processes (Chapters 3 and 5) or collected year-round during consecutive years, including winter months (Chapter 4). These types of data are sought after by the scientific community to help constrain carbon fluxes (Swart et al., 2019). The approach is based on identifying local processes and mechanisms driving the marine carbonate system, which may be relevant in other polar regions and on larger spatial scales (Rintoul, 2018).

Approach and overarching themes

The research presented in this PhD thesis is based on **observational seawater measurements of carbonate system components** in regions of polar oceans that are **difficult to reach** (i.e. Antarctic coastlines and the perennially sea ice-covered Central Arctic Ocean), collected at frequencies and at times in the year when these types of observations are **rare** (i.e. 3-hourly repeat casts and year-round measurements, including wintertime). These observations are used to study physical and biogeochemical processes affecting the carbonate system of the surface layer and air-sea CO_2 flux on **various time scales**, including semi-diurnal-, daily-, and inter-annual variability, and seasonal transitions.

1.5 Outline of the thesis

Chapter 2 covers the theory of the analytical methods used for the determination of dissolved inorganic carbon and total alkalinity. These are two components of the seawater carbonate system on which the bulk of this PhD research is based. This chapter also provides a general context of the oceanography of the study regions where field work was done. **Chapters 3, 4, and 5** present the results of three individual pieces of research. As they have their own specific objectives and research questions, each of these chapters are complete with their own introduction, methods, results, discussion, and conclusions sections. In **Chapter 3**, I present the results of a study done on the impact of tides on the variability of the carbonate system in a coastal polynya in the Weddell Sea, and the implications for sampling strategies in these types of regions. In **Chapter 4**, I present the results of a unique year-round time series spanning almost a decade of the surface carbonate system along the West Antarctic Peninsula and discuss the drivers of interannual variability in CO_2 flux. In **Chapter 5**, I present the results of changes in the surface carbonate system in the Central Arctic Ocean at the onset of annual freeze-up. **Chapter 6** concludes with a synthesis of the above research topics and the PhD project itself.

CHAPTER 2 |

The marine carbonate system, methods, and study regions

Contents

2.1 Marine carbonate system and the marine carbon cycle

About 98 % of the CO_2 in the atmosphere and ocean combined is found in the ocean where it dissolves into bicarbonate and carbonate ions (Eq. 2.1; Zeebe and Wolf-Gladrow, 2001). Combined, dissolved CO_2 and its dissolved ions are referred to as dissolved inorganic carbon (DIC), of which an in-depth definition is given below (Section 2.2.1). More that 97 % of the total ocean carbon consists of DIC, with the remaining carbon consisting of dissolved organic carbon, particulate organic carbon, and particulate inorganic carbon. Carbon in the surface ocean can be exported to deeper ocean layers through downwelling of water masses, biological uptake in the surface layer and subsequent sinking of biomass particles that remineralise at depth (i.e., the biological carbon pump), and through sinking of dense water masses created by brine rejection during sea ice formation (i.e., sea ice pump; Rysgaard et al., 2009; Rysgaard et al., 2011). Once at depth, the exported carbon circulates the global ocean along with currents driven by global seawater temperature and salinity gradients, known as the thermohaline circulation. This is how the ocean sequesters carbon on a timescale of tens of thousands of years. Upwelling of deep water transports DIC back to the ocean surface layer, where it can be used in biological processes or exchange with the atmosphere. On longer geological timescales, the ocean sequesters a small fraction of the CO_2 in the form of calcium carbonate ($CaCO_3$) and organic material, which after burial will form rocks or oil and gas, respectively. These sequestration processes are slow and only occur in certain conditions. For example, $CaCO_3$ will only accumulate at depths in the ocean where the seawater is supersaturated in $CaCO_3$ and/or the supply of $CaCO_3$ is larger than the rate of dissolution (e.g., Sulpis et al., 2021).

$$\mathrm{CO_{2(gas)}} \rightleftharpoons \mathrm{CO_{2(aq)}} + \mathrm{H_2O} \rightleftharpoons \mathrm{H_2CO_{3(aq)}} \rightleftharpoons \mathrm{HCO_{3(aq)}}^{-} + \mathrm{H_{(aq)}}^{+} \rightleftharpoons \mathrm{CO_{3(aq)}}^{2-} + \mathrm{H_{(aq)}}^{+} \qquad \text{(Eq. 2.1)}$$

DIC content is spatially variable across the global ocean and has a latitudinal gradient whereby it increases towards the higher latitudes. This latitudinal gradient is driven partially by low seawater temperature towards the polar regions, which increases CO_2 solubility and thus uptake from the atmosphere, and by upwelling (Wu et al., 2019). Globally, the ocean is increasing its CO_2 uptake from the atmosphere, because atmospheric CO_2 concentrations are increasing due to anthropogenic emissions. The ocean thus has a buffering effect on atmospheric CO_2 increase.

However, seawater is not a simple, infinite atmospheric CO_2 sink, because CO_2 dissolution changes its chemistry and thereby its capacity to absorb more CO_2. When CO_2 dissolves in seawater, it shifts the chemical equilibria towards more protons, acidifying the water (Eq. 2.1). Incidentally, seawater contains proton-accepting ions that help resist a decreasing pH. The total number of proton-acceptors in excess over proton-donors is referred to as total alkalinity (TA). An in-depth definition of TA is given in Section 2.2.2. This is the ocean's own buffering system that helps it maintain a stable pH at ~8.07 (Jiang et al., 2019). If the rate of CO_2 uptake increases, as is happening to oceans globally, the ocean's buffering system loses its effectiveness, with resulting decreases in pH and a shift of the carbonate system towards lower content of carbonate ions (i.e., towards the left in Eq. 2.1). This global trend is referred to as ocean acidification, which has detrimental consequences to marine calcifying organisms that depend on carbonate ions and a certain seawater pH (Cyronak et al., 2016; Orr et al., 2005). Although observations show that biological calcification rates by many species are affected by these changing environmental conditions, the dominant driving forces and mechanisms are complex and continue to be an active field of research (Beaufort et al., 2011; Cyronak et al., 2016).

The strength of CO_2 uptake or release by the ocean is a complex function of many different variables that are represented in parameterisations based on experimental and observational studies. The sign of the CO_2 flux denotes whether CO_2 is taken up by the ocean from the atmosphere (negative) or whether CO_2 is released from the ocean to the atmosphere (positive). It is determined relatively simply according to the sea-air gradient in pCO_2, or rather the fugacity of CO_2 (fCO_2), which also represents the CO_2 partial pressure, but adjusted for non-ideal gas behaviour. For instance, if the ocean has a lower fCO_2 than the atmosphere, it will take up atmospheric CO_2, and vice versa. The concentration of atmospheric CO_2 (from which the fCO_2 can be calculated) is continuously monitored all over the globe. Although vertical and horizontal gradients exist across the troposphere, atmospheric CO_2 is considered to be relatively well mixed. Seawater fCO_2 is spatially more heterogeneous (Takahashi et al., 2009) and needs to be determined carefully for accurate CO_2 flux estimates. The CO_2 mixing ratio (xCO_2) in seawater can be determined, for example, by directly measuring xCO_2 with an infrared analyser in the headspace that has equilibrated with seawater in a headspace-equilibrator (see Chapters 3 and 5, Pfeil et al., 2013). fCO_2 can then be calculated from xCO_2. It can also be calculated from any two of the other marine carbonate system components, using sets of thermodynamic dissociation constants (functions of salinity, temperature, and pressure) that describe the dissociation of dissolved molecules into ions (Zeebe and Wolf-Gladrow, 2001). Accuracy of calculated values is enhanced if additional information, such as the content of macro-nutrients, is also known. These calculations are done by sophisticated programs (e.g., Humphreys et al., 2022) that take an input pair from the marine carbonate system. The four marine carbonate system components include: fCO_2 (or pCO_2), pH, DIC, and TA. These programs will also typically determine the speciation of DIC into CO_2, bicarbonate, and carbonate content, as well as the saturation state of $CaCO_3$ (aragonite and calcite).

DIC and TA can both be measured in discrete seawater samples at high precision (e.g., within 1-2 μmol kg^{-1}, see Section 2.3; Dickson et al., 2007), which is necessary for the detection of trends over time within a highly variable marine system. The research in Chapters 3, 4, and 5 has a strong basis in discrete seawater DIC and TA measurements, which are used as input variables to determine the seawater fCO_2, as well as to investigate biogeochemical effects on the capacity of seawater to absorb CO_2 from the atmosphere. It should be noted that the uncertainty in calculated fCO_2 depends on the input pair. For example, using DIC and TA as the input pair can lead to higher uncertainties in fCO_2 compared to using a combination of pH and DIC *or* TA, despite high-quality measurements (García-Ibáñez et al., 2022). One of the reasons for this is the fact that the use of pH as one of the two input components avoids the use of the thermodynamic constant for the dissociation of bicarbonate, which currently has high uncertainties. Alkalinity due to organic components in seawater can also increase uncertainties, as these are not considered in the parameterisation of the thermodynamic constants used to calculate fCO_2 (García-Ibáñez et al., 2022). For themean pH of the surface layer in the polar oceans (i.e., around 8), upon which my research is based, the difference in the uncertainty of calculated fCO_2 is small or indistinguishable between using DIC and TA or pH and DIC / TA as the input pairs (García-Ibáñez et al., 2022).

Chapters 3, 4, and 5 contain descriptions of the methods and data for each particular, respective study. Given that the bulk of the research is based on seawater measurements of DIC and TA, this methods chapter provides more detail on definitions and analytical methods not covered in other methods sections. It additionally provides a general overview of the study regions and sampling locations where seawater samples were collected.

2.2 Definitions of DIC and TA

2.2.1 Dissolved inorganic carbon (DIC)

Dissolved inorganic carbon (DIC) content is defined as the sum of the contents of the following dissolved inorganic carbon species: carbon dioxide (CO_2), carbonic acid (H_2CO_3), bicarbonate ($HCO_3{}^-$), and carbonate ($CO_3{}^{2-}$) (Zeebe and Wolf-Gladrow, 2001). As the contents of H_2CO_3 is low in the marine aquatic system, it is commonly combined with CO_2 into a hypothetical species, denoted as $CO_2{}^*$ (Eq. 2.2).

Dissolved inorganic carbon (DIC)

$$[\mathrm{DIC}] = [\mathrm{CO_2}^*] + [\mathrm{HCO_3}^-] + [\mathrm{CO_3}^{2-}] \qquad \text{(Eq. 2.2)}$$

In Eq. 2.2, square brackets denote the content (in units μmol kg^{-1}) or concentration (in units μmol L^{-1}) of each species. In this work, I refer to DIC and other seawater constituents in μmol per unit mass of seawater (μmol kg^{-1}). The speciation of DIC is governed by the following equilibrium equations:

$$\mathrm{CO_{2(gas)}} \overset{\mathrm{K_0}}{\rightleftharpoons} \mathrm{CO_2}^*{}_{\mathrm{(aq)}} \qquad \text{(Eq. 2.3)}$$

$$\mathrm{CO_2{}^*{}_{(aq)}} \xrightleftharpoons{K_1} \mathrm{HCO_{3(aq)}{}^- + H_{(aq)}{}^+} \qquad \text{(Eq. 2.4)}$$

$$\mathrm{HCO_{3(aq)}{}^-} \xrightleftharpoons{K_2} \mathrm{CO_{3(aq)}{}^{2-} + H_{(aq)}{}^+} \qquad \text{(Eq. 2.5)}$$

The dissolution of gaseous CO_2 in seawater depends on the solubility of CO_2 in seawater (K_0, mol kg^{-1} atm^{-1}) and the seawater fCO_2 (**Weiss1973**):

$$\mathrm{CO_2{}^*{}_{(aq)} = K_0 \cdot fCO_2} \qquad \text{(Eq. 2.6)}$$

The relative abundance of $CO_2{}^*$, $HCO_3{}^-$, and $CO_3{}^{2-}$ depends on the equilibration constants (also referred to as the carbonic acid dissociation constants), K_1 and K_2. Their definitions are shown below in terms of apparent stoichiometric constants (denoted with *) that relate the dissociation constants to content in seawater:

$$\mathrm{K_1{}^*} = \frac{[\mathrm{HCO_3{}^-}]\,[\mathrm{H^+}]}{[\mathrm{CO_2{}^*}]} \qquad \text{(Eq. 2.7)}$$

$$\mathrm{K_2{}^*} = \frac{[\mathrm{CO_3{}^{2-}}]\,[\mathrm{H^+}]}{[\mathrm{HCO_3{}^-}]} \qquad \text{(Eq. 2.8)}$$

When $[HCO_3{}^-]$ is equal to $[H_2CO_3]$, K_1^* is equal to $[H^+]$. Phrased differently, the negative logarithm with base 10 of K_1^* (pK_1^*) is equal to the pH of the solution, as pH is defined as:

$$pH = -\log_{10}[\mathrm{H^+}] \qquad \text{(Eq. 2.9)}$$

Similarly, the negative logarithm with base 10 of K_2^* (pK_2^*) is equal to the pH of the solution when $[CO_3{}^{2-}]$ is equal to $[HCO_3{}^-]$. In this manner, we can view the content of the DIC species as a function of pH, as illustrated by a Bjerrum plot in Fig. 2.1. At pH 8.07, which is the estimated mean surface ocean pH between 60°S and 60°N (Jiang et al., 2019), most of the DIC content consists of $HCO_3{}^-$. The figure helps to visualise the process of ocean acidification, when uptake of CO_2 decreases seawater pH, resulting in a shift along the curves towards lower $[CO_3{}^{2-}]$ and higher $[CO_2]$ (Doney et al., 2009). The shape of the curves depend on seawater conditions, because K_1^* and K_2^* are a function of temperature, salinity, and pressure (Zeebe and Wolf-Gladrow, 2001). Different formulations for the parameterisation of the carbonic acid dissociation constants exist, which are based on field observations or laboratory experiments.

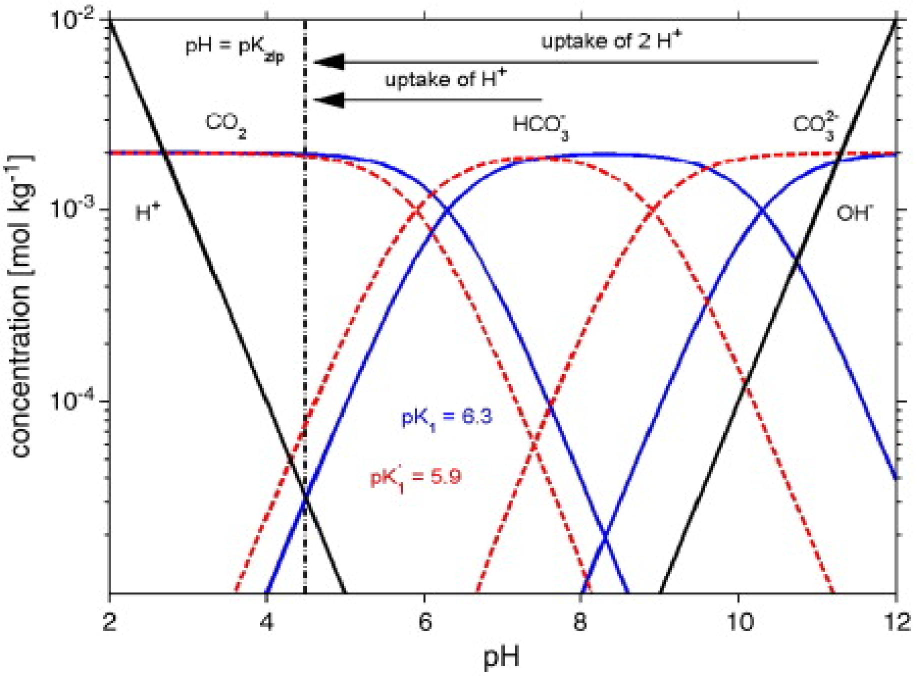

Figure 2.1: Figure from Wolf-Gladrow et al. (2007), illustrating the content of DIC species ($CO_3{}^{2-}$, $HCO_3{}^{-}$, and CO_2), H^+, and OH^- as a function of pH. Blue lines indicate the content determined according to thermodynamic pK values when ionic strength is zero. Red dashed lines indicate the contents determined according to typical seawater stoichiometric pK* values. pK_{zlp} is at pH 4.5, used in the definition by Dickson (1981) to set CO_2 as the zero level of proton species.

One of the advantages of working with DIC is that it is a conservative quantity. What is meant with "conservative" can vary depending on the author. For the purposes of defining DIC (and TA, below) and outlining its importance in studying the marine carbonate system, this work adopts the definition used in (Wolf-Gladrow et al., 2007). They define "conservative quantities" as quantities of a chemical species or a group of chemical species (such as DIC) that remain constant under temperature and pressure changes and follow a linear mixing behaviour. In contrast, the individual components of DIC, such as $CO_3{}^{2-}$, are not conservative according to this definition, because their abundances are a function of temperature and pressure.

2.2.2 Total alkalinity (TA)

Total alkalinity (TA) is loosely described as the buffering capacity of seawater, which helps maintain pH stability when protons are added or removed to a solution. This is because TA is defined according to the number of hydrogen ions that can be accepted by the total number of proton acceptors. More precisely, the definition for TA commonly adopted by marine carbonate chemists is that it is equivalent to "... the number of moles of hydrogen ion equivalent to the excess of proton acceptors (bases formed from weak acids with a dissociation constant $K <= 10^{-4.5}$ at 25 °C and zero ionic strength) over proton donors (acids with $K > 10^{-4.5}$) in 1 kilogram of sample" (Dickson, 1981) (Eq. 2.10).

Total alkalinity (TA)

$$\begin{aligned}\mathrm{TA} = {} & [\mathrm{HCO_3}^-] + 2\,[\mathrm{CO_3}^{2-}] + [\mathrm{B(OH)_4}^-] + [\mathrm{OH}^-] \\ & + [\mathrm{HPO_4}^{2-}] + 2\,[\mathrm{PO_4}^{3-}]^+\,[\mathrm{SiO(OH)_3}^-] + [\mathrm{NH_3}] + [\mathrm{HS}^-] + \ldots \\ & - [\mathrm{H}^+]^-\,[\mathrm{HSO_4}^-] - [\mathrm{HF}] - [\mathrm{H_3PO_4}]\end{aligned} \tag{Eq. 2.10}$$

In Eq. 2.10, TA is the total alkalinity and the square brackets denote the content of each chemical species that are part of an acid-base system (e.g., the boric acid, phosphoric acid, and hydrogen sulphate systems) able to accept or donate protons. For example, the phosphoric acid system consists of H_3PO_4, $H_2PO_4{}^-$, $HPO_4{}^{2-}$, and $PO_4{}^{3-}$. The reason that only the contents of $HPO_4{}^{2-}$, $PO_4{}^{3-}$, and H_3PO_4 are included in Eq. 2.10 is because of the dissociation constants specified in the definition of TA by Dickson (1981). The pK value of $K = 10^{-4.5}$ is 4.5, and is chosen as the "zero level of protons" used to 1) find the dominant species within each acid-base system, and 2) to determine which species within the acid-base system are proton donors or acceptors relative to the dominant species (Wolf-Gladrow et al., 2007). For example, at pH = 4.5, $H_2PO_4{}^-$ is the dominant species. $HPO_4{}^{2-}$ and $PO_4{}^{3-}$ have dissociation constants with pK values > 4.5, and thus will accept protons, whereas H_3PO_4 has a pK value < 4.5 and is therefore a proton donor. Relative to $H_2PO_4{}^-$, the number of protons that $HPO_4{}^{2-}$ and $PO_4{}^{3-}$ can accept is 1 and 2, respectively. The number of protons that can be accepted or donated by each species according to this definition is used to weigh the contribution of each chemical species to TA (Eq. 2.10, Wolf-Gladrow et al., 2007). For the carbonate acid-base system, CO_2 is the dominant species at pH = 4.5, and so the contribution of $HCO_3{}^-$ and $CO_3{}^{2-}$ to TA is 1 and 2, as in these conditions they can accept 1 and 2 protons, respectively.

The choice of pK = 4.5 in the definition of TA is conventional and based on it being lower than the stoichiometric constants for the carbonate species found in natural seawater (Dickson, 1981; Wolf-Gladrow et al., 2007). Similarly to DIC, TA is also a conservative quantity, meaning that its abundance in a solution does not change due to pressure or temperature changes. When learning about the concept of alkalinity, it is worth understanding that its definition is based on a number of conventional decisions that are adhered to within the marine chemistry community for the sake of inter-comparison between studies.

2.3 Principles of analytical methods

Seawater samples were analysed for DIC and TA content using a VINDTA 3C system (Versatile Instrument for Determination of Titration Alkalinity; Fig. 2.2) (Mintrop, 2003). Besides swapping the samples manually, the system is fully automated to determine DIC using a coulometric titration system and TA using a potentiometric titration system (Fig. 2.3). Different VINDTA 3C instruments were used for different parts of the research, details for which are given in Chapters 3, 4, and 5.

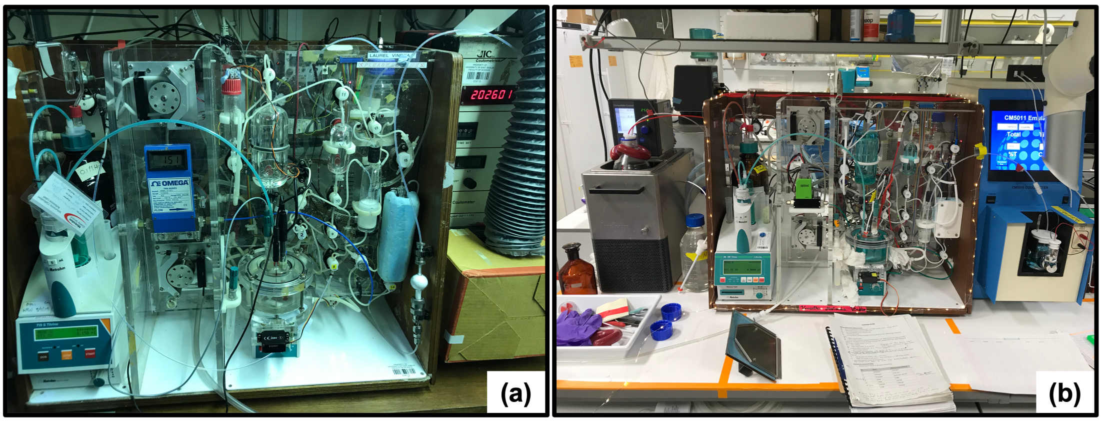

Figure 2.2: Photo of VINDTA 3C systems at the University of East Anglia (a) and at the Alfred Wegener Institute (b).

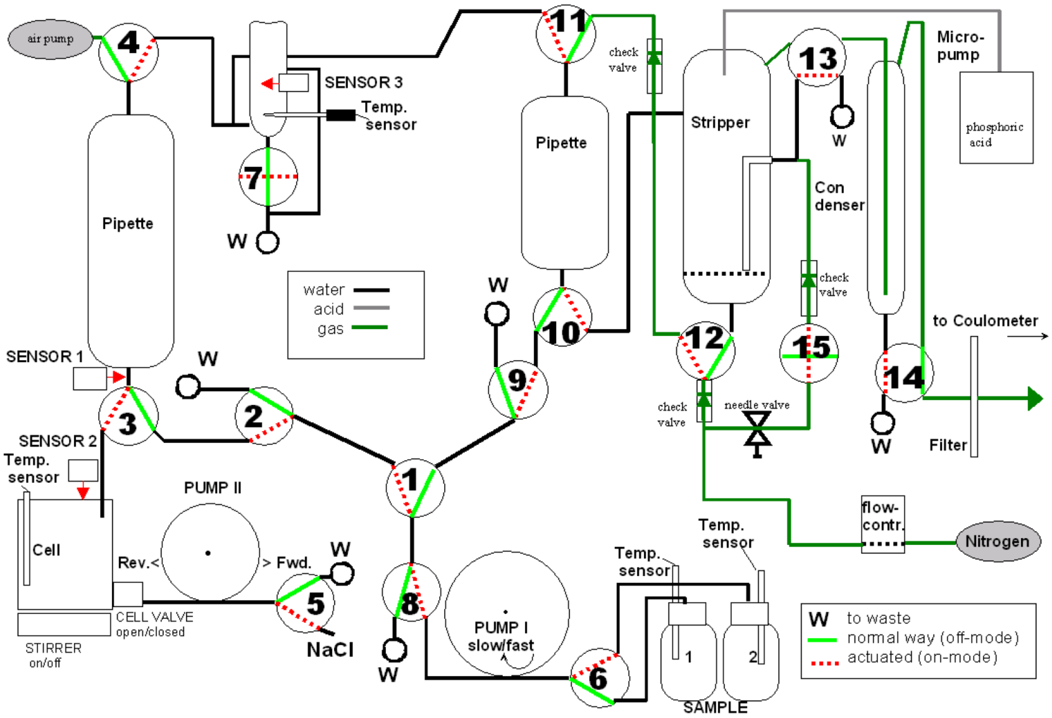

Figure 2.3: Diagram of the VINDTA 3C system, from Mintrop (2003).

2.3.1 Coulometry for the detection of total dissolved inorganic carbon

The method for the determination of DIC content in the aliquot of the sample taken by the VINDTA (Standard Operating Procedure (SOP) 2 in Dickson et al. (2007)) rests upon the shift in chemical equilibria that occurs in Eqs. 2.3 - 2.5 when the solution is strong acidified. The addition of a few mL of H_3PO_4 (8.5 %)) is sufficient to increase the acidity of the aliquot to such an extent that all inorganic carbonate species are converted to CO_2, which is released from the solution in gas form. The CO_2 gas is subsequently stripped from the aliquot using an inert gas and bubbles through a cathode solution in a coulometer cell. The cathode solution contains ethanolamine and a pH-sensitive blue dye (thymolphthalein). The CO_2 gas is absorbed by the ethanolamine solution, creating a weak acid, which decreases the pH of the solution and causes the pH indicator to lose its blue colour. The coulometer continuously photometrically monitors the transmittance of light at ∼610 nm. When transmittance increases as the indicator becomes transparent, the coulometer applies a current to the platinum cathode to electrolise the water and generate hydroxide ions until the pH and transmittance have recovered to their original levels. It effectively titrates the weak acid with an electrolytically generated base. The silver anode dissolves in a potassium iodide-saturated anode solution within an isolated cell, connected to the cathode cell by a glass frit to maintain electrical conduction. A silver iodide precipitate forms, removing silver ions from the solution and reducing migration to the cathode cell where they could participate in redox reactions. The total current applied during the coulometric titration to maintain pH levels in the cathode solution is expressed in coulombs and is directly proportional to the number of moles of CO_2 in the aliquot.

2.3.2 Potentiometry for the detection of total alkalinity

TA was determined similarly to SOP 3b for a potentiometric, open cell volumetric titration method described by Dickson et al. (2007). A Metrohm Dosimat® added a titrant (hydrochloric acid (HCl), 0.1 M) to a known volume of sample aliquot in constant small volume additions and monitored the electrochemical potential across the sample solution, i.e. the analyte.

Two electrodes are used: the indicator electrode and the reference electrode. Each serves as an electrochemical half cell. The electrochemical potential is determined by keeping the potential in the reference electrode half cell (E_{ref}) constant and calculating the potential in the half cell of the indicator electrode (E_{ind}) relative to the former. The electrochemical potential of the analyte is determined according to equation 2.11, where E_{cell} is the difference between the electrochemical potential of the half cell of the indicator electrode (E_{ind}) and the half cell of the reference electrode (E_{ref}).

$$E_{cell} = E_{ind} - E_{ref} \qquad \text{(Eq. 2.11)}$$

2.4 Calibration and computational determination of DIC and TA

Coulometer readings were calibrated against Certified Reference Materials (CRMs) from A. Dickson's laboratory at the Scripps Institute of Oceanography (U.S.A). CRMs were run in duplicates at the start and end (and occasionally in the middle) of all sample runs on the VINDTA on each analysis day. The mean counts of the coulometer for

CRM runs and the certified DIC content value were used to determine the counts per μmol within the volume of the aliquot for each analysis day. This calibrated value was then applied to all samples run on that same day.

The certified TA content of CRMs were used to calibrate the molinity of the HCl titrant. The calibrated titrant molinity was subsequently used to determine the TA per sample by applying a non-linear least squares method to each individual titration curve. Both the titrant calibration and non-linear least squares method were completed using the Calkulate Python package version 23.1 (Humphreys and Matthews, 2022).

2.5 Analytical uncertainty and quality checking

Analytical uncertainties are based on the standard deviation of the determined DIC and TA content of the CRMs that are run along with the samples. The results per CRM batch are plotted in a control chart to 1) check if any drift occurred over time in the coulometer and electrodes, or changes in titrant molinity (e.g., through evaporation), and 2) to mark any clearly faulty CRM measurements that would have to be removed from the analysis. An example of such a control chart is shown in Fig. 2.4 for DIC and TA analyses of CRMs done for samples collected from the Weddell Sea (PS117), using CRM batch no. 176. It shows good results, as datapoints of the DIC and TA content determined for the CRMs are randomly distributed within the range of the mean $\pm$ 2 σ (in this case, 2 σ is 6.6 μmol kg^{-1} and 6.4 μmol kg^{-1} for DIC and TA, respectively), and are rarely outside of this range.

2.6 Study regions

A specific oceanographic description of the study regions is provided in Chapters 3, 4, and 5. In this section, I provide a general description of large-scale circulation and dynamics in the wider Southern and Arctic Oceans as context to subsequent chapters.

2.6.1 Southern Ocean

Even though scientists have long used the name "Southern Ocean" to refer to the body of water around Antarctica, it has only been officially recognised as the fifth distinct ocean on planet Earth by the National Oceanic and Atmospheric Administration (NOAA) and National Geographic Society during the course of this PhD project in 2021. Relatively low salinity and cold temperatures are characteristics of the Southern Ocean, as well as a strong current: the Antarctic Circumpolar Current (ACC; Fig. 2.5). Wind-driven, the ACC flows eastwards around Antarctica, dragging along deep water from the Pacific, Atlantic, and Indian Oceans (Orsi et al., 1995). The ACC acts as a barrier between Antarctica and the rest of the planet, harbouring and protecting its cold climate and unique ecosystems.

The strength of the ACC creates strong meridional gradients in the water column, the properties of which are used to define oceanographic fronts, such as the Subantarctic

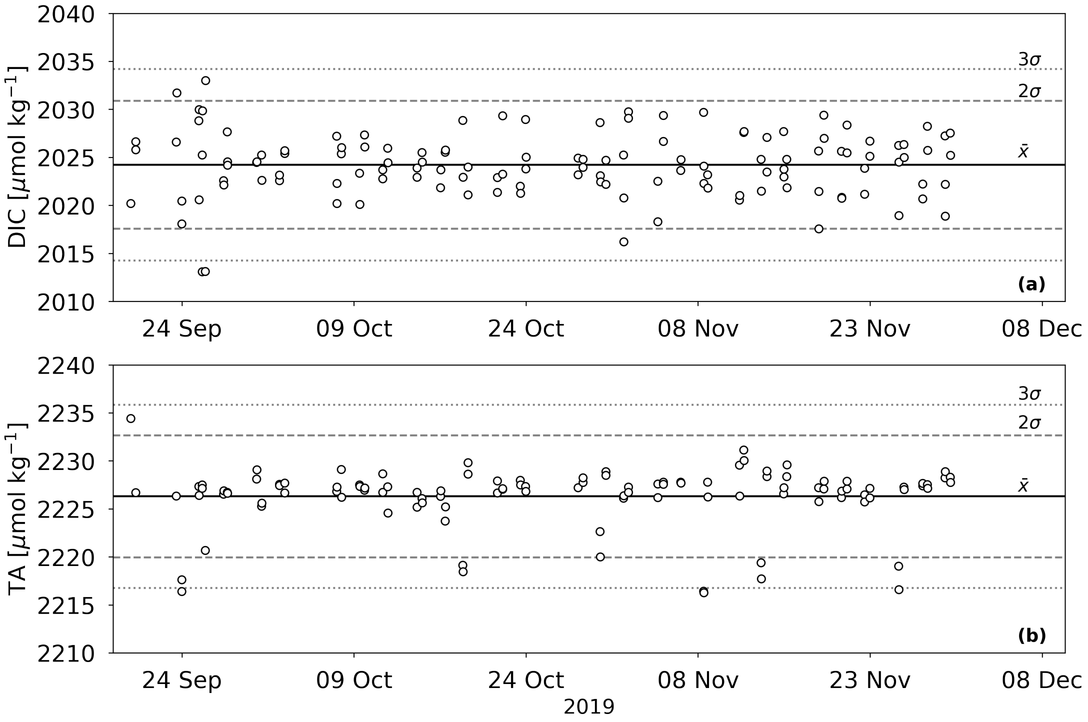

Figure 2.4: Example of a control chart of CRM runs (batch no. 176) for the analysis of (a) DIC and (b) TA content of seawater samples from the Weddell Sea collected on the PS117 expedition. These analyses were done on the VINDTA 3C system at the Alfred Wegener Institute, Bremerhaven, Germany.

Front and the Polar Front (Orsi et al., 1995). The numerous fronts within the Southern Ocean contribute to its complex character. They are important for the Southern Ocean carbon cycle, as they suppress horizontal mixing (Chapman and Sallée, 2017; Naveira Garabato et al., 2011; Thompson and Sallée, 2012) and enhance upwelling and subduction of water masses (Morrison et al., 2015; Stukel et al., 2017), thereby strongly affecting the exchange of carbon between the deep ocean and atmosphere. Note that the fronts vary in space and time, and numerous definitions exist that are sometimes inconsistent (Chapman et al., 2020). The fronts are relevant for large-scale Southern Ocean sea-air CO_2 fluxes and therefore need mentioning in the overall context of the system. However, as the physical mechanisms that create the fronts are not directly relevant to the specific work in this thesis, I will not go into detail (see Chapman et al. (2020) for an overview).

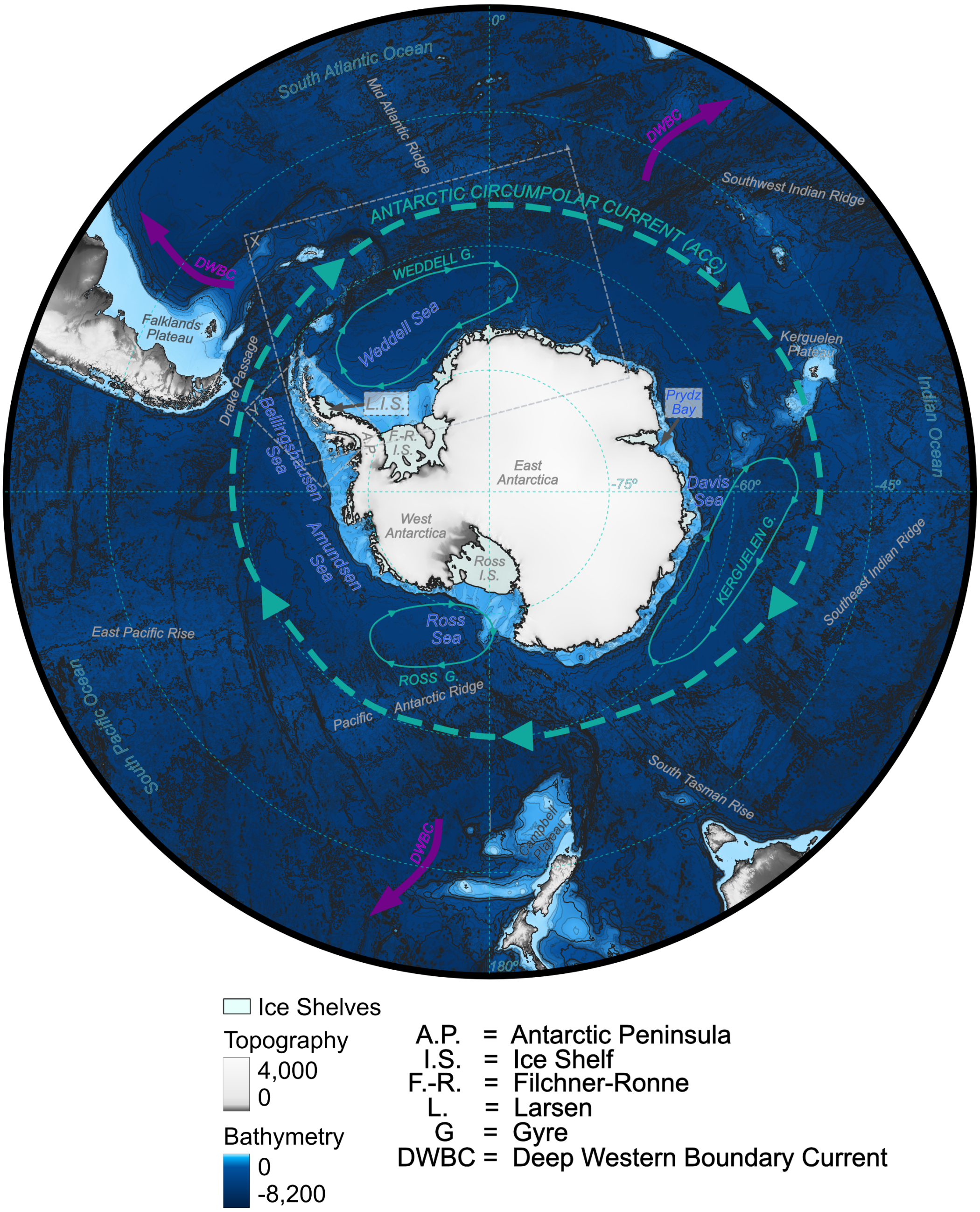

Figure 2.5: Map of the Southern Ocean south of 30°S and its bathymetry (GEBCO, 2022). Arrows indicate the main currents and gyres, modified from Vernet et al. (2019). Regions marked by grey dotted squares X and Y indicate the boundaries for the maps of the Weddell Sea and West Antarctic Peninsula in figures 2.6 and 4.1, respectively. Fig. 4.1 is found in Chapter 4. Credit: James Christie.

Displacement of surface water by the ACC causes upwelling of relatively warm Circumpolar Deep Water (CDW) roughly south of ∼50 °S, surfacing DIC and CO_2 sequestered many years ago, which can then be released to the atmosphere (Morrison et al., 2015). The upwelled deep water mass splits up between a northwards and a southwards flow. In either direction, it is modified by ocean-sea ice-atmosphere interactions (Abernathey et al., 2016). The water flowing northwards due to Ekman transport mixes with northerly water and forms mode and intermediate waters near the northern boundary of the Southern Ocean (i.e., Subantarctic Mode Water and Antarctic Intermediate Water) that subduct and transport any carbon that it absorbed from the atmosphere to the subsurface ocean. The water flowing southwards is modified by mixing with surface water (Foster and Carmack, 1976) and brine rejection during sea ice growth, especially on the continental shelves, creating very dense Antarctic Bottom Water (AABW) that flows down the continental slopes to the abyssal ocean (Foster and Carmack, 1976; Orsi et al., 1999). Hotspots for AABW formation include the Ross Sea, Prydz Bay, and the south-western Weddell Sea (Rodehacke et al., 2007). The overturning occurring in the Southern Ocean provides a unique link between deep water masses and the atmosphere, and drives the global thermohaline circulation, distributing nutrients, heat, and carbon around the global ocean.

On smaller regional scales, the water masses described above are given localised nomenclature as they are modified differently around Antarctica. For example, some of the CDW branches off from the ACC in the Atlantic sector of the Southern Ocean and flows into the cyclonic gyre of the Weddell Sea (Deacon, 1979) (Fig. 2.6). From then on, it is locally known as Warm Deep Water (WDW) and is modified through Ekman-driven upwelling and entrainment of surface water (Orsi et al., 1993). Eventually, a part of it forms Central Intermediate Water (Hoppema et al., 2002) or Weddell Sea Bottom Water (WSBW) (Carmack, 1974). Enhanced CO_2 content at the surface due to upwelling is counteracted by biological productivity (Bakker et al., 2008) and export to the deep ocean (Hoppema, 2004), resulting in the Weddell Sea being a small annual CO_2 sink of about 0.033 ± 0.021 Pg C yr^{-1} (Brown et al., 2015).

The mean maximum sea ice extent in the Southern Ocean is about 19 million km^2. About 84 % of this sea ice cover (16 million km^2) is formed seasonally, while the remaining sea ice is perennial (Stammerjohn and Maksym, 2017). Multi-year sea ice in the Southern Ocean is limited due to the strong connectivity between relatively warm subsurface waters to the surface layers, which enhances ocean heat flux and thereby limits formation of sea ice that is thick enough to survive the melting season (Martinson and Iannuzzi, 1998). Perennial sea ice is found along Antarctic coastlines and especially in the western Weddell Sea, where deformation through extensive ridging and low ocean heat flux promotes thicker ice (Martinson and Iannuzzi, 1998).

2.6.1.1 Weddell Sea field work: PS117 Expedition

I collected seawater samples from the Weddell Sea during the Alfred Wegener Institute (AWI)-led PS117 expedition on the German Research Vessel (R.V.) *Polarstern*. The

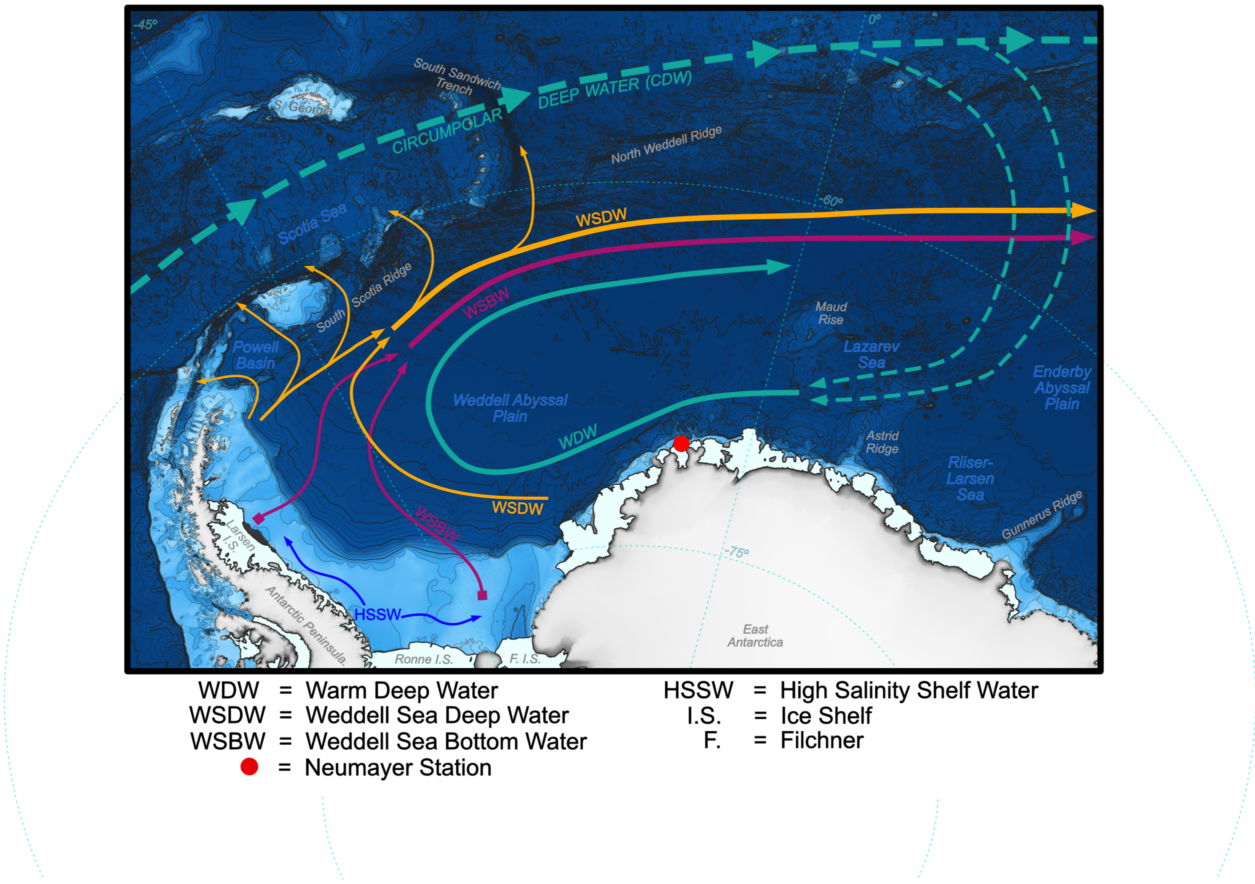

Figure 2.6: Map of the Weddell Sea and its bathymetry (GEBCO, 2022). Arrows indicate the main currents and water masses, modified from Vernet et al. (2019). Credit: James Christie.

expedition started in Cape Town, South Africa, on 15 December 2018 and was completed in Punta Arenas, Chile, on 7 February 2019. Samples were collected from Niskin bottles mounted on a conductivity-temperature-depth (CTD) rosette from AWI and an Ultra-Clean CTD (UCC) run by the Royal Netherlands Institute for Sea Research (NIOZ). Samples were collected between 5 m and the bottom of the ocean at > 5000 m depth. Locations of CTD casts from which seawater DIC / TA samples were collected are shown in Fig. 2.7. While all PS117 data were originally intended to be used in analyses for this PhD research, only a unique suite of samples collected in a summer coastal polynya near the German research station, Neumayer III, were eventually studied in depth (Chapter 3). Further information on sampling methods is provided Section 3.2.

2.6.1.2 West Antarctic Peninsula: Rothera Time Series

Seawater samples in Ryder Bay at the British Rothera research station on the West Antarctic Peninsula (marked in Fig. 2.7) have been collected year-round since the end of 2010 by staff and marine assistants of the British Antarctic Survey as part of the on-going Rothera Time Series. Chapter 4 provides an overview of the regional oceanography and a thorough description of sampling location and methods (Section

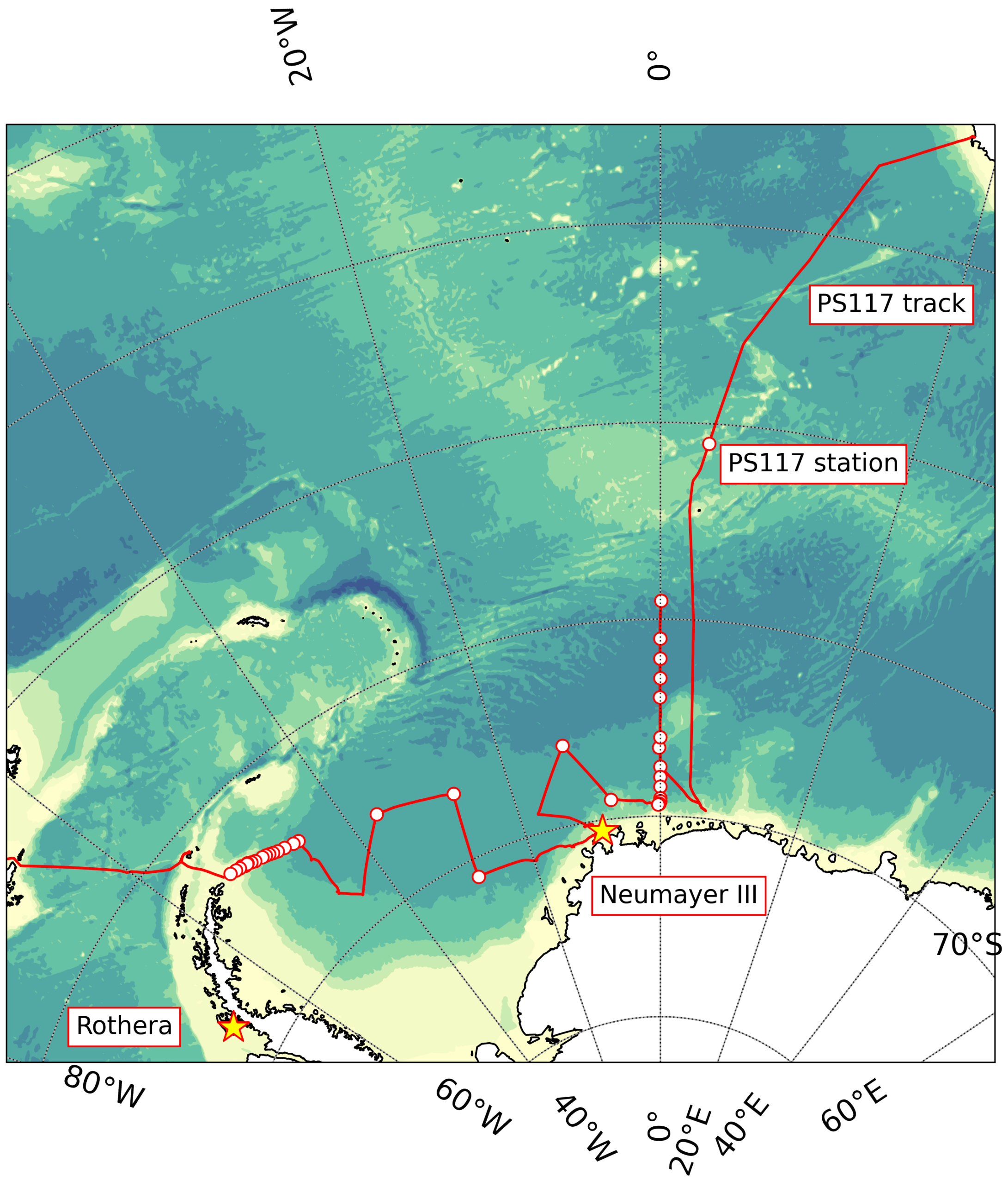

Figure 2.7: Map of the bathymetry of the Weddell Sea and the Southern Ocean in the Atlantic sector, made with Natural Earth data. The PS117 expedition track is shown in red. White markers indicate the locations where DIC / TA samples were collected from the water column. Neumayer III research station and Rothera research station are marked with yellow stars. The research presented in Chapter 3 is based on seawater samples collected at the ice shelf near Neumayer III station and the research presented in Chapter 4 is based on seawater samples collected in Ryder Bay, where Rothera research station is situated.

4.2). I analysed seawater DIC / TA samples collected in 2017-2019, and Gareth Lee and I analysed DIC / TA samples collected in 2019-2020. I processed the DIC / TA data for 2016-2020 of the time series.

2.6.2 Arctic Ocean

While the Southern Ocean circulates the driest continent on Earth, the Arctic Ocean consists of multiple basins surrounded by shallow continental shelves and land rich in precipitation and organic matter. The two largest basins are the Canadian and Eurasian Basins, separated by the Lomonosov Ridge (Fig. 2.8). The Alpha Ridge within the Canadian Basin separates the Makarov and Canada Basins. The Eurasian Basin consists of the Nansen Basin to the south of the Gakkel Ridge, and the Amundsen Basin to the north of the Gakkel Ridge.

Salty, warm Atlantic Ocean water is the main oceanic input into the Arctic Ocean and enters through the deep Fram Strait between Greenland and Svalbard, and through the shallow Barents Sea (Beszczynska-Möller et al., 2012). Pacific Water enters the Arctic Ocean through the shallow Bering Strait between Alaska and Russia (Woodgate et al., 2012). Like Atlantic Water, Pacific Water is also a source of heat. Compared to Atlantic Water, it is relatively fresh and therefore considered an important source of low salinity water (Woodgate and Aagaard, 2005; Woodgate et al., 2012). The main circulation patterns are an anti-cyclonic flow of the Beaufort Gyre in the Canadian Basin, and a cyclonic flow along the continental slopes, driven by atmospheric circulation and steered by topography. The strength and position of atmospheric pressure systems (i.e. the Beaufort High above the Beaufort Gyre and the Icelandic Low towards the Eurasian Basin) result in strong wind forcing across the Arctic, resulting in the Transpolar Drift Stream. Stretching between the Laptev Sea and the Fram Strait, the Transpolar Drift Stream is an important transport pathway for water and sea ice. The Norwegian explorer, Fridtjof Nansen, used the Transpolar Drift Stream (originally) to attempt to reach the North Pole by means of freezing his ship, *The Fram*, into the sea ice.

Seawater leaves the Arctic Ocean via the East Greenland current on the west side of the Fram Strait (e.g., Woodgate et al., 1999) and the Canadian Arctic Archipelago (e.g., Münchow et al., 2006). Through these same exit pathways, fresh water leaves the Arctic Ocean in the form of sea ice (Aagaard and Carmack, 1989). Between entering and leaving the Arctic Ocean, watermasses undergo chemical transformations by sea ice, atmospheric exchange (Tanhua et al., 2009), shelf processes (Fransson et al., 2001), and continental freshwater input (Timmermans and Marshall, 2020), the latter of which fuels the Arctic Ocean margins with nutrients and organic and inorganic carbon at the surface (Holmes et al., 2012; Tank et al., 2012).

Riverine input and sea ice meltwater are important drivers of the buoyancy forcing in the Arctic Ocean (Aagaard and Carmack, 1989), causing strong stratification with cold, fresher water in the upper 50-200 m and warm, salty water below (Rudels et al., 1996). The feature that defines this stratification is the Arctic halocline (Aagaard et al., 1981). Brine rejection during sea ice formation produces dense deep waters that drive the thermohaline circulation in the northern hemispere. As the strong density gradient at the Arctic halocline challenges deep convection in the Central Arctic basin, deep water formation in the Arctic Ocean has been mostly observed along the continental slopes (Ivanov et al., 2004; Jones et al., 1995).

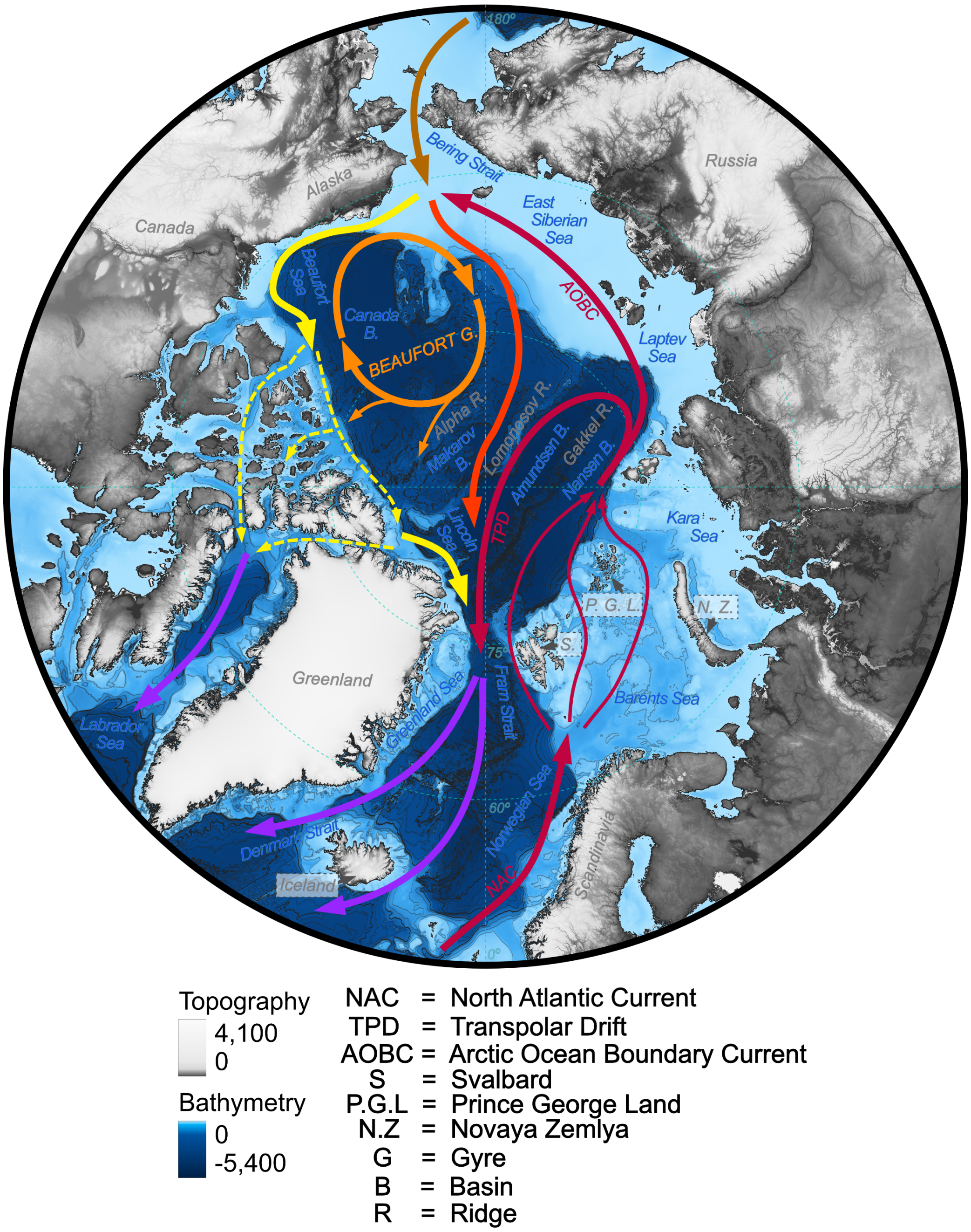

Figure 2.8: Map of the Arctic Ocean and its bathymetry (GEBCO, 2022). Coloured arrows indicate the major upper ocean currents and circulation patterns of the Arctic Ocean, modified from Wang and Danilov (2022) and Greene et al. (2008). The entry of Atlantic Water into the Central Arctic Ocean through the Fram Strait and Barents Sea is shown in red. The entry of Pacific Water through the Bering Strait is shown in brown. The outflow of water from the Central Arctic Ocean through the Fram Strait and Arctic Archipelago is shown in purple. Internal upper ocean circulation within the Central Arctic Ocean is illustrated in different colours and is labelled in the figure, including boundary currents, the Beaufort Gyre, and the Transpolar Drift current. Credit: James Christie.

The mean maximum sea ice extent in the Arctic Ocean reaches about 15 million km^2, of which about 9 million km^2 forms every year and about 6 million km^2 persists year-round (Stammerjohn and Maksym, 2017). The Arctic Ocean is able to produce thicker sea ice than the Southern Ocean, because of the Arctic halocline insulating the warmer deep water, such as the Atlantic Water (Carmack et al., 2015). Thicker ice has higher chances to survive the melting season, subsequently forming multi-year ice. Older ice is found north of Greenland, where older ice accumulates thanks to the Transpolar Drift Stream, and north of the Canadian Archipelago (Barber et al., 2015).

2.6.2.1 Central Arctic Ocean: MOSAiC Expedition

The Multidisciplinary Drifting Observatory for the Study of Arctic Climate (MOSAiC) project, led by the Alfred Wegener Institute, was split into different teams, each covering a discipline and taking responsibility for organising sampling and measurement activities for a set of variables. The MOSAiC expedition started in Tromsø, Norway, on 20 September 2019 and ended in Bremerhaven, Germany, on 12 October 2020. The expedition was split into five different legs. I participated as a member of Team ECO on Leg 5, which, after modifications to the expedition planning due to the COVID-19 pandemic, started on 3 August 2020 and ended on 12 October 2020. Team ECO was responsible for collecting data on a wide range of ecological variables, and a set of biogeochemical variables, such as DIC and TA. Chapter 5 provides a summary of the expedition and sampling locations for Leg 5, as well as objectives, results, and discussions on scientific data collected on the expedition.

CHAPTER 3

The influence of tides on the carbonate chemistry in a coastal polynya in the south-eastern Weddell Sea

My contributions

ESD developed the concept for this manuscript, led the writing process, and collected/analysed/processed the PS117 DIC and TA samples. This work was funded by the Natural Environment Research Council (NERC) through the EnvEast Doctoral Training Partnership (NE/L002582/1). Work done by ESD for the P117 expedition was supported by funding from the NERC for the PICCOLO project (NE/P021395/1).

Contributions by others

DCEB, MH, GDO, BQ, HJV, MGD, and JMSC provided valuable input and guidance for the development of this work. MGD and JMSC independently collected/analysed/processed the PS89 DIC and TA samples. BQ processed the PS117 ADCP data. DS and SO collected/analysed/processed the PS89 and PS117 nutrient data, respectively. GR ran the tidal model. STK collected and analysed the Winkler O_2 samples for the calibration of the dissolved O_2 sensors on PS117. All authors contributed to the manuscript. Work done by DCEB for the PS117 expedition was supported by funding from the NERC for the PICCOLO project (NE/P021395/1). Partial support to JMSC and MGD was received from EU FP7 project CARBOCHANGE (Grant agreement No. 264879) for the participation in the PS89 ANT-XXX/2 cruise. MH was partly funded by the European Union's Horizon 2020 Research and Innovation Program under grant agreement N821001 (SO-CHIC).

Publication status

This work has been published in Ocean Science in 2022:

Droste, E. S., Hoppema, M., González-Dávila, M., Santana-Casiano, J. M., Queste, B. Y., Dall'Olmo, G., Venables, H. J., Rohardt, G., Ossebaar, S., Schuller, D., Trace-Kleeberg, S., and Bakker, D. C. E. (2022). The influence of tides on the marine carbonate chemistry of a coastal polynya in the south-eastern Weddell Sea. Ocean Science, 18(5), 1293-1320.

Abstract. Tides significantly affect polar coastlines by modulating ice shelf melt and modifying shelf water properties through transport and mixing. However, the effect of tides on the marine carbonate chemistry in such regions, especially around Antarctica, remains largely unexplored. We address this topic with two case studies in a coastal polynya in the south-eastern Weddell Sea, neighbouring the Ekström Ice Shelf. The case studies were conducted in January 2015 (PS89) and January 2019 (PS117), capturing semi-diurnal oscillations in the water column. These are pronounced in both physical and biogeochemical variables for PS89. During rising tide, advection of sea ice meltwater from the north-east created a fresher, warmer, more deeply mixed water column with lower dissolved inorganic carbon (DIC) and total alkalinity (TA) content. During ebbing tide, water from underneath the ice shelf decreased the polynya's temperature, increased the DIC and TA content, and created a more stratified water column. The variability during the PS117 case study was much smaller, as it had less sea ice meltwater input during rising tide and was better mixed with sub-ice shelf water. The contrasts in the variability between the two case studies could be wind and sea ice driven, and underline the complexity and highly dynamic nature of the system.

The variability in the polynya induced by the tides results in an air-sea CO_2 flux that can range between a strong sink (- 24 mmol m^{-2} day^{-1}) and a small source (3 mmol m^{-2} day^{-1}) on a semi-diurnal time scale. If the variability induced by tides is not taken into account, there is a potential risk of overestimating the polynya's CO_2 uptake by 67 % or underestimating it by 73 %, compared to the average flux determined over several days. Depending on the timing of limited sampling, the polynya may appear to be a source or a sink of CO_2. Given the disproportionate influence of polynyas on heat and carbon exchange in polar oceans, we recommend future studies around the Antarctic and Arctic coastlines to consider the timing of tidal currents in their sampling strategies and analyses. This will help constrain variability in oceanographic measurements and avoid potential biases in our understanding of these highly complex systems.

Contents

3.1 Introduction

Tides in polar regions have recently gained increasing attention in investigations focusing on understanding the physical interaction between the ocean and sea ice (e.g., Dmitrenko et al., 2012; Kirillov et al., 2013; Skogseth et al., 2013) and how they affect ice shelf melt (e.g., Huot et al., 2021; Makinson et al., 2011; Mueller et al., 2018; Padman et al., 2018; Padman et al., 2009). Tidal effects on the biogeochemistry along polar coastlines, however, have not yet received similar attention, even though tides have been shown to affect the chemical properties and the fugacity of seawater CO_2 (fCO_2) in other regions (Andersson and MacKenzie, 2012; Rogachev et al., 2001; Sims et al., 2022).

The tides in the Weddell Sea are the largest in the Southern Ocean (Padman et al., 2018). Here, relatively warm, carbon-rich Warm Deep Water (WDW) upwells in the east and is physically and chemically altered along its route towards the western Weddell Sea, a hotspot for Antarctic Bottom Water (AABW) formation and carbon sequestration (Anderson et al., 1991; Fahrbach et al., 1994; Huhn et al., 2013). Water on the eastern shelf also has the potential to be exported to the deep ocean by northward transport into the Upper Circumpolar Deep Water (uCDW) (Orsi et al., 2002), along with any modifications to the dissolved inorganic carbon (DIC) content on the continental shelf. Studying processes that modify the physical and chemical properties of these water masses on the shelf, such as tides, will enable a better understanding of the transport of carbon to the deep ocean.

A common feature along the Antarctic coastline are coastal polynyas, described as areas of open water where sea ice cover is expected. Absence of sea ice enables strong direct interaction between the ocean and the atmosphere in regions and at times of the year when sea ice cover would otherwise restrict it and strong gradients between ocean and atmosphere exist. Polynyas are therefore thought to have a disproportionally large impact on the polar oceans considering their relatively small surface area (Barber and Massom, 2007). The direct exposure of the ocean to the atmosphere has an impact on the marine carbonate system, altering the seawater fCO_2 and thus the capacity for ocean CO_2 uptake. Whether the polynya is a source or a sink of CO_2 strongly depends on the interplay between processes that increase the seawater fCO_2 beyond the atmospheric fCO_2, and those that decrease it. For example, polynyas can have an enhancing role in sea ice production as they can release heat directly to the atmosphere (Renfrew, 2002). In this process, brine, including DIC, is rejected from the sea ice matrix into the ocean (Rysgaard et al., 2011; Skogseth et al., 2013). In the summer, dilution by sea ice melt and calcium carbonate ($CaCO_3$) dissolution draws down CO_2 (Rysgaard et al., 2011). Additionally, enhanced light availability supports biological productivity (Arrigo and van Dijken, 2003), which consumes CO_2 that can thereby typically generate a strong CO_2 sink (Arrigo et al., 2008b; Yager et al., 1995). The prolonged ice-free conditions also potentially allow enough time for the polynya to take up as much CO_2 as is necessary to reach equilibrium with the atmosphere (Hoppema and Anderson, 2007). However, biological productivity is found to be variable among

Antarctic coastal polynyas (Arrigo et al., 2015), and in some cases is not sufficient to keep a polynya from outgassing CO_2 (Arroyo et al., 2019). Tides can displace water on short timescales (Llanillo et al., 2019; Skogseth et al., 2013) and modify the water column structure through enhanced mixing (Padman et al., 2009). On the one hand, tidal mixing in coastal polynyas can replenish nutrients at the surface (Tremblay et al., 2002), stimulate biological production, and thereby enhance CO_2 drawdown. On the other hand, mixing with CO_2-rich deep water can increase surface water $f\mathrm{CO_2}$ (Rogachev et al., 2001), or in some cases erode a stable mixed layer necessary to support phytoplankton growth (Arrigo and van Dijken, 2003).

The effects of tides on the marine carbonate chemistry of these biogeochemically impactful regions along the Antarctic coastline remain largely unexplored. Understanding the tidal influence may help us to quantify some of the variability observed among Antarctic polynyas, such as the variability in the biological productivity (Arrigo et al., 2015) as well as the capacity of coastal polynyas to absorb or release atmospheric CO_2 (Arroyo et al., 2019). Practically, this improved understanding can help develop more reliable sampling activities that consider the timing and strength of tidal currents, thereby obtaining representative data of a highly dynamic system.

In this work, we illustrate the effect of tides on the marine carbonate system with two case studies in a coastal polynya in the south-eastern Weddell Sea (Fig. 3.1). We present biogeochemical observations for two tidal sampling campaigns in the austral summer. To the best of our knowledge, this is the first time that tidal influences on the seawater carbonate chemistry are studied in a coastal Antarctic polynya. We discuss the variability induced by tidal forces and explore the differences between the two tidal observations in terms of their physical and biogeochemical characteristics, and what it means for ocean CO_2 uptake.

3.2 Methods

3.2.1 Sampling location

The data were collected during two repeat hydrographic expeditions in the Weddell Sea with the German icebreaker *R.V. Polarstern*: expedition PS89 (2 December 2014 - 31 January 2015; Cape Town - Cape Town; Boebel, 2015) and expedition PS117 (12 December 2018 - 7 February 2019; Cape Town - Punta Arenas; Boebel, 2019). During both expeditions, the tidal cycle was recorded by means of repeat CTD casts at the same location at a frequency that was high enough to constrain the tidal oscillation in the water column. These recordings will hereafter be referred to as *tidal observations*. The tidal observations were performed at the same site in a coastal polynya, 56 km west of Atka Seaport, directly at the edge of the Ekström Ice Shelf (Fig. 3.1), the geometry of which is thought to be representative of most ice shelves of Dronning Maud Land (Smith et al., 2020). The polynya is bordered by the Ekström Ice Shelf along its southern edge, and by sea ice along the rest of its perimeter. It regularly forms in the summer months (Arrigo and van Dijken, 2003; Arrigo et al., 2015; Boebel, 2019). Coastal polynyas in this region are typically formed by katabatic winds from the continent that advect the newly produced sea ice away from the coastline in the spring and summer (Eicken and Lange, 1989; Renfrew, 2002). At the Ekström Ice Shelf, a number of grounded ice bergs to the east can also create a sea-ice free lee downstream from the westward-flowing coastal current (Boebel, 2019).

The size and shape of the polynyas at the Ekström Ice Shelf are highly variable, depending on the wind direction and speed. For the PS89 tidal observations, the average width (between the ice shelf and sea ice) of the Ekström polynya is about 0.8 km, estimated from Synthetic Aperture Radar (SAR) images (Fig. A.1). The length was approximately 12 km. During the PS117 tidal observation, the polynya was substantially larger, having an approximate average width of 3 km and a length of about 40 km (Fig. A.2). Given that the average area of coastal polynyas in the eastern Weddell Sea in summer is 7.75 x 10^3 km^2 (coastal polynyas numbers 12-17 in Arrigo and van Dijken (2003)), the polynya during both tidal observations at this location is considered to be relatively small.

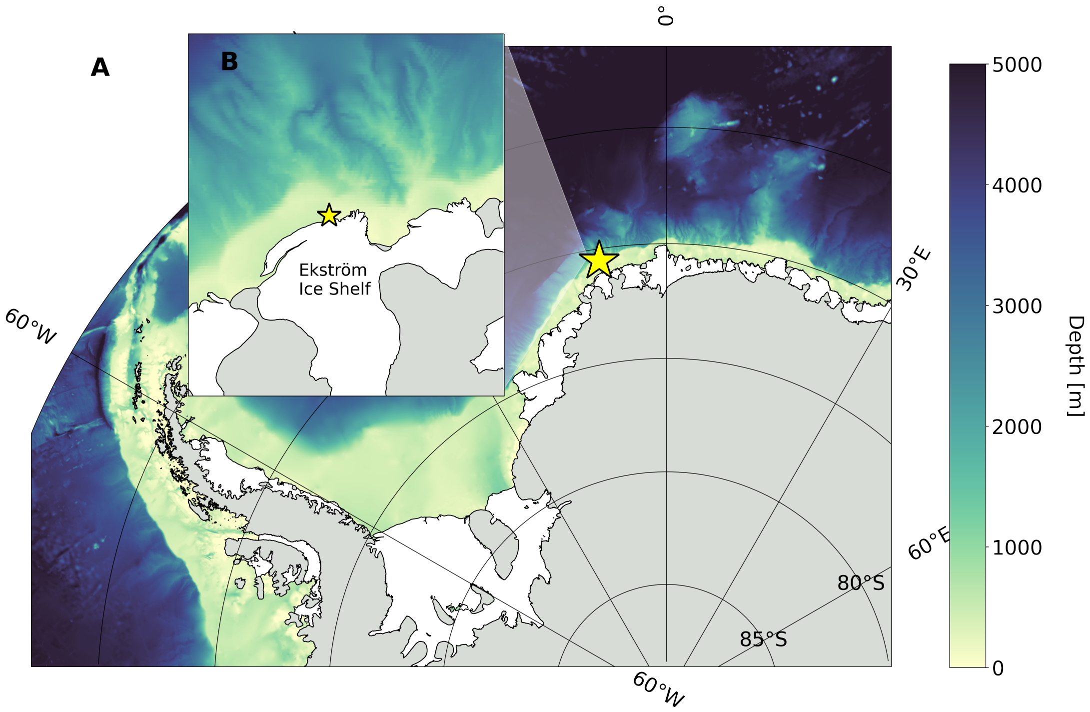

Figure 3.1: Map of study site: (a) Weddell Sea with bathymetry: IBSCO Version 1.0 (Arndt et al., 2013). Grey regions represent the Antarctic continent and land-fast ice, white regions represent ice shelves. (b) Enlarged map of coastal study site along the Ekström Ice Shelf. Yellow star shows the location of tidal measurements. See Table 3.1 for coordinates.

Information about the tidal observations is shown in Table 3.1. Sources of supporting data used in this study can be found in the Supplementary Materials (Table A.1). Both tidal observations were made at the same time of year (i.e. mid-January). The sampling during PS89 (75 hours) lasted ∼3 times longer than during PS117 (22 hours). The exact location of the hydrographic stations differed slightly between the two expeditions due to shifting of the Ekström Ice Shelf extent between 2015 and 2019. The sampling sites for PS117 were chosen in such a way that the distance to the ice shelf was approximately the same as during PS89. Due to other ongoing scientific activities on board during the PS117 tidal observation, the exact location of sampling within the coastal polynya varied slightly per CTD cast, but the casts remained within a maximum distance of 300 m from each other.

3.2.2 Hydrographic and biogeochemical observations

In addition to a SBE911plus CTD sensor, each rosette sampler (SBE32, 24 x 12 L bottles) was equipped with a fluorometer (EcoFLR, Wetlabs), an oxygen optode (SBE43, Seabird Electronics), and an Acoustic Doppler Current Profiler (ADCP) system (2x 300 kHz RDI Workhorse ADCPs) (Table A.2). The oxygen measurements were calibrated using discrete oxygen samples from deep CTD casts only, analysed with the Winkler method (Boebel, 2015; Boebel, 2019; Rohardt and Tippenhauer, 2020). During the PS117 tidal observation period, two different CTD rosettes with their own set of sensors were used in alternation. On one of these two CTD rosettes, the oxygen optode sensor malfunctioned and thus its data had to be excluded from further analysis. The fluorescence data for this particular rosette is also not available. The minor implication of this is addressed in Section 3.3.3.

Dissolved inorganic carbon (DIC) and total alkalinity (TA) samples were collected following Dickson et al. (2007). DIC and TA samples were analysed on a VINDTA 3C system (Mintrop, 2016), which uses coulometry for DIC and potentiometric titration for TA determination. TA was calculated according to Dickson et al. (2007) for PS89 and using the Python package Calkulate (Humphreys and Matthews, 2022) for PS117. On PS89, dissolved phosphate (PO_4^{3-}), silicate (SiO_4), and nitrate (NO_3^-) analyses performed by UV-Vis spectrophotometric methods were carried out on board with a SEAL Analytical continuous-flow AutoAnalyzer (Boebel, 2015). During PS117, nutrient samples were analysed simultaneously for PO_4^{3-}, SiO_4, nitrite (NO_2^-), and the combination of NO_3^- + NO_2^- on board on a continuous gas-segmented flow TRAACS 800 Auto-Analyzer (Technicon, a.k.a. SEAL Analytical) within 4-5 hours after sampling (Boebel, 2019). Samples were calibrated with standards diluted in low nutrient seawater within the salinity range of the Southern Ocean. Analytical uncertainties can be found in Tables A.3 and A.4 .

To complement the ADCP data, a tidal model (Model CATS2008) was used to determine the times of high (rising) and low (ebbing) tide during the tidal experiments. This model has been optimised for the Antarctic seas, using available measurements and including ice shelf cavities to improve performance (Padman et al., 2002). All tidal constituents, which represent each mode of the tidal oscillation on a different time-scale, are used (e.g. M2, S2, K1). The modelled currents are averaged over the entire water column for tidal currents only, i.e. they are not total currents. Total currents (measured by the ADCP) include contributions from, for example, mean flow along the continental shelf.

Table 3.1: Details of the tidal observations based on repeat CTD casts and discrete seawater sampling during the two hydrographic expeditions: PS89 and PS117. For both observation periods, casts were lowered into the water during times of ebbing and rising tide. Depth of the polynya was around 165 m and 200 m during PS89 and PS117, respectively.

	PS89	PS117
Start observations [UTC]	21:09 9 Jan. 2015[a]	14:27 11 Jan. 2019
End observations [UTC]	01:00 11 Jan. 2015	11:57 12 Jan. 2019
Location latitude	70° 31′ 24″ S	70°31′ 19.56″ S
Location longitude	8° 45′34.2″ W	8°46′ 6.76″ W
Deepest depth of CTD cast [m]	160	190.5 - 201.5
No. of CTD casts	40	8
No. DIC/TA bottle samples	260	67
Mean (min. - max.) wind speed [m s^{-1}]	10.7 (4-16)	6.6 (3-10)

[a] Two casts done on 8 January 2015 have not been included into this case study, as they were too disconnected from the rest of the time series. However, the CO_2 flux based on any discrete measurements available from these casts has been included in Fig. 3.8. ADCP measurements started on 7 January 2015. The underway $f\mathrm{CO}_2$ measurements started on 7 January, 2015, at 23:00 (Fig. A.5).

3.2.3 The marine carbonate system and CO_2 flux calculations

The air-sea CO_2 flux was calculated according to:

$$F = kK_0(fCO_{2sw} - fCO_{2atm}) \qquad \text{(Eq. 3.1)}$$

F is the CO_2 flux in mol m^{-2} hr^{-1}, k is the gas transfer velocity, K_0 is the CO_2 solubility at *in situ* temperature and salinity, and $f\mathrm{CO}_2$ is the fugacity of CO_2 in seawater (sw) and in the atmosphere (atm). The gas transfer velocity is calculated according to the parameterisation of Wanninkhof (2014). Minimum, maximum, and average wind speed for the duration of the tidal observation period, as measured on board and reported at 10 m above sea level, were used as input to this parameterisation (Table 3.1). For the Schmidt number, i.e. the parameter that relates the gas transfer velocity of different gases, we use Wanninkhof (2014), which gives a refitted polynomial updated from Wanninkhof (1992) to cover a temperature range of -2 to 40 °C and is virtually the same as the parameterisation by Ho et al. (2006). The CO_2 solubility is calculated according to Weiss (1974). The fugacity of CO_2 is numerically similar to the partial pressure of CO_2 ($p\mathrm{CO}_2$), but accounts for the non-ideal behaviour of the gas. The $f\mathrm{CO}_{2atm}$ is calculated using the virial- and cross-virial coefficients from Weiss (1974) in the equation to convert the atmospheric CO_2 mole fraction to $f\mathrm{CO}_2$ by Weiss and Price (1980). It requires the dry air mole fraction of CO_2 ($x\mathrm{CO}_2$), for which we use discrete air sample measurements from Syowa Station at 69° 0′ 16″S, 39° 34′ 54″E (Dlugokencky et al., 2019), and the water vapour pressure, which is derived from *in situ* seawater temperature and salinity in the parameterisation of Weiss and Price (1980). We use the average $x\mathrm{CO}_2$ of January 2015 and 2019 for the PS89 and PS117 experiment, respectively, and shipboard atmospheric pressure reported at sea level.

The $f\mathrm{CO_2}$ of surface seawater ($f\mathrm{CO}_{2sw}$) is determined from the DIC, TA, nitrate, and phosphate content, as well as the temperature and salinity, of the shallowest discrete seawater samples (typically between 15 and 5 m deep), using PyCO2SYS (Version 1.3) (Humphreys et al., 2022), based on the original work of Lewis and Wallace (1998). Parameterisations by Lueker et al. (2000) were used for the carbonic acid equilibrium constants, by Dickson (1990) for the bisulfate ion dissociation constants, by Uppström (1974) for the boron:salinity relationship, and by Dickson and Riley (1979) for the hydrogen fluoride dissociation constants. Additionally, continuous surface water $f\mathrm{CO_2}$ was measured at the ship's seawater supply with an intake at 11 m depth by a General Oceanics $p\mathrm{CO_2}$ analyser on board, for the PS89 tidal observation only. The discrete surface seawater samples were collected at the same depth as the underway water intake depth (∼11 m) or shallower (∼5 m). The measured and calculated $f\mathrm{CO_2}$ values are comparable for the periods where they overlap (Fig. A.5). Small discrepancies between the measured and calculated values are likely due to the difference in depth and spatial and temporal variability. As is shown in Section 3.4.2, these discrepancies are not large enough to affect the agreement between the $\mathrm{CO_2}$ flux estimates based on these two sets of $f\mathrm{CO_2}$ data. Alongside $f\mathrm{CO_2}$, the PyCO2SYS package simultaneously resolves other carbonate system parameters with DIC, TA, and auxiliary data (listed above) as input parameters (Humphreys et al., 2022; Zeebe and Wolf-Gladrow, 2001). These include the saturation state for calcite and aragonite (polymorphous forms of calcium carbonate) and pH.

3.3 Results

3.3.1 Tidal current

The u (east-west) and v (north-south) components of the current velocity measured by the ADCP are significantly positively correlated to each other (Fig. A.7). They synchronously alternate sign roughly twice a day throughout the water column (Padman et al., 2002), resulting in a barotropic (depth-averaged) component of the flow that matches the modelled tidal velocity (Fig. 3.2). The semi-diurnal tidal currents are thus a dominant component of the total current velocity at this sampling location. The vertical grey areas in Fig. 3.2 (and in other figures) indicate the time and duration of ebbing tide, here defined as the time when both the u and v components of the modelled current velocity are positive, i.e. the direction of the current is towards the north-east. When both components are negative, the direction is towards the south-west and here considered to be rising tide. Note that the white vertical areas in the figures include the rising tide as well as times when either the modelled u or v component is negative.

The velocity profiles are generally homogeneous during ebbing tide. More vertical structure is seen in both velocity components after peak velocities are reached during rising tide during PS89. These baroclinic (depth-dependent) flows induce short-lived vertical shear between the surface and subsurface layers before velocity profiles homogenise again towards the north-east (ebb). The range of current velocities is slightly

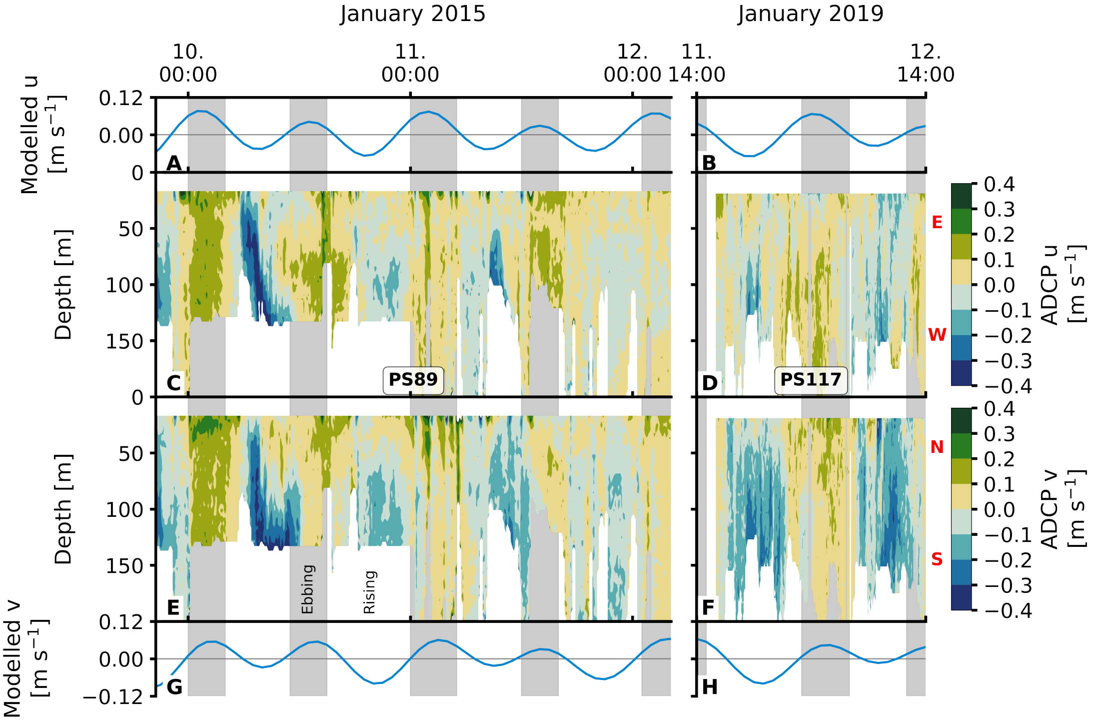

Figure 3.2: Current velocity for PS89 (a, c, e, g) and PS117 (b, d, f, h). Modelled u component of the tidal currents is shown in panels (a) and (b). The modelled v component is shown in (g) and (h). Modelled tidal velocities are averaged over the full water column. The u component of the ADCP profile data is shown in (c) and (d). The v component of the ADCP data is shown in (e) and (f). Vertical grey-shaded areas indicate times of ebbing tide, here identified as times when the u and v components in the modelled tidal current are both positive, i.e. the direction of the current is north-east. Directions associated to the positive and negative values of the u and v components are indicated by the red letters next to the colour bars: N (north), S (south), E (east), W (west).

larger during the PS89 tidal observation than during PS117 (Fig. A.7), which is mainly due to the higher velocities in the morning of 10 January 2015. The modelled tidal current at this time is not particularly stronger than at any other time point in the observation period, including PS117. The stronger current in the first half of 10 January 2015 is thus likely the result of other enhancing factors, such as wind speed and direction.

Both the PS89 and PS117 discrete tidal observations were made five days after spring tide, although the spring tide prior to the PS89 observations was at full moon (5 January 2015) and the spring tide prior to the PS117 observations was at new moon (6 January 2019; dates obtained from https://tidesandcurrents.noaa.gov/historic_tide_tables.html, last access: 16 February 2022). The tidal observations of both case studies are thus set at a similar time in the spring-neap tidal cycle. Peak-to-peak tidal heights in this region are around 2 m, but may increase by a factor of two during spring tides (Padman et al., 2018; Padman et al., 2002). Our datasets only capture a small fraction of time, and we cannot judge the relative strength of the tide beyond its time limits. However, considering that the dominant constituent of tidal oscillations in the

Weddell Sea is the semi-diurnal constituent (Padman et al., 2002) and that the modelled velocities are similar between both tidal observations, we regard the two case studies as comparable in terms of tidal influence on the system.

3.3.2 Physical variability

A clear semi-diurnal tidal cycle is observed in the physical properties of the water column during the PS89 tidal observation period in January 2015 (Fig. 3.3). Over the depth horizons, salinity increases and temperature decreases throughout the water column during ebbing tide. Isopycnals rise to the surface, resulting in a shallow stratification. A mixed layer forms at the surface during ebbing tide with relatively uniform properties and an average depth of ~20 m. The mixed layer depth (MLD) is determined by a 0.03 kg m^{-3} density difference with the average of the top 10 m. During rising tide, the MLD tends to either deepen or the mixed layer breaks down altogether as the density decreases. When a steep density gradient is absent, which typically occurred during rising tide, the water column is considered to be relatively well mixed. The isolines for salinity and temperature deepen as the surface water becomes fresher and warmer. These semi-diurnal fluctuations occur throughout the water column, down to the bottom at almost 200 m depth.

While a similar tidal pattern is also recorded in the salinity and temperature profiles of the shorter PS117 tidal observation, the amplitude of variability for salinity is much smaller compared to PS89. The salinity values for PS117 range only between 34.13 and 34.29, while they range between 34.03 and 34.34 for PS89. With values between -1.58 °C (at the surface) and near freezing -1.89 °C (at the bottom), the temperatures measured during PS117 have a smaller range and are generally lower than those measured for PS89 (-1.42 to -1.85 °C). In contrast to PS89, no mixed layer was identified at any point during the PS117 tidal period, as a steep density gradient was absent and the entire water column was better mixed.

3.3.3 Biogeochemical variability

Despite the lower vertical resolution compared to the continuous sensor measurements, the discrete bottle measurements capture the variability in the water column well, as shown by comparing the discrete bottle and continuous profile measurements for density (Fig. A.6). We are therefore confident that the discrete biogeochemical measurements are also representative of the variability in the water column at the time of sampling.

The DIC and TA content mimic the tidal signature as seen for salinity (Fig. 3.4): their content decreases throughout the water column when the tide comes in, and increases as the tide goes out. The variability is, again, much lower during PS117 than during PS89. For the PS89 tidal observation, the DIC (TA) varied between 2174.3 and 2217.9 μmol kg^{-1} (2307.3 and 2327.1 μmol kg^{-1}) at the surface (<50 m) and between 2186.8 and 2222.7 μmol kg^{-1} (2312.3 and 2328.7 μmol kg^{-1}) at greater depths (>50 m). During PS117, DIC and TA content overall ranged from 2202.6 to 2220.1 μmol kg^{-1} and 2311.5 to 2322.3 μmol kg^{-1}, respectively. In the ocean, changes to salinity are driven

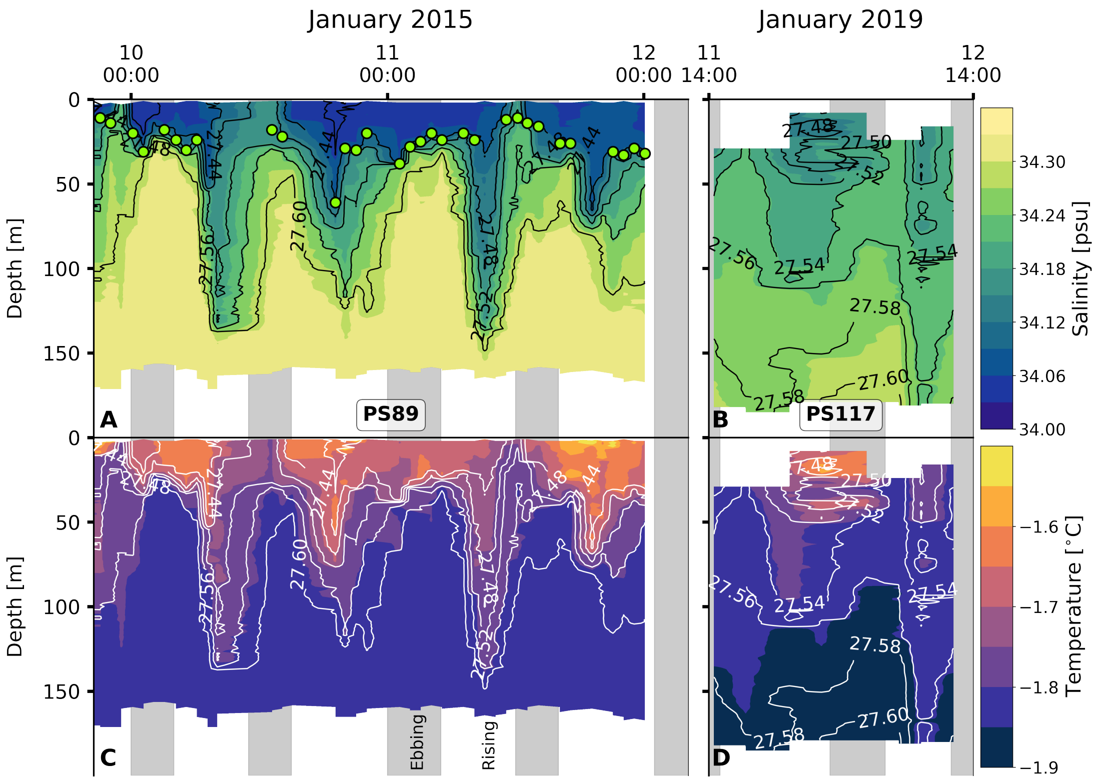

Figure 3.3: (a) and (b) show the salinity for PS89 and PS117, respectively. Green markers in (a) indicate the mixed layer depth (MLD) for casts where a mixed layer could clearly be identified according to a strong density gradient. MLD is identified as the depth at which the density difference with the average density values of the top 10 m is 0.03 kg m^{-3}. Temperature profiles are shown in (c) (PS89) and (d) (PS117). White contour lines represent isopycnals in kg m^{-3}. Vertical grey shaded areas indicate times of ebbing tide.

by oceanographic processes, such as dilution, ice formation, and mixing. These physical processes also impact DIC and TA, which is why DIC and TA are often strongly correlated to salinity (Middelburg et al., 2020). This is also the case in our dataset. However, DIC and TA content are additionally a function of biological (e.g. photosynthesis, respiration, and remineralisation) and chemical (e.g. $CaCO_3$ dissolution and precipitation) processes (Zeebe and Wolf-Gladrow, 2001). To be able to study the role of biogeochemical processes on DIC and TA content, it is useful to separate the effect of physical processes, such as dilution and mixing of different water masses, from the rest. This can be done by normalising the DIC and TA values to the salinity, which we have done here according to methods by Friis et al. (2003). The salinity-normalised DIC (nDIC) and TA (nTA) profiles lose much of the semi-diurnal variability seen in the profiles of the non-salinity-normalised values, suggesting that physical processes are the dominant drivers of the observed variability in DIC and TA (Fig. A.9). PS117 nDIC values are markedly higher than those for most PS89 samples (Fig. 3.5). A part of this increase in nDIC over time could be result of the increase in atmospheric CO_2, assuming at least partial equilibration with the atmosphere. The atmospheric fCO_2 increase (10 μatm) alone could contribute ~6 μmol kg^{-1} to the surface DIC content if all other variables remained the same. This upper-bound estimate is based on average values of the top 10 m during PS89 and assumes equilibration of the surface water with the atmosphere.

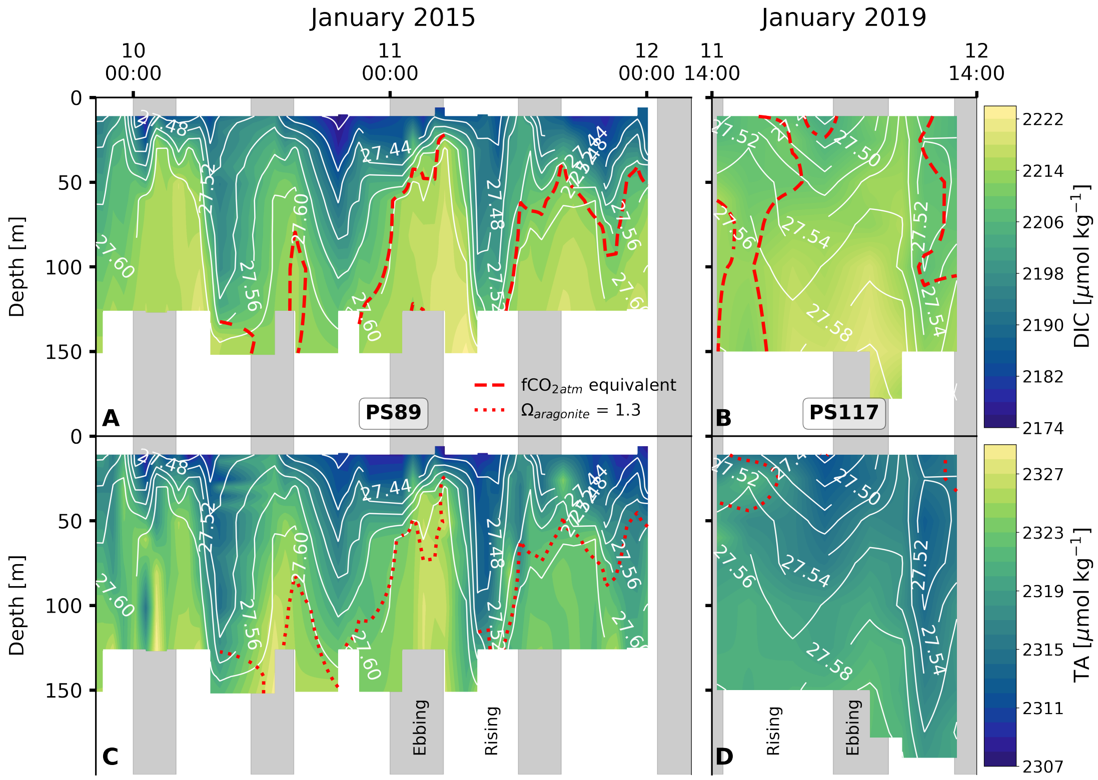

Figure 3.4: DIC content at the sampling site during the PS89 (a) and PS117 (b) tidal observations. TA content for the PS89 (c) and PS117 (d) observations. White contour lines indicate sigma-t in kg m^{-3}. Vertical grey shaded areas indicate periods of ebbing tide, as defined in the text. Red dashed line in A and B represents the depth at which the seawater $f\text{CO}_2$ is equal to the atmospheric $f\text{CO}_2$, which is 377 μatm in January 2015 and 387 μatm in January 2019. Seawater shallower than this depth is undersaturated in $f\text{CO}_2$ compared to the atmosphere. The red dotted line in C and D represents the depth at which $\Omega_{ar} = 1.3$. Ω_{ar} is lower at depths below this line. The value 1.3 is arbitrary, used to illustrate the vertical variability in the water column. Ω_{ar} ranges between 1.22-1.52 and 1.21-1.34 for PS89 and PS117, respectively.

PS117 nitrate (28.9 - 30.1 μmol kg^{-1}), phosphate (2.0 - 2.1 μmol kg^{-1}), and dissolved oxygen (322.0 - 333.2 μmol kg^{-1}) concentrations throughout the water column have similar values as those at the bottom of the water column during PS89 (Fig. 3.6, A.10, A.12). This is not the case for silicate, for which its PS117 values lie around the mean silicate values measured for PS89 (60.0 ± 1.1 μmol kg^{-1}; Fig. A.10, A.12). This observation illustrates that silicate behaves differently from phosphate and nitrate, as its content is affected by other processes, i.e. by diatom growth and remineralisation at depth or in the sediment rather than by photosynthesis and biological respiration (Sarmiento and Gruber, 2013). Similarly to nDIC and nTA, the nutrients were salinity-normalised (following Friis et al. (2003)). Consistent to nDIC and nTA, no obvious deviations from the mean salinity-normalised values are observed that could indicate a dominant biological influence (Fig. A.13). It supports the observation made above that the dominant driver of the variability observed within each tidal case study is mostly physical. For the salinity-normalised silicate content, the averages of both tidal observations are similar to each other (59.5 ± 0.5 μmol kg^{-1} for PS89 and 59.2 ± 0.2 μmol kg^{-1} for PS117; Fig. A.13), indicating that processes affecting silicate content did not differ much between the two case studies. However, a consistent offset between the case studies is observed for the salinity-normalised values for nitrate and phosphate, where PS117 values are on average higher by 1.6 μmol kg^{-1} and 0.1 μmol kg^{-1}, respectively. Even though biogeochemical processes might not be able to explain the variability within each tidal observation, these results suggest that the polynya may have had a higher input and/or a lower loss of nitrate and phosphate during January 2019 compared to January 2015. Fluorescence is here used as a proxy for the presence of photosynthetic cells. While the rising tide increased fluorescence in the water column during PS89, it was barely detected during PS117 (Fig. 3.6). In the absence of active photosynthetic cells, remineralisation enhancing the nitrate and phosphate content may have been an important process in the water observed during PS117.

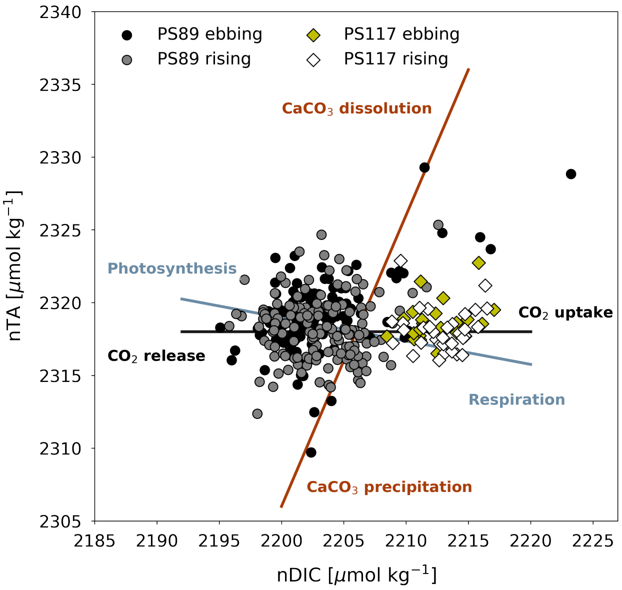

Figure 3.5: Salinity-normalised TA (nTA) and DIC (nDIC) plotted against each other for PS89 (circles) and PS117 (diamonds) tidal data. Samples collected during ebbing (black circles and yellow diamonds) or rising tide (grey circles and white diamonds) are differentiated by different marker colours. Theoretical process lines are drawn for $CaCO_3$ dissolution/precipitation, photosynthesis/respiration, and CO_2 uptake/release (Zeebe and Wolf-Gladrow, 2001).

Due to complications with the data for dissolved oxygen and fluorescence on four of the CTD casts of the PS117 tidal observation, these data were excluded from analysis. The implication of this reduced temporal resolution is that we risk losing representation of water column variability in our dataset for these two variables. However, the low water column variability over time for the physical and other biogeochemical variables (for which we do have data from every cast) strongly suggest that there likely is not a

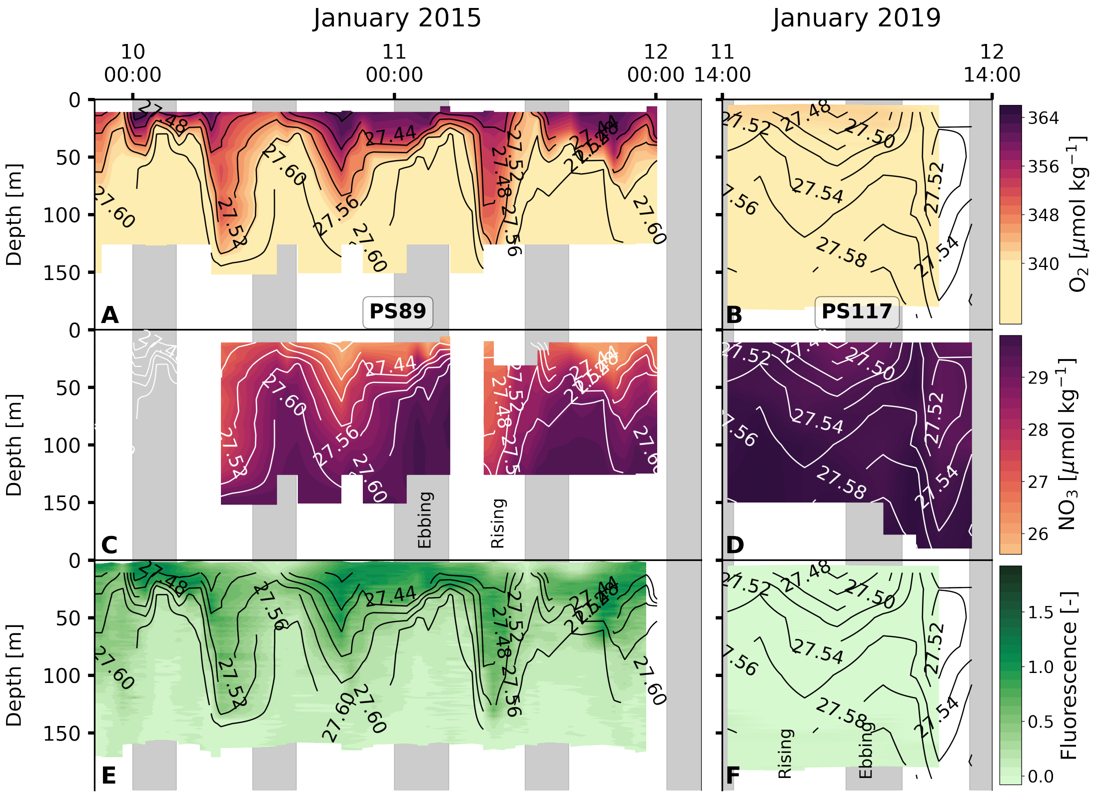

Figure 3.6: Same as Fig. 3.3, but for dissolved O_2 ((a) and (b)), NO_3^- ((c) and (d)), and fluorescence ((e) and (f)). Fluorescence during PS117 varied at values < 0.09.

lot of variability in the dissolved oxygen or fluorescence content that we are missing out on due to missing profiles (Fig. 3.6).

3.4 Discussion

3.4.1 Water masses and biogeochemistry

Hydrographically, the water measured during both tidal observations is identified as Eastern Shelf Water (ESW), which is found south of the Antarctic Slope Front (ASF) where pycnoclines slope downwards towards the south at the edge of the narrow continental shelf of the Dronning Maud Land coastline (Heywood et al., 1998). ESW is characterised by salinities between 34.28 and 34.4 and temperatures close to freezing point (Carmack, 1974). ESW itself is a mixture of the following water mass types (Fahrbach et al., 1994):

- Winter Water (WW, winter surface water capped by a warmer summer stratification; characterised by a subsurface temperature minimum (Nicholls et al., 2009))
- Antarctic Surface Water (AASW, derived from WW that has been freshened by sea ice melt and heated by solar radiation in the spring and summer)
- modified Warm Deep Water (mWDW, which is the result of mixing between WW and WDW along the ASF (Ryan et al., 2020))

- glacial meltwater (GMW, formed by melting of glaciers, and of ice shelves induced by intrusions of warmer water, such as mWDW and AASW, underneath the ice shelf (Fahrbach et al., 1994; Zhou et al., 2014)).

However, the oscillations in the physical and biogeochemical properties induced by the incoming and outgoing tide suggests that the tide is enabling movement and possibly mixing of water masses, which is especially pronounced in the PS89 dataset (Fig. 3.3). While water in the Ekström polynya can broadly be categorised as one water mass (i.e. ESW) according to the physical properties, we will here explore the deepening and shoaling of the isopyncals, as well as the changing water physico-chemical properties.

At rising tides during PS89, the tide brings in water from the north-east that is fresher and warmer compared to the water present at the sampling location during ebbing tide (Fig. 3.3a and 3.3c). A well-defined mixed layer with relatively uniform properties is seen at the surface during ebbing tide (∼ 20 m depth), which tends to disappear or deepen when the tide comes in and the water column density decreases. Similar observations of tide-driven shoaling and deepening of isopycnals have been made in other Antarctic coastal systems, although in lower wind conditions (Llanillo et al., 2019, $<$4 m s^{-1}, see Table 3.1 for PS89 wind speeds). A destabilising (stabilising) water column has previously been associated with the rising (ebbing) tide observed in coastal polynyas in the Arctic (Skogseth et al., 2013). In the latter study, the tidal variability was characterised by a salinity front that moved back and forth with the tide. This "salinity front" is characterised by lower and higher salinities in the water column on either side of a sharp horizontal salinity gradient. A salinity front of this description might have been moving back and forth with the tide over the sampling site in the Ekström polynya, which from a Eulerian perspective resulted in the properties of the water column changing as shown in Fig. 3.3 and 3.4.

In our case study, the fresher water with lower DIC and TA content on the north-eastern side of the salinity front (and sampling site) is likely advection of AASW, influenced by summer sea ice melt. Based on the fluorescence increase during rising tide for PS89 (Fig. 3.6e), the water on this side of the front seems to be richer in phytoplankton cells compared to the south-western side of the front. In addition to a dilution effect, the accompanying increased fluorescence signal during rising tide suggests that photosynthesis in this water has likely contributed to its lower DIC, TA, and nutrient content (Fig. 3.4, 3.6), which is sustained by solar radiation. The advection of fresher, lower DIC and TA seawater from the north-east during rising tide is likely enhanced by high winds (4 - 16 m s^{-1}) that consistently came from the north-east during - and in the week prior to - the PS89 tidal observation (Fig. A.14a and A.15a).

In comparison to PS89, the sampling site during PS117 has less pronounced freshening of the surface water during rising tide, thereby highlighting the interannual variability of the system. Instead, the entire water column is much more uniform with very few vertical gradients during the observation period. Differences in shape and size of the polynya between the two case studies may have affected the proximity of a salinity front to the sampling site. Even though the average sea ice concentration in the immediate vicinity of the sampling site was highly variable in the two months leading up to both PS89 and PS117 (not shown), the polynya was at least three times larger and more well-defined during PS117 than during PS89 (Section 3.2.1, Fig. A.1 and A.2). If a salinity front existed during PS117, it could have been located further away from the ice shelf edge, and the sharp horizontal salinity gradient might therefore not have passed directly over the sampling site during PS117 as it did during PS89. Moreover, winds during PS117 may not have had the same enhancing effect on the advection of fresher, diluted water during rising tide compared to PS89. Whereas high winds during PS89 consistently came from the north-east, the wind speeds during PS117 were lower (3 - 10 m s^{-1}) and their direction was more variable, mainly coming from the ice shelf in the south-east (Fig. A.14b and A.15b). Modulating effects of winds on tidally-induced changes in physical water column properties, whether enhancing or counter-balancing, have also been observed in coastal systems at the Antarctic Peninsula (Llanillo et al., 2019).

The other side of the salinity front (i.e from the south-west) brings in higher salinity and lower temperatures into the polynya during ebbing tide. This water is less ventilated than AASW and shares physical properties with ice shelf water. Ice shelf water is characterised by potential temperatures of <-1.8 °C and salinity >34.6 (Carmack, 1974). However, recent work by Smith et al. (2020) has shown that the temperature and salinity from a number of CTD profile measurements underneath the Ekström Ice Shelf in the same summer season as PS117 (2018/2019) ranged from -2.08 to -1.83 °C and 34.21 to 34.38, respectively (Fig. 3.7). These values overlap with the temperature and salinity measured within ~10 m of the bottom of the sampling site during both tidal observations, especially when the tide goes out.

It is possible that the ebbing tide draws out water from underneath the ice shelf which is expected to be colder. Indeed, this possibility is supported by findings in Smith et al. (2020), which includes a repeat profile of the Ekström Ice Shelf's cavity water at one of the measurement stations on the ice shelf (EIS-4; Fig. 3.7). The two repeat profiles at EIS-4 were taken 11 hours apart. The small difference observed in the vertical salinity and temperature profile between these two casts was attributed to tidal influences extending underneath the ice shelf (Smith et al., 2020). As well as some vertical displacement of the ice shelf by the tidal force (Legrésy et al., 2004), horizontal displacement also occurs underneath the ice shelf. Another study found 12-h and 14-d fluctuations in a temperature time series 70 m underneath the Ekström Ice Shelf (June 2012 to February 2013), ranging between -1.94 and -1.6 °C (Hoppmann et al., 2015). It also described effects of the tide on the glacial meltwater outflow, which could be seen in the orientation and growth of platelet ice crystals in Atka Bay (Hoppmann et al., 2015), adjacent to the Ekström Ice Shelf and east of the sampling site in the current study. In terms of biogeochemical properties, the sub-ice shelf water is expected to be less ventilated compared to the AASW and to have relatively high nutrient and DIC content, and lower dissolved oxygen content, as a result of net remineralisation and lack of exchange with the atmosphere. Due to the lack of exposure to the atmosphere,

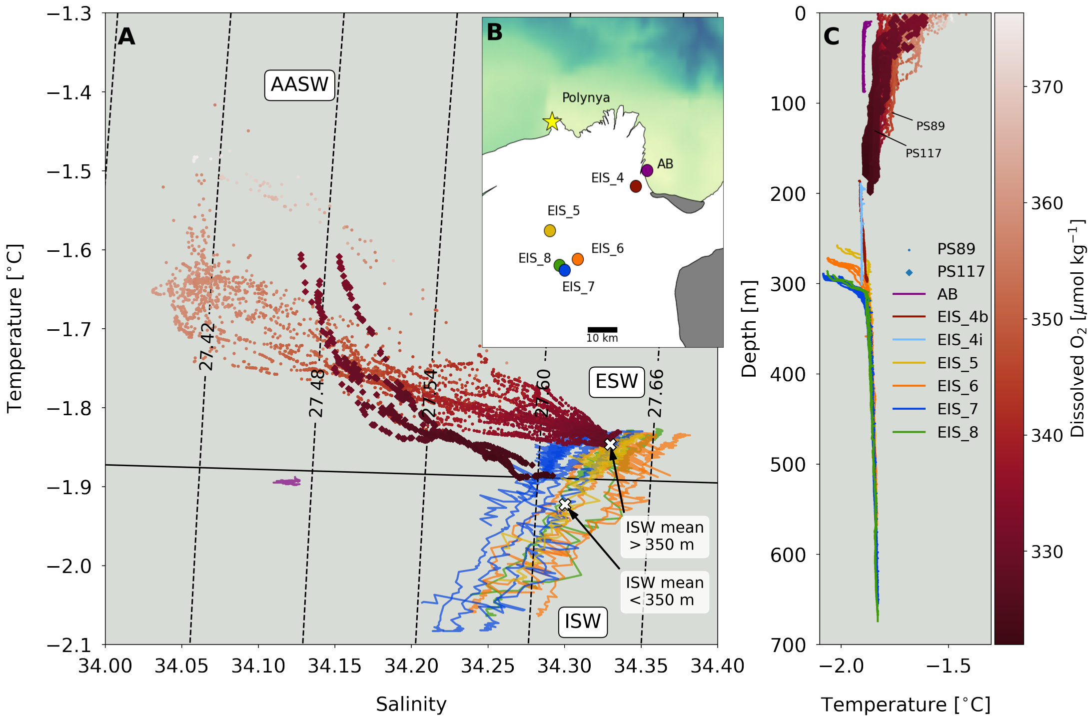

Figure 3.7: a) Temperature-salinity diagram for PS89 (circles) and PS117 (diamonds) tidal observation periods, which are coloured according to dissolved oxygen concentrations. CTD profiles of the ice shelf's cavity water were collected and made available by Smith et al. (2020) (coloured lines). The cavity CTD profiles were taken by hot water drilling through the ice at various locations on the ice shelf, which are shown on the map in (b) in corresponding colours to the profiles in (a). AASW = Antarctic Surface Water, ESW = Eastern Shelf Water, ISW = Ice Shelf Water. The average temperature and salinity of water deeper and shallower than 350 m underneath the ice shelf are plotted as single white crosses. Contour lines indicate sigma-t in kg m^{-3}. Black line indicates freezing point at mean atmospheric pressure. (b) Map of measurement locations of the Ekström Ice Shelf cavity CTD profiles by Smith et al. (2020) denoted by "EIS_", a measurement location in Atka Bay by Smith et al. (2020) denoted with "AB", and the sampling location of the tidal observations indicated by the yellow star. (c) Temperature profiles for PS89 (circles) and PS117 (diamonds) tidal observation periods, coloured according to oxygen concentrations, and for the hot water drill CTD profiles underneath the ice shelf from Smith et al. (2020).

phytoplankton cells (for which we use fluorescence as a proxy) are expected to be mostly absent. This description of water properties is consistent for the properties observed during ebbing tide (Fig. 3.4, 3.6). It therefore seems feasible that less ventilated, colder water from underneath the ice shelf with lower oxygen and higher nutrient and DIC content can extend to the edge of the ice shelf during ebbing tide and into the polynya.

A relevant topic to consider is therefore the circulation within the ice-shelf cavity. A study using a box model indicated that the temperature and salinity at the ice shelf front is important for basal melting rates (Olbers and Hellmer, 2010). Considering the high variability in the physical properties of the water column shown for the edge of the Ekström ice shelf, the relative forces of tides, wind, and sea ice melt at the ice shelf front may have implications for the complex physical processes at the ocean-ice shelf interface, and thus basal melting rates. Basal melting from major ice shelves have been shown to be a significant source of meltwater to the Southern Ocean (Timmermann et al., 2012). Changes in ice-shelf cavity circulation over time, such as those caused by ocean warming, and thus basal melt rates (Olbers and Hellmer, 2010), may in turn have consequences for the water mass properties at the ice shelf's edge, including DIC, TA, fCO_2, and the air-sea CO_2 flux. Although challenging to simulate with ocean models due to the high resolution required to represent the bottom topographies (Timmermann et al., 2012), accurate ice-shelf cavity circulation may be important to understand the carbonate system variability in coastal regions in the Weddell Sea.

Even though mWDW is a source for eastern shelf water (Nicholls et al., 2009), we do not see a direct signal of mWDW in our dataset. The bathymetry of the cavity underneath the Ekström Ice Shelf slopes from about 450 m depth at the ice shelf edge to a maximum depth of 1100 m southwards towards the grounding-line (Smith et al., 2020). Although troughs sculpted into the cavity's bathymetry (Smith et al., 2020) potentially allow WDW (or its modified form) to enter it (Fahrbach et al., 1994) (a process that may be enhanced by tides), the warmer water is usually restricted to the north of the continental shelf in this region by prevailing easterly winds (Heywood et al., 1998; Thompson et al., 2018). The cavity is instead likely influenced by ESW that enters through Ekman transport (Zhou et al., 2014).

As explained in Section 3.3.3, the salinity normalisation removes the impact of physical processes from the DIC and TA data. Therefore, any variability that remains in the nDIC and nTA results needs to be explained according to other processes. These processes are represented in Fig. 3.5 by theoretical lines that indicate how nTA and nDIC would change relative to each other as a result of photosynthesis/respiration, $CaCO_3$ dissolution/precipitation, and CO_2 uptake/release (Zeebe and Wolf-Gladrow, 2001). For example, factors that could be relevant to net photosynthesis are variable sea ice cover affecting light availability, nutrient replenishment during ebbing tide, and mixing of phytoplankton cells into deeper water during rising tide (Gleitz et al., 1994). Yet, none of these processes seem particularly dominant in changing the nTA and nDIC content within each tidal observation (Fig. 3.5). The results in Fig. 3.5 show a legacy of processes that may have occurred in the weeks to months prior to sampling, as the marine carbonate system's equilibration time with the atmosphere is slow, especially in sea ice covered regions. Additionally, the data during rising tide might also reflect processes that happened in the sea ice, which will have affected the carbonate chemistry of the sea ice meltwater and thus the properties of the AASW. While we here consider the tides to transport a salinity front back and forth across the sampling site, we must also recognise that the sampled mass of water on each side of the front is not exactly the same during each tidal phase. This contributes to the variability observed in the dataset. Finally, even though there is good agreement between the high vertical resolution sensor data and the discrete bottle data for salinity and temperature (exemplified with density in Fig. A.6), biogeochemical processes could imprint additional variability in the DIC and TA profiles that are not reflected in salinity and temperature measurements. We must therefore consider that the discrete seawater samples might not have captured the full scale of the variability in the polynya, limiting our interpretation of relevant biogeochemical processes.

Coastal polynyas have been described as "the most productive waters in the Southern Ocean" (Arrigo et al., 2015). Their chlorophyll *a* levels are found to peak in January, roughly coinciding with the peak of coastal polynyas' area of open water (Arrigo et al., 2015). In polynyas around Antarctica, iron supplied by basal melting of ice shelves is a major contributing factor to the variability in phytoplankton biomass (Arrigo et al., 2015). Considering that the observations in the current study were made in a coastal polynya of variable size directly adjacent to the Ekström Ice Shelf with an estimated basal melt rate of 4.2 Gt year^{-1} (Rignot et al., 2013), the lack of observable *in situ* nutrient and inorganic carbon uptake by primary productivity at the surface is perhaps unexpected. This also applies to times at rising tide in the PS89 observation period when the fluorescence signal increases in the water column, suggesting advection of phytoplankton cells into the polynya. Tidal mixing that replenishes nutrients at the surface has been described to drive phytoplankton productivity in other tidal regions (Rogachev et al., 2001). However, primary productivity and its peak in the summer have been shown to be highly variable among Antarctic coastal polynyas, and important drivers of low primary productivity are deep MLD and grazing pressure (Arrigo and van Dijken, 2003). These are likely highly relevant factors in our case study. High phytoplankton growth rates require water column stability that lasts several weeks (Gleitz et al., 1994), which is absent during the case studies presented here. Even during ebbing tide, when the water column stratifies at a shallow depth during PS89, the duration of stratification is too short to support substantial *in situ* DIC and nutrient uptake by growth and primary production.

In a study in the Amundsen Sea, stations close to the Pine Island Glacier were characterised by a deep MLD and low phytoplankton biomass and Chl *a* despite high dissolved Fe availability (Alderkamp et al., 2012), suggesting that upwelling of Fe-rich basal meltwater mixed the water at the ice shelf's edge (Alderkamp et al., 2012; Gerringa et al., 2012). A colder, more buoyant layer along the base of the Ekström Ice Shelf similarly indicates outflows of ice shelf meltwater (Smith et al., 2020). The temperature and salinity at the bottom of the profiles during PS117 compare to those measured near the base of the ice shelf (mean of top 350 m of the ice shelf CTD casts EIS4-8 (Smith et al., 2020)). The bottom water temperature and salinity values for PS89 resemble more closely those deeper in the cavity (e.g. the mean of the water deeper than 350 m of the ice shelf CTD casts EIS4-8; Fig. 3.7). Earlier, we noted that southerly winds during PS117 may have counter-acted some of the advection of fresher, more ventilated water from the north-east during rising tide. The comparisons to the work by Smith et al. (2020) support the idea that - in addition to less sea ice meltwater input from the north-east - outflow and mixing of ice shelf meltwater might have been stronger during PS117 than PS89, dominating the polynya water properties. Along with a more mixed water column, this difference in connectivity to the ice shelf cavity is consistent with the less ventilated water of the polynya during PS117, and can be responsible for the higher nDIC (and salinity-normalised nitrate and phosphate) content, compared to PS89.

From an ecological perspective, it is relevant to consider the effect of the carbonate system variability on the diversity, structure, and production of pelagic-benthic organism communities. Calcifying organisms, such as pteropods, foraminifera, and coccolithophores, depend on the seawater calcium carbonate saturation state to form their shells and skeletons, which are made from $CaCO_3$ (Orr et al., 2005). The pH in the Ekström polynya varied between 8.02-8.12 and 8.02-8.06 for PS89 and PS117, respectively (see Fig. A.9 for vertical variability). The saturation state of aragonite (Ω_{ar}; the less stable polymorph compared to the other common $CaCO_3$ polymorph: calcite) concurrently varied between 1.22-1.52 and 1.21-1.34, respectively. A contour in Fig. 3.4c and 3.4d at an arbitrary value of 1.3 for Ω_{ar} gives a sense of the vertical variability driven by tides. Even at the lowest pH values recorded here, the Ω_{ar} does not fall under 1, which means that the marine chemical environment does not thermodynamically promote $CaCO_3$ dissolution. The dynamic nature of the polynya might foster a resilience among the pelagic and benthic organism communities to rapid (semi-diurnal) changes of Ω_{ar}. However, even at a carbonate saturation level > 1, the rate of biogenic calcification has been shown to be affected by the $CaCO_3$ saturation state (Feely et al., 2004). The Southern Ocean is especially vulnerable to ocean acidification driven by marine anthropogenic CO_2 uptake (Negrete-García et al., 2019; Orr et al., 2005). Tidally induced variability may increase the sensitivity of high-latitude coastal systems to shoaling aragonite and calcite saturation state horizons. Alongside ecological impacts of tides along the Antarctic coastline, future studies can look into the tidal impacts on long-term changes of the vulnerability of pelagic-benthic organism communities.

In this study, we have argued that the DIC variability in the coastal polynya is driven by back-and-forth movement of water under the force of tidal currents across the sampling site located in a region where there is a horizontal gradient in DIC content: lower DIC content to the north-east, influenced by summer sea ice melt, and higher DIC content to the south-west, influenced by unventilated ice shelf cavity water. This led us to investigate whether there is evidence in our dataset for a tidally-driven horizontal DIC pump. For example, net transport away from the ice shelf could transport DIC and nutrients (and perhaps even iron) from the ice shelf towards surface waters on the continental shelf that are exposed to sea ice and the atmosphere. Subsequent biological carbon uptake will then remove DIC. However, when we calculate the trajectory of a water parcel (using the ship's position as a starting point and the average current velocity of the water column) the net transport is south/south-east, i.e. towards the ice shelf (Fig. A.8). This implies that surface waters would be modifying the properties of the water underneath the ice shelf over time (instead of the other way around), for example by dilution. If this is the case, we would expect to see a trend in the DIC content of the polynya during ebbing tide. However, this is not the case and the net change in DIC content over six hour periods (including ebbing and rising tide) is zero

(Fig. A.11 for PS89). Our observations are a snapshot of a highly dynamic system and consequently they do not provide enough data to analyse such modifications and trends of the seawater physico-chemical properties. Nevertheless, they can be the beginning of future studies into this topic.

While a tidal movement of a salinity front or gradient across the sampling site is a possible and realistic explanation for the oscillations observed in the water column, validating it would require physico-chemical profiles between the Ekström Ice Shelf and the edge of the continental shelf. Without them, other relevant physical processes, such as regional circulation, tidal straining, or mixing, cannot be excluded. For the same reason, the distance from the ice shelf at which the tidally-driven deepening and shoaling of the isolines (most clearly seen for PS89) can be observed remains uncertain. The distance will depend on the strength of the tidal current and would have to be investigated with repeat transects from the ice shelf towards the open ocean at various points in the tidal cycle. Other mediating factors, such as winds and internal tidal waves generated by uneven bathymetry, would have to be additionally considered (Llanillo et al., 2019). Moreover, tidal mixing may erode fronts and modify water masses (such as at the ice shelf edge or of the ESW) over time, adding a temporal dimension to the effect of the tide on the shelf waters in this region.

Despite the unknowns outlined above, the case studies presented in this work show that strong tidal influences on the physical structure and biogeochemical properties of the water column can be expected along the Weddell Sea coastline (and other polar regions subject to strong tides), especially in close proximity to ice shelves and regions of sea ice melt. They also show that local winds and ice shelf meltwater outflows can increase the complexity of the tidal impact within a region such as a coastal polynya. In addition to studies on the physical role of tides on (for example) basal ice shelf melt, ecological, biogeochemical, and air-sea gas exchange studies can benefit from a better understanding of tidal impacts on the water column.

3.4.2 Air-sea CO_2 exchange

The tidally-induced variability in the water column implies that the timing of sampling matters when estimating the relative contribution of coastal regions to the total CO_2 flux of the Weddell Sea. We first present the variability in the CO_2 flux during the tidal observation periods. We then illustrate that bias can be introduced in our understanding of the relative importance of coastal regions along the Weddell Sea if sampling strategies do not take tidal influences into account.

The difference in the $f\mathrm{CO}_2$ between the seawater and the atmosphere is what drives a positive or negative CO_2 flux at the air-sea interface. For the flux calculations, we used the average wind speed recorded during the PS89 and PS117 tidal observation periods: 10.7 and 6.6 m s^{-1}, respectively (Table 3.1). This choice implies that the computed variability in the flux results within each case study is mainly driven by the air-sea gradient of $f\mathrm{CO}_2$. During the PS89 tidal observation period in January 2015, the surface water at the Ekström Ice Shelf was undersaturated in $f\mathrm{CO}_2$ relative to the atmosphere (Fig. 3.4), creating a CO_2 sink (Fig. 3.8). However, the depth at which the fCO_2 of the seawater is equal to that of the atmosphere (marked by a dashed line in Fig. 3.4a) fluctuates from near the bottom of the water column during incoming tide to near-surface during outgoing tide. Direct fCO_2 measurements were made using the vessel's underway system (at 11 m depth) during (as well as 2.5 days prior to the start of) the discrete seawater sampling, i.e. the start of the PS89 tidal observation period (Fig. A.5). fCO_2 correlates very well with the salinity, again indicating that physical movement of water is the dominant driver of the variability. CO_2 fluxes determined from the underway measurements a) compare well with the fluxes calculated from the discrete seawater carbonate chemistry results where they overlap in time, and b) show an even stronger fluctuation on 7 and 8 January 2015, when the flux status of the sampling site swung between a sink (rising tide) and a source (ebbing tide) of CO_2 twice within 24 hours (Fig. 3.8). This suggests that water with higher DIC content reached the surface during ebbing tide. The CO_2 sink during PS89 is as large as -23.6 mmol m^{-2} day^{-1}, while the largest CO_2 source reaches 3.1 mmol m^{-2} day^{-1} (Fig. 3.8).

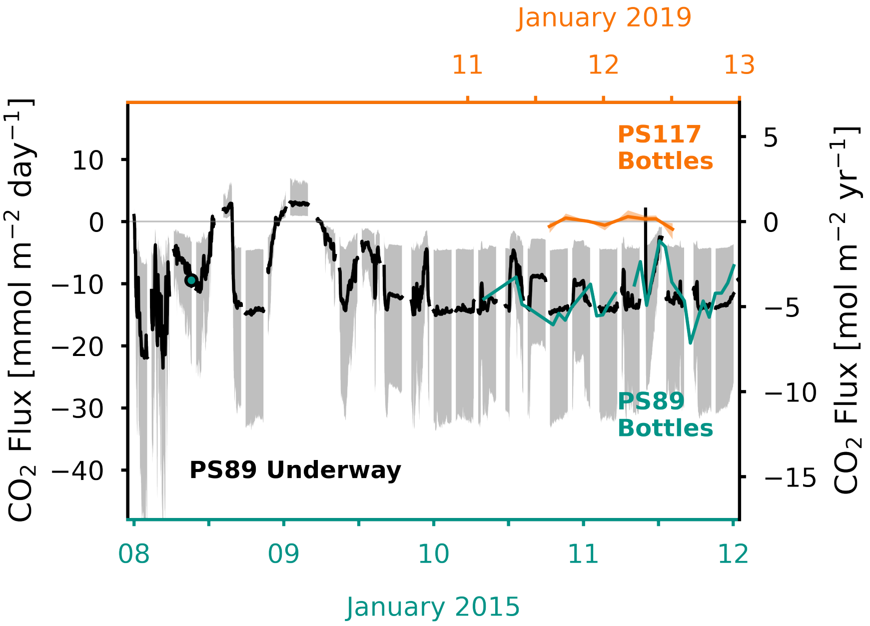

Figure 3.8: Air-sea CO_2 flux (in mmol m^{-2} day^{-1} on the left y-axis and in mol m^{-2} year^{-1} on the right y-axis) determined from the discrete surface seawater sample measurements and average wind speed for the PS89 (green, bottom x-axis) and PS117 (orange, top x-axis) tidal observation periods, and from the PS89 underway fCO_2 measurements (black, bottom x-axis), which started on 7 January 2015. The CO_2 flux based on a discrete surface seawater sample collected on 7 January 2015 is also shown with a green marker. The filled shading indicates the range of the flux calculated using the minimum and maximum wind speed measured during PS89 and PS117, respectively (Table 3.1). Negative flux represents CO_2 uptake by the ocean.

During PS117, the seawater fCO_2 also dips below the atmospheric value at times of rising tide. However, the fCO_2 gradient and the wind speed are much lower compared to PS89 (Fig. 3.4b), resulting in a low CO_2 flux (Fig. 3.8). Even though not all PS117 CTD cast measurements started as shallow as those from PS89, the few casts that did have measurements starting <20 m showed a lack of a strong gradient in the DIC and TA content at the surface. The shallowest discrete carbonate chemistry water samples are therefore considered to be representative enough of the water properties at the surface. Accordingly, the site is likely to have had a relatively neutral CO_2 flux at this time in January 2019. Using the fCO_2 results based on the discrete water sampling, the average CO_2 uptake during the PS89 tidal observation period is -11.7 ± 3.7 mmol m^{-2} day^{-1} (± 1σ). For PS117, the average air-sea CO_2 flux is -0.1 ± 0.9 mmol m^{-2} day^{-1}. Even though the size of the coastal polynya was variable, the sampling site was free of sea ice during the tidal observations and it is assumed to have been ice free for the entire summer. We therefore have not scaled the gas transfer velocity with the fraction of open water area. At times during the summer when the site does get covered by sea ice, the amplitude of the CO_2 flux would be subdued.

The importance of strategic seawater sampling for the purpose of obtaining reliable air-sea gas exchange values in regions such as the Ekström coastal polynya is illustrated by the following. Assuming the scenario we know for the PS89 tidal observation period, if discrete water samples had unknowingly only been collected during ebbing tide (higher seawater fCO_2), the calculated CO_2 flux (-3.1 mmol m^{-2} day^{-1}) would have underestimated the strength of the CO_2 uptake by the polynya by up to 73 %, compared to the average uptake (-11.7 mmol m^{-2} day^{-1}). However, if samples had only been collected during times of rising tide (lower seawater fCO_2), the capacity of the polynya to take up CO_2 (-19.6 mmol m^{-2} day^{-1}) would have been overestimated by up to 67 %, compared to the average uptake value. Since the variability of the CO_2 flux during PS117 was much lower (ranging between -1.2 and 0.8 mmol m^{-2} day^{-1}), samples collected at any time during this 24 hour period would have been relatively representative of this tidal observation period, but not necessarily of the month or the entire summer season.

We emphasise the potential misrepresentation of the role of coastal polynyas in the Weddell Sea CO_2 uptake if tidal influences are not accounted for. For this, we again use the two extreme scenarios based on the PS89 observations that were also used above to illustrate the maximum potential over- and underestimation of the CO_2 uptake. I.e., we use the hypothetical cases where surface seawater samples are either collected at peak rising tide (overestimation of CO_2 uptake) or at peak ebbing tide (underestimation of CO_2 uptake) during PS89. We constrain results and comparisons to the summertime, assume that all coastal polynyas in the south-eastern Weddell Sea are influenced by the same water masses present in the Ekström polynya during the PS89 tidal observation, and assume the same wind speed to highlight the role of the seawater fCO_2 variability. Using the total area of polynyas along the south-eastern Weddell Sea coastline in the summer of 49×10^3 km^2 (as estimated by Arrigo and van Dijken (2003)), the total net CO_2 uptake for all polynyas along the south-eastern coastline would be -0.97×10^9 mol day^{-1}, if data had only been collected during rising tide. It would have been -0.15×10^9 mol day^{-1}, if data had only been collected during ebbing tide.

Brown et al. (2015) estimated a summer marine uptake of CO_2 for the entire Weddell Sea of -0.044 to -0.058 ± 0.010 Pg C yr^{-1}, based on a summertime ocean inversion. In our hypothetical, biased upscaling case of collecting carbonate chemistry samples during ebbing tide, we would determine that the contribution of eastern shelf polynyas to the upper summer CO_2 uptake estimate of Brown et al. (2015) is 1.2 % (using the same area for the Weddell Sea: 6.2×10^{12} m^2 and scaling the daily flux up to the whole year). If seawater samples had only been collected during rising tide, the contribution of the eastern shelf polynyas would have been estimated at 7.3 % to the total summer CO_2 uptake of the Weddell Sea. This is quite substantial considering that the area used here for the south-eastern coastal polynyas is less than 0.8 % of the total Weddell Sea area (including regions covered and not covered by sea ice). If the average CO_2 flux of PS89 had been used in this simplistic upscaling exercise instead of the extreme high- and low-end scenarios, then the total CO_2 flux of all Weddell Sea coastal polynyas would be -0.58 ± 0.18 $\times 10^9$ mol day^{-1} (4.4 % of Weddell Sea flux) for January 2015. Results are two orders of magnitude lower when the same upscaling exercise is done with the average flux for the PS117 case study: 0.003 ± 0.034 $\times 10^9$ mol day^{-1} (0.02 % of Weddell Sea flux).

The purpose of the above exercise is to simply highlight the variability in these coastal systems. Given both the scarcity of data in these regions and the challenges in reaching them, tides may be an important aspect to consider to explain some of the variability seen in previous and future oceanographic data. Although the Weddell Sea is considered to be an - albeit small - annual net CO_2 sink (Bakker et al., 2008; Brown et al., 2015; Hoppema et al., 1999), its CO_2 uptake is sensitive to the balance of physical, chemical, and biological processes, such as sea ice growth/melt, regional wind strength/patterns, circulation, and biological CO_2 drawdown (Brown et al., 2015). The coastal marine regions and the processes that govern their water properties may be equally sensitive and their changes on time-scales of hours to weeks or months may be mediated by the tides.

3.5 Conclusion

We present the significant semi-diurnal influence of tides on the water properties and carbonate chemistry at the margins of a coastal polynya hugging the Ekström Ice Shelf in the south-eastern Weddell Sea. Advection of lower DIC and TA waters from the north-east during rising tide influenced by sea ice melt decreases the salinity and fCO_2 at the sampling site and results in CO_2 draw-down from the atmosphere. As the sampling site is located directly next to the ice shelf, it sees the extension of the water underneath the ice shelf, which is drawn out from underneath during ebbing tide. This water is less ventilated and has a higher DIC and TA content (and higher fCO_2) compared to the water to the north-east, which decreases the strength of the CO_2 sink and can even reverse the direction of the CO_2 air-sea flux on a semi-diurnal time scale.

Differences in the variability between the two tidal observations between January 2015 and January 2019 suggest a complex interaction between timing of the tide, local and regional sea ice melt, polynya area, basal melt, and local forces, such as wind speed and direction. The datasets of the two short case studies presented here are too small to fully explore the modulating effects of these processes on the water column variability. To be able to do so, longer tidal observations are required that cover different parts of the spring-neap tidal cycle, and at different times of the year to capture varying wind and ice melt/growth conditions. Alongside carbonate system state variables, an array of co-collected measurements, such as micro-nutrients, biological productivity, and oxygen stable isotopes, can help to constrain interacting processes. An understanding of the carbonate chemistry of the cavity water underneath the ice shelf - although challenging to obtain - would help understand the influence of this water on the polynya during ebbing tide.

The observations presented here were obtained from a stationary sampling site. Without knowing the hydrological conditions in the surrounding area at various time points in the tidal cycle, we must consider that our conclusions only apply to a very local area, the margins of polynyas, or the edges of ice shelves. Hydrographic transects between the ice shelf and well into the sea ice cover at ebbing and rising tide can help identify the extent to which the tidal oscillation, as seen in the case studies, is relevant further away from the coastline and from the polynya's margins. It may also help identify the formation and characteristics of a horizontal coastal salinity gradient - here referred to as a "salinity front" - that moves back and forth with the tide.

This case study has shown that tides can swing the status of coastal polynyas on the south-eastern continental shelf of the Weddell Sea from a strong sink to a source of CO_2 on a semi-diurnal time-scale. Seawater CO_2 uptake can be underestimated by 73 % and overestimated by 67 %, if these tidal changes are ignored. Awareness of the tidal impacts is required to implement strategic sampling techniques to obtain representative data in these extremely variable - and rarely accessible - systems that play a role in the sensitive balance of the Weddell Sea's net air-sea CO_2 exchange.

CHAPTER 4 |

Drivers of interannual variability in the CO_2 uptake along the West Antarctic Peninsula

My contributions

I analysed the DIC / TA samples for 2017-2020 of the time series in the laboratory at UEA. I processed and quality-checked the DIC / TA data for 2016-2020 part of the time series. I did the data analyses and wrote all components of this work. This work was funded by the Natural Environment Research Council (NERC) through the EnvEast Doctoral Training Partnership (NE/L002582/1).

Contributions by others

Seawater DIC / TA samples were collected at Rothera by the marine assistants from the British Antarctic Survey. Elizabeth Jones analysed the DIC / TA samples for 2014-2016 of the time series in the laboratory at UEA and at NIOZ. Marcos Cobas-Garcia co-analysed samples for 2014-2016. Gareth Lee contributed to DIC / TA sample analyses for 2014-2016 and 2019-2020. Hugh Venables provided data on physical oceanography and sea ice cover in Ryder Bay. Dorothee Bakker designed the concept for this work. Michael Meredith provided the stable oxygen isotope data. Dorothee Bakker, Gareth Lee, and Hugh Venables are responsible for the continuation of the Rothera carbonate chemistry time series and its logistics. Dorothee Bakker, Mario Hoppema, Hugh Venables, Giorgio Dall'Olmo, Elizabeth Jones, Oliver Legge, Michael Meredith, and Bastien Queste gave feedback on the text of the manuscript and contributed to discussions about the data, which significantly improved this work.

Publication status

This work will be split into multiple manuscripts that will be submitted for publication (journal TBD) with the following confirmed co-authors: Dorothee C. E. Bakker, Hugh J. Venables, Elizabeth Jones, Mario Hoppema, Giorgio Dall'Olmo, Bastien Queste, Oliver Legge, Michael Meredith, and Gareth Lee.

Abstract. The Southern Ocean plays a large role in climate regulation by absorbing and sequestering large amounts of anthropogenic carbon dioxide (CO_2) from the atmosphere. While atmospheric CO_2 concentrations are steadily rising, the Southern Ocean's CO_2 uptake is highly variable over time. The driving mechanisms behind the seasonal and interannual variability in the Southern Ocean carbon sink are poorly understood due to a paucity of year-round data, especially in the wintertime. The Rothera Time Series (RaTS) at Ryder Bay along the West Antarctic Peninsula (WAP) provides a unique opportunity to study the physical and biogeochemical processes that affect the marine carbonate system in the marginal sea ice zone. We investigate the carbonate chemistry in context of sea ice variability, meltwater input, and atmospheric forcing to determine the main drivers of interannual variability in the fugacity of CO_2 (fCO_2) and the CO_2 flux. We found that mean wintertime seawater fCO_2 in Ryder Bay varies from year-to-year, and is a major component of the interannual variability in the annual mean fCO_2. Wintertime fCO_2 is driven by 1) the onset and duration of sea ice cover affecting water column stratification, 2) meltwater input in the previous melting season, and 3) dissolution of calcium carbonate in the surface layer. Large-scale changes in atmospheric circulation, such as the Southern Annular Mode and El Niño Southern Oscillation, have an indirect effect on the surface layer carbonate system by changing ocean heat uptake and sea ice dynamics. In other seasons, sea ice indirectly affects the marine biogeochemistry by regulating the onset of phytoplankton blooms and direct sea-air CO_2 exchange. Interannual variability in seasonal fCO_2 often has inter-seasonal dependencies, which shows the importance of year-round observations. This study highlights the contribution of wintertime processes in the interannual variability of the marine carbonate system and sea-air CO_2 flux along the WAP coastline. It shows that wintertime sea-air CO_2 exchange may be more variable within the season, as well as between years, than previously considered. Although the contribution of physical and biogeochemical processes to interannual variability in the CO_2 uptake may be different on larger spatial scales, Ryder Bay can be used as a case-study to gain a mechanistic understanding that can help find important missing pieces in the puzzle of the variability in the Southern Ocean CO_2 sink.

Contents

4.1 Introduction

The Southern Ocean is estimated to account for 40 % of global anthropogenic carbon dioxide (CO_2) uptake by the oceans (DeVries, 2014; Khatiwala et al., 2009). Observation-based estimates of Southern Ocean CO_2 flux show substantial decadal and interannual variability (Landschützer et al., 2015; Le Quéré et al., 2007), which strongly influence the global interannual variability in sea-air CO_2 flux (Rödenbeck et al., 2014). Large-scale atmospheric circulation patterns, such as the Southern Annular Mode and El Niño Southern Oscillation, play an important role in this variability by driving regional upwelling of carbon-rich subsurface water, and driving sea-air CO_2 exchange by wind stress (Landschützer et al., 2015; Le Quéré et al., 2007; Lenton and Matear, 2007). However, ocean models struggle to capture the Southern Ocean interannual variability (DeVries, 2022; Le Quéré et al., 2007), as uncertainties in drivers of year-to-year variability remain high (Lenton et al., 2006). Yet, understanding the variability of the Southern Ocean, including Antarctic shelf seas, and its response to increasing seawater temperatures and changes in sea ice regimes is important for studies on carbon budgets, such as the annually updated Global Carbon Budget (Friedlingstein et al., 2022).

Antarctic coastal systems contribute significantly to the Southern Ocean CO_2 flux by supporting extensive biological CO_2 drawdown in the melting season and by impeding direct sea-air CO_2 fluxes in winter and spring when sea ice cover persists (Arrigo et al., 2008a; Legge et al., 2015; Legge et al., 2017; Monteiro et al., 2020; Roden et al., 2013). In addition to strong seasonality, the carbonate system components in the coastal surface water layer vary interannually (Lencina-Avila et al., 2018; Monteiro et al., 2020), but what controls this variability is uncertain due to a lack of multi-year, year-round data, especially in the wintertime. Consequently, Antarctic coastal regions are often not given special attention in carbon budgets (e.g., Friedlingstein et al., 2022).

The Rothera Time Series (RaTS) is a unique time series of oceanographic and biogeochemical variables maintained by the British Antarctic Survey at Rothera Research Station in Ryder Bay on the West Antarctic Peninsula (WAP; Fig. 4.1; Clarke et al., 2008). As part of the RaTS, we present data on the surface water marine carbonate system in Ryder Bay from 2011 to 2020. It consists of year-round discrete sampling of dissolved inorganic carbon (DIC) and total alkalinity (TA), which are used to compute other carbonate system components. The time series presented in this communication is an extension of the first three years of data published by Legge et al. (2015) and Legge et al. (2017), who performed an in-depth analysis of the seasonal drivers in DIC, TA, and sea-air CO_2 flux. They found that atmospheric CO_2 draw-down in the melting season was driven by photosynthetic uptake and that wind-driven mixing with deep, DIC-rich water led to CO_2 outgassing to the atmosphere in winter.

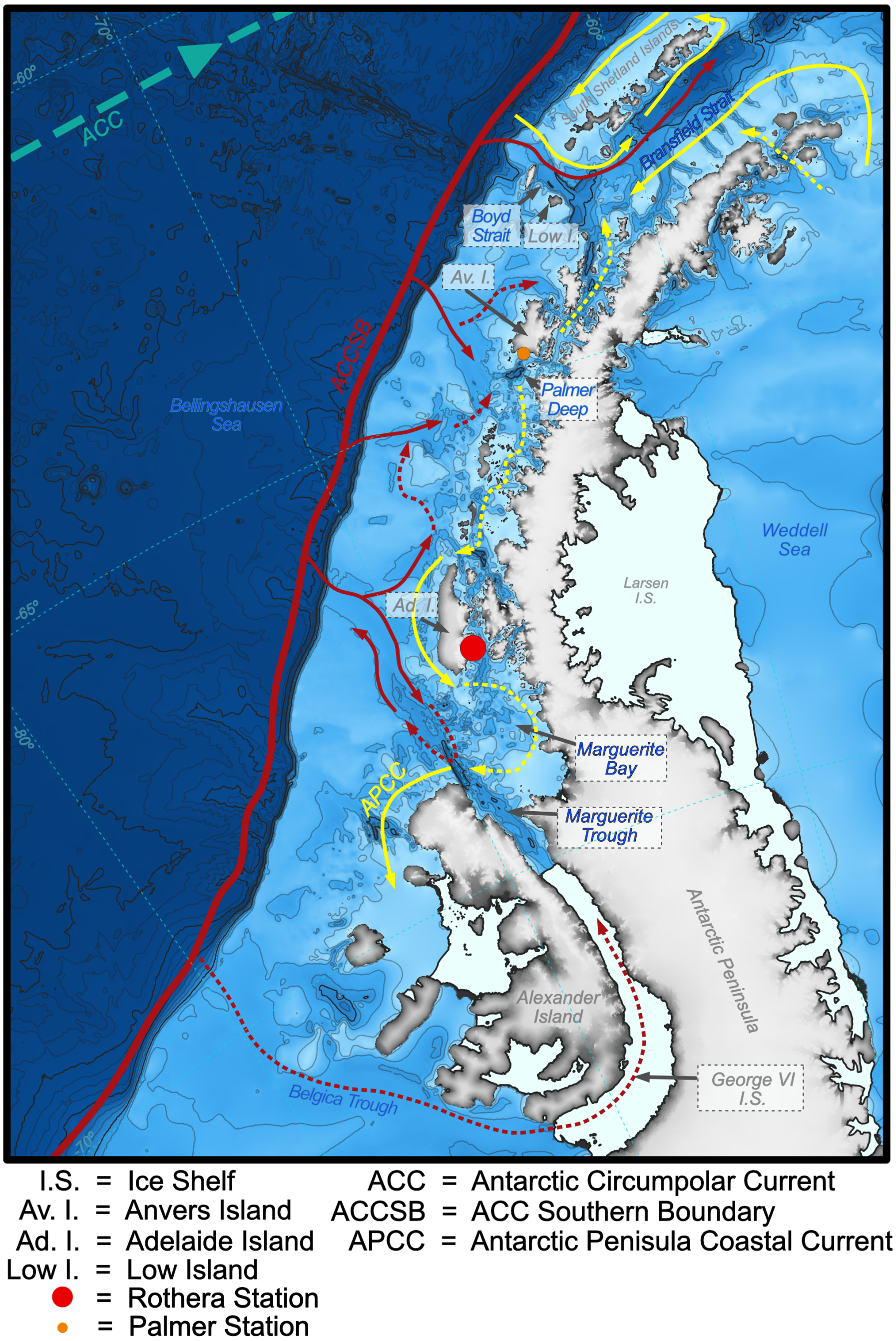

Figure 4.1: Map and bathymetry along the West Antarctic Peninsula (GEBCO, 2022). Arrows indicate the main coastal currents along the WAP. Red arrows illustrate the mCDW accessing the shelf. Yellow arrows illustrate shelf currents along the Antarctic Peninsula. Figure is modified from Moffat and Meredith (2018). Credit: James Christie.

Sea ice along the WAP influences carbon cycling in the surface layer, in particular with respect to its influence on water column mixing (Venables and Meredith, 2014), phytoplankton blooms and changes in biomass (Clarke et al., 2008; Rozema et al., 2017; Venables et al., 2013), atmospheric heat exchange (Stammerjohn et al., 2008a; Venables and Meredith, 2014), ecological community composition (Saba et al., 2014), nutrient cycling (Henley et al., 2017), and calcium carbonate precipitation / dissolution (Jones et al., 2017b; Jones et al., 2021). As the onset and duration of sea ice cover along the WAP differs from year to year (Stammerjohn et al., 2008a), its interannual variability is expected to be reflected in that of the sea-air CO_2 flux. We use the RaTS that now spans almost a decade to explore the regulatory effect of sea ice on the marine carbonate system through its influence on physical and biogeochemical properties of the seawater, especially in wintertime. Data in offshore polar regions during wintertime are extremely scarce. While coastal systems are very different from offshore systems, the relatively data-wealthy system of Ryder Bay can reveal pieces of the puzzle that are currently missing in our understanding of regional temporal variability in the surface carbonate system and sea-air CO_2 flux in polar regions.

4.2 Methods

4.2.1 Study area and its physical oceanography

Ryder Bay is an embayment located in the south-east of Adelaide Island (Fig. 4.1), surrounded by marine terminating glaciers (Fig. 4.2). It is part of the larger Marguerite Bay, which is constrained by Alexander Island in the south, the WAP in the east, and Adelaide Island in the north (Fig. 4.1). To the west, Marguerite Bay is open to the Bellingshausen Sea. South of Anvers Island, the circulation on the WAP shelf is dominated by the Antarctic Peninsula Coastal Current (APCC) flowing to the southwest, following the WAP coastline (Beardsley et al., 2004; Moffat et al., 2008; Savidge and Amft, 2009). Velocities of the APCC are seasonally driven by input from glacial and sea ice meltwater and winds favouring downwelling (Moffat et al., 2008). At the edge of the WAP continental shelf, currents are associated with the Antarctic Circumpolar Current (ACC) and flow parallel to the shelf to the northeast (Savidge and Amft, 2009). Circumpolar Deep Water (CDW) is transported with these currents along the southern edge of the ACC. The CDW accesses the shelf primarily via deep, glacially scoured canyons (Moffat et al., 2009) and via eddies (Martinson and McKee, 2012). These canyons provide effective conduits for flow across the shelf towards the coast. The hydrographic properties of the deeper shelf waters are those of a modified form of CDW (mCDW), as it navigates the complex topography of the WAP shelf while undergoing heat exchange and ventilation. The mCDW is a major source of heat, inorganic nutrients, and inorganic carbon along the WAP coastline (Carrillo and Karl, 1999; Henley et al., 2018; Martinson and McKee, 2012; Moffat et al., 2009; Prezelin et al., 2000; Tortell et al., 2014). Glacier calving events and (sub-)glacial meltwater plumes are common phenomena in the region. The mCDW input from the west and glacial meltwater input off the western flank of the Peninsula create a cross-shelf gradient in physical and biogeochemical properties that is most pronounced during the melting season (Hauri et al., 2015; Jones et al., 2021; Meredith et al., 2021). The mCDW enters Ryder Bay via Marguerite Trough (Moffat et al., 2009), then via a narrow channel to Laubeuf Fjord, including several ridges across it, and finally overflowing a sill at 350 m depth (Venables et al., 2017) (Fig. 4.1).

Strong ocean-to-atmosphere heat fluxes in winter cool the upper water column and lead to sea ice production. Wind stress deepens the upper ocean mixed layer, sometimes to 150 m depth. Surface heating and meltwater cap the mixed layer in summer, creating a cold subsurface layer dubbed Winter Water (WW); this and the overlying surface waters are often termed Antarctic Surface Water (AASW). Wind-driven mixing in the following autumn and convection from brine rejection during sea ice formation subsequently deepen the mixed layer, creating a new WW layer.

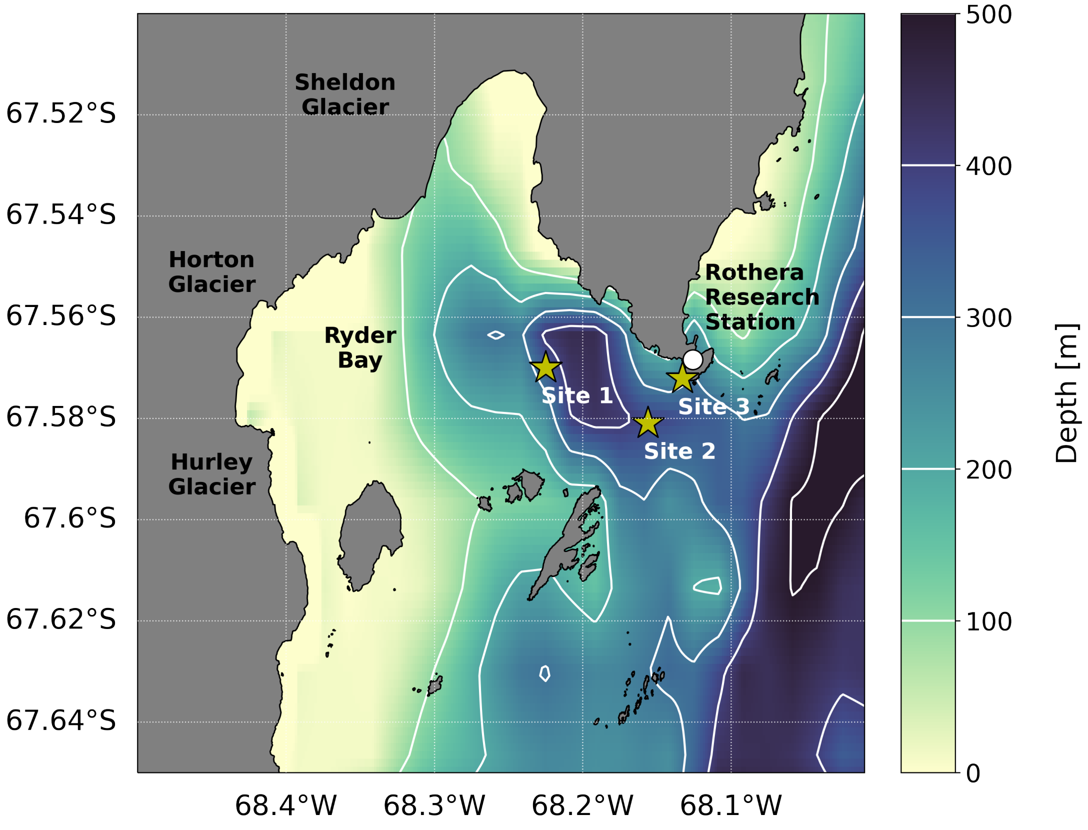

Figure 4.2: Map of Ryder Bay, coloured by bathymetry (IBSCO Version 1.0; Arndt et al., 2013) (Table B.4). Sampling sites are numbered and marked by yellow stars: Site 1 (67.570°S, 68.225°W), Site 2 (67.581°S, 68.156°W), and Site 3 (67.572°S, 68.122°W).

4.2.2 Water column measurements

Site 1 is the primary sampling location for the RaTS, with a bottom depth of ∼500 m (Fig. 4.2). Depending on sea ice cover and/or weather conditions, Sites 2 and 3 are used as alternatives. Site 3 is located by the wharf where the bottom depth is less than 100 m and is therefore quite different from the other sampling sites. However, Legge et al. (2017) found that Site 3 is nevertheless representative for the processes regulating the surface layer carbonate system among all sampling sites. The time series of full water column conductivity-temperature-depth (CTD) casts started in 1998 (see Table B.1 for details; (Clarke et al., 2008)). Chlorophyll *a* is additionally determined with a WetLabs in-line fluorometer and calibrated against the seawater samples collected at 15 m depth (Clarke et al., 2008). The CTD casts are done approximately twice-weekly in the melting season and every 1 to 2 weeks during the winter season, or whenever weather and sea ice conditions permit. Sampling sites are reached by a small inflatable boat, or by skidoo and sledge when land-fast ice covers the sites. The latter circumstance requires cutting a hole in the ice with a chainsaw to access the ocean.

Mixed Layer Depth (MLD) is calculated as the depth at which the density is greater than that at a surface reference depth (usually 10 m depth) by a certain density difference. Following previous RaTS studies (Legge et al., 2017; Meredith et al., 2010; Meredith et al., 2013), we use 0.05 kg m^{-3} as the density difference criterion for consistency. In addition to the MLD, we determine stratification, here defined in a bulk sense as the additional energy that would be required if the water in a certain depth range were homogenised by mixing (Simpson et al., 1978; Venables and Meredith, 2014).

4.2.3 Discrete seawater sampling and analysis

Discrete seawater samples were collected at 15 m depth, concurrently with the CTD casts. Dissolved inorganic nutrients (nitrate plus nitrite, phosphate, silicate) have been collected since the start of the RaTS in 1998. See Clarke et al. (2008) for information on the nutrient sample analyses. Collection of samples for the determination of $\delta^{18}O$ (the standardised ratio of stable oxygen isotopes in seawater, $H_2^{18}O$ to $H_2^{16}O$) of seawater started in 2002, about which more detailed information can be found in Meredith et al. (2008) and Meredith et al. (2010).

In December 2010, DIC and TA were added as variables to the RaTS sampling. These were sampled at 15 m depth every week in the melting season and as often as possible during the winter months. Occasionally, samples at additional depths (0, 2, 5, or 40 m) were collected. Samples for DIC / TA from these alternative depths were not collected frequently enough to study the changes in the carbonate system at these depths over time, but they do give additional information on gradients in the upper surface layer. The DIC and TA samples were collected in 250 mL borosilicate glass bottles, fixed with mercuric chloride, and sealed on site for later analysis, according to Standard Operating Procedure (SOP) 1 in Dickson et al. (2007). Most samples were analysed at the University of East Anglia, UK, using a VINDTA 3C (Versatile INstrument for the Determination of Total inorganic carbon and Alkalinity) system (Mintrop, 2003), which includes a coulometer for the measurement of DIC (Johnson et al., 1985) following SOP 2 in Dickson et al. (2007), and a Titrino® for the potentiometric titration for TA (Mintrop, 2003) following SOP 3b in Dickson et al. (2007). Over the years, various batches of the Certified Reference Material (CRMs) from A. Dickson's laboratory at the Scripps Institution of Oceanography (U.S.A.) were used to calibrate the VINDTA instruments and to derive the analytical uncertainties (Table B.2). The first three years of DIC / TA data from the RaTS (2010-2014) have been published in Legge et al. (2015) and Legge et al. (2017).

4.2.4 Sea ice

Daily sea ice cover and type were recorded by personnel at the Rothera Research Station. The fraction of sea ice was estimated visually and attributed to one of the following sea ice types: brash, grease, pancake, pack, and fast ice. We count days with 80 % or higher percentages of fast sea ice as "fast sea ice days", which are used in the figures below to illustrate high and low sea ice years in Ryder Bay.

4.2.5 fCO_2 and CO_2 flux calculations

The fugacity of CO_2 (fCO_2) is a thermodynamic property of a gas (very similar to the partial pressure of CO_2) that describes its pressure exerted within a solution (in this case: seawater), and which has been corrected for non-ideal gas behaviour. Determining the fCO_2 of the seawater is useful, because comparison to its atmospheric counterpart indicates whether the seawater is likely to take up CO_2 or release it to the atmosphere. The fCO_2 is not measured directly as part of the RaTS sampling, but it can be calculated from any two of the other variables of the carbonate chemistry system, in our case the measured DIC and TA. To derive fCO_2, we use the PyCO2SYS Python package (version 1.8, based on Lewis and Wallace (1998)), with data inputs for DIC, TA, phosphate, silicate, temperature, salinity, and pressure (Humphreys et al., 2022). The settings used are summarised in Table B.3. Settings include a choice of parameterisation of the carbonic acid equilibration constants. Here, we provide a brief elaboration on our choice of parameterisation. The carbonic acid dissociation constants (K_1^* and K_2^*) are a set of stoichiometric equilibrium constants at a given temperature, pressure, and salinity. They allow us to determine the speciation of DIC into carbonic acid ($H_2CO_3^* = H_2CO_3 + CO_2$), bicarbonate (${HCO_3}^-$), and carbonate (${CO_3}^{2-}$) content (Zeebe and Wolf-Gladrow, 2001). The equilibration constants K_1^* and K_2^* need to be determined for a certain salinity and temperature range, but only few parameterisations include temperatures close to the freezing point of seawater, which are common in high-latitude surface oceans (Sulpis et al., 2020). Goyet and Poisson (1989) produced a parameterisation for K_1^* and K_2^* using artificial seawater that applies to temperatures down to -1 °C, hence it was used for the first three years of the RaTS in Legge et al. (2015). Sulpis et al. (2020) more recently produced another parameterisation that applies to temperatures down to -1.67 °C, using field data. To remain consistent with the work by Legge et al. (2015) on the first part of the DIC / TA time series, we have used the K_1^* and K_2^* constants of Goyet and Poisson (1989) to determine the seawater fCO_2. Unless otherwise specified, all carbonate system components used in the current work that have been derived from DIC and TA are determined according to the K_1^* and K_2^* parameterisation by Goyet and Poisson (1989). We have additionally used the constants from Sulpis et al. (2020) for comparison to highlight the differences and thus to get a measure of the uncertainty due to the use of certain K_1^* and K_2^* constants in cold seawater conditions.

The sea-air CO_2 flux (FCO_2) is calculated according to Eq. 4.1, in which k is the gas transfer velocity, K_0 is the CO_2 solubility, and ΔfCO_2 is the difference between the fCO_2 in the seawater and the atmosphere at the sea-air interface (Eq. 4.2).

$$F_{CO_2} = k \cdot K_0 \cdot \Delta fCO_2 \qquad \text{(Eq. 4.1)}$$

$$\Delta fCO_2 = fCO_{2_{sw}} - fCO_{2_{atm}} \qquad \text{(Eq. 4.2)}$$

The atmospheric fCO_2 (in μatm) is determined from the atmospheric mole fraction of CO_2 in dry air (xCO_2) measured in air samples collected at Palmer Research Station on Anvers Island (Dlugokencky et al., 2019). These were smoothed using a weighted linear least-squares regression method (Lowess, using Statsmodels Python Package) that weighed 30 % of the data around each datapoint, following Legge et al. (2015). The conversion to fCO_2 was done using the method by Weiss and Price (1980), including the second virial coefficient given in Weiss (1974). This method requires a conversion of the dry mole fraction to the mole fraction in water vapour-saturated air, for which we used the water vapour pressure calculation by Weiss and Price (1980). The CO_2 solubility (K_0) is a function of temperature and salinity and determined according to the parameterisation in Weiss (1974) that calculates K_0 in units of mol kg^{-1} atm^{-1}. Multiplication with density converts the units to mol m^{-3} atm^{-1}. The gas transfer velocity (in cm hr^{-1}) is calculated according to Wanninkhof (2014) and Ho et al. (2006). It has a quadratic relationship to wind speed and depends on the Schmidt number, for which we use the parameterisation by Wanninkhof (2014). Legge et al. (2015) used the older Schmidt number parameterisation by Wanninkhof (1992), but differences in CO_2 flux results between these two methods are negligible. Wind speed at Rothera is measured at 42 m above sea level (asl; Connolley, 2004). We use Eq. 4.3 to adjust the wind speed to the reference height at 10 m above sea level, as is appropriate for the k parameterisation. The formulation for the wind speed adjustment is taken from the COARE model (Fairall et al., 2011). The term z_h is the height of the wind speed measurement, z_{10} denotes the reference height at 10 m, U_h is the measured wind speed at height z_h, and U_{10} is the wind speed adjusted to the reference height of 10 m asl.

$$U_{10} = U_h \cdot \frac{\log_{10} \frac{z_{10}}{10^{-4}}}{log_{10} \frac{z_h}{10^{-4}}} \qquad \text{(Eq. 4.3)}$$

The CO_2 flux is attenuated by the presence of sea ice, which therefore needs to be taken into account. Sea ice is a complex, interactive matrix, but its role is not yet sufficiently understood to be accurately represented in sea-air gas flux calculations

(Rysgaard et al., 2011). Following Legge et al. (2015), we apply a simple linear scaling to the gas transfer velocity according to the fraction of open water. At 100 % sea ice cover, the gas transfer velocity is scaled down by a maximum of 99 % (i.e., always leaving a minimum of 1 % "open water") (Bates et al., 2006; Legge et al., 2015; Mucci et al., 2010; Roden et al., 2013). This is done in an attempt to include a representation of the complex mechanisms that explain sea ice-atmosphere gas fluxes recorded in previous studies (Delille et al., 2014; Loose and Schlosser, 2011; Miller et al., 2011; Semiletov et al., 2004). For the current length of the Rothera carbonate chemistry time series, maintaining a maximum reduction to the gas transfer velocity of 99 % at 100 % sea ice cover results in a change in CO_2 flux between -0.2 and 0.2 mol m^{-2} yr^{-1} relative to allowing the contribution of the gas transfer velocity (and therefore the CO_2 flux) to decrease to 0 %. At a difference of < 0.004 mol m^{-2} between the cumulative CO_2 flux results between 2011 and 2020, the effect of maintaining 1 % of CO_2 flux at full sea ice cover is negligible. We nevertheless apply this method to remain consistent with the work by Legge et al. (2015). To scale the gas transfer velocity, we use sea ice cover of all types, unless specified differently. For an overview of all supporting datasets used in this work for the calculations shown above, see Table B.4.

4.2.6 Meltwater input

Salinity and $\delta^{18}O$ are both conservative tracers away from the ocean surface and share a number of processes that affect them in similar ways, e.g., evaporation and precipitation. The great utility of $\delta^{18}O$ in polar waters is that it is only minimally affected by sea ice formation and melt, whereas salinity is very strongly affected by these processes. Conversely, high-latitude meteoric water input (glacial melt and net precipitation combined) strongly affects both $\delta^{18}O$ and salinity. This decoupling of the two tracers allows calculation of different freshwater sources. This is achieved quantitatively using a three-component mass-balance method, which has been used in previous RaTS studies (Legge et al., 2017; Meredith et al., 2008; Meredith et al., 2010). It consists of three mass-balance equations: one for mass conservation (Eq. 4.4), one for salinity (Eq. 4.5), and one for $\delta^{18}O$ (Eq. 4.6). Each contains a component for the mCDW, sea ice meltwater, and meteoric water. Following previous work, we reasonably assume a system where the mCDW is the main oceanic water mass source, which is annually diluted at the surface by sea ice and glacial melt, and annually salinified at the surface by sea ice production. Solving these equations results in fractions of each of these water mass types that contributed to the seawater sample.

$$f_{mCDW} + f_{sim} + f_{met} = 1 \tag*{(Eq. 4.4)}$$

$$S_{mCDW} \cdot f_{mCDW} + S_{sim} \cdot f_{sim} + S_{met} \cdot S_{met} = S \tag*{(Eq. 4.5)}$$

$$\delta^{18}O_{mCDW} \cdot f_{mCDW} + \delta^{18}O_{sim} \cdot f_{sim} + \delta^{18}O_{met} \cdot S_{met} = \delta^{18}O \qquad \text{(Eq. 4.6)}$$

In equations 4.4, 4.5, and 4.6, the variable f denotes the fraction of either the local version of mCDW in Ryder Bay (mCDW), sea ice meltwater (sim), or meteoric water (met). In Ryder Bay, the latter will mostly consist of glacial ice meltwater. S and δ^{18}O are the salinity and oxygen isotope ratio measured in the sample. For consistency, we use the same endmembers as Legge et al. (2017), shown in Table 4.1. The uncertainty in the endmembers is estimated to be ± 1 % (Meredith et al., 2008). The meteoric endmember harbours most uncertainty, as it combines glacial meltwater, runoff, and net precipitation, all of which can have different endmember values (Meredith et al., 2008).

Table 4.1: Endmembers for three water mass types relevant to Ryder Bay, using the same values as Legge et al. (2017).

Water mass type	**Salinity endmember**	**δ^{18}O endmember [‰]**
mCDW	34.62	0.08
Sea ice meltwater	7	2.1
Meteoric water	0	-17

4.2.7 Definitions of seasons

Asymmetric seasonal changes in the water column in Ryder Bay (Legge et al., 2017; Meredith et al., 2010; Venables and Meredith, 2014) highlight a need for a Ryder Bay-specific definition of the seasons that we can use to look at the interannual variability of seasonal processes, as well as inter-seasonal dependencies. We define the range of the winter season between day of the year (DOY) numbers 152 and 281 (1 June - 8 October). The summer season starts on DOY 349 (15 December) and ends on DOY 64 (5 March). The choice of these DOYs is based on the seasonal variability of certain key variables, using RaTS data available since 1997, as follows. The onset of winter coincides with the time when the seawater between 0 and 15 m depth (where we have most of the chemical time series data) is well mixed (i.e., no detectable salinity gradient) (Fig. B.1). The seawater temperature gradient is also very low at this point, although the surface is still cooling. The end of winter is the average of time points when the salinity at 15 m depth, the contribution of mCDW at 15 m depth, and the MLD have reached their maxima and the contribution of meteoric water has reached its minimum (Fig. B.1 and B.2). The summer starts when daily mean air temperatures at 2 m above sea level continuously exceed 0 °C. The summer ends at a time when air temperatures continuously remain below 0 °C. The end of summer is also characterised by a minimum in salinity and mCDW fraction, maxima in sea ice melt fraction, and glacial melt fraction, and maximum seawater temperature at 15 m depth. The exact choice of DOY for the ending and beginning of the seasons harbours an element of subjectivity. However, these choices are reasonable for the purpose of isolating times in the year when - on average - rapid changes occur in the water column and when variables at the surface on average reach their maxima and minima.

4.3 Results

4.3.1 Water column structure

Driven by the seasonal growth and melting of sea ice, Ryder Bay is characterised by a strong seasonal cycle of many processes and variables, which is strongest at the surface (Clarke et al., 2008). Solar heating starting in early spring and the subsequent melting of sea ice and glaciers surrounding the bay lead to the formation of a stratified surface layer, reaching average minimum salinity values of 31.97 and average maximum temperature values of 2.32 °C in the top 15 m (Fig. 4.3a and 4.3b). Throughout the melting season, the stratified, warm, and fresh surface layer erodes the cold WW from the previous winter. Sandwiched between the warmer mCDW below and the warmer surface water above, the remnant WW is characterised by a temperature minimum, ranging between -1.93 °C (in late winter) and 0.02 °C (in late summer). Heat loss to the atmosphere in autumn and winter reduces the surface seawater temperature to the freezing point. The stratification subsequently collapses, as the MLD deepens partly due to convection by brine rejection from sea ice formation, but mainly due to mechanical mixing by surface wind stress (Clarke et al., 2008; Venables and Meredith, 2014). The average salinity in the top 15 m sometimes reaches values above 34.0. Interannual variability in the water column structure is largely driven by sea ice cover and its duration (Venables and Meredith, 2014). Less sea ice and shorter duration of sea ice cover reduce protection of the water column from wind-induced mixing (Wallace et al., 2008), allowing more heat release to the atmosphere in the winter (cooling effect). Counterintuitively, the reduced stratification tends to lead to enhanced heat uptake in the subsequent summer and higher heat content by autumn (warming effect), potentially affecting the onset of sea ice formation in the following winter (Venables and Meredith, 2014).

Deep isohalines and isotherms shoal between 2011 and ∼2016 (white and grey lines in Fig. 4.3a and 4.3b, respectively), which is part of the recovery of a regional freshening and cooling event that occurred in 2008. In 2008, low ice cover across Marguerite Bay led to deep mixing and a deepening of the thermocline, which then led to cooler and less saline water being entrained into lower parts of the basin as water overflowed the sills towards Ryder Bay (Venables et al., 2017). The summers of 2010 / 2011, 2013 / 2014, 2016 / 2017, 2017 / 2018, and 2019 / 2020 saw enhanced heat uptake from the atmosphere (Fig. 4.3a), which coincides with higher atmospheric temperatures well above freezing (see Section 4.4.8). Interannual variability in the meteoric and sea ice meltwater contributions (Fig. 4.3c) is mirrored in lower surface salinity. The summers of 2016/2017 and 2019/2020 stand out as particularly fresh summers (Fig. 4.3b). Maximum chlorophyll *a* values, as well as the persistence of chlorophyll *a* levels, vary from year to year (Fig. 4.3d).

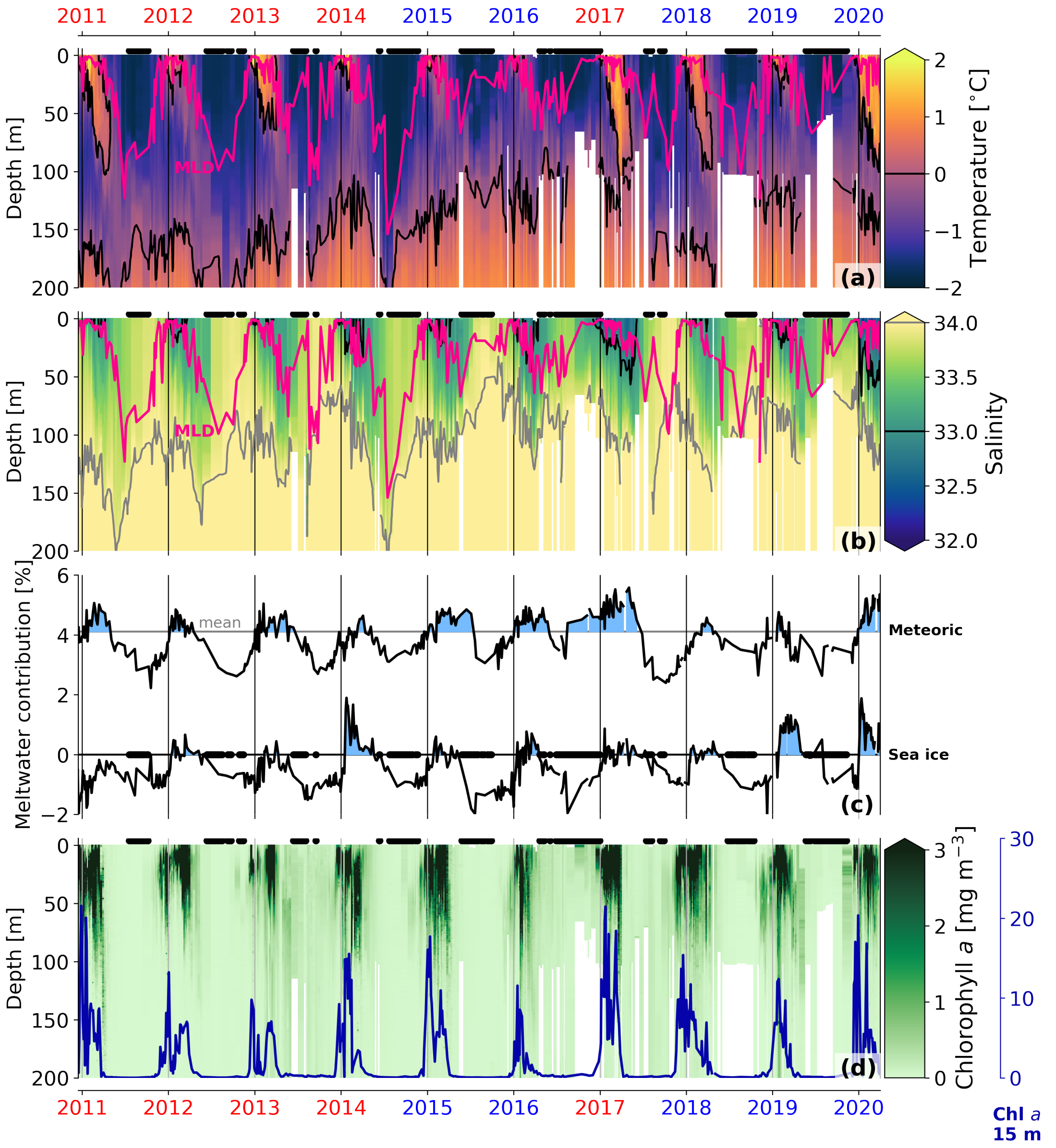

Figure 4.3: (a) Temperature in the upper 200 m of the RaTS between 2011 and 2020. White lines indicate the isoline of 0 °C. The dotted white line indicates the MLD. Years that have been categorised as high- or low stratification years are marked in blue and red, respectively. (b) same as (a) but for salinity. The black and grey lines indicate the isolines at salinity of 33 and 34, respectively. The MLD is shown as a black dotted line. (c) The meteoric and sea ice meltwater contributions, based on stable isotope data. Sea ice contribution is positive for meltwater and negative for freezing/brine rejection. Meteoric fractions higher than the mean meteoric fraction (4.1 %, based on the RaTS since 2001) are highlighted with a blue colour. Sea ice meltwater contributions above 0 % are highlighted with a blue colour. Green markers along the 0 % line indicate days when the fast sea ice cover in Ryder Bay was > 80 %. (d) Same as (a) but for chlorophyll. The secondary y-axis shows the chlorophyll concentration at 15 m depth, in blue.

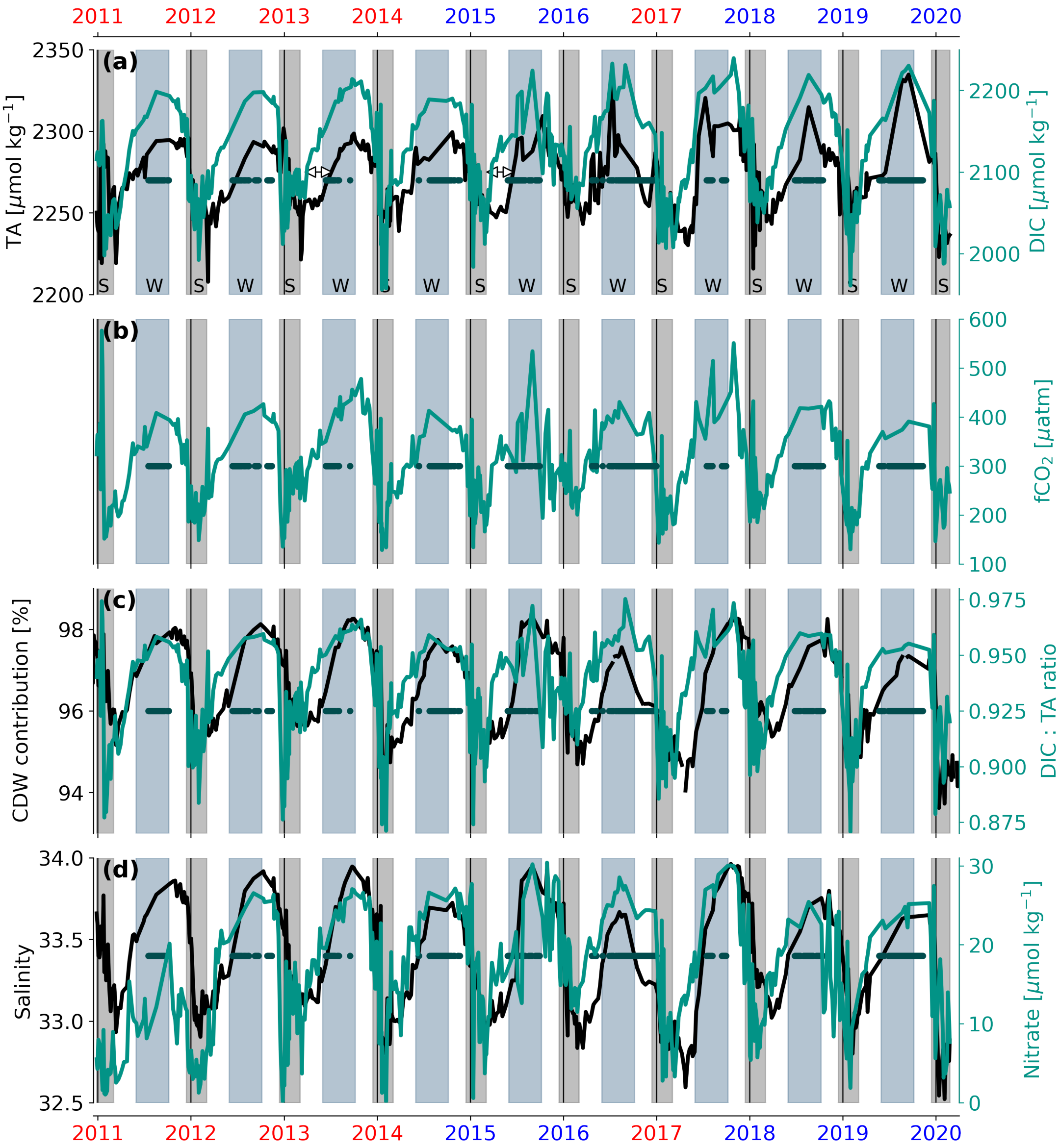

Figure 4.4: Summer (S) and winter (W) time, as defined in this work, are shown by the vertical grey and light blue bars. Green markers placed at an arbitrary level of the y axis indicate the days when the fast sea ice in Ryder Bay was recorded to be higher than 80 %. Years that have been categorised as high- or low stratification years are marked in blue and red, respectively. Variables that co-vary most similarly in time have been plotted in the same colour. (a) TA (black, left) and DIC (teal, right) at 15 m depth for the RaTS between 2011 and 2020. The double arrows serve to draw the attention to the decoupling in the changes between the DIC and TA content in the autumn, which applies to most years but is particularly clear in 2013 and 2015. (b) Same as (a) but only for fCO$_2$. (c) Same as (a) but for the contribution of mCDW based on stable isotope data, and the DIC:TA ratio. (d) Same as (a) but for salinity and nitrate content.

4.3.2 Surface carbonate system

The DIC and TA contents at the standard 15 m depth for RaTS show a clear and asymmetric seasonality (Fig. 4.4a). The temporal patterns are generally characterised by a sharp decrease in DIC during the spring and summer seasons, driven by biological carbon uptake (Legge et al., 2017), and reduction in DIC and TA through meltwater dilution. The DIC and TA content gradually increase in the transition into winter, which is predominantly driven by mixing (Legge et al., 2017) and partly by brine rejection during sea ice formation. Other studies along the WAP have reported net respiration as a source of DIC in the winter (Wang et al., 2010). The differences in DIC and TA content between wintertime and summertime range within 280 and 170 μmol kg^{-1}, respectively. This is somewhat larger than reported for the first three years of the timeseries (2011-2014; Legge et al., 2015; Legge et al., 2017), i.e., subsequent years show higher interannual variability. Summertime values are comparable to those reported for the surface seawater in Ryder Bay in Jones et al. (2017b), Hauri et al. (2015), and Jones et al. (2021) along the coast and shelf of the WAP. The seasonality of fCO_2 closely follows that of DIC and the DIC:TA ratio (Spearman's rank correlation coefficient 0.956 and 0.995, respectively; Fig. 4.4b and 4.4c), indicating that it is mostly driven by DIC content. Most intra-seasonal variability in fCO_2 is recorded for the winters of 2015, 2016, and 2017 due to the variability in the DIC and TA content. The TA content closely follows the seasonal trends seen in the mCDW input and salinity, suggesting that TA has a closer relationship to its mCDW source than DIC.

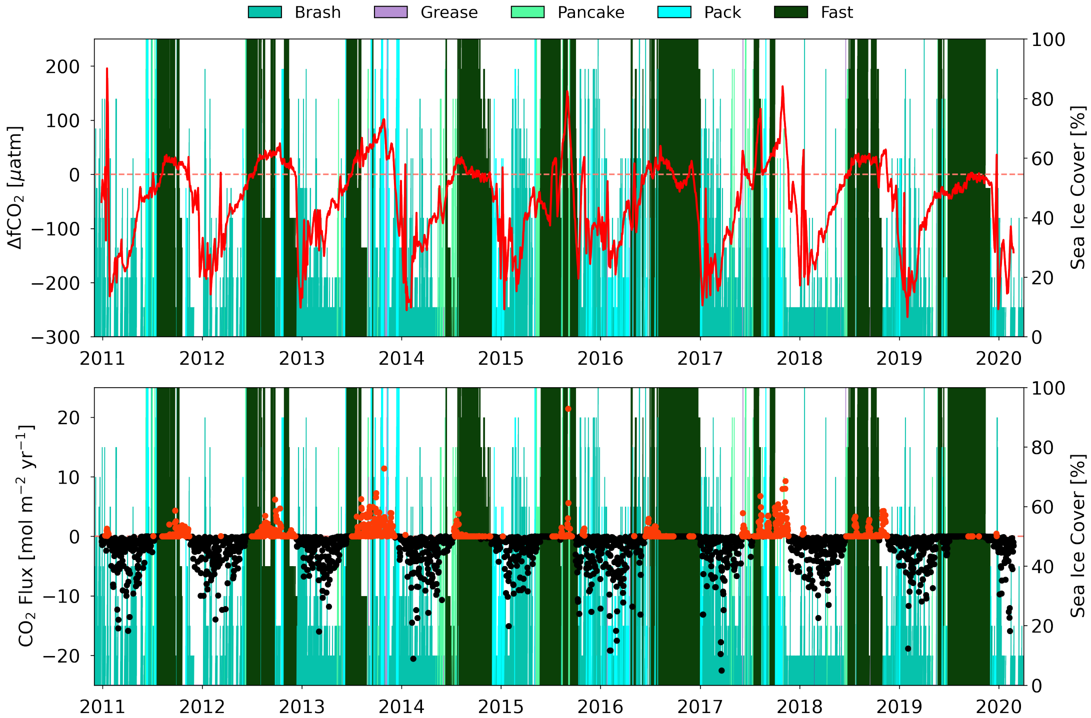

Figure 4.5: (a) The ΔfCO_2 for the RaTS between 2011 and 2020, with sea ice cover of different sea ice types plotted in the background. Seawater fCO_2 is determined using the carbonic acid dissociation constants by Goyet and Poisson (1989). (b) Same as (a) but for the CO_2 flux, for which the gas transfer velocity (using Wanninkhof (2014)) has been scaled according to the fraction of open water in Ryder Bay when considering all sea ice types. Positive fluxes indicate sea-air CO_2 release to the atmosphere, marked in red. Negative fluxes indicate CO_2 uptake by the seawater, shown in black markers.

The difference between the seawater and atmospheric fCO_2 (ΔfCO_2) determines the sign of the sea-air CO_2 flux and ranges between -260 and 200 μatm, indicating a strong potential for CO_2 uptake during the summer and a potential (i.e. if direct sea-air gas exchange is unobstructed by sea ice) for CO_2 release during the winter (Fig. 4.5a). The strength of the CO_2 flux is mainly dependent on wind speed (Wanninkhof, 2014) and sea ice cover. We find clear interannual variability in the seasonal CO_2 flux (Fig. 4.5b). Negative CO_2 flux values indicate atmospheric CO_2 uptake by the ocean, positive CO_2 flux values indicate outgassing / release of CO_2 from the ocean to the atmosphere. Consistent with Legge et al. (2017), all summer seasons indicated strong atmospheric CO_2 uptake between 10 and 25 mol m^{-2} yr^{-1}. The winter seasons are more variable between years, as illustrated by some years with high outgassing (larger positive flux) for a large part of the wintertime (e.g., 2013), by others with shorter durations of lower outgassing (lower positive flux; e.g., 2011), and even by some years with both CO_2 uptake and outgassing (negative to positive flux; e.g., 2016).

4.4 Discussion

4.4.1 Sea ice cover as a driver for interannual variability in ΔfCO_2

Fig. 4.6 shows the same ΔfCO_2 data as Fig. 4.5a, but the data have been aggregated into annual and seasonal means to distinguish the contributions of interannual variability of the seasons to the interannual variability of the years. The results clearly show interannual variability in both annual and seasonal means. It also shows a similar pattern between the variability of the winter and the annual means. This significant positive relationship is more clearly shown in Fig. 4.7, suggesting that years with less negative / more positive ΔfCO_2 in winter have higher annual ΔfCO_2 means ($p\text{-value} < 0.05$). A similarly significant relationship is found between spring and annual means (not shown), due to preconditioning of the springtime carbonate system by the preceding winter, which is a topic explored below. No significant relationship with annual means is found for the summer and autumn values (not shown). While summer and autumn ΔfCO_2 show a similar degree of interannual variability as the wintertime means, their individual measurements are much more variable (with some exceptions, e.g., winters of 2015 and 2017 have high intra-seasonal variability).

The fCO_2 in the surface layer is dependent on DIC and TA content, and seawater temperature. As surface seawater temperature in winter remains invariably close to the freezing point of seawater, the wintertime fCO_2 (and ΔfCO_2) is mainly driven by DIC and TA content. Considering the relationship between wintertime and annual ΔfCO_2, understanding the processes affecting DIC and TA content in winter becomes important to understand the overall interannual ΔfCO_2 variability.

The timing of sea ice formation, its persistence, and its retreat varies from year to year (Fig. 4.8). We find that the duration of sea ice cover in autumn and winter combined explains much of the year-to-year differences in wintertime ΔfCO_2 ($R = -0.79$; Fig. 4.9a). Earlier onset of sea ice formation and more persistent sea ice during the winter leads to lower potential sea-air CO_2 outgassing or even more potential sea-air

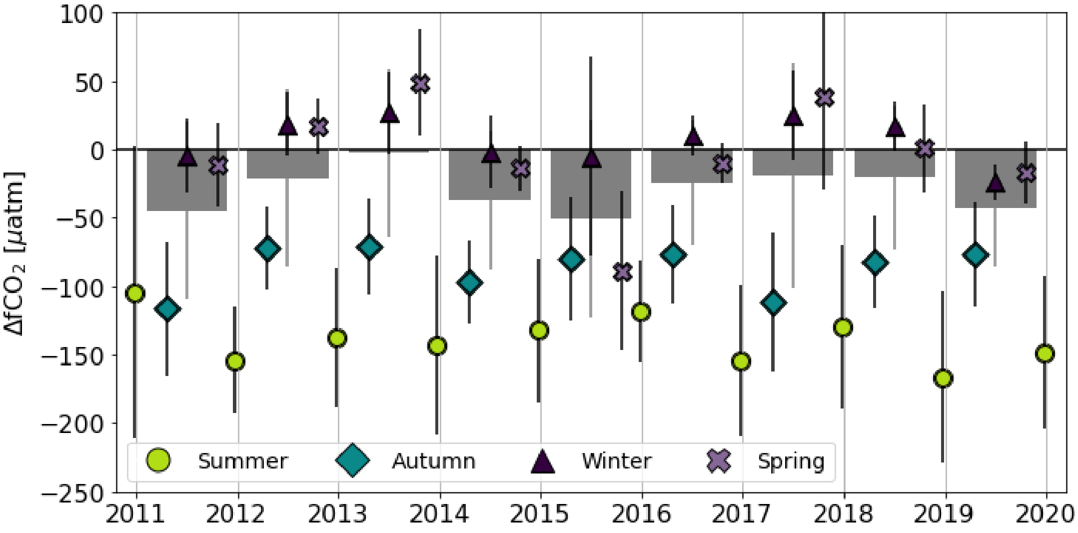

Figure 4.6: Annual means of ΔfCO_2 for each year between 2011 and 2020 of the RaTS are shown in grey bars. The annual mean is calculated starting at the beginning of autumn of the year and ending at the end of summer into the following year. Seasonal means in ΔfCO_2 are shown by markers: circles represent summer, diamonds represent autumn, triangles represent winter, and crosses represent spring. All error bars indicate 1 standard deviation of the data. Negative values indicate potential atmospheric CO_2 uptake, positive values indicate potential CO_2 release to the atmosphere.

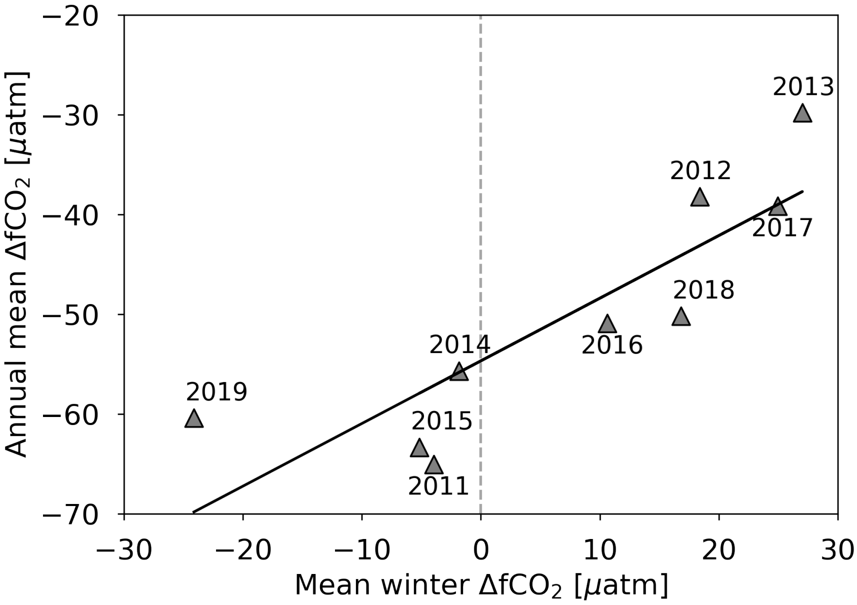

Figure 4.7: Annual mean ΔfCO_2 plotted against the mean winter ΔfCO_2 per year between 2011 and 2019 in Ryder Bay.

CO_2 uptake in winter. A similar relationship is found when looking at the springtime values, further discussed below. When substituting ΔfCO_2 with CO_2 flux, the negative relationship to sea ice continues to exist, although the relationship flattens for years with early onset of sea ice or persistent wintertime sea ice cover, as sea ice restricts direct gas exchange (Fig. 4.9b). These findings indicate that the duration of sea ice cover is an important driver in the interannual variability of annual CO_2 flux.

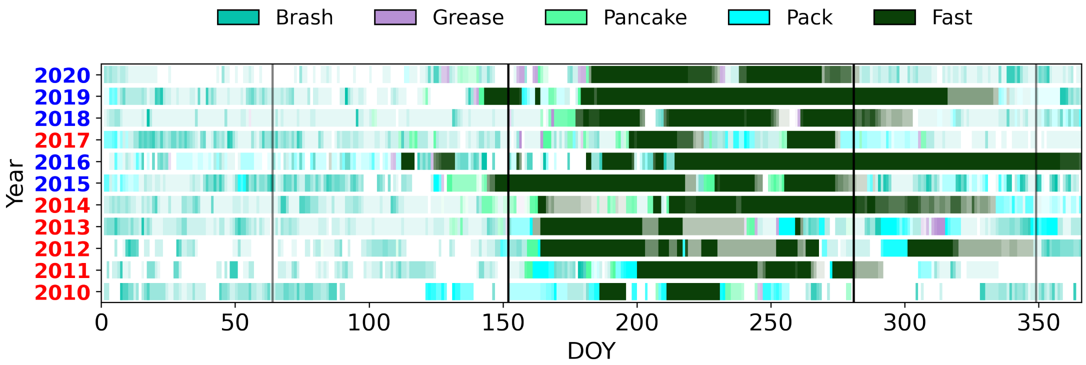

Figure 4.8: Occurrence of sea ice in Ryder Bay for 2010-2020. The different colours indicate different recorded sea ice types. The transparency of the colours gives a qualitative indication of the sea ice cover. Years that have been categorised as high- or low stratification years are marked in blue and red, respectively.

The role of sea ice cover duration in the interannual variability of Ryder Bay has been demonstrated in previous studies for various other variables, such as for chlorophyll *a* levels (Venables et al., 2013), surface nutrient content (Henley et al., 2017), and heat exchange with the atmosphere (Venables and Meredith, 2014). As the surface carbonate system is closely related to all these variables, the association of the interannual variability of CO_2 flux to sea ice is to be expected, as mCDW is warm, has a higher salinity, and is rich in nutrients and carbon due to being an older water mass. However, we would like to underline the specific role of sea ice cover duration on the wintertime CO_2 flux, the processes behind which are discussed in the next section.

4.4.2 Drivers of fCO_2 between winters with high and low stratification

Previous studies in Ryder Bay have demonstrated that wind-driven mixing and upwelling of mCDW are the physical processes that replenish DIC, TA, and inorganic nutrients in the surface layer during winter (Clarke et al., 2008; Legge et al., 2017). In this location, sea ice cover protects the water column from wind-driven mixing to a greater extent than extra brine rejection drives mixing. Sea ice thereby regulates the connectivity between the surface layer and mCDW and thus also to some extent the exchange of heat and CO_2 between the surface layer and the atmosphere. In Ryder Bay, years with low stratification in winter are associated with short sea ice cover duration and release of heat derived from mCDW to the atmosphere (Stammerjohn et al., 2008a; Venables and Meredith, 2014). Winters with higher stratification and less mixing tend to have less heat loss deriving from mCDW (Venables and Meredith, 2014). Despite different equilibration times[1], we investigated whether parallels can be drawn between heat and carbon dioxide (i.e., ΔfCO_2) when it comes to the role of mCDW ventilation

---

[1] The equilibration time for CO_2 in seawater is considered to be relatively slow, even compared to oxygen, because changes in CO_2 are buffered by DIC, slowing down equilibration (Zeebe and Wolf-Gladrow, 2001). Moreover, mass diffusion is slower than thermal diffusion across gradients, as the former propagates by particle movement and the latter through particle contact.

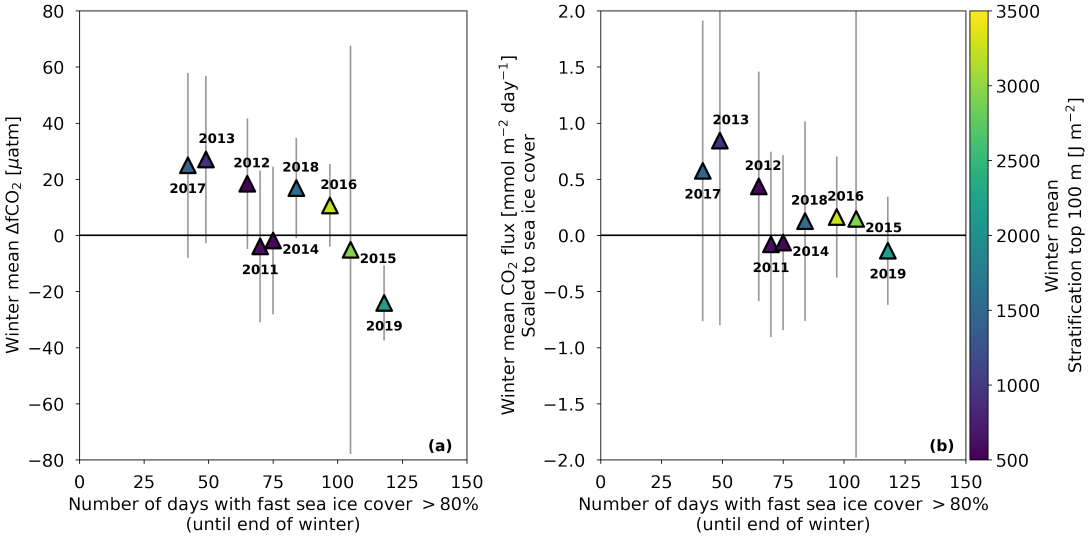

Figure 4.9: (a) Mean ΔfCO_2 for the winter of each year in the RaTS between 2011 and 2020, plotted against the number of days with fast sea ice cover > 80 % between the end of summer and the end of winter of each year, coloured according to the mean stratification in winter. Error bars indicate 1σ of the means. (b) Same as (a) but for CO_2 flux (k scaled by sea ice cover). The x-axis shows the number of days with fast sea ice cover > 80 % between the summer and the end of winter of each year.

and connectivity to the surface layer, understood through the strength of water column stratification.

Fig. 4.10 is an updated and modified one from Venables and Meredith (2014), including the more recently added data and using the seasonal definitions from the current work. Using threshold values of 50 m for the mean winter MLD and 1500 J m^{-2} for the mean winter stratification (as in Venables and Meredith (2014)), we categorise winters between "high stratification" with shallow mixing and "low stratification" with deep mixing. We found that 2015, 2016, and 2019 are years with high stratification in winter. Winters in 2011, 2012, 2013 and 2014 have comparatively low stratification.

Based on Fig. 4.10, winters of 2017 and 2018 fall between the low- and high-stratification categories, which shows that the degree of mixing during winter cannot always be described in a binary manner. The time series for salinity at 15 m depth and stratification in the upper 100 m were de-seasonalised by decomposing the time series into its trend and seasonal components using the Statsmodels Python package and subtracting the seasonal component from the observations. These results are shown in Fig. B.3 and indicate clearly diverging behaviour at the beginning of winter for high and low stratification years. For years with winters characterised as "low stratification winters", the de-seasonalised stratification decreases and salinity increases. In winters characterised as "high stratification winters" the de-seasonalised stratification and salinity in winter increase and decrease instead, respectively. The divergence between low and high stratification winters reaches a maximum difference in averaged de-seasonalised values of about 500 J m^{-2} for stratification and 0.25 for salinity. The de-seasonalised results for 2017 are more similar to those of low stratification winters (decreasing stratification

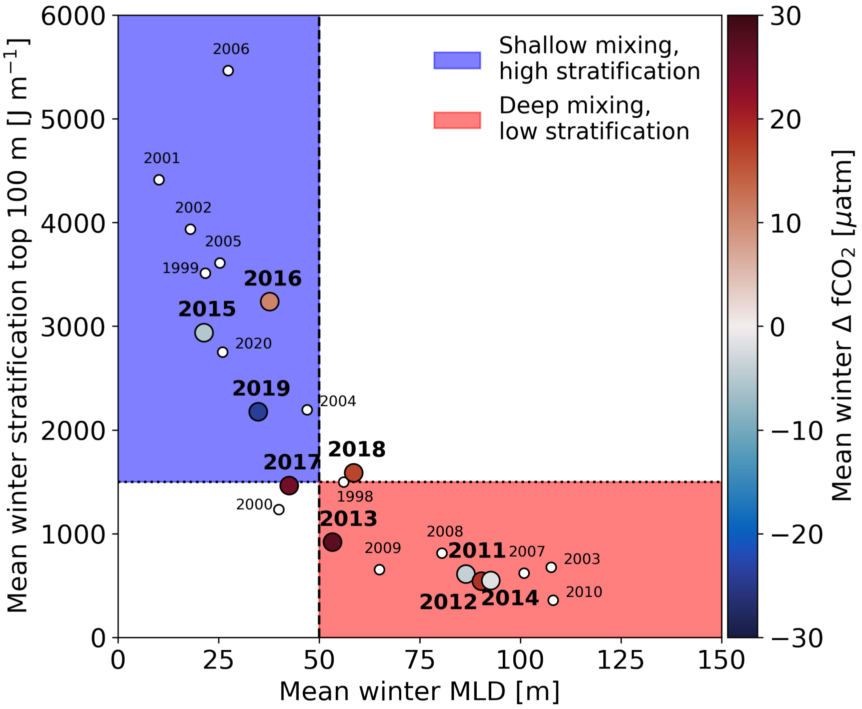

Figure 4.10: Mean winter stratification in the top 100 m plotted against the mean winter mixed layer depth (MLD) for the RaTS since 1999. This figure is updated from Venables and Meredith (2014), using the seasonal definitions of the current work. For years between 2011 and 2019, markers have been enlarged and coloured according to the mean winter ΔfCO$_2$. Markers for years before 2011 are kept small and are not given a colour, as no carbonate chemistry data was collected in these years. Following Venables and Meredith (2014), winters with a mean MLD > 50 m are categorised as deep mixing, low stratification years. Winters with a mean MLD < 50 m are marked as shallow mixing, high stratification years. Often this coincides with a stratification threshold of 1500 J m^{-2}.

and increasing salinity) and the de-seasonalised results for 2018 are more similar to the evolution seen for high stratification winters (increasing stratification and lower salinity). Although the distinction is not as clear for 2017 and 2018 as for other years, for the purposes of this work, we describe the winters of 2017 and 2018 as low and high stratification winters, respectively.

The markers in Fig. 4.10 are coloured according to the mean winter ΔfCO$_2$ (also featured in Fig. 4.6). Winters of 2013 and 2017 stand out with low stratification and deep mixing due to particularly low sea ice cover duration, leading to high mean ΔfCO$_2$, as well as CO$_2$ outgassing (Fig. 4.9). The winter of 2012 is less extreme than 2013 and 2017, but has variable sea ice cover in Ryder Bay due to warm, northerly winds that increased mixing and CO$_2$ outgassing. However, when considering all years in the time series, the association of high mean ΔfCO$_2$ to low stratification in winter (as exemplified by 2012, 2013, and 2017) seems to be the exception rather than the rule. For example, 2011 and 2014 have deep mixing in winter yet have a similar mean ΔfCO$_2$ to the winter in 2015, which had high stratification and low mixing.

Given that heat in the surface layer during winter is linked to wintertime stratification, the RaTS ΔfCO_2 results suggest that the role of wintertime connectivity between the deeper mCDW and the surface layer may be different for mCDW-derived CO_2 compared to heat, despite affecting both. Instead, the relationship between winter stratification / mixing and ΔfCO_2 is confounded by ice meltwater input in the preceding melting season (e.g., 2014); large-scale atmospheric circulation, such as El Niño-Southern Oscillation (ENSO; e.g., 2015-2016) and the Southern Annular Mode (SAM; e.g., 2015-2017, 2019); and ocean-sea ice interactions. How these factors affected the wintertime interannual variability in Ryder Bay between 2011 and 2019 is discussed in the following sections.

4.4.3 The melting season preconditions fCO_2 in winter

Winter 2014 is characterised as a low stratification winter and has the deepest MLD recorded during the period 2011-2020 (Fig. 4.10). Despite deep mixing, mean surface ΔfCO_2 remained slightly negative (potential CO_2 uptake) in winter due to enhanced sea ice meltwater input in the preceding melting season (Fig. 4.3c). Sea ice formed late in 2014 (Fig. 4.8), which enabled wind-driven mixing of the ice-free, lower salinity surface waters in the autumn and early winter. Deep winter mixing in 2014 not only caused a strong cooling, but also strong freshening of the water column down to ~200 m depth (Fig. 4.3a and 4.3b), to such a degree that it diluted DIC content in the upper water column throughout the winter. The increased salinity and DIC content derived from mixing with mCDW seen in other similarly low stratified winters was thus suppressed in 2014.

The enhanced sea ice meltwater signature in 2014 is a phenomenon observed for a larger region along the WAP (Meredith et al., 2021), caused by anomalous winds at the end of 2013 that dynamically diverged the sea ice field while it melted (Meredith et al., 2017; Meredith et al., 2021). The regional sea ice cover along the WAP persisted long into the year in 2013, continuing to provide *in situ* sea ice meltwater (Meredith et al., 2017). Although the small number of days with fast ice cover ($>$ 80 %) in Ryder Bay does not reflect the prolonged sea ice season duration recorded for the larger region, pack ice was observed late in the season in 2013 (Fig. 4.8), which is consistent with regional observations (Meredith et al., 2017). Advection of sea ice meltwater in Marguerite Bay may have contributed to the high sea ice meltwater contribution observed in Ryder Bay in early 2014.

Enhanced sea ice melt water input also occurred in early 2019 (Fig. 4.3c). Unlike in 2014, early onset of sea ice formation protected the water column from deep mixing, constraining the fresh surface water to the top 50 m and the carbon-rich mCDW below the mixed layer. The combined effect of shallow mixing and high sea ice meltwater input resulted in a particularly low winter ΔfCO_2, leading to the highest net annual CO_2 uptake in Ryder Bay between 2011 and 2019. These findings suggest that it is important to consider the meltwater input in addition to the MLD to understand the potential wintertime CO_2 flux in polar coastal regions.

4.4.4 Role of ENSO and SAM on interannual variability in Ryder Bay

The ENSO and the SAM are two large-scale meteorological cycles that affect the air temperatures along the Antarctic Peninsula (Clem et al., 2016)(Table B.4). The ENSO phenomena (El Niño and La Niña) are characterised by air temperature anomalies above the equatorial Pacific Ocean (e.g., Wang and Fiedler, 2006). The SAM describes the latitudinal position and strength of the westerly winds around Antarctica (Marshall, 2003), where a positive value indicates a southward movement of the westerly winds. Both systems affect the climate along the WAP through their influence on the position and strength of a meta-stable low-pressure system above the adjacent Bellingshausen Sea (e.g., Fogt et al., 2011). The timing of sea ice advance and retreat is influenced by both phenomena as they change wind patterns and air temperatures (Stammerjohn et al., 2008b). The sensitivity of the WAP climate to effects of these large-scale circulation anomalies depends on when they occur in the year: interannual variability in WAP climate is dominated by the SAM when a negative or positive phase of the SAM occurs in the summer and autumn, whereas the variability is dominated by ENSO when La Niña or El Niño occurs in the winter and spring (Clem and Fogt, 2013; Clem et al., 2016).

In 2015, a positive SAM occurred in the autumn and continued into winter, while an El Niño started in the winter and carried on into the spring (Fig. 4.11e and 4.11f). The strong pairing of the two phenomena caused a strong and anomalous atmospheric cooling in the winter (Fig. 4.11b), resulting in early sea ice formation (in late autumn) in Ryder Bay (Fig. 4.8). Continued cold air and seawater conditions primed early sea ice formation in 2016 (Fig. 4.8 and 4.11b). The sea ice cover restricted wind-induced mixing, causing mean winter MLDs shallower than 50 m in both 2015 and 2016 (Fig. 4.10 and 4.11d). In winter 2016, the contribution from mCDW was relatively low, as is also seen in the low winter salinity in the surface layer (Fig. 4.3b and 4.4c). Nevertheless, silicate content in winter 2016 was the highest in any other season between 2011 and 2019, suggesting that remineralisation within the surface mixed layer, instead of mCDW input, might have made an important contribution to the 2016 wintertime fCO_2.

In spring 2016, sea ice retreated at its fastest recorded rate for the Southern Ocean (Turner et al., 2017), driven by atmospheric warming caused by a strong negative SAM late in the year. The rate of sea ice retreat was different for different sectors of the Southern Ocean, but in September 2016 it was fastest in the Amundsen-Bellingshausen Sea sector (Turner et al., 2017). Rapid sea ice retreat was not observed in spring 2016 at RaTS, which instead showed a contrary trend with sea ice cover that lasted until early 2017 (Fig. 4.8). This was due to sea ice compaction, as westerly winds pushed remaining sea ice into the WAP where it accumulated and subsequently melted (Meredith et al., 2021). The persistent sea ice in Ryder Bay in late 2016 was thus advected, along with glacial meltwater from the surrounding region, compounding meltwater derived directly from glaciers around Ryder Bay (Fig. 4.3c). It exemplifies how the interannual variability caused by sea ice cover on the surface carbonate system components and CO_2 flux in Ryder Bay may not be representative on a larger regional scale due to spatial

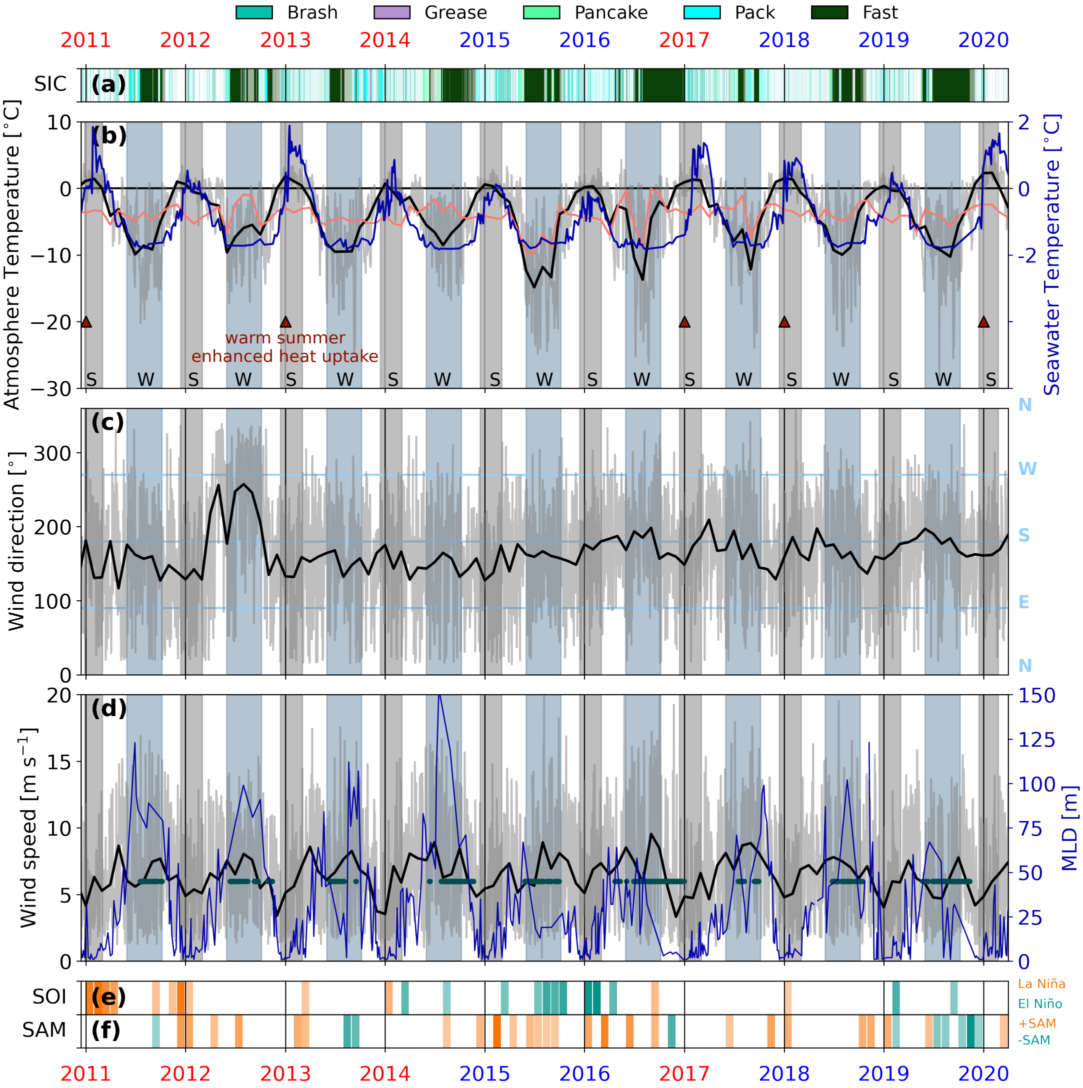

Figure 4.11: (a) Occurrence of different types of sea ice in Ryder Bay for 2010-2020. The transparency of the colours gives a qualitative indication of the sea ice cover. (b) Air temperature at 2 m above sea level (left y-axis). Daily means shown in grey, monthly means shown in black, and de-seasonalised values shown in light pink. Seawater temperature at 15 m depth (right y-axis). Warm summers are marked with red triangle markers. Vertical grey and light blue bars indicate summer and winter, respectively. (c) Wind direction at Rothera. Daily means shown in grey and monthly means shown in black. (d) Wind speed at Rothera, adjusted from 42 m to 10 m above sea level (see Section 4.2.5; left y-axis). Daily means shown in grey and monthly means shown in black. Mixed layer depth (MLD) in Ryder Bay shown in blue (right y-axis). (e) Vertical bars indicate months when the Southern Oscillation Index (SOI) was higher (orange) or lower (teal) than one standard deviation from the mean, used as an indication of La Niña or El Niño, respectively. SOI indices were obtained from the Climate Prediction centre (**cpc2003**) (Table B.4). (f) Same as (e), but for the Southern Annular Mode (SAM) index, indicating a positive SAM in orange and negative SAM in teal. SAM indices are based on Marshall (2003) and were obtained online (CPC, 2023) (Table B.4).

and temporal heterogeneity in annual sea ice conditions (Stammerjohn et al., 2008b).

Atmospheric warming in the summer of 2016 / 2017 maintained an unusually high contribution of glacial meltwater in Ryder Bay, causing strong stratification lasting until the end of autumn 2017. It also led to strong ocean heat uptake typical in this region when sea ice retreats early, warming the water column in early 2017 down to ∼120 m depth (Fig. 4.3a), and subsequently delaying the onset of sea ice formation to late in the winter of 2017 (Fig. 4.8); Stammerjohn et al., 2008a). This led to enhanced atmospheric CO_2 uptake in autumn and enhanced outgassing in winter, 2017 (Fig. 4.5). Meltwater and stratification led to low DIC content in the surface layer in autumn 2017 (Fig. 4.4a) through 1) dilution, 2) biological CO_2 uptake driven by sustained phytoplankton blooms as indicated by chlorophyll *a* concentration (Fig. 4.3d), and 3) suppressed mixing with mCDW (Fig. 4.4c). Relative to the autumns between 2011 and 2019, autumn 2017 had the lowest mean DIC and TA content. At the onset of winter 2017, the stratified water column was swiftly broken down by increasing wind stress. DIC from mCDW was mixed into the surface layer, such that CO_2 could escape to the atmosphere as the sea ice cover in the beginning of winter 2017 was still low (Fig. 4.8). The sea ice extent in 2017 was recorded as the lowest recorded extent for the Southern Ocean since 1979 (Turner et al., 2017). Wind-driven mixing and exposure of the seawater to the atmosphere in winter 2017 in Ryder Bay might therefore have been processes that were important for sea-air CO_2 exchange on a wider regional scale.

Worth noting is the similarity in atmospheric and oceanic conditions at Ryder Bay in 2016 and 2019. In a similar fashion to 2016, a negative SAM in 2019 caused atmospheric warming, leading to high meltwater input and atmospheric heat uptake in the 2019 / 2020 summer and 2020 autumn (Fig. 4.3). Moreover, 2016 and 2019 both have high stratification winters and both follow years with a high stratification winter, which possibly means that more time has passed since the surface mixed layer was in contact with the mCDW in 2016 and 2019 compared to 2015 and 2018, which followed years with low stratification winters. Future work extending the RaTS will indicate whether sea ice extent and CO_2 outgassing in 2020 follows the patterns observed for 2017.

Despite the dominant effects of SAM on the WAP climate in summer and autumn (Clem and Fogt, 2013; Clem et al., 2016), a negative SAM in the second half of the winter in 2013 nevertheless led to a brief but significant and sudden increase in wind speed (Fig. 4.11d) and concomitant sea ice cover decrease (Fig. 4.8), resulting in a deepened MLD down to 100 m depth (Fig. 4.11d) and outgassing of CO_2 (Fig. 4.5). Immediately prior to the retreat in sea ice cover, the MLD in winter 2013 was not particularly deep. This rapid turn-around in atmospheric and sea ice conditions illustrates the speed and magnitude at which ocean outgassing can respond, leading to one of the winters with highest CO_2 outgassing in the 2011-2019 period in Ryder Bay.

The winter of 2018 has not been discussed so far, as we do not associate any significant large scale wind patterns to its CO_2 flux. However, it does nicely illustrate the enhanced CO_2 outgassing events during the winter at times when sea ice cover is advected out of the bay by wind (Fig. 4.5). It also suggests that leads can be an important window between the ocean and atmosphere for winter CO_2 outgassing.

The winters of 2011 and 2012 have low stratification, but reasons for this are not yet well understood. The winter of 2011 had a mCDW contribution and salinity similar to other low stratification winters (e.g., 2012 and 2013), as sea ice appeared late in the winter, likely due to enhanced ocean heat uptake in the previous summer, which was possibly driven by a La Niña event. However, its ΔfCO_2 was just as low as that in 2014, without signs of enhanced meltwater input. The inorganic nutrient content was unusually low in 2011 (Fig. 4.4d), which cannot be explained by the contribution of mCDW to the surface (Fig. 4.4c). Regional deep mixing occurred in 2008, affecting the properties of mCDW in Marguerite and Ryder Bay (Venables et al., 2017). This was followed by a "recovery period" of the deep waters that mixed with new mCDW on the shelf, during which deep water might not have been a strong source of nutrients to the surface layer. This idea remains speculative.

In autumn and winter of 2012, anomalous northerly winds likely advected warmer air to Ryder Bay, locally causing relatively warm temperatures in the winter (Fig. 4.11b). The cause of the northerly winds is unknown. Although sea ice cover was not persistent in 2012, the northerly winds did not cause a particularly low sea ice cover year (Fig. 4.8). These unresolved conditions illustrate the complexity of the system.

Although ENSO and SAM phases have a significant influence on the climate and sea ice extent of the WAP region, single extreme and/or small-scale events, such as storms, can also strongly influence local stratification, wind-induced mixing, and sea ice dynamics. Occurrences of such events may have contributed to the observed variability in the surface layer carbonate chemistry in Ryder Bay. While their effect on DIC and TA content cannot be evaluated here, it should be noted that single and small-scale events could confound interpretations of large-scale drivers of interannual variability discussed here.

In summary, large scale modes of climate variability affect the interannual variability of the marine carbonate system through a) regulating the onset of sea ice formation and retreat, and b) affecting dynamic and thermodynamic pathways of delivering meltwater to different locations along the WAP (Meredith et al., 2017; Meredith et al., 2021). By supporting or delaying sea ice formation or retreat with anomalous temperatures and wind direction, ENSO and SAM affect the stratification of the water column, which influences the amount and timing of mixing with meltwater (reduced surface seawater fCO_2) or with mCDW (elevated surface seawater fCO_2). The effect of SAM and ENSO on wind patterns and sea ice along the WAP is complicated by topography, and off-to-onshore and south-to-north gradients (Orr et al., 2004; Stammerjohn et al., 2008b). On an annual basis, Ryder Bay is a net atmospheric CO_2 sink (Fig. 4.12; Legge et al., 2015). From the perspective of cumulative atmospheric CO_2 uptake between 2011-2020, the rate of net CO_2 uptake increases during El Niño and positive SAM phases (2015-2016; Fig. 4.12), as well during negative SAM phases (e.g., 2019; Fig. 4.12), by decreasing wintertime CO_2 outgassing. The winter interannual variability of CO_2 flux in Ryder Bay is strongly driven by SAM and ENSO, which also have decadal variability

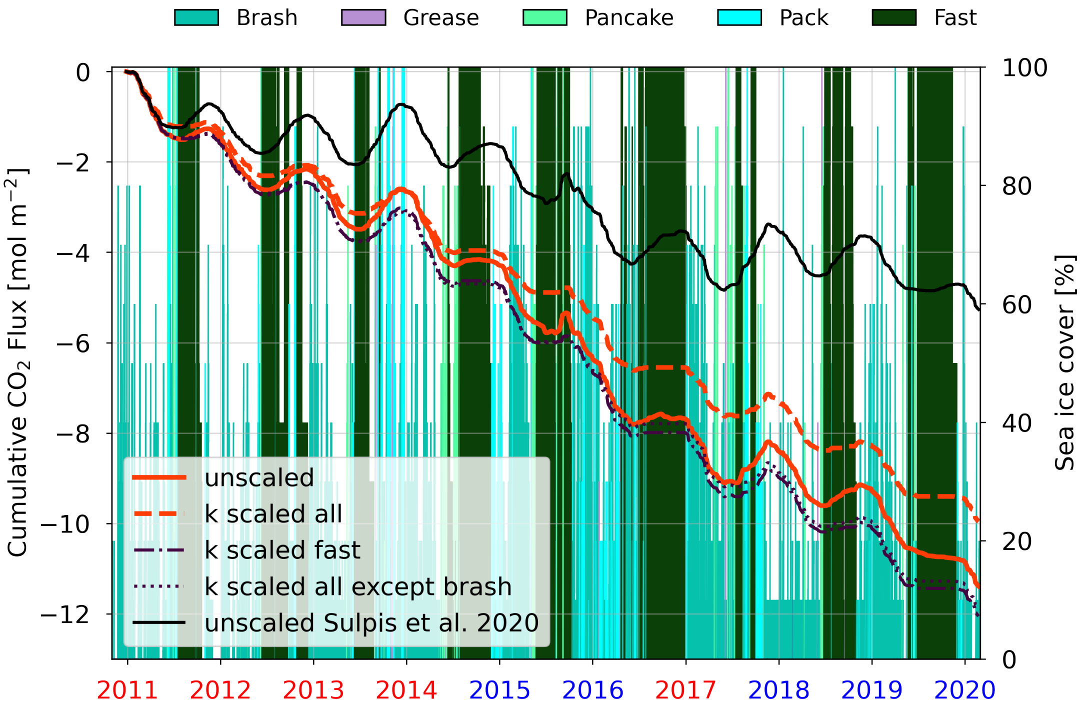

Figure 4.12: Cumulative sea-air CO_2 flux for the RaTS between 2011 and 2020, using CO_2 flux values calculated with gas transfer velocities that are not scaled (full red line), scaled according to fraction of open water (red dashed line), scaled according to the fraction of open water using only fast sea ice (purple dash-dotted line), and scaled according to the fraction of open water using all sea ice types except brash sea ice (dotted purple line). The black full line shows the cumulative sea-air CO_2 flux using an unscaled gas transfer velocity and the carbonic acid dissociation constants by Sulpis et al. (2020), instead of Goyet and Poisson (1989), to determine seawater fCO_2 from DIC and TA. Negative fluxes indicate atmospheric CO_2 uptake by the ocean. Years with high- and low stratification are marked in blue and red, respectively.

that needs to be accounted for in the CO_2 uptake in this region.

4.4.5 Ocean-sea ice interactions in winter

Besides the connectivity of the surface layer to mCDW, which is influenced by meltwater input and atmospheric forcing (see Section 4.4.4), processes occurring within the surface layer also affect the interannual variability of the CO_2 uptake. The DIC and TA content have a higher (temporal) variability in high stratification winters than in low stratification winters (Fig. 4.4a), an observation which is mostly explained by a number of samples with relatively high DIC and TA values in the second half of the season, which cannot be explained by mixing. When combining the high and low stratification winter data into means, the DIC and TA content during high stratification winters peak earlier in the season than in high stratification winters (Fig. 4.13). Salinity-normalised DIC and TA (nDIC and nTA), *sensu* Friis et al. (2003) using the mean salinity at 15 m depth in 2011-2020 (i.e., 33.34) as the reference salinity, provide a way to explore the impact of biogeochemical processes by removing any co-variation with salinity caused

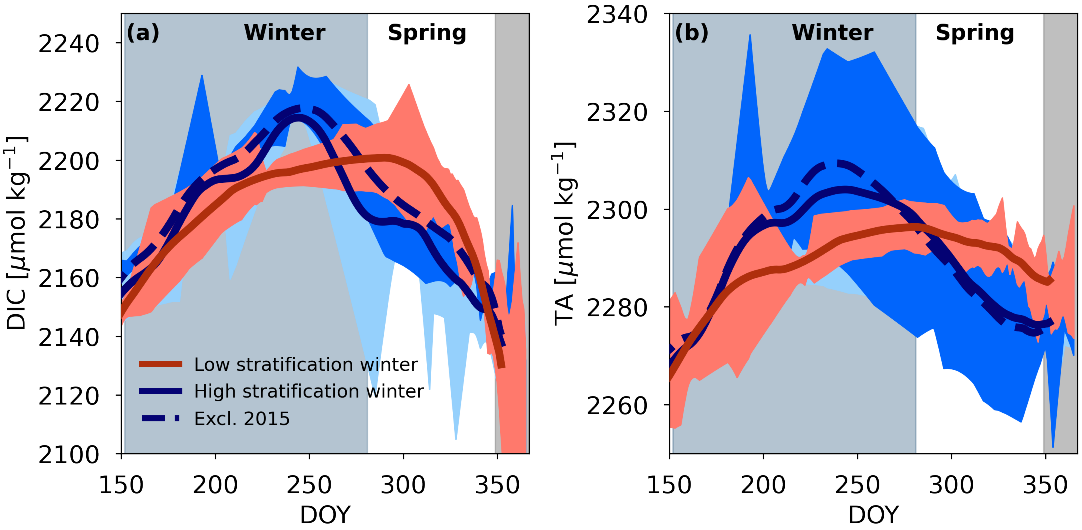

Figure 4.13: (a) Running mean for mean DIC content between day 150-165, separated by low stratification years (2011, 2012, 2013, 2014, 2017; full red line), high stratification years (2015, 2016, 2018, 2019; full blue line), and high stratification years excluding 2015, as it has the most intra-seasonal variability (dashed blue line). Shading indicates the mean ± 1 σ for low stratification years (red), high stratification years (light blue), and high stratification years excluding 2015 (dark blue). (b) Same as (a), but for TA content. Vertical blue and grey shading indicate timing of winter and summer.

by mixing-processes. In Fig. 4.14, nTA and nDIC are plotted against each other for each season. The lines (placed at an arbitrary position in the plot) represent how nTA and nDIC content would theoretically change in a relative manner if any of the following processes had a driving role in causing this change (Zeebe and Wolf-Gladrow, 2001):

- Atmospheric CO_2 uptake / release: one mol CO_2 uptake will increase DIC by 1 mol, but TA remains unchanged.
- Organic matter production / remineralisation: one mol of DIC uptake by algae during photosynthesis is associated to a decrease in TA equal to the 16 N:106 C ratio, as algae maintain electroneutrality when consuming $NO_3{}^-$ by parallel uptake of H^+ or release of OH^- (Brewer and Goldman, 1976; Goldman and Brewer, 1980).
- Calcium carbonate ($CaCO_3$) dissolution / precipitation: dissolution of one mol $CaCO_3$ releases two mol bicarbonate ions and consumes one mol CO_2, thereby increasing TA by two mol (Eq. 4.7). $CaCO_3$ precipitation reduces TA and DIC by the same 2:1 ratio, producing CO_2 (Sarmiento and Gruber, 2013).

$$\mathrm{CaCO_{3}}_{(s)} + \mathrm{H_2O_{(l)}} + \mathrm{CO_{2(aq)}} <=> \mathrm{Ca^{2+}_{(aq)}} + 2\,\mathrm{HCO_3{}^-{}_{(aq)}} \qquad \text{(Eq. 4.7)}$$

On several sampling days, high nDIC and nTA content were measured for winter samples in 2015, 2016, 2018, and 2019 (all of these years had high stratification winters

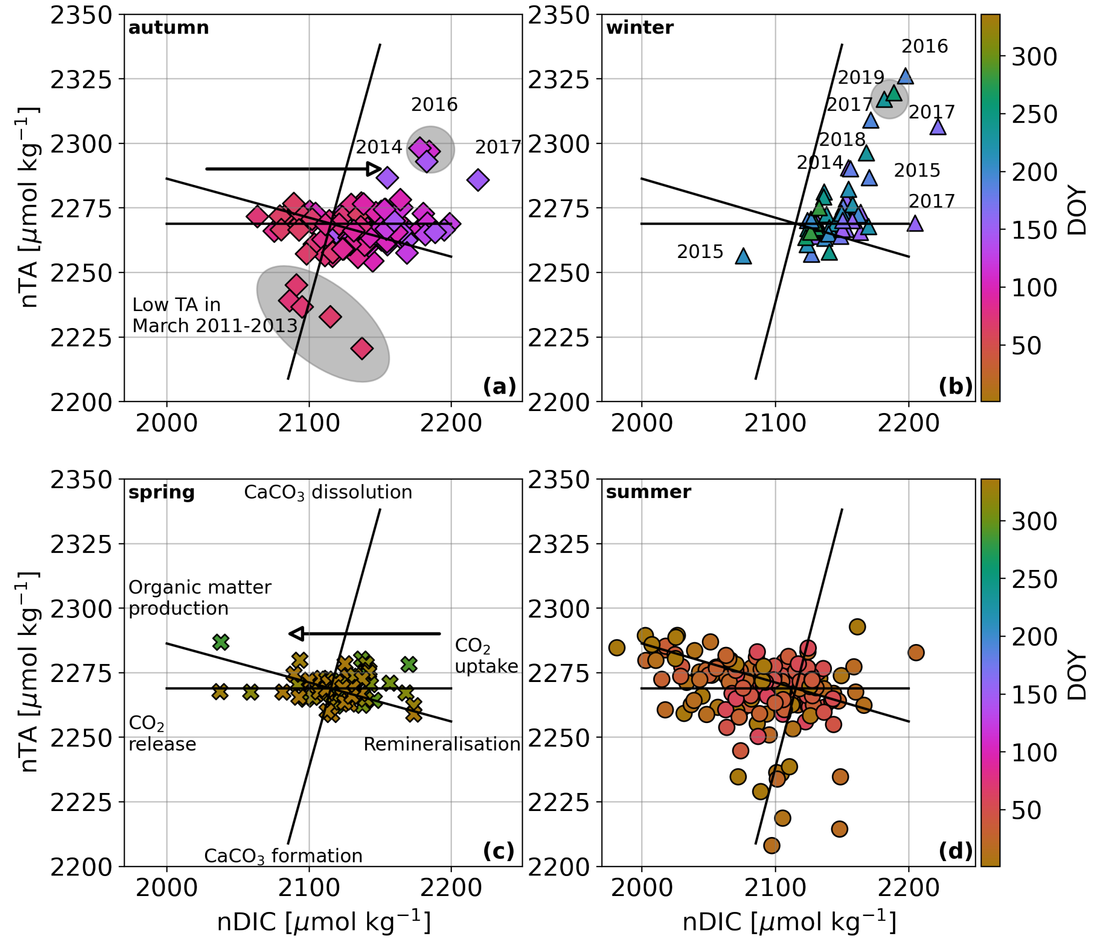

Figure 4.14: Salinity-normalised TA and DIC (nTA and nDIC) plotted against each other for the autumn (a), winter (b), spring (c), and summer (d), coloured according to day of year (DOY). Theoretical lines for $CaCO_3$ dissolution / formation, organic matter production / remineralisation, and CO_2 uptake / release are shown on all panels and are annotated in (c). See text for an explanation on the theoretical process lines. Specific datapoints discussed in the text are annotated according to the year.

with long sea ice cover duration), and 2017 (low stratification with short sea ice cover duration; Fig. 4.14b). Within the nTA-nDIC field, these datapoints line up in parallel to the $CaCO_3$ dissolution line, suggesting that this may have been an important process. As shown in Eq. 4.7, dissolution of ikaite ($CaCO_3 \cdot 6\,H_2O$) formed in sea ice increases the TA of the surface layer and decreases dissolved CO_2, thereby decreasing fCO_2 (Delille et al., 2014; Rysgaard et al., 2013). Gravity drainage of ikaite to the seawater below can occur if sea ice porosity is high enough, even in winter (Delille et al., 2014; Fransson et al., 2013; Rysgaard et al., 2013). If ikaite dissolution was the only process that contributed to the nTA increase between 20-55 μmol kg^{-1} (Fig. 4.14b), then about 10-28 μmol kg^{-1} of ikaite would have had to dissolve in the seawater after gravity drainage. Ikaite dissolution in seawater in winter of high stratification years in Ryder Bay may be associated to more persistent sea ice conditions and gravity drainage of ikaite, while the signs of ikaite dissolution in winter 2017 may be associated to sea ice porosity and early sea ice melt.

4.4.6 Sea ice and winter stratification preconditions spring CO_2 flux

The interannual variability in springtime mean ΔfCO_2 closely follows that of wintertime (Fig. 4.6 and 4.7), because the result of wintertime mixing processes set the starting conditions for DIC and TA content in the surface layer at the beginning of spring. The mean DIC and TA content in the spring surface layer are lower when spring followed a high stratification winter than when spring followed a low stratification winter. The reason is that DIC and TA content in high stratification winters generally started decreasing well before the start of spring (Fig. 4.13). In contrast, the DIC and TA content only started decreasing after the start of spring when the previous winter stratification was low, leading to a ΔfCO_2 at the beginning of spring that was higher by almost 70 μatm than after high stratification winters (50 μatm when excluding year 2015, which had particularly high intra-seasonal variability; Fig. 4.15a).

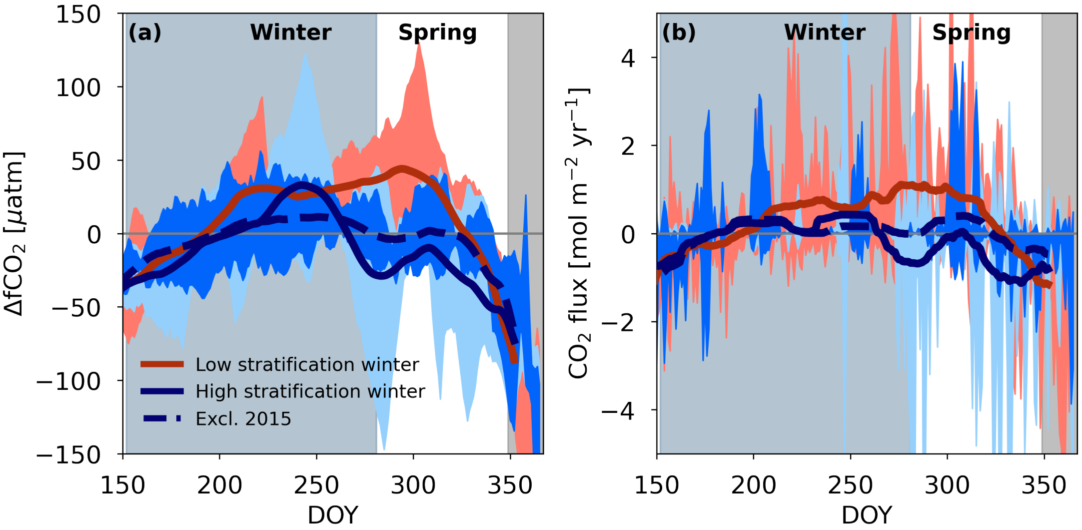

Figure 4.15: Same as Fig. 4.13, but for ΔfCO_2 (a) and CO_2 flux (b), for which the gas transfer velocity has been scaled according to all types of sea ice cover.

Earlier decrease in ΔfCO_2 in high stratification winters (Fig. 4.15a) was driven by a decrease in DIC content (Fig. 4.13a), which coincides with a simultaneous decrease in nutrients and salinity (not shown). We suggest that advanced meltwater input from melt of thicker sea ice or by advection (e.g., in the case of 2016) in late winter preconditioned years with high sea ice cover for lower ΔfCO_2 in early spring.

Substantial intra-seasonal variability exists in wintertime ΔfCO_2, especially in high stratification years, and the mean differences between high and low stratification winters are not significant. Nevertheless, low stratification years tend to have positive and higher ΔfCO_2 at the start of spring than high stratification years, resulting in CO_2 outgassing to the atmosphere (Fig. 4.15b). CO_2 outgassing is particularly clear in 2013 and 2017, the two years with lowest sea ice cover duration (Fig. 4.5b and 4.8). Complementarily, the relative change of nDIC to nTA supports CO_2 loss to the atmosphere by ice-free surface waters in spring 2013 and 2017 (not shown).

We note that measurements during winter and spring of 2015 were unusually variable, reasons for which are difficult to interpret. The mean nDIC content in spring 2015 was lower by ~20 μmol kg^{-1} compared to other years, while the nTA content remained stable. However, there was no CO_2 release to the atmosphere, as ΔfCO_2 during this period was negative. Due to lack of relationships with nutrient consumption and sea ice processes, drivers of the ΔfCO_2 variability during 2015 remain unclear.

4.4.7 Annual differences in onset of phytoplankton blooms

Spring is a time of rapid change in the surface layer carbonate system, characterised by a rapid decline in fCO_2 due to dilution of DIC by meltwater (Legge et al., 2017; Rysgaard et al., 2011), alkalinity input as a result of sea ice $CaCO_3$ cycling (Fransson et al., 2013; Fransson et al., 2017; Jones et al., 2022; Rysgaard et al., 2011), and onset of phytoplankton blooms stimulated by replenished inorganic nutrient content over the winter (Henley et al., 2017). As shown above, the interannual variability in springtime mean ΔfCO_2 is preconditioned by wintertime processes. Differences in timing of sea ice retreat and phytoplankton blooms cause additional interannual variability in springtime mean ΔfCO_2, which are explored in this section for the RaTS data from end 2010 until the beginning of 2020.

Once primary production rates increase in spring, DIC and nutrient content concomitantly decrease (for example, compare DIC and nitrate in Fig. 4.4a and 4.4d). Henley et al. (2017) showed that the interannual variability of near-surface macronutrient consumption in Ryder Bay depends on levels of chlorophyll. Chlorophyll *a* concentration is used as a proxy for primary production and biological carbon (and nutrient) uptake. Any interannual variability in chlorophyll *a* can therefore largely explain variability in biological carbon uptake. Chlorophyll *a* concentration is driven by sea ice cover duration, because sea ice enhances water column stability in spring, thereby reducing the extent of mixing for a given energy input and preconditioning the system towards supporting phytoplankton growth at the surface, rather than mixing cells deeper in the water column where variable light levels reduce photosynthetic efficiency (Saba et al., 2014; Venables et al., 2013). Consistent with this relationship, we find the highest chlorophyll *a* concentration at 15 m depth between 2011 and 2019 in summer 2016 / 2017 and 2019 / 2020, which followed seasons with long sea ice duration and high stratification (Fig. 4.3d). However, contrary to the previously-found relationship between sea ice duration and chlorophyll levels, the melting season of 2015 / 2016 was also preceded by a high sea ice season, but had a moderate level of chlorophyll.

For years 2010-2020, we find that the difference in the timing of chlorophyll *a* increase is more consistent between high and low stratification years than the difference in the *abundance* of chlorophyll in the spring and summer between these years. Specifically, the timing of chlorophyll increase started ~20 days earlier in spring seasons following low stratification winters (2011, 2012, 2013, 2014, 2017) compared to spring seasons following high stratification and high sea ice winters (2015, 2016, 2018, 2019) (Fig. 4.16a). Reduced light availability by sea ice cover might have prompted delayed phytoplankton blooms in years with sea ice cover lasting into spring.

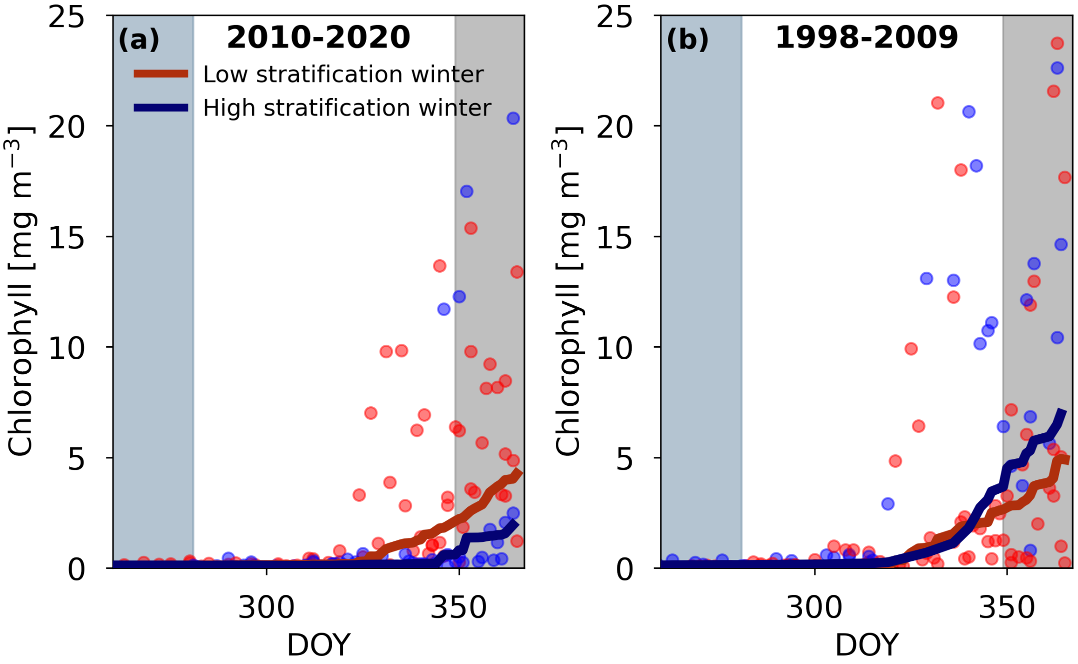

Figure 4.16: Chlorophyll *a* for the RaTS in the transition from winter to summer since 2010 (a) and between 1998 and 2009 (b). Chlorophyll *a* content is shown in red and blue markers for years categorised as having low and high stratification in winter, respectively. Thin lines indicate the average per day of year (DOY) and the thick lines indicate the 30-day running average. Colours correspond to the deep and shallow mixing years, as for the markers. Data for years 2000, 2001, and 2005 are omitted from this plot, as no measurements were made near the end of winter and/or during spring. Vertical light blue and grey bars indicate the timings of winter and summer, respectively.

Years 2013 and 2017 exhibited particularly variable and short duration sea ice cover (Fig. 4.8). Unlike most other years in 2011-2019[2], chlorophyll *a* in 2013 and 2017 reached a concentration higher than 4 mg m^{-3} by the end of spring. nDIC and salinity-normalised nutrients indicate that 2013 and 2017 are also the only years when decreases in both n-phosphate and nDIC content (and n-nitrate for 2017) during spring are significantly related to increasing chlorophyll *a* concentration (p-value < 0.05) (Fig. B.4, B.5, and B.6). Based on the decrease in n-phosphate, the contribution of biological consumption of DIC to the decrease in DIC content in spring is estimated to be about 25 μmol kg^{-1} and 66 μmol kg^{-1} for 2013 and 2017, respectively. When the melting season progresses into summer, biological consumption becomes a dominant driver in drawdown of DIC and nutrients for most years.

Two sea ice-related processes may have impacted the (lack of) relationships in other years between salinity-normalised values and chlorophyll *a* at 15 m depth in spring. One is the increase in biomass upon increasing light availability of sea ice-associated (i.e., sympagic) algae (mostly diatoms) incorporated during sea ice formation (van Leeuwe et al., 2022). Their contribution to under-ice DIC would have been missed by chlorophyll

---

[2] with the exception of 2019, which only has two datapoints in spring, and 2011

measurements at 15 m depth. "Seeding" of sympagic algae to seawater upon sea ice melt (van Leeuwe et al., 2022) may be accounted for in the chlorophyll measurements at 15 m, but their CO_2 uptake during growth is likely not captured in the seawater measurements of DIC and TA content. The other sea ice-related process is dissolution of ikaite (previously trapped in sea ice) in seawater, which consumes CO_2 (Fransson et al., 2011; Jones et al., 2022; Rysgaard et al., 2012). However, we find no clear evidence of this in spring and summer (Fig. 4.14).

In contrast to our findings for 2010-2020, an earlier onset of phytoplankton blooms in years with lower winter stratification is not found for the RaTS before 2010. Between 1998 and 2009, the timing of chlorophyll increase is indistinguishable between low and high stratification years (Fig. 4.16b). Much higher peaks in chlorophyll *a* at 15 m depth (up to 27 mg m^{-3}) have been recorded in 1998-2010 (usually in years with long sea ice duration) than in years since 2011. It is conceivable that relationships between sea ice cover duration and mixing (on the one hand), and chlorophyll *a* levels and onset of blooms (on the other hand) have changed over time. In particular, spring and early summer chlorophyll levels following high stratification winters were much higher in 1998-2009 than in 2010-2020 (Fig. 4.16). Identifying drivers for changes in the onset of phytoplankton blooms in Ryder Bay is outside the scope of this work. Regardless of whether the timing of blooms is shifting or whether it is an artefact for the latter decade of the time series, it shows that the role of biological carbon uptake by phytoplankton in the surface layer might not be a dominant process affecting springtime sea-air CO_2 flux in years with shallow mixing in the wintertime between 2011 and 2019.

4.4.8 Contribution of summertime biogeochemical processes to inter-annual variability in sea-air CO_2 flux

The decrease in fCO_2 from spring into summer is promoted by photosynthetically-driven DIC drawdown (Carrillo and Karl, 1999; Legge et al., 2017), which slows down over the course of the summer as respiration catches up with photosynthesis. Complex interactions between biogeochemical processes result in high variability in the carbonate system state variables (Fig. 4.4). Variability is amplified by winds and tidal currents affecting the stratification of the water column in coastal Antarctic regions in close proximity to meltwater sources (Droste et al., 2022; Llanillo et al., 2019; Wallace et al., 2008).

A fraction of the samples collected in summer 2017 / 2018 have particularly low nTA content (Fig. 4.14d), which could indicate biogenic $CaCO_3$ formation by calcifying organisms, such as coccolithophorids, pteropods, or foraminifera. Microorganism community composition can differ from year to year depending on varying environmental conditions, such as nutrient availability and light conditions (Rozema et al., 2017). Production of calcifying foraminifera, for example, has a strong seasonality on the continental shelf of the WAP, growing in the summertime when food availability, such as diatoms, is high (Mikis et al., 2019). Foraminifera morphology and production are highly dependent on food availability and sea ice extent, and therefore also have an interannual variability. Early sea ice retreat (such as in 2017) due to positive SAM and / or La Niña phases have been shown to result in higher production of foraminifera along the WAP (Mikis et al., 2019). Diatoms are a dominant phytoplankton species in Ryder Bay during summer (Clarke et al., 2008; Henley et al., 2017) and could therefore promote foraminifera production. However, the presence, abundance, and production of calcareous marine organisms (foraminifera, coccolithophorids, or other) have not been recorded for Ryder Bay and so we cannot confirm their role in the summertime interannual variability of nTA and nDIC. This shows that a good understanding of shifts in marine community composition is necessary to understand summertime fCO_2.

Summer nutrients and DIC content remained high in summer 2015 / 2016, following a spring season of unusually rapid decline of these variables relative to other years (Fig. 4.4c). Iron limitation as a limiting factor to biological DIC consumption is an unlikely explanation for the excess nutrient content, because glacial and sea ice melt are expected to have provided the system with micronutrients (Bown et al., 2017).

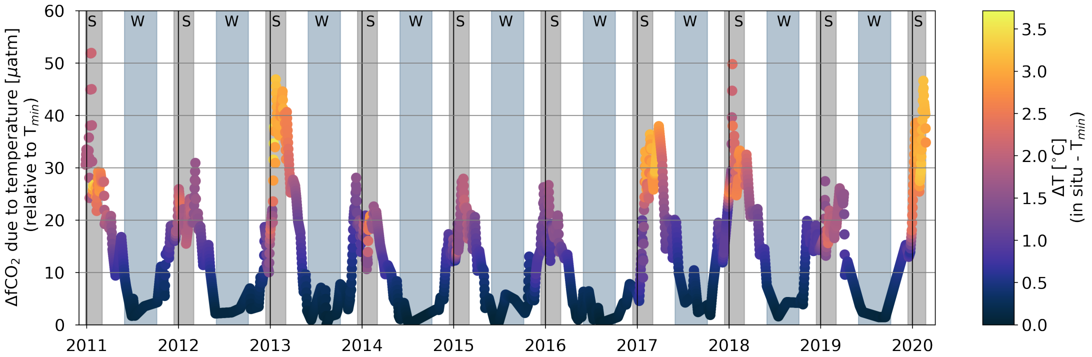

Figure 4.17: The difference between the fCO_2 determined for *in situ* temperature and the fCO_2 determined using the minimum recorded temperature (T_{min}) at 15 m depth (-1.8 °C), coloured according to the difference between the *in situ* temperature and T_{min} for the RaTS between 2011 and 2020.

As fCO_2 is dependent on temperature (Weiss, 1974), seawater temperature will have affected the summer CO_2 sink. We estimate the relative difference of the temperature effect on fCO_2 between warmer summers and cooler summers by re-calculating fCO_2 (Section 4.2.5) using the minimum temperature measured at 15 m depth in 2011-2020 (T_{min} = -1.8 °C) as a reference, and subtracting it from the fCO_2 determined for measured temperatures. Summers of 2011 / 2012, 2013 / 2014, 2014 / 2015, 2015 / 2016, and 2018 / 2019 had similar fCO_2 differences between temperature *in situ* and the reference temperature. Any influence of temperature on surface fCO_2 was similar between these summers. Surface layers in the summers of 2010 / 2011, 2012 / 2013, 2016 / 2017, 2017 / 2018, and 2019 / 2020 were warmer by ~1-2 °C due to enhanced heat uptake from the atmosphere (Fig. 4.11b), which is also evident from the heat penetrating the water column shown in Fig. 4.3a (Stammerjohn et al., 2008a). Temperature in warmer summers counteracted biologically driven decreases in fCO_2 by ~10-20 μatm, compared to the cooler summers in 2011-2020.

4.4.9 Autumn decoupling in seasonal variability of DIC and TA

Before DIC and TA content in the surface layer increase due to mixing with mCDW in the second half of autumn, their seasonal co-variation decouples. In all years, DIC content increased earlier than TA (Fig. 4.4 and 4.18a) and salinity (not shown), indicating that DIC and TA content in the surface layer were driven by different processes in the transition from summer to autumn. The two most likely candidates for processes causing the DIC-TA decoupling before mixing of the surface layer with mCDW are CO_2 uptake from the atmosphere and net respiration. Legge et al. (2017) found that atmospheric CO_2 uptake was a dominant process in the autumn of years 2011-2014 and that net respiration or remineralisation of organic material was a major contributing factor in January and February, i.e., at the end of summer, according to the seasons defined in the current work. However, a strong co-variation of DIC content and nutrients in the autumn for all years in 2011-2019 suggests that net respiration was nevertheless also an important contributor to DIC increase in autumn (Fig. 4.4).

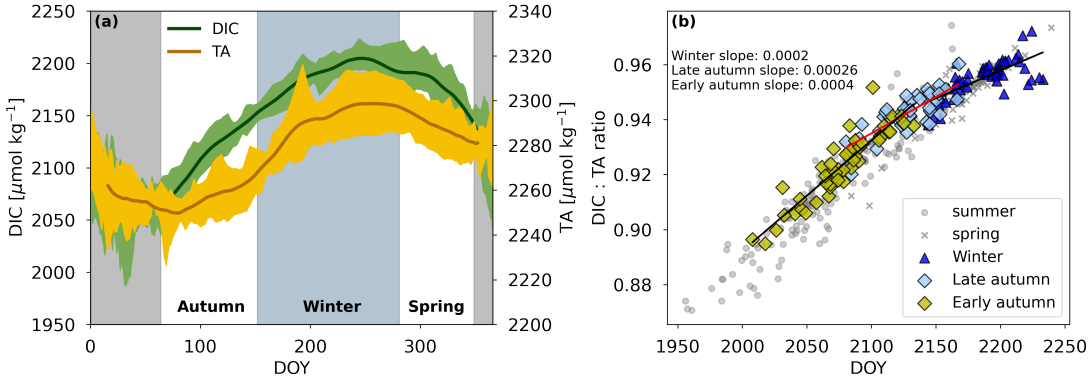

Figure 4.18: (a) Mean DIC (leftgreen line) and mean TA (right, orange line) content between 2011 and 2020 plotted versus the day of year (DOY). Lines are smoothed using a 30-day running mean. Green and orange shaded areas indicate the one standard deviation of the mean per DOY (not smoothened) for DIC and TA, respectively. Summer- and wintertime are indicated with the vertical shaded grey and light blue bars. (b) The DIC:TA ratio plotted against DIC content for the RaTS at 15 m between 2011 and 2020 in summer and spring (grey markers). Early autumn, late autumn, and winter datapoints are highlighted with larger markers. Linear regression lines for the early autumn and winter data are shown in black. The linear regression line for the late autumn data is shown in red.

As discussed in Section 4.4.8, atmospheric temperatures enhanced heat uptake in the summers of 2010 / 2011, 2013 / 2014, 2016 / 2017, and 2017 / 2018 (and 2019 / 2020, but we do not yet have the data to assess the carbonate chemistry in the following autumn; Fig. 4.3a). Heat uptake during these summers led to a higher seawater temperature at 15 m depth in the first half of autumn by ~1 °C relative to autumns following cool summers (Fig. 4.19a). If the effect of net respiration on autumn DIC content was similar between years, then higher ΔfCO_2 would be expected in autumns after warm summers than after cool summers by about 16 μatm, driven by a temperature effect on fCO_2. However, no clear systematic differences are seen for ΔfCO_2 in autumns after warm or cool summers (Fig. 4.19b). If anything, the mean ΔfCO_2 after cool summers appears to increase earlier in the autumn, along with increased mean DIC (Fig. 4.19b and 4.19c) and nutrients (not shown). This suggests that net respiration had a more dominant role in decoupling DIC and TA in autumn than CO_2 uptake. Years with earlier DIC increase caused by interannual variability in autumn respiration processes can decrease the capacity of CO_2 uptake in autumn of those years prior to sea ice formation.

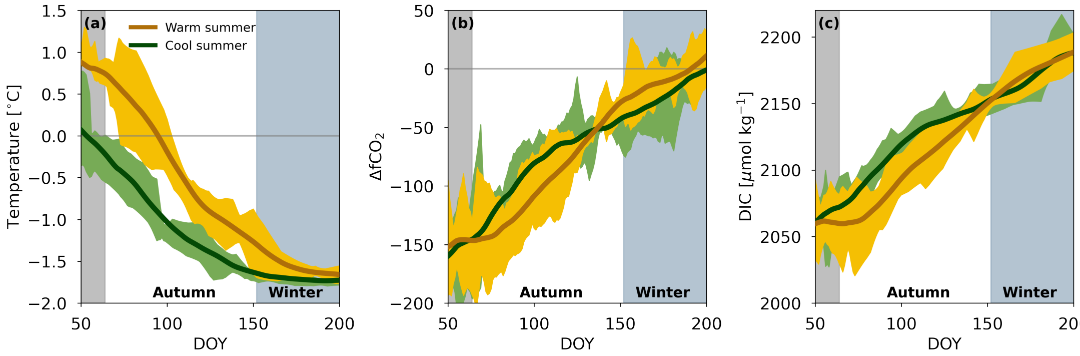

Figure 4.19: (a) 30-day running mean of seawater temperature over day of year between end of summer until winter, split up between years preceded by warm summers (i.e., summers 2010 / 2011, 2013 / 2014, 2016 / 2017, and 2017 / 2018) and cool summers (i.e., summers 2011 / 2012, 2014 / 2015, 2018 / 2019). Light grey and light blue shading indicates time of summer and winter. (b) Same as (a) but for ΔfCO_2. (c) Same as (a) but for DIC.

Occasional low TA values were measured in March 2011, 2012, and 2013 (Fig. 4.4a and 4.14a), which has previously been cautiously attributed to $CaCO_3$ precipitation (Legge et al., 2017). It is unclear how abiotic $CaCO_3$ precipitation (such as ikaite in sea ice) may have contributed to these observations, but it is possible that biotic $CaCO_3$ was formed during secondary late phytoplankton blooms in March (Clarke et al., 2008). Similar sudden decreases in TA were not measured in any of the autumn seasons in following years, but do occur in the summertime of 2017 and 2018, as evidenced by the low nTA values in Fig. 4.14d. Variability in marine organism community composition and production by marine calcifiers with associated biotic $CaCO_3$ formation could increase the variability in nTA in summer, but have thus far not been observed in Ryder Bay.

4.4.10 Uncertainties

4.4.10.1 Biases in CO_2 flux estimates due to gradients in upper surface layer

Sea-air CO_2 fluxes depend on the fCO_2 within the top micrometres of the ocean surface layer. Therefore, any flux derivations based on seawater samples collected deeper in the surface layer have the inherent limitation that their values are over- or under-estimated if a significant fCO_2 gradient exists between the sampling depth and the sea-air interface.

Note that the vertical gradients in fCO_2 discussed here apply to the top 1-15 m of the surface ocean. Vertical gradients also exist in the thermal boundary layer (top millimeters) and mass boundary layer (top 10-350 μm of the seawater), the latter of which controls CO_2 exchange at the sea-air interface (Jähne, 2019). Computational methods exist to estimate the fCO_2 at the base of the mass boundary layer, using temperature and salinity measurements to account for partitioning of the carbonate system (Woolf et al., 2016). The topic of gradients of fCO_2 in the top millimeters of the ocean, although relevant to sea-air CO_2 flux, is outside the scope of this work. Nevertheless, calculations that account for the effect of salinity and temperature gradients on fCO_2 in the top millimeters of the ocean cannot account for fCO_2 gradients due to biogeochemical factors. *In situ* observations of fCO_2 collected as close to the sea-air interface as possible are therefore necessary for the most accurate sea-air CO_2 flux estimates. For logistical reasons, samples are usually collected deeper in the water column, which - in stratified high-latitude oceans - can have consequences for CO_2 flux estimates, as is discussed in this section.

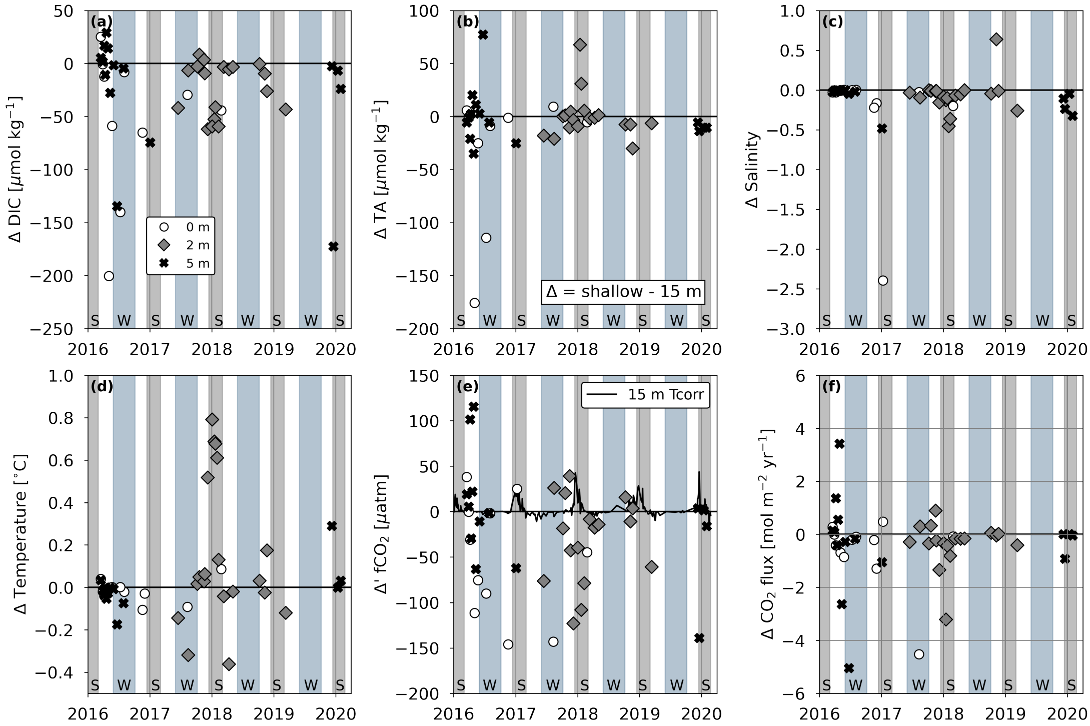

Figure 4.20: The difference in (a) DIC, (b) TA, (c) salinity, (d) temperature, (e) fCO_2, and (f) CO_2 flux (determined with gas transfer velocity that is not scaled to fraction of open water) between samples collected shallower than 15 m (either at 0, 2, or 5 m, shown with circle, diamond, or cross marker) and those collected at the standard RaTS depth of 15 m on the same sampling day. Summer and wintertime are indicated by the vertical grey and light blue (respectively) shaded bars in the background of each plot. In panel (e), the difference in fCO_2 between the fCO_2 corrected to the surface temperature according to Takahashi et al. (2009) and the fCO_2 determined for the *in situ* temperature at 15 m depth is shown by the black line.

In winter, the surface layer in Ryder Bay is well-mixed, and therefore we have high confidence that values based on samples collected at 15 m depth are representative for fCO_2 values at the surface interface. However, in the melting season, strong gradients occur as a result of buoyant meltwater at the surface, and as a result of the distribution of phytoplankton communities throughout the photic zone (Dong et al., 2021; Miller et al., 2019). In the Arctic, it has been demonstrated that these gradients can cause a mean overestimation of surface fCO_2 of 39 μatm (Dong et al., 2021), leading to an underestimation of the summertime ocean CO_2 sink (Miller et al., 2019).

To investigate the potential effect of surface stratification on the fCO_2 and CO_2 flux results, we compared the values based on samples collected at 15 m (the standard depth for discrete RaTS samples), to those based on 47 samples collected at shallower depths (0, 2, or 5 m) since 2016. Shallow samples (shallower than 15 m) have been collected at various time points of all seasons, although at sporadic intervals (Fig. 4.20).

The results for samples collected in summer of 2017 / 2018 illustrate the potential summertime bias due to vertical gradients in DIC, TA, salinity, and temperature (Fig. 4.20). That summer, seawater temperature at the surface was up to 0.8 °C warmer and salinity was up to 0.5 lower than at 15 m depth. The fCO_2 at the surface was lower at the surface by up to 130 μatm. The DIC content at the surface was also ~50 μmol kg^{-1} lower, which could have partly been due to meltwater dilution, but more likely reflects a stronger influence of other drivers, such as biological CO_2 uptake at the surface, as TA content is not similarly reduced. To explore this, particulate organic carbon (POC) was estimated using chlorophyll *a* according to Legendre and Michaud (1999) (Fig. B.7, see Section VIII for further details). A positive relationship is found for the summer of 2017 / 2018, between the vertical gradients in DIC and POC (Fig. B.8), which shows that both DIC and POC content at the surface are lower than at 15 m depth. It is possible that biologically assimilated CO_2 at the surface has sunk deeper into the water column, but these results also show that the drivers of the vertical gradients in the upper 15 m can be complex.

On average, the fCO_2 values closer to the surface were 45 ± 12 μatm (± standard error) lower than at 15 m depth (when only considering the shallowest sample collected on any day). This finding compares well with the average overestimation at depth of 39 μatm that Dong et al. (2021) found for the Arctic, who compared fCO_2 derived from eddy-covariance CO_2 flux data to measured fCO_2 at ~6 m depth. However, in contrast to findings in Dong et al. (2021), the surface does not consistently have lower values. Where the fCO_2 at the surface is lower than at 15 m depth, the mean overestimation of fCO_2 is 70 ± 12 μatm ($n = 30$, ± standard error). Where fCO_2 at the surface is higher than at 15 m depth, the mean underestimation of fCO_2 is 29 ± 11μatm ($n = 10$, ± standard error). Surface fCO_2 values higher than at 15 m depth are scattered throughout the various seasons.

Shallow samples collected in autumn 2016 have similar salinity values as at 15 m depth, indicating that the vertical gradient observed DIC and TA is likely dependent on biogeochemical processes instead of physical processes. Brine rejection might therefore not have been the reason for events with higher DIC content at the surface, even though sea ice formed early that year.

Occasionally when the fCO_2 at the surface is higher than at 15 m depth, it leads to

CO_2 outgassing to the atmosphere even though fCO_2 at 15 m depth is lower than the atmospheric value. The gradient in the upper 15 m of the surface layer can thus result in mistaking the system for a CO_2 sink rather than correctly identifying it as a CO_2 source to the atmosphere.

The temperature contribution to the vertical fCO_2 gradient is estimated by calculating the difference in fCO_2 values based the temperatures at 15 m depth and at the surface (using the formula of Takahashi et al. (2009); Fig. 4.20e). The temperature contribution is much smaller than differences in fCO_2 between surface and 15 m samples at their *in situ* temperatures, indicating that the temperature gradient is only a minor factor in the fCO_2 gradient and that other physical and biogeochemical processes are more important.

The CO_2 flux estimates are on average 0.5 ± 0.2 mol m^{-2} yr^{-1} lower when using the shallow samples instead of the 15 m samples (Fig. 4.20f). In the more extreme examples, the CO_2 flux (not scaled according to sea ice cover) based on shallow samples collected in Ryder Bay can be lower or higher by 5 and 3 mol m^{-2} yr^{-1}, respectively, compared to the flux calculated based on the 15 m samples. These results suggest that the uncertainty in sea-air CO_2 exchange estimates due to gradients in physical and biogeochemical variables in the upper meters of the ocean can be large when the water column is highly stratified. More frequent sampling for DIC and TA at ~2 m depth throughout the year as part of the RaTS - in addition to the standard 15 m depth sampling - can help to understand the seasonality of such gradients and potentially to find a way to correct for biases in fCO_2.

4.4.10.2 Uncertainties in sea-ice-air CO_2 flux estimates due to unknowns related to sea ice

Without taking sea ice cover into account, the cumulative atmospheric CO_2 uptake in Ryder Bay has reached 11 mol m^{-2} for the period when DIC / TA samples have been collected for the RaTS (end 2010 - beginning 2020; Fig. 4.12). When the gas transfer velocity in Eq. 4.1 is scaled according to the fraction of open water determined using all sea ice cover types, the cumulative CO_2 uptake by 2020 is lower by 13 % compared to the unscaled results, because brash sea ice cover limits CO_2 uptake in times of the year when ΔfCO_2 is negative. When the gas transfer velocity is scaled according to the fraction of open water considering all sea ice cover types except for brash ice, or only fast ice, the cumulative CO_2 uptake by 2020 is higher by 4 %, because these types of sea ice usually cover Ryder Bay only when ΔfCO_2 is positive and therefore decrease CO_2 outgassing and increase net CO_2 uptake. Irrespective of the sea ice scaling method, interannual variability in CO_2 flux is present in all results, which means that ΔfCO_2 drives the interannual variability more than the restriction of sea ice cover on direct sea-air CO_2 exchange. More sophisticated methods to incorporate the effect of sea ice cover in sea-air gas exchange exist, such as the parameter model by Loose et al. (2014), which accounts for the effects of shear- and convection-driven turbulence on the gas transfer velocity. However, their validity in the field still needs be tested. The effect of sea ice on sea-air CO_2 flux remains highly uncertain with potentially large consequences for CO_2 sink estimates in seasonally sea ice-covered regions.

Even though the RaTS covers year-round observations, winters have somewhat fewer datapoints than other seasons due to less frequent sampling. This might limit the interpretation of wintertime results if key processes that affect surface water fCO_2 are not captured, e.g., production and export of CO_2-rich brines from growing sea ice. These data thus need to be interpreted with care.

4.4.10.3 Uncertainties in carbonic acid dissociation constants

An important source of uncertainty in CO_2 flux estimates based on seawater samples that we would like to highlight in this time series is that of the carbonic acid dissociation constants used to determine seawater fCO_2 from DIC and TA content. Polar surface waters have low salinity and temperature conditions that are not always captured in the formulation of the carbonic acid dissociation constants and therefore requires extrapolation when applied in calculations.

Within temperature and salinity conditions typical for Ryder Bay, results for seawater fCO_2 using the formulation by Goyet and Poisson (1989) tend to lead to lower values relative to other formulations that are designed for low temperature and salinity conditions (e.g., Lueker et al., 2000; Millero et al., 2002). The results using the formulation by Sulpis et al. (2020) within high latitude seawater conditions lead to higher estimates of seawater fCO_2. The formulations of Goyet and Poisson (1989) and Sulpis et al. (2020) therefore currently bracket our current estimates of fCO_2 in Ryder Bay. The fCO_2 results based on DIC and TA using Sulpis et al. (2020) are consistently higher than when using Goyet and Poisson (1989) by a mean of 18 ± 0.1 μatm (± standard error). Largest differences occur in winter, when the seawater temperature is coldest and largest discrepancies between the results by Sulpis et al. and other formulations have been found (Sulpis et al., 2020).

To illustrate the range of different outcomes on the CO_2 uptake over time, we have determined the cumulative CO_2 uptake in Ryder Bay using the formulation by Sulpis et al. (2020), which suggests that the cumulative atmospheric CO_2 uptake using Goyet and Poisson (1989) is overestimated by 116 % in Ryder Bay between 2010 and 2020 (Fig. 4.12). Results using Sulpis et al. (2020) lead to decreased CO_2 uptake and increased CO_2 outgassing, as well as a longer season with potential CO_2 outgassing. Using Sulpis et al. (2020), the effect of ENSO/SAM on the interannual variability is still present, but is dampened in 2016, because it estimates more CO_2 outgassing prior to sea ice formation in that year. In 2012-2014 and 2016-2018, the seasonality in CO_2 uptake and outgassing according to Sulpis et al. (2020) seem to offset each other, in contrast to the formulation by Goyet and Poisson (1989), which indicates seasonal CO_2 uptake is larger than outgassing every year.

One must carefully choose the most appropriate carbonic acid dissociation constants when calculating components of the marine carbonate system. For process studies on the marine carbonate system and sea-air CO_2 exchange or carbon budget studies in high latitude regions, the choice becomes critical and can implicate our understanding of the progression of atmospheric CO_2 uptake by the ocean over time.

4.4.11 Insights from RaTS for regional sea-air CO_2 flux

Sea ice conditions, physical properties, and processes influencing marine carbonate chemistry of Ryder Bay are considered representative for the larger Marguerite Bay region (Jones et al., 2017b; Venables and Meredith, 2014). The RaTS therefore has the potential to provide useful insights into the interannual variability of the surface carbonate system in that region. Further offshore, however, sea ice cover duration and meltwater input are different, as shown in several studies indicating gradients in the surface water carbonate system between the WAP coastline and the Bellingshausen Sea (Carrillo et al., 2004; Hauri et al., 2015; Jones et al., 2021). Nevertheless, the RaTS can provide helpful insights into which processes might be important to represent in modelling studies to improve the representation of seasonal, interannual and decadal variability in the regional and Southern Ocean CO_2 flux. To illustrate this, we compare the RaTS fCO_2 and CO_2 flux data to regional means (Fig. 4.21) of fCO_2 reconstructed by a Self-Organising Map (SOM) method using a feed-forward neural network (FFN) approach (Landschützer et al., 2016; Landschützer et al., 2014) that uses Surface Ocean CO_2 ATlas (SOCAT) data (Bakker et al., 2016, Version 2022) to interpolate over time and space. For ease, these results are referred to as SOM-FFN data. We also calculated the means of all available SOCAT fCO_2 data on the WAP shelf south of 65°S, which we will from now on refer to as SOCAT data. Spatial variability in climatological means for fCO_2 reflect heterogeneity in the region caused by bathymetry, glacial meltwater input, deep water properties, weather conditions and mixing regimes (Fig. 4.21).

4.4.11.1 Summertime interannual variability

We observe strong interannual variability in summertime ΔfCO_2 in the monthly mean of the SOCAT data on the WAP shelf, which mostly follows that seen in the RaTS with exceptions in summer 2012 / 2013, 2018 / 2019, and 2019 / 2020 where monthly averages in Ryder Bay have more extreme negative values (Fig. 4.22a). The interannual variability in summertime for Box A, which roughly comprises Marguerite Bay, also compares well with that for Ryder Bay and mean SOCAT data for the region. For example, low monthly ΔfCO_2 in summer 2011 / 2012, 2014 / 2015, and 2018 / 2019 occur in both the RaTS as well as the data product. RaTS data do not feed into the SOCAT database. The agreement is explained by the fact that the timing of most observations feeding into the data product is biased towards the sea ice-free summertime. However, the decrease in ΔfCO_2 in summer 2016 / 2017 at Ryder Bay due to locally advected sea ice meltwater input is not clearly observed in the regional means for Box A. Besides years when highly local processes such as this occur, the year-to-year variability in the summertime surface fCO_2 on a small regional scale are generally captured by the SOM-FFN data product.

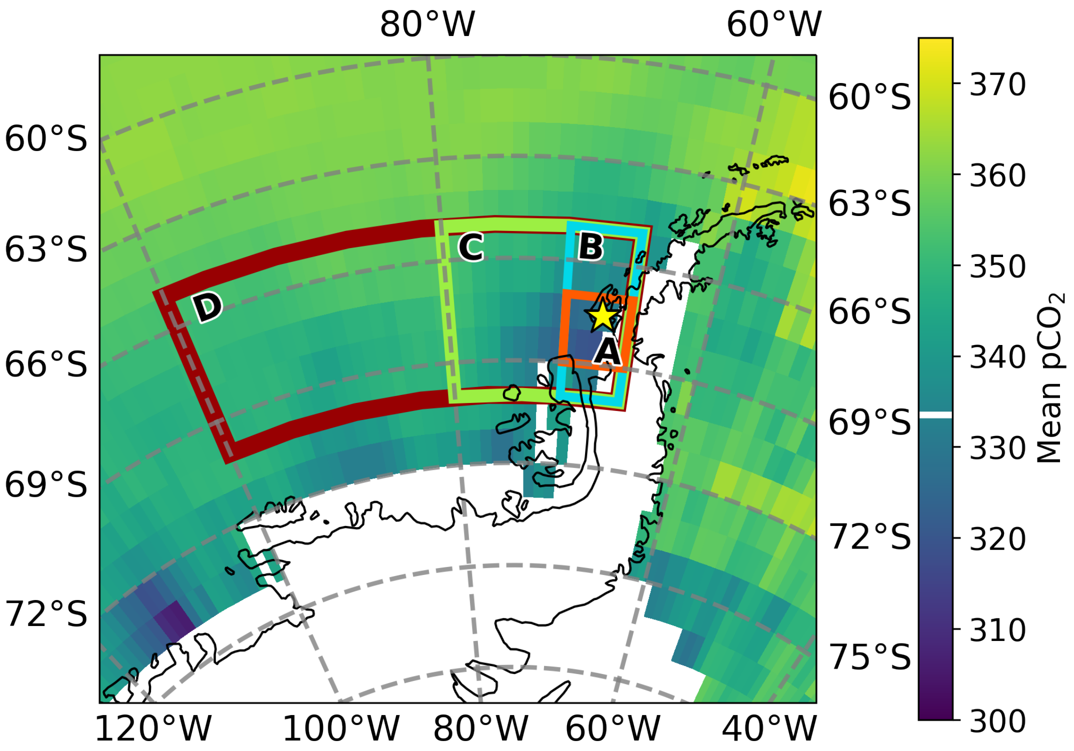

Figure 4.21: Map of the Antarctic Peninsula, marking regions for which monthly means are calculated for various variables in the Landschützer data product (Landschützer et al., 2016). The colourmap shows the climatological mean of pCO_2 in the region around the Antarctic Peninsula to illustrate spatial variability. Rothera Research Station is marked with the yellow star. The white line on the colourbar indicates the mean pCO_2 determined for the RaTS for 2010-2020.

4.4.11.2 Wintertime interannual variability

Observations on the shelf are limited in the wintertime, but some SOCAT data in the sea ice covered WAP are available and, similarly to the RaTS, display interannual variability in wintertime ΔfCO_2 (Fig. 4.22a). In contrast, the SOM-FFN mean for Box A shows very little interannual variability in the wintertime and also less positive ΔfCO_2 wintertime values. Additionally, while the SOM-FFN means for boxes A-D vary in the summertime, the wintertime means converge to the same values, suggesting little spatial variability despite very different environments (e.g., shelf versus open ocean). It is possible that due to a lack of wintertime observations, the SOM-FFN results in winter are more dependent on the interpolation method of the neural-network technique, which uses a climatological mixed layer product (de Boyer Montégut et al., 2004; Landschützer et al., 2016). It can therefore not account for interannual variability in the MLD and stratification of the water column. Empirical estimates of ΔfCO_2 for the Southern Ocean have linked wintertime interannual variability to changes in MLD (Gregor et al., 2018), which supports our findings for Ryder Bay. It also demonstrates the value of studying process-linkages on a local scale and high temporal resolution to understand processes on larger regional scales with lower temporal consistency in data acquisition.

Extending these comparisons to CO_2 flux, the summertime interannual variability

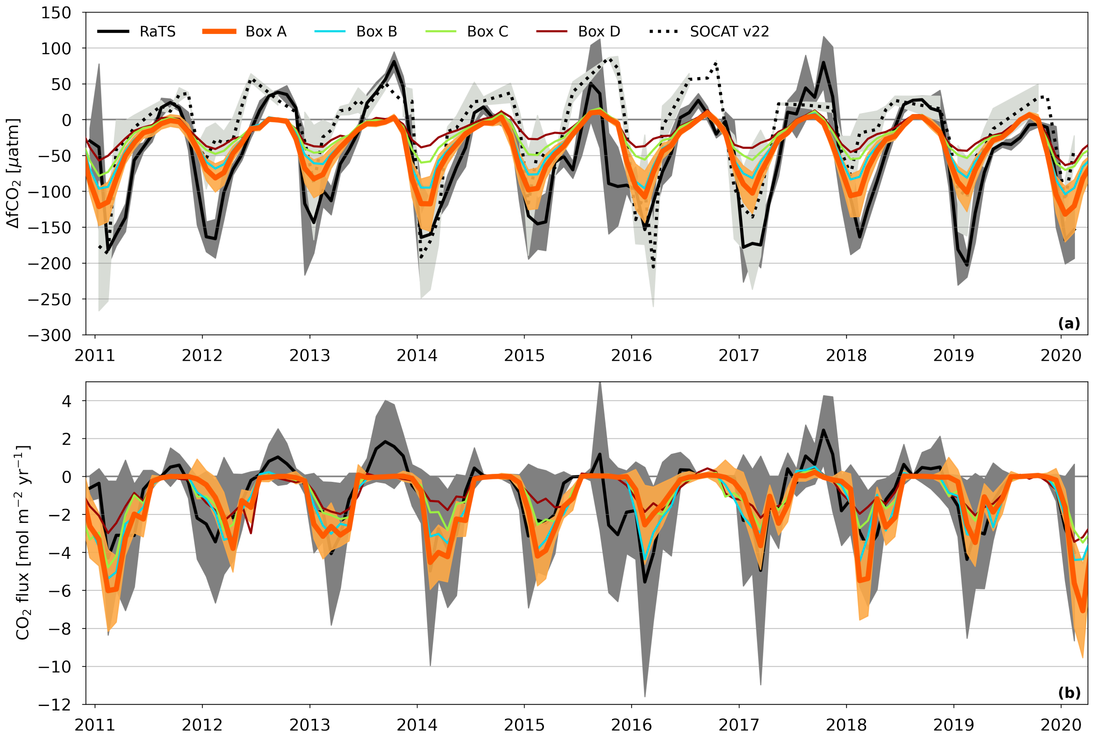

Figure 4.22: (a) Monthly means of SOM-FFN data for each region marked in Fig. 4.21 (coloured lines), as well as for the RaTS (black full line) and any available SOCAT v2022 data on the WAP shelf south of 65°S (black dotted line). Light grey shading indicates one standard deviation from the monthly mean for SOCAT data. Dark grey shading is the indicates one standard deviation from the monthly mean for RaTS data. (b) Same as (a), but for the CO$_2$ flux and excluding SOCAT v2022 data. The monthly means for RaTS are of CO$_2$ flux values determined with gas transfer coefficients according to Wanninkhof (2014) and scaled according to fraction of open water considering all sea ice types (full black line). The gas transfer velocity used for the SOM-FFN CO$_2$ flux estimates is determined according to the Wanninkhof (1992) parameterisation and is also scaled to the fraction of open water (Landschützer et al., 2016).

of the SOM-FFN product matches that measured in Ryder Bay (Fig. 4.22). However, wintertime CO$_2$ flux is mostly inhibited by sea ice cover in the SOM-FFN data, while enough ice-free periods occur that allow for wintertime CO$_2$ outgassing in Ryder Bay. Exceptions are winter 2016 (when sea ice cover retreated rapidly across the Southern Ocean) and winter 2017 (when sea ice cover duration was short), when the SOM-FFN product indicates some outgassing, but at a much lower magnitude than suggested by the RaTS. More dynamic sea ice cover in winter caused by winds occasionally transporting sea ice out of the bay is likely one of the explanations for the higher variability in CO$_2$ flux in Ryder Bay compared to SOM-FFN results for Box A. Also important to consider is that the SOM-FFN uses a wind speed product in its flux calculations, while the RaTS CO$_2$ fluxes have been determined using local wind speed measurements. However, Ryder Bay's winter ΔfCO$_2$, which unlike CO$_2$ flux is not scaled to sea ice cover, is much more variable within the season, as well as interannually, compared to the SOM-FFN mean ΔfCO$_2$ for Box A. In many years, the winter mean ΔfCO$_2$ in

Ryder Bay is clearly positive, while the wintertime ΔfCO_2 of the SOM-FFN for Box A has very low spatial variability (indicated by the low standard deviation from the mean) and remains near equilibrium with the atmosphere. This indicates that sea ice cover is not the only explanation for the lack of outgassing in the SOM-FFN product relative to the RaTS sea-air CO_2 flux estimates in winter. This comparison suggests that the product possibly underestimates wintertime fCO_2 interannual variability along the WAP.

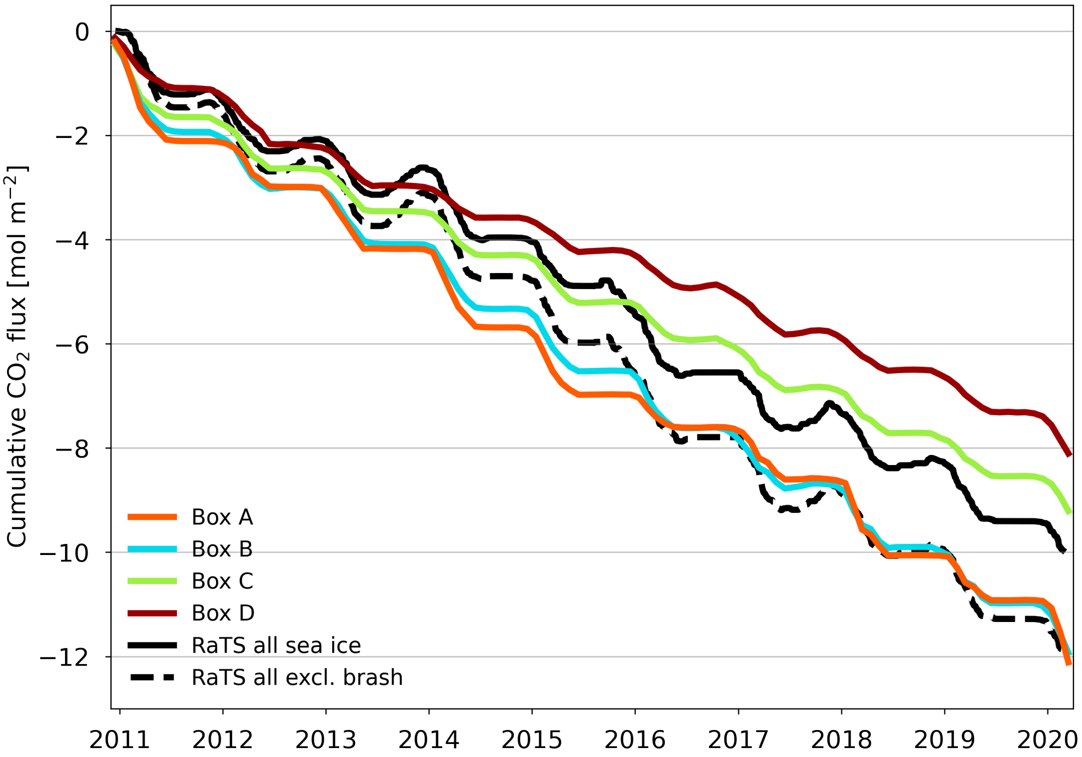

Figure 4.23: Cumulative CO_2 flux between end of 2010 and beginning of 2020 for mean CO_2 flux within regions indicated in Fig. 4.21 and for the RaTS data. All CO_2 fluxes have been scaled according to the fraction of open water. For RaTS, we additionally show the cumulative CO_2 flux scaled according to the fraction of open water when using all sea ice types, except for brash sea ice. Negative values indicate CO_2 uptake by the ocean from the atmosphere.

When comparing the sea-air CO_2 flux in Ryder Bay to the spatial means of the different boxes in Fig. 4.21 from a cumulative CO_2 uptake perspective, the total CO_2 uptake between the end of 2010 and the beginning of 2020 is higher for the spatial averages of boxes A and B by about 2 mol m^{-2} (Fig. 4.23). Interannual variability in Ryder Bay, especially in the wintertime CO_2 outgassing, results in a less efficient atmospheric CO_2 sink over time relative to the SOM-FFN results for the wider shelf area. The slightly higher net annual CO_2 uptake between 2014 and 2016 within Box A (small area on the WAP shelf) compared to Box B (large area including shelf and open ocean) illustrates how interannual variability along the coastline can be different from the wider region. However, the spatial means in boxes A and B show remarkably little interannual variability in their cumulative CO_2 uptake relative to Ryder Bay. When the

CO_2 flux for Ryder Bay is scaled to the fraction of open water excluding the fractions of brash sea ice cover, then the total CO_2 uptake between end 2010 and beginning 2020 in Ryder Bay is virtually identical to the mean of boxes A and B at about 12 mol m^{-2} (Fig. 4.23). Brash sea ice restricts CO_2 uptake in times of the year when ΔfCO_2 is negative. Excluding brash sea ice from the sea-air CO_2 flux estimation for Ryder Bay compares better to the results for Box A, because either it more closely represents the sea ice conditions of the wider WAP shelf region, or because the sea ice cover product used for the SOM-FFN results is not able to capture low concentrations of sea ice, including brash ice. Along the WAP, low sea ice cover could affect annual sea-air CO_2 flux and are important to consider in estimates.

Lead fractions in the Southern Ocean are estimated to be between 0.66-1.24 % (Petty et al., 2021), but are not always represented in sea ice cover estimates. I.e., sea ice cover estimates of 100 % might not represent the contribution of lead fractions. Although ephemeral, leads allow direct gas exchange at a time of year when ocean mixing increases surface seawater fCO_2 (i.e., winter). Sea ice cover estimates that do not capture lead fractions can therefore result in an underestimation of the CO_2 flux of the SOM-FFN product. Specifically, it could underestimate CO_2 outgassing to the atmosphere in the wintertime, as water column mixing increases the seawater ΔfCO_2.

Progress in lead fraction estimates based on improving resolution of satellite data, such as Sentinel-2 imagery and ICESat-2 (Petty et al., 2021; Reiser et al., 2020), will make it possible to parameterise the effect of leads on wintertime sea-air CO_2 flux. However, a good understanding of wintertime seawater fCO_2 and its drivers is also required. For example, if data products, such as those by Landschützer et al. (2016), lack surface seawater fCO_2 interannual variability in wintertime, then wintertime CO_2 flux estimates using those products and accounting for lead fractions would 1) solely depend on wind speed variability, and 2) continue to underestimate CO_2 flux interannual variability, as wintertime seawater is estimated to be near-equilibrium with the atmosphere (Fig. 4.22a).

The cumulative CO_2 uptake for the regional means in boxes C and D are also shown in Fig. 4.23 for illustrative purposes, but as these regions cover a large area, most of which is open ocean of the Bellingshausen Sea, their total CO_2 uptake between 2010 and 2020 are not expected to be similar to Ryder Bay. However, the comparison contrasts the steady annual CO_2 uptake for larger offshore regions to highly variable systems along the WAP coastline.

4.5 Conclusion

The Southern Ocean is a strong contributor to the global interannual variability in sea-air CO_2 flux (Rödenbeck et al., 2014). However, drivers of the Southern Ocean seasonal and interannual variability are still poorly understood (Lenton et al., 2006). Using year-round data of the Rothera Time Series, we find that wintertime interannual variability greatly contributes to annual means of the fCO_2 in the marine surface layer. Wintertime fCO_2 is closely associated to sea ice cover, which protects the water column from wind-induced mixing, although the contribution of meltwater in the preceding season may modulate the effect of sea ice on the surface layer fCO_2. Large-scale atmospheric forcing has an indirect effect on the sea-air CO_2 flux, as it induces interannual variability in ocean heat uptake from the atmosphere, sea ice dynamics, meltwater input, and wind-driven sea-air fluxes. Sea ice is key in preconditioning water column stability and heat uptake in multiple consecutive seasons (Saba et al., 2014; Stammerjohn et al., 2008a; Venables and Meredith, 2014), resulting in inter-seasonal dependencies in the marine biogeochemistry of the surface layer. This highlights the significance of year-round observations to develop our understanding of variability in the Southern Ocean CO_2 sink. However, major uncertainties in CO_2 flux estimates still exist that are related to methodologies, including the implications of vertical physical and biogeochemical gradients within the upper surface layer, and the parameterisation for the carbonic acid dissociation constants that are applied to temperature and salinity ranges typical for high-latitude surface waters, year-round. For instance, the cumulative CO_2 uptake in Ryder Bay between the end of 2010 and beginning of 2020 differs by 6 mol m^{-2} between using K_1^* and K_2^* formulations by Goyet and Poisson (1989) and Sulpis et al. (2020) for the determination of fCO_2.

Many of the mechanisms discussed in this work might be local to Ryder Bay and the directly surrounding region. However, it illustrates how the variety of variables collected as part of the RaTS can help constrain variability in the marine carbonate system and CO_2 flux. To further develop our understanding of the role of sea ice on the sea-air CO_2 flux in Ryder Bay, next steps might include testing the relationships between sea ice cover and its timing of onset and retreat to the surface layer fCO_2 with, for example, a one-dimensional model. Findings of how sea ice-associated processes interact can feed into understanding other coastal systems along the WAP, and perhaps even waters offshore.

CHAPTER 5

Drivers of the marine carbonate system at the onset of freeze-up in the Central Arctic Ocean

My contributions

I collected many of the DIC and TA samples from the CTD rosette, the ship's underway system, and under-sea ice water. As a Team ECO member on board Leg 5, I collected many samples for a range of ecological and biogeochemical variables, some of which are included in - or inform - this work, such as nutrients and dissolved oxygen (and on board analysis). I co-designed the concept of the study on underway carbonate chemistry and the study on changes in the upper water column. I processed the data for Leg 5 DIC and TA samples that were collected from the CTD rosettes and that were analysed at UEA. This work was funded by the Natural Environment Research Council (NERC) through the EnvEast Doctoral Training Partnership (NE/L002582/1) and the Department for Business, Energy and Industrial Strategy through the UK Arctic Office.

Contributions by others

Daiki Nomura co-designed the concept for the study on the underway carbonate chemistry during Leg 5. Daiki Nomura and his student, Manami Kozowa, did the DIC and TA analyses for the discrete underway samples, the under ice samples, and a few CTD casts, although the latter are not shown in this work. Dorothee Bakker co-designed the concept for the study on changes in the carbonate chemistry in the upper water column. Allison Fong facilitated and initiated many of the opportunistic sampling during Leg 5, including carbonate chemistry work. All members of Team ECO and Team BGC on Leg 5 worked together to sample a wide array of ecological and biogeochemical samples from various platforms, including samples collected underneath the sea ice and from the CTD rosette. Gareth Lee analysed MOSAiC Leg 5 DIC / TA samples in the laboratory at UEA. Nicholas Roden processed the underway fCO_2 data. Mario Hoppema was involved in discussions during quality checking of these data. Adam Ulfsbo combined the DIC and TA data from all CTD casts during MOSAiC (analysed in various laboratory) and did the secondary quality control for it. Sinhué Torres-Valdés and Laura Wischnewski analysed the nutrient samples, and Sinhué processed and quality checked the nutrient data. Mario Hoppema and Dorothee Bakker gave feedback on the text of the chapter. Bastien Queste gave feedback on the introduction and conclusion sections of this chapter. MOSAiC is a huge collaborative effort, and I would hereby like to acknowledge all crew and scientists involved for their contributions (Nixdorf et al., 2021).

Publication status

The work presented in this chapter will be submitted for publication as multiple manuscripts in the next year, but is currently still in preliminary stages.

Abstract. The Arctic Ocean is a sink for atmospheric carbon dioxide (CO_2) due to a combination of processes closely associated to sea ice that keep seawater fugacity of CO_2 (fCO_2) lower than atmospheric fCO_2. However, Arctic sea ice extent is rapidly changing due to climate change, with consequences for the marine biogeochemical system and atmospheric CO_2 uptake. Lack of year-round data and high spatial variability of surface fCO_2 in the Arctic Ocean prevent a clear mechanistic understanding of the processes behind seasonal variability of the marine carbonate system. This study uses data collected on Leg 5 of the Multidisciplinary drifting Observatory for the Study of Arctic Climate (MOSAiC) expedition (3 August - 12 October 2020) to understand mechanisms driving the marine carbonate system at the onset of annual freeze-up in the Central Arctic Ocean. At the onset of freeze-up in 2020, the Central Arctic Ocean was an atmospheric CO_2 sink, but fCO_2 values varied. Spatial heterogeneity of surface layer salinity, temperature, and marine carbonate system components explained most of the fCO_2 variability during Leg 5. An increase in fCO_2 due to temporal changes in the region was likely due to a cessation of meltwater input and the transition into freeze-up. Two storm events caused rapid, small-scale variability in the surface mixed layer, including temporary freshening and mixing with subsurface water with enhanced dissolved inorganic carbon. This work highlights the importance of high resolution observational data to observe and constrain small-scale processes that influence large-scale seasonal transitions, such as the onset of freeze-up. From a methodological perspective, results warn about uncertainties in fCO_2 estimates caused by inconsistent choice among marine carbonate studies for the parameterisation of the carbonic acid dissociation constants used to calculate fCO_2 from dissolved inorganic carbon and total alkalinity in polar oceans. Multiple parameterisations for the carbonic acid dissociation constants exist that apply to certain environmental conditions. However, none of them apply to the full range of salinity and temperature typical for sea ice-covered oceans, and therefore require extrapolation. In low salinity and cold seawater typical for the surface layer in sea ice-covered regions, the discrepancies between calculated and measured fCO_2 can be significant depending on which formulation is used. These results express the need to agree on a consistent choice of carbonic acid dissociation constants for marine carbonate system studies related to MOSAiC, as well as the wider polar marine carbonate system community, to enhance inter-comparability and carbon budget estimates. For the most accurate estimations of seawater fCO_2 and CO_2 flux, new parameterisations need to include the low salinity and temperature conditions of Arctic surface waters.

Contents

5.1 Introduction

The Arctic Ocean is generally a sink for atmospheric CO_2 (Bates and Mathis, 2009; Fransson et al., 2009; Rogge et al., 2023; Schuster et al., 2013; Yasunaka et al., 2018). As water flows northwards from lower latitudes, cooling increases its CO_2 solubility. Biological CO_2 drawdown in the melting season is another major driver for the Arctic CO_2 sink, as light availability initiates widespread phytoplankton blooms (Arrigo et al., 2008b; Bates et al., 2006; Fransson et al., 2017). This especially applies to the wide expanse of shallow shelves on the margins of the almost fully land-locked Central Arctic Ocean, where nutrient input from river runoff can sustain prolonged primary production (Fransson et al., 2001). Shelf edges are also an important location for sequestration of carbon, as brine rejection during sea ice formation increases the density of shelf water masses, which are subsequently incorporated into deeper water masses as they flow down the shelf slopes into the Arctic basins (Fransson et al., 2001; Ivanov et al., 2004; Jones et al., 1995). Although CO_2 release to the atmosphere occurs at the ice-air interface during sea ice formation (Delille et al., 2014; Geilfus et al., 2013; Nomura et al., 2018; Papadimitriou et al., 2003), sea ice more strongly contributes to the annual Arctic CO_2 uptake during melt through physical, chemical, and biological processes.

The fugacity of CO_2 (fCO_2) is similar to the partial pressure of CO_2, but accounts for non-ideal gas behaviour. The gradient of fCO_2 between sea ice brine (when in contact with the atmosphere) or seawater and the atmosphere drives CO_2 uptake from ($fCO_{2brine/seawater} < fCO_{2atmosphere}$) or release to ($fCO_{2brine/seawater} > fCO_{2atmosphere}$) the atmosphere. In the melting season, sea ice physically reduces the fCO_2 of the brine and seawater through dilution with its fresh meltwater. Chemically, sea ice melt reduces seawater fCO_2 during melt by releasing calcium carbonate minerals (i.e., ikaite; $CaCO_3 \cdot 6\,H_2O$) previously formed within its brine channels, that consume CO_2 upon dissolution in the seawater (Fransson et al., 2011; Fransson et al., 2013; Rysgaard et al., 2009; Rysgaard et al., 2012). Although ikaite dissolution mainly occurs in the spring and summer, it has also been observed to decrease seawater fCO_2 in the winter (Fransson et al., 2017). Biologically, sea ice hosts microorganism communities that consume CO_2 during photosynthesis. Sea ice meltwater also supports biological CO_2 drawdown by pelagic phytoplankton communities by stratifying the ocean surface layer (Arrigo et al., 2008b; Bates et al., 2006; Fransson et al., 2017). Moreover, the overall stratified nature of the upper Arctic Ocean leads to low exchange rates and mixing between the surface layer and deeper DIC-rich waters below the Arctic halocline (Aagaard et al., 1981; Bates and Mathis, 2009).

The combined processes mentioned above make the Arctic Ocean a highly efficient annual atmospheric CO_2 sink (Tanhua et al., 2009). However, Arctic climate is changing rapidly as a consequence of global climate change and interlinked positive feedback mechanisms, often referred to as Arctic Amplification. Although the possible causes for the Arctic's high sensitivity to environmental changes, including ocean warming and ice-albedo feedback, are still debated, observational and modelling studies have led to a strong consensus that the Arctic is undergoing a major transition. Air temperatures in the Arctic are warming at a rate four times faster than the global mean (e.g., Rantanen et al., 2022; You et al., 2021), resulting in rapid decline in sea ice extent (Notz and Stroeve, 2016; Stroeve and Notz, 2018). Sea ice regimes are changing, too. For instance, sea ice forms later in the year and melts earlier (Markus et al., 2009; Stammerjohn et al., 2012). Moreover, thicker, multi-year sea ice that has survived at least one melting season is replaced by thinner, first-year sea ice (Kwok, 2018; Kwok and Rothrock, 2009), thereby shifting sea ice from perennial to seasonal lifecycles.

The Arctic Ocean has a relatively low pH buffering capacity and is therefore sensitive to ocean acidification (Shadwick et al., 2013). A decreasing seawater pH is detrimental to calcifying biota, as it affects the pH homeostasis between the internal cellular environment of the calcifying organisms and the bulk seawater (Beaufort et al., 2011; Cyronak et al., 2016). Additionally, a lower pH also decreases the saturation of aragonite and calcite (two forms of calcium carbonate produced by different calcifying marine organisms), which can also affect biological calcification rates (e.g., Riebesell et al., 2000). Aragonite undersaturation has already been recorded in Arctic surface waters, and is driven by uptake of anthropogenic CO_2 and is enhanced by sea ice melt and upwelling (Chierici and Fransson, 2009; Yamamoto-Kawai et al., 2009). Aragonite producers in the high-latitude Arctic Ocean, such as pteropods, are therefore at risk, which can have cascading effects on higher trophic levels, as well as calcium carbonate export to deeper water (Buitenhuis et al., 2019). Due to the intimate connection between sea ice and the marine carbonate system, a shift in seasonal sea-air CO_2 flux is expected with implications for climate and the marine ecosystem.

However, concurrent changes of multiple factors that can have counteractive effects on sea-air CO_2 exchange make it challenging to predict the fate of the Arctic Ocean's CO_2 sink (Bates and Mathis, 2009). On the one hand, light availability due to less sea ice cover may promote phytoplankton growth and thereby increase atmospheric CO_2 uptake (Anderson and Kaltin, 2001; Arrigo et al., 2008b), but only if such enhanced phytoplankton blooms can be supported by nutrient availability. More wind-driven mixing due to less protective sea ice cover might supply these nutrients from subsurface water. On the other hand, CO_2 equilibration of the shallow Arctic mixed layer and rising seawater temperatures will diminish CO_2 uptake rates (Cai et al., 2010; Else et al., 2013). Moreover, weaker stratification due to less ice melt and stronger wind-induced mixing due to less sea ice cover may allow more entrainment of dissolved inorganic carbon (DIC), including CO_2, from deeper layers into the surface layer (Lannuzel et al., 2020). Less brine rejection due to less sea ice formation also jeopardises efficient carbon export to deep water from the shelf.

Constraining the effect of sea ice on the marine carbonate system in the Central Arctic Ocean is challenging, because of the spatial heterogeneity of Arctic Ocean surface fCO_2 (Fransson et al., 2009; Mucci et al., 2010; Yasunaka et al., 2018) and because of lack of year-round data. A lack of data is a common problem among many disciplines that aim to understand the seasonal cycle in the Central Arctic Ocean, impeding improvement of climate model predictions. To address this issue, the Multidisciplinary drifting Observatory for the Study of Arctic Climate (MOSAiC) was established. Its objective was to obtain a full year of continuous measurements in the Central Arctic Ocean, closely monitoring the annual life cycle of an ice floe. Inspired by the Fram Expedition in 1893-1896, led by Fridtjof Nansen (Nansen, 1897), the R.V. *Polarstern* was frozen into the Arctic Pack ice. Like the Fram Expedition, it used the Transpolar Drift Stream to drift across the ocean along an ice floe, starting north of Siberia and ending near north of Greenland (Shupe et al., 2022).

The MOSAiC time series captured the onset of annual freeze-up in the Central Arctic Ocean, a seasonal transition accompanied by rapid changes in atmospheric processes with propagating effects on the upper surface ocean. Sea ice formation, cessation of sea ice meltwater input, wind-driven mixing, and shifts in microorganism community structures alter the physical and biogeochemical properties of the surface layer (Schanke et al., 2021), with impacts on fCO_2 and the capacity for atmospheric CO_2 uptake. Driven by continued anthropogenic CO_2 emissions, the Arctic summer sea ice is predicted to disappear within the 21st Century (Overland and Wang, 2013). To understand how the CO_2 uptake capacity of the Arctic Ocean will respond to a shift from perennial to seasonal sea ice cover (and eventually to complete absence of sea ice cover), we need to have a grasp on which processes govern the system during the transition from summer into autumn, and how these processes interact with each other.

In this study, I focus on the drivers of change in the marine carbonate system within the upper 100 m prior, during, and after the onset of annual freeze-up. Using a combination of underway continuous measurements and discrete samples from the water column, the ship's underway system, and from under-ice water, I first assess the discrepancy between measured and calculated fCO_2 using different carbonic acid dissociation constants (Section 5.3.1). This is followed by a discussion on the variability in carbonate chemistry that can be explained by spatial variability (Section 5.3.2), storm events (Section 5.3.3), and biogeochemical processes (Section 5.3.4).

5.2 Methods

5.2.1 Circulation and physical oceanography of the Arctic Ocean

As the Arctic Ocean is surrounded by land and shallow shelves (Fig. 2.8), the narrow, but ∼2600 m deep Fram Strait is the dominant inflow of low latitude seawater, which can be classified as Atlantic Water (AW). AW is relatively warm and salty. In its journey northwards, AW gradually cools at the surface, but can still be identified within the Arctic Ocean at intermediate depth by a maximum temperature (Timmermans and Marshall, 2020). Through the eastern part of the Fram Strait, AW is transported to the Central Arctic Ocean along the West Spitsbergen Current (WSC; Fig. 2.8). A second important entry of AW is through the Barents Sea, from where it circulates cyclonically along the boundaries of the Arctic Ocean. The depth of AW ranges between the depth of the stratified surface water (∼150 m depth) and ∼500 m depth, below which the deep and bottom waters are found. Pacific Water (PW) enters through the Bering Strait, which is part of the continental shelf and thus shallow. As opposed to AW, the PW is characterised by relatively low salinity water caused by freshening in the Bering Strait and on the Chukchi Shelf. PW mainly circulates within the Canadian Basin, between 50 and 250 m depth, depending on proximity to the Chukchi Shelf.

The circulation in the Arctic Ocean is driven by wind and buoyancy forcing through freshwater fluxes from land and sea ice. Combined, these forcings establish the Beaufort Gyre within the Canadian Basin and the Transpolar Drift Stream (Fig. 2.8; Timmermans and Marshall, 2020). The Beaufort Gyre is an anti-cyclonic system driven by winds, which in turn drive Ekman convergence of seawater that has been freshened by input derived from Pacific Water, rivers, and sea ice melt (Timmermans and Marshall, 2020). Its surface water, therefore, has a typical low salinity. The Transpolar Drift Stream (used by the MOSAiC expedition to drift through the Arctic pack ice) transports water and ice from the Siberian Shelf towards Greenland and finally to the western Fram Strait, where the East Greenland Current (EGC) transports the water and sea ice southwards. The Transpolar Drift Stream borders the northern edge of the Beaufort Gyre and is therefore associated with a front of warmer, low saline Pacific water at the side of the Canadian Basin and colder, saltier Atlantic water at the side of the Eurasian Basin. The geographic boundary between the Pacific and Atlantic Water depends on the dynamics of the atmospheric pressure systems above the Canadian and Eurasian Basins and wind forcing patterns, but generally is observed to sit close to the Lomonosov Ridge.

5.2.2 Expedition and sea ice conditions

The MOSAiC expedition began on 20 September 2019 when *Polarstern* set sail from Bremerhaven towards the Arctic. A suitable ice floe to set up the so-called Central Observatory (CO) was found on 4 October 2019 in the northern Laptev Sea (Fig. 5.1). From here, *Polarstern* drifted with the floe along with the Transpolar Drift Stream. The only time the ship temporarily left the floe was in May 2020, for the transfer of scientists and crew to Svalbard in the midst of the COVID-19 pandemic. The ship returned to the floe and continued its scientific program until it reached the Fram Strait in July 2020. There, the floe melted and broke up on 19 July 2020 northeast of Greenland, marking the end of its life cycle. The final transfer of crew and scientists happened on 12 August 2020, when Leg 5 officially started. *Polarstern* went back north to find a new floe on 21 August in the Amundsen Basin, in the same region as where the ship last drifted during Leg 2. The ship drifted northwards along this new floe (referred to here as the "Leg 5 floe") until 20 September 2020, when it abandoned the floe near the northern edge of the Eurasian Basin at the Lomonosov Ridge. Measurements continued en route southwards until 5 October 2020, crossing the Amundsen Basin, Gakkel Ridge, and Nansen Basin. Leg 5 and the MOSAiC expedition ended on 12 October 2020 upon return to Bremerhaven, Germany.

Leg 5 measurements cover the end of summer and the beginning of autumn. Measurements made during the tracks going north (finding a new floe) and going back

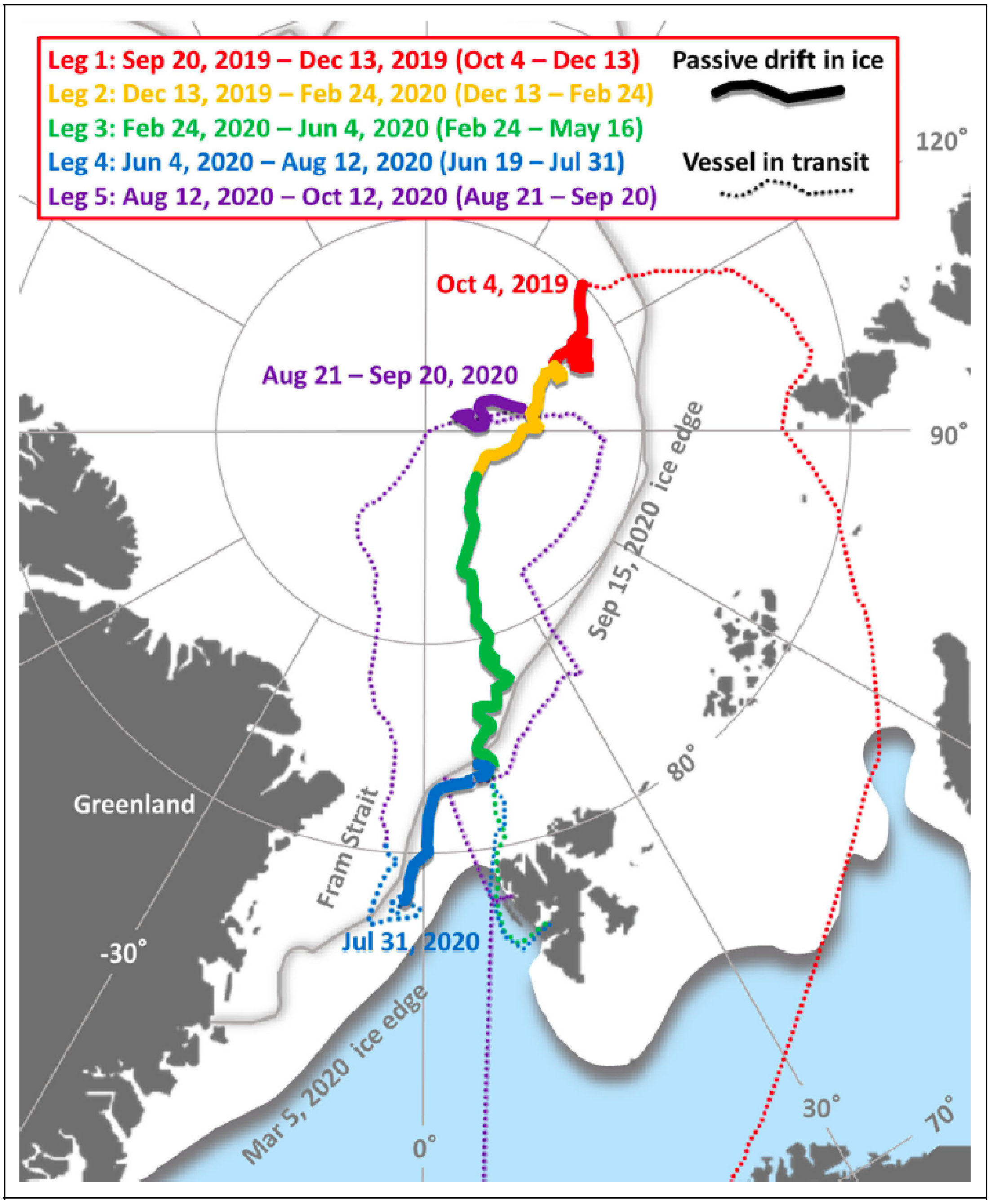

Figure 5.1: Figure from Shupe et al. (2022) showing the different legs of the MOSAiC expedition in different colours, as well as corresponding transit tracks. Leg 5 is shown in purple.

south (end of expedition) are used as an opportunity to look at the spatial variability and wider regional seawater properties at this time of year. Noteworthy is the low sea ice concentration anomaly in August 2020, especially between Greenland and the North Pole. Low sea ice concentrations are linked to large positive air temperature anomalies in the central Arctic 2020 summertime, driven by advection of warm air (Rinke et al., 2021). Along the MOSAiC track, July and August 2020 had record high mean air temperatures relative to years from 1979 onwards, and the melting season lasted a month longer than in most other years (Rinke et al., 2021). Lower sea ice extent (Krumpen et al., 2021) meant that *Polarstern*'s position in the pack ice would be closer to warmer and wetter conditions of the ice edge, which may explain part of the warmer and more humid conditions recorded during the expedition (Rinke et al., 2021). The freshest and warmest surface waters for the MOSAiC expedition were recorded during Leg 5, indicating a typical summer profile of the water column (Rabe et al., 2022).

Two phenomena observed during of Legs 4 and 5 that are characteristic for the summer Arctic Ocean are briefly mentioned here: melt ponds and the meltwater lens. When the top of the ice (and any snow layers) gradually melts, a melt pond is formed. During Leg 5, melt ponds were heavily surveyed and sampled by various disciplinary teams (e.g., gas and heat flux, biogeochemistry, micro-organism community structure, ice structure). From a carbonate chemistry perspective, melt ponds are important in sea-ice-air CO_2 exchange (Semiletov et al., 2004). As their areal coverage is large at peak summer, melt ponds can have a substantial impact on the Arctic Ocean CO_2 uptake. Contributions to these investigations are on progress (e.g., Yoshimura et al., in prep.), but it is beyond the scope of this chapter. During Leg 4 and at the beginning of Leg 5, a thin meltwater lens of less than one meter was observed in leads and underneath the sea ice. It was characterised by a steep salinity gradient within which visible organic material accumulated. The presence of a thin meltwater layer at the surface can have an impact on meltwater budgets, air-sea particle and gas exchange, and sea ice. While the current work does not show any carbonate chemistry data collected for the meltwater lens, its influence on the top 10-20 m of the surface ocean will be part of the discussion.

Between August and the end of September, the icescape of the Central Arctic Ocean went through a dramatic transition as annual freeze-up began (Fig. 5.2). Aerial images of the Leg 5 floe at the end of August and beginning of September show sea ice covered in melt ponds in various hues of blue, depending on the sea ice thickness. After 7 September 2020, the albedo of the ice surface started increasing as melt ponds and leads froze over. By the end of the Leg 5 drift, the ice surface was white and new ice formation started in leads.

The transition into freeze-up was accompanied by a number of rapid changes in environmental and sea ice conditions, which are here referred to as "events". These are summarised in Table 5.1 and include sudden lead openings near the ship and high wind conditions. Most events are driven by atmospheric processes and fluxes that impact the heat content of the ocean mixed layer and prepare the system for the onset of freeze-up (Shupe et al., 2022). Two of the events are storms. Using meteorological predictions, these storms were targeted by the scientific teams on board, by collecting higher frequency or higher resolution measurements from various platforms for cross-disciplinary studies of fast and small-scale processes. These coordinated set of scientific activities are referred to as Intense Observation Periods (IOPs). The under-ice water was targeted as one of the environments where seawater properties were likely to change during such a high-wind event. Measurements and water samples were collected from water underneath the ice about every two hours during the IOP for a range of biogeochemical and ecological variables, including marine carbonate system components.

On 6 September, the first of two storms passed over the Leg 5 floe (Rabe et al., 2022). IOP 1 during this storm was completed in ~22 hours. Air temperatures dropped below 0 °C and the radiative balance switched from positive to negative, indicating heat loss to the atmosphere (Shupe et al., 2022). This event is therefore associated to the onset of freeze-up in the Central Arctic. The surface albedo started increasing rapidly after this event (Fig. 5.2c). Another important change at this time was the disappearance of the meltwater layer due to wind-induced mixing within the surface layer. The second storm on 13 September temporarily interrupted freeze-up through advection of warm air (Shupe et al., 2022). Warm temperatures triggered a rain-on-snow (ROS) event on the same day and ice temperatures increased as well (Nicolaus et al., 2022). Melt ponds and leads previously frozen over and covered in a layer of snow became visible again (Fig. 5.2g). Air temperature once again decreased below zero on 15 September when freeze-up resumed (Nicolaus et al., 2022). IOP 2 was completed within ~25 hours during this storm event.

Table 5.1: Dates with "events" that occurred during Leg 5 of MOSAiC.

Date	**Event**	**Conditions and observations**	**Notable measurements**	**Reference**
12 August 2020	Start Leg 5 (start track northwards)	Low sea ice conditions while sailing		-
21 August 2020	Start drift Leg 5			-
23-24 August 2020	Lead opening and vertical turbulence caused by wind forcing thin ice movements	Wind speed relatively constant between 5-8 m s^{-1}, wind direction changed through one full vector cycle		(Fer et al., 2022)
1 September 2020	Start of annual freeze-up	Air temperature (2 m) < 0 °C, ice formation in leads		(Kawaguchi et al., 2022; Nomura et al., 2023)
6-7 September 2020	Storm (cyclone) event, meltwater lens ($<$ 1 m) disappears	Air temperature (2 m) $< 0\ ^{-1}$C, wind speed > 10 m s^{-1}	IOP 1 (~22 hours)	(Rabe et al., 2022; Shupe et al., 2022)
9 September 2020	Snowfall			-
13 September 2020	Storm (cyclone) event and ROS event	Air temperature > 0 °C, wind speed > 10 m s^{-1}	IOP 2 (~25 hours)	(Nicolaus et al., 2022; Shupe et al., 2022)
15 September 2020	Re-start freeze-up	Air temperature (2 m) < 0 °C	IOP 2 (~25 hours)	(Nicolaus et al., 2022)
20 September 2020	End drift Leg 5 (start track south)	New sea ice formation		
12 October 2020	End Leg 5 and MOSAiC expedition			-

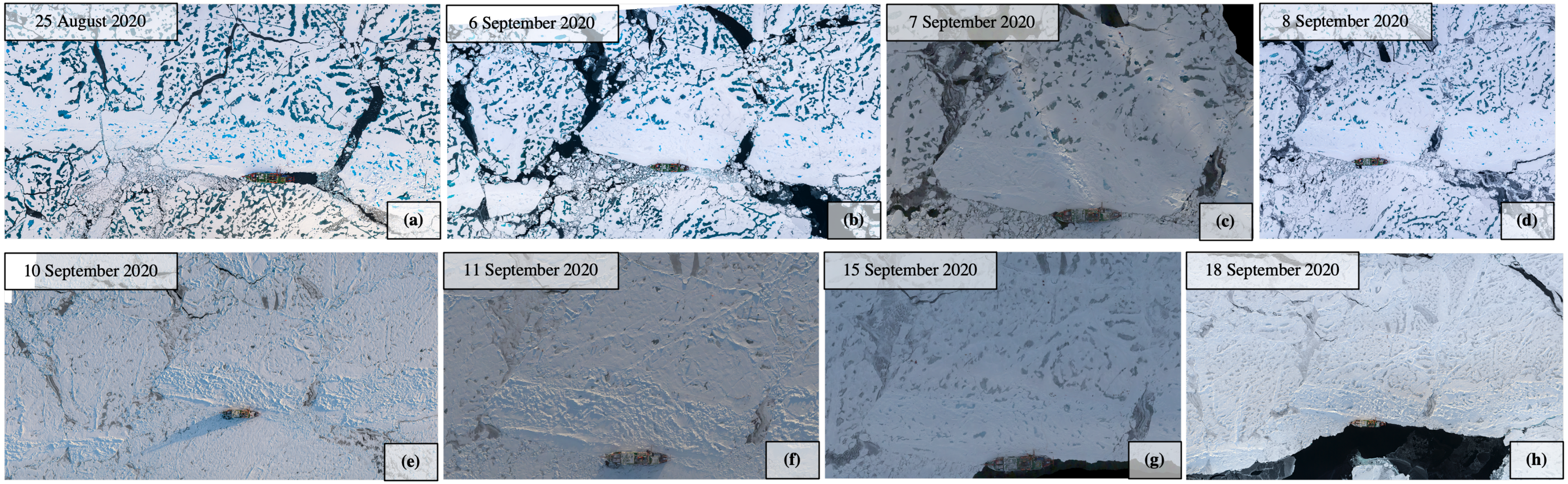

Figure 5.2: (a)-(h) Aerial photos of the MOSAiC Leg 5 floe on different dates during the Leg 5 drift. Photos are positioned so that R.V. *Polarstern* is always seen at the bottom of the photo. The Leg 5 floe is always to the starboard side of the ship. Heights at which photos are taken varies (Credit: Stephen Graupner).

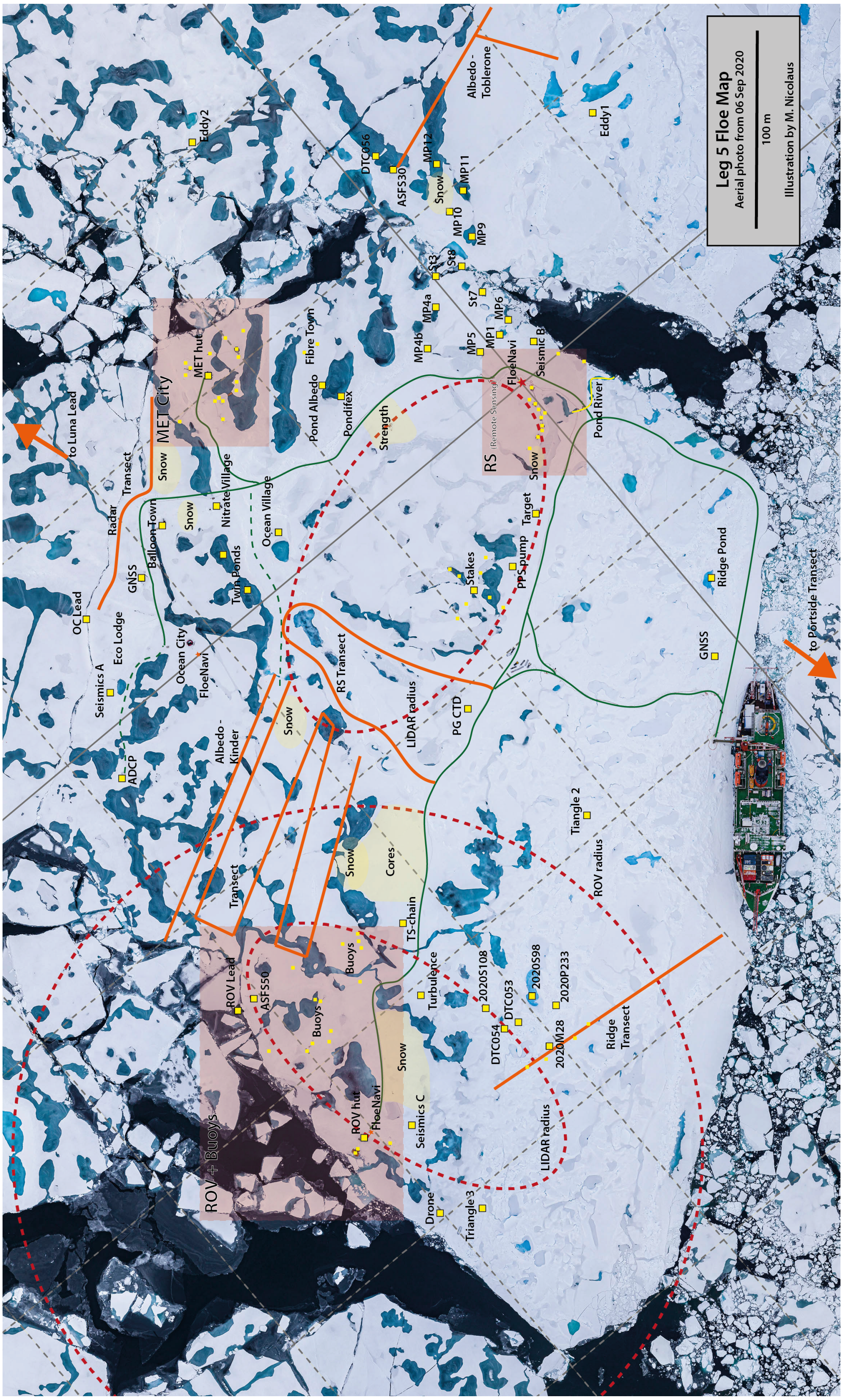

Figure 5.3: Aerial photo of the MOSAiC Leg 5 floe taken on 6 September 2020 with locations and transects mapped for various sampling activities. R.V. *Polarstern* is positioned at the bottom of the photo and has the ice floe to its starboard side. Credit: Photo by Stephen Graupner and illustration by Marcel Nicolaus/AWI.

5.2.3 Sampling methods and locations

All DIC and TA samples were collected following Dickson et al. (2007). DIC and TA were analysed from the same sample. After fixing DIC / TA samples with 100 μL of a 50 % saturated mercuric chloride ($HgCl_2$) solution and sealing the bottles with Apiezon™ grease, samples were stored at 4 °C until transport to the laboratories on land. Most DIC / TA samples were collected in 250 mL borosilicate (Duran Co., Ltd., Germany) bottles, except the underway samples, which were collected in 500 mL ones. All nutrient samples were collected in 50 mL screw cap Falcon™ tubes and stored in -20 °C containers until analysis at the Alfred Wegener Institute in Bremerhaven, Germany. Depending on the source of the water, the mode of sampling differed slightly for the CTD cast, shipboard underway system, and under-ice samples.

5.2.3.1 Water column

The rosette with the conductivity-temperature-depth (CTD) instrument was deployed on the starboard side of the ship, through a large man-made hole in the sea ice. CTD casts could only be deployed when the ice hole was intact, which was not always the case. The rosette had a SeaBird SBE911plus system, and in addition had a sensor for dissolved oxygen, fluorescent chlorophyll *a*, and chromophoric dissolved organic carbon, photosynthetically active radiation, beam transmission, and rhodamine (tracer for grey water from the ship), as well as a Satlantic Submersible Ultraviolet Nitrate Analyzer (for depth of profiles < 2000 m) (Rabe et al., 2022). As only the salinity and temperature measurements have been calibrated at the time of writing, only these data are shown and used for analysis. Temperature and salinity measurements are better than ± 0.01 °C and ± 0.01 g kg^{-1}, respectively.

Tethered microstructure probes (MSS90L, Sea & Sun Technology, Germany) were used to collect profiles through a hole in the ice at Ocean City, a sampling site set up on the ice floe at least 250 m away from the ship (Fig. 5.3). See Schulz et al. (2022) for details on data acquisition. Sensors on the MSS included pressure, conductivity, temperature, and various acceleration sensors, from which the dissipation rate of turbulent kinetic energy was derived (Schulz et al., 2022). Data for salinity and the turbulent dissipation rate are used in this work (Table C.1).

5.2.3.2 Underway system

A General Oceanics (GO) fCO_2 analyser on board *Polarstern* continuously measures fCO_2 from seawater supplied from an intake at ~11 m depth at the keel of the ship. The system has an equilibrator where inflowing seawater equilibrates with the headspace. The CO_2 in the headspace is subsequently quantified by a nondispersive infrared analyser (LiCOR®-7000). Temperature and salinity were measured at the water inlet at the keel by a thermosalinograph (SeaBird SBE4). The GO fCO_2 is corrected for temperature differences between the inlet and the equilibrator due to heating by the ship's interior. A tap on the seawater supply prior to reaching the GO fCO_2 system was used to collect discrete underway DIC / TA and nutrient samples. A Tygon® tube was secured to the tap, allowing to remove any bubbles from the line before the seawater sample was collected.

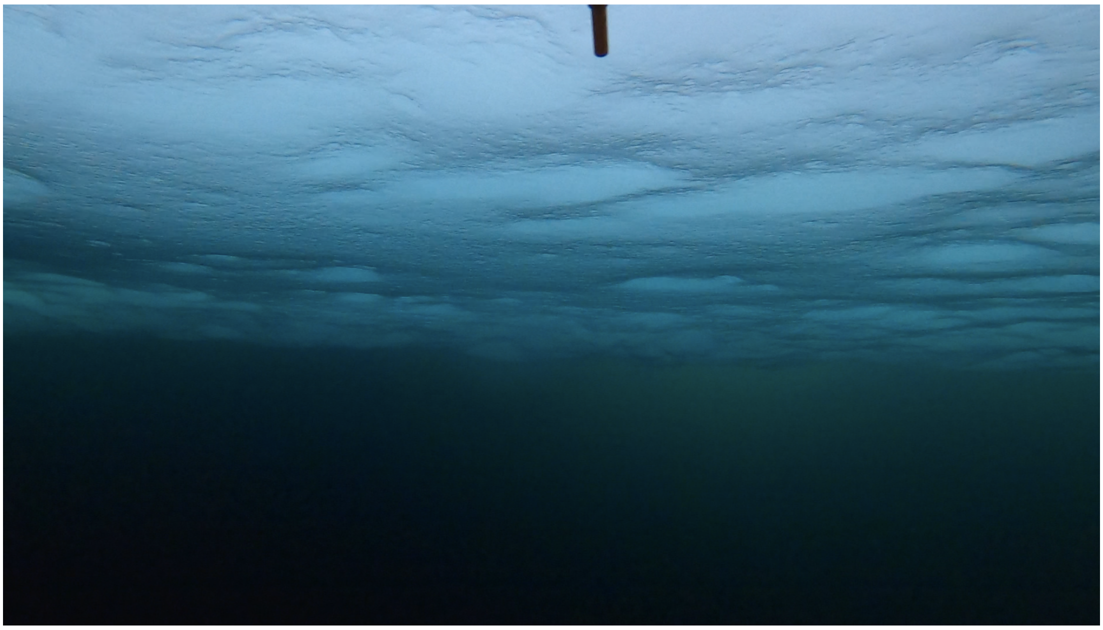

Figure 5.4: Snapshot of GoPro video taken through the hole in the sea ice at EcoLodge during IOP 1 (6-7 September 2020), showing the sampling tube (connected to a peristaltic pump) at the top, the under-ice topography, and the seawater below (Credit: Emelia Chamberlain).

5.2.3.3 Under ice water

Discrete samples for DIC / TA were collected from water directly underneath the sea ice during IOP 1 and IOP 2 at EcoLodge, a sampling site located at the opposite end of the floe from the ship's starboard side (Fig. 5.3). Inside a tent, a hole was cored in the ice. Under ice water samples were filtered and stored immediately on site. The same hole in the ice was used for both IOPs. Water was collected using a peristaltic pump, roughly every 2-3 hours. The Teflon® tube was attached to a pole positioned vertically into the cored hole in the ice and secured to maintain the same depth throughout the IOP. The ice was 113 cm thick with 7 cm freeboard. Samples were collected at 150 cm depth, which is ~40 cm underneath the bottom of the sea ice. The sea ice thickness is representative of the thickness of the ice in the direct vicinity of EcoLodge, as the bottom sea ice topography was relatively flat (Fig. 5.4). Ice thickness for two ice holes near EcoLodge measured 117 and 104 cm, with 10 and 3 cm freeboard, respectively.

Samples for DIC / TA were fixed with mercuric chloride and made gas-tight immediately after sampling. Freezing of the samples was avoided by storing them in insulated boxes until transport back to the ship. The salinity of the sample was measured in the lab from an aliquot taken of the remaining sample after DIC and TA measurements were completed. Temperature measurements were made with a multi-probe (YSI) that measures conductivity and temperature, with an accuracy of 0.5 % of measured value and ± 0.15 °C, respectively.

5.2.4 Analytical methods

Most of the Leg 5 rosette/CTD samples for DIC / TA were analysed on VINDTA 3C systems (Versatile INstrument for the Determination of Total inorganic carbon and total Alkalinity; (Mintrop, 2003)) at the University of East Anglia (UEA), Norwich/U.K. Certified Reference Material (CRM) from Prof. A. G. Dickson's laboratory (Scripps Institution of Oceanography, La Jolla, CA, USA) was used 1) to calibrate the coulometry counts per μmol of sample, 2) to calibrate the acid concentration used in the TA titration, and 3) to monitor the VINDTA for any drift or unreliable measurements. The standard deviation of the CRM measurements is used to estimate the analytical uncertainties in DIC and TA measurements (Table 5.2).

Table 5.2: Analytical uncertainties of DIC and TA measurements for Leg 5, for different instruments in two laboratories.

Laboratory	**Reference material (Batch no.)**	**DIC uncertainty [μmol kg^{-1}]**	**TA uncertainty [μmol kg^{-1}]**	**Number of runs (reference material)**	**Sample types**
UEA (VINDTA 1)	CRM # 182 (Prof. A. G. Dickson, Scripps)	1.9	2.4	24	CTD
UEA (VINDTA 2)	CRM # 182 (Prof. A. G. Dickson, Scripps)	1.6	2.0	20	CTD
Hokkaido University	Batch AR, AU (KANSO Technos Co., Ltd., Osaka, Japan)	<1.4	<1.2	10	CTD, underway, under-ice water (IOP)

Discrete underway samples for DIC and TA, as well as the IOP samples and a small fraction of the rosette/CTD samples of Leg 5, were analysed at Hokkaido University/Japan, on a hand-made CO_2 extraction system, using the same principles for the analytical technique as the VINDTA 3C. DIC content was measured using coulometry (Johnson, 1992; Johnson et al., 1985, CM5012, UIC Inc., Binghamton, NY, USA). TA content was determined using potentiometric titration (Dickson et al., 2007) and a TA analyser (ATT-05, Kimoto electric Co, Ltd., Japan). Calibration of the measurements was done using internal reference seawater material (Batch AR, AU; KANSO Technos Co., Ltd., Osaka, Japan), which has been cross-calibrated against CRMs from Prof. A. Dickson. Analytical uncertainties in DIC and TA measurements are determined based on the standard deviation of measurements of 10 subsamples taken from the reference water.

5.2.5 Marine carbonate system components

Knowing two of the carbonate system components, and given the temperature, salinity, silicate, and phosphate content, any two of the other carbonate system components can be calculated with formulations for the dissociation constants of each system (Zeebe and Wolf-Gladrow, 2001). Here, the DIC and TA contents are used as carbonate system input parameters in the PyCO2SYS Python package (Humphreys et al., 2022, Version

1.8). The formulations by Dickson (1990) were used for the bisulfate ion dissociation constants, by Uppström (1974) for the boron-salinity relationship, and by Dickson and Riley (1979) for the hydrogen fluoride dissociation constants.

The accuracy of fCO_2 determined from DIC and TA mainly depends on the accuracy of the stoichiometric ("apparent") dissociation constants of carbonic acid (K_1^* and K_2^*). These dissociation constants are a function of pressure, temperature, and salinity. Various previous attempts to resolve the inconsistencies in K_1^* and K_2^* have resulted in an extensive list of K_1^* and K_2^* parameterisations, using different ranges of temperature and salinity as state variables, and different methodologies (e.g., artificial seawater, real seawater, field measurements). The parameterisation by Lueker et al. (2000) has been recommended as best practice for global ocean estimations (Dickson et al., 2007). However, the cold seawater temperatures typical for the surface waters of high latitude oceans require extrapolation from the temperature range within which the parameterisation is valid (Lueker et al., 2000, Table 5.3). For the specific seawater conditions of the Southern and Arctic Oceans, it might therefore be more appropriate to use a parameterisation that is designed for sub-zero degree temperatures, such as those by Goyet and Poisson (1989), Millero et al. (2002), and Sulpis et al. (2020) (Table 5.3). The K_1^* and K_2^* parameterisation by Millero et al. (2002) is based on a salinity range between 34 and 37, which is typically higher than the surface seawater salinity during the sea ice melting season and might therefore be a less viable option than the parameterisations by Goyet and Poisson (1989) and Sulpis et al. (2020). Without aiming to do an exhaustive analysis, the current study calculates the fCO_2 from the MOSAiC Leg 5 DIC and TA samples using the parameterisations listed in Table 5.3 to be able to compare the results to the direct underway fCO_2 measurements. This list includes the parameterisation by Lueker et al. (2000), as well as all available parameterisations in the PyCO2SYS package that start at temperatures below 0 °C (Humphreys et al., 2022). In addition, the parameterisation by Dickson and Millero (1987) is added for comparison, despite its temperature range starting at 2 °C, because various studies on high latitude oceans have used this setting in their calculations (e.g., Jones et al., 2017b; Mucci et al., 2010; Shadwick et al., 2011).

5.2.6 Salinity normalisation

DIC and TA have a close relationship to salinity, as they share common sources (e.g., upwelling) and also share some common processes that affect their content (e.g., evaporation, dilution by freshwater input, mixing with proportional parts to salinity). To estimate the contribution of non-conservative biogeochemical processes, the DIC and TA contents must be normalised to the salinity measurements to exclude the contribution by mixing.

There are two methods of normalising DIC and TA to salinity. The first - and perhaps more common - one simply scales the content of X (i.e., DIC or TA) to the ratio of a reference salinity (S_{ref}) to the measured salinity (S; Eq. 5.2). The problem with the traditional normalisation method is that it can over-adjust the salinity-normalised

Table 5.3: Summary of the temperature and salinity range for which various parameterisations of the carbonic acid dissociation constants are defined.

Parameterisation	**Temperature range [°C]**	**Salinity range**	**Note**	**Reference**
DM78	2<T<35	20<S<40	Seawater pH scale, real seawater, Mehrbach et al. (1973) refit by Dickson and Millero (1987)	(Dickson and Millero, 1987)
GP89	-1<T<40	10<S<50	Seawater pH scale, artificial seawater	(Goyet and Poisson, 1989)
LU00	2<T<35	19<S<43	Total pH scale, real seawater. Refit from Mehrbach et al. (1973) to total pH scale. Best practice (Dickson et al., 2007)	(Lueker et al., 2000)
MI02	-1.6<T<35	34<S<37	Seawater pH scale, field measurements	(Millero et al., 2002)
SU20	-1.67<T<31.80	30.73<S<37.57	Total pH scale, field data	(Sulpis et al., 2020)

values when the fresh endmember (S = 0) has a significant non-zero DIC or TA content (Friis et al., 2003). This is exemplified by the green markers in Fig. 5.5, which show the results for the Leg 5 DIC and TA data when the traditional normalisation method is applied. The normalised results according to the traditional normalisation concept have a negative dependency on salinity. Instead, Friis et al. (2003) recommend using an empirical linear relationship between salinity and X in the form of Eq. 5.2 (where m is the slope and describes the dependency of X on S, and $X_{S=0}$ is the non-zero endmember), and to normalise X according to Eq. 5.3. The blue markers in Fig. 5.5 show what results looks like when this method is applied to the DIC and TA content of Leg 5, using the mean measured salinity of 33.75 as S_{ref}. There is no longer a dependency of the normalised values on salinity. The orange markers show the normalised results for measurements made in the top 100 m, using Eq. 5.2 and 5.3 applied to only the measurements in the top 100 m.

$$nX = X.\frac{S_{ref}}{S} \tag{Eq. 5.1}$$

$$X = m.X + X_{S=0} \tag{Eq. 5.2}$$

$$nX = (X - X_{S=0}).\frac{S_{ref}}{S} + X_{S=0} \tag{Eq. 5.3}$$

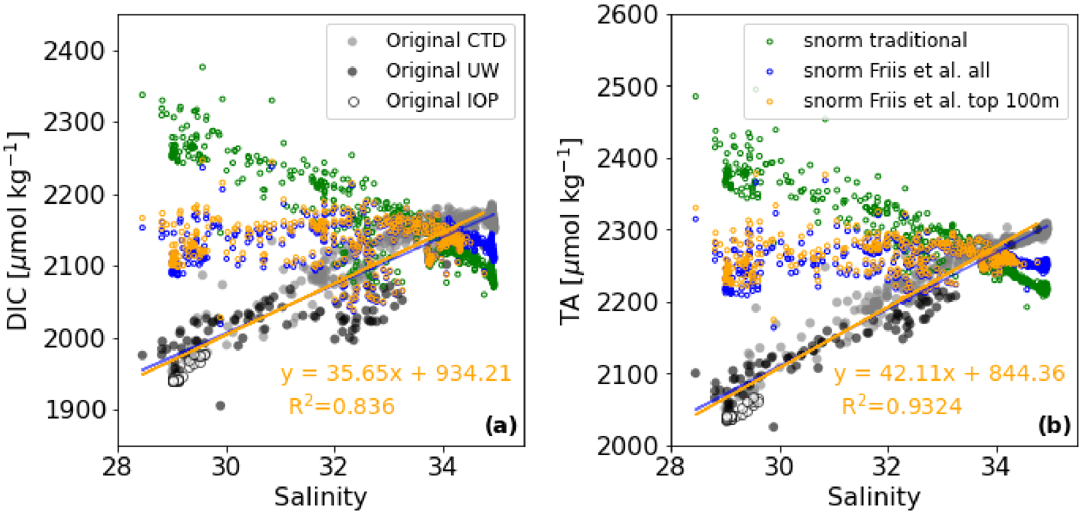

Figure 5.5: (a) DIC content plotted against salinity for all CTD discrete seawater samples (including all legs of MOSAiC, grey markers), as well as for the underway (black markers) and IOP samples (white markers). The linear regression applied to all data and only the data in the top 100 m, are shown in the blue and orange lines, respectively. The DIC content normalised to salinity according to each of these linear regression analyses is shown in the respective blue and orange markers. The green markers indicate the salinity normalisation according to the "traditional" method, which does not take into account non-zero DIC end members (Friis et al., 2003). The equation for the linear regression and the R-squared are shown for the orange line, i.e. the linear regression done for all datapoints in the upper 100 m. (b) Same as (a) but for TA.

5.3 Results and discussion

5.3.1 fCO_2 results using different carbonic acid dissociation constants

The discussion on the choice of parameterisation for the carbonic acid dissociation constants consists of two parts. In the first part, the results for fCO_2 between the different parameterisations are compared. In the second part, the results are compared to the underway GO fCO_2 measured on Leg 5 of MOSAiC. We refer the reader to Table 5.3 for reference to the abbreviations used in the text for the K_1^* and K_2^* formulations: GP89, DM89, LU00, MI02, SU20.

5.3.1.1 Differences among formulations

The boxplot in Fig. 5.6a shows the Leg 5 underway fCO_2 results when calculated from DIC and TA using five different formulations for K_1^* and K_2^* (Table 5.3). To better compare the differences among the sets of results, we use the GP89 results as a reference, from which the other results are subtracted (Fig. 5.6b). GP89 results are chosen as a reference, because its parameterisation produces the lowest fCO_2 values in this dataset. Additionally, GP89 is used in the fCO_2 and CO_2 flux analyses for the Rothera Time Series (RaTS) in Chapter 4, and insights gained in the current chapter can therefore easily be considered for the RaTS results. Important to note is that the internal consistencies between - on the one hand - GP89 (based on laboratory experiments on artificial seawater), and - on the other hand - Mehrbach et al. (1973), DM78, and LU00 (based on laboratory experiments on real seawater) are low relative to other formulations that are also based on real seawater (Millero et al., 2002). However, the salinity range for GP89 covers the low salinities in the polar surface ocean, which that for MI02 and many other formulations do not (Table 5.3). I therefore deem it a relevant comparison.

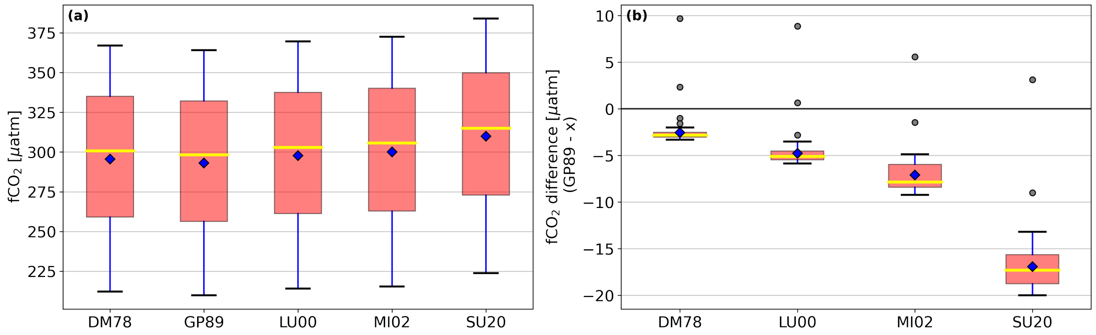

Figure 5.6: (a) Boxplots for fCO_2 calculated from DIC and TA content in the underway discrete samples collected during Leg 5, using the carbonic acid dissociation constants of DM78, GP89, LU00, MI02, and SU20. (b) The difference between the calculated underway fCO_2 using GP89 and other formulations. See Table 5.3 for a summary of the labels on the x-axis. The yellow line within each box indicates the median and the blue diamond within each box indicates the mean.

The formulations of K_1^* and K_2^* by DM78 and LU00 are both refits from Mehrbach et al. (1973) and are converted from a NBS (US National Bureau of Standards, a.k.a. National Institute of Standards and Technology) pH scale to a seawater and total pH scale, respectively. fCO_2 results are slightly higher using LU00 compared to DM78. The median of the difference between GP89 and LU00 is ~2 μatm lower than between GP89 and DM78 (Fig. 5.6b). Most formulations of dissociation constants for other seawater acid-base systems (e.g., bisulfate ion dissociation and hydrogen fluoride dissociation/silicate, phosphate, and ammonia speciation) are based on the total pH scale, which has become the standard procedure and it is why LU00 is recommended as best practice (Dickson et al., 2007).

Most parameterisations are based on tests in the laboratory, but Millero et al. (2002) used field data, arriving at a formulation that agrees well with that by Mehrbach et al. (1973); converted to seawater pH scale). Millero et al. (2002) concluded that formulations for K_1^* and K_2^* are more reliable when based on real seawater. The median of MI02 results is higher than that of GP89 by ~8 μatm and higher than that of LU00 by ~3 μatm.

In a similar approach to Millero et al. (2002), Sulpis et al. (2020) also used field data to derive a formulation for the carbonic acid dissociation. They found that the formulations by Lueker et al. (2000) and Millero et al. (2002) overestimated K_1^* and K_2^* at temperatures < 8 °C, which lead to an underestimation of fCO_2 and $H_2CO_3{}^*$ content (= $H_2CO_3 + CO_2$) and an overestimation of the ${CO_3}^{2-}$ content. This explains why the fCO_2 results based on SU20 are the highest relative to other formulations (Fig. 5.6a). The median of the difference with GP89 is ∼17 μatm (Fig. 5.6b).

5.3.1.2 Differences between GO fCO_2 and calculated fCO_2 using different formulations

Fig. 5.7a shows the distribution of the differences between the measured fCO_2 by the GO system and the fCO_2 values calculated from discrete DIC and TA samples from the underway system. Discrepancies between the measured and calculated values occur for all parameterisations, ranging between -46 and 39 μatm for individual datapoints, depending on the parameterisation. Based on the mean of the differences over the entire Leg, MI02 has the lowest mean discrepancies (Fig. 5.7a). However, when the data are split up between the track north (during Arctic melt season), the Leg 5 drift, and the track south (after the drift and Central Arctic onset of freeze-up), offsets vary depending on both the parameterisation used and the part of the expedition's track (Fig. 5.7b). GP89 results fit the direct underway measurements best for the data along the track north (median offset < 1 μatm), while the SU20 fCO_2 results have the smallest offset to the direct measurements during the drift and the track south (median offset -4 and -2 μatm, respectively). The remaining discussion on the effects of different K_1^* and K_2^* formulations will focus only on those by Goyet and Poisson (GP89), Millero et al. (MI02), and Sulpis et al. (SU20).

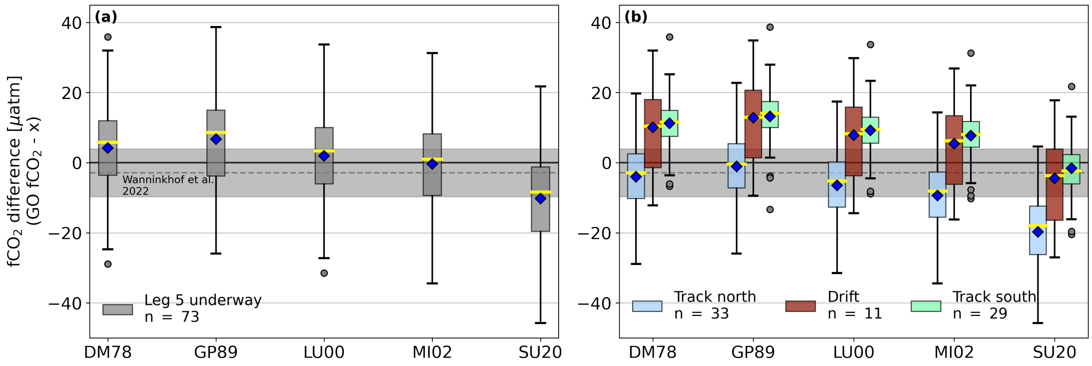

Figure 5.7: (a) Boxplots for differences between the measured GO fCO_2 and the calculated fCO_2 from discrete underway seawater samples for all datapoints of Leg 5 using different formulations for the carbonic acid dissociation constants. Horizontal grey band shows the range of mean ± 1 σ as reported in a global ocean study in Wanninkhof et al. (2022), for comparison. (b) Same as (a), but the results are split between three parts of Leg 5: the track north, the drift, and the track south. See Table 5.3 for a summary of the labels on the x-axis.

Fig. 5.8a shows the data collected during the three different parts of the Leg 5 track (track north, drift, and track south) within the temperature and salinity field. Markers in Figs. 5.8b, 5.8c, and 5.8d are coloured according to the discrepancy between the measured and calculated fCO_2 values using the K_1^* and K_2^* formulations by GP89, MI02, and SU20, respectively. There is no evidence for a consistent link between the fCO_2 discrepancies and temperature or salinity. The black lines in the plots indicate

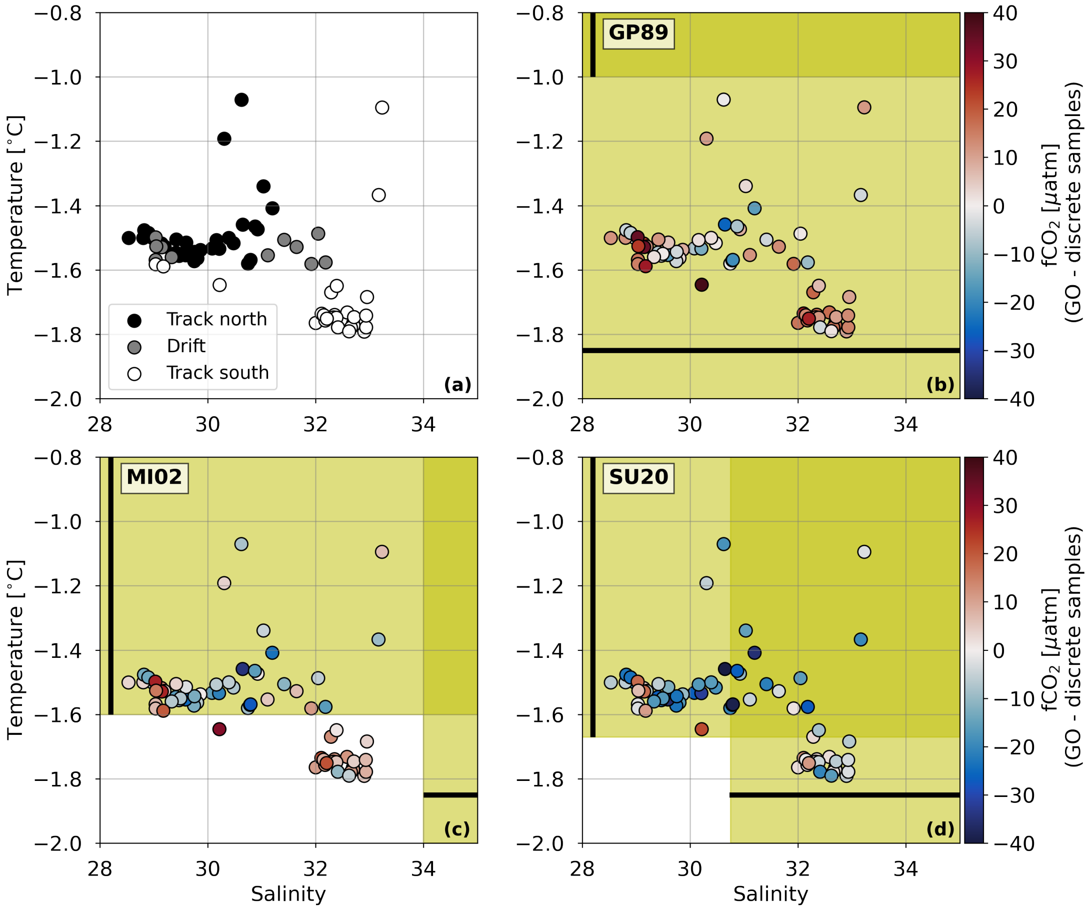

Figure 5.8: (a) Datapoints for discrete underway seawater samples plotted in T-S space and coloured according to the three sections of the Leg 5 track: the track north, the drift, and the track south. (b) Same as (a) but datapoints are coloured according to the difference in measured and calculated fCO_2 using the GP89 formulation. Black lines indicate the range of temperature and salinity that are included in the formulation. (c) Same as (b), but using the MI02 formulation. (d) Same as (b), but using the SU20 formulation.

the temperature and salinity ranges within which each respective parameterisation applies (also see Table 5.3). GP89 results generally underestimate fCO_2 relative to the direct measurements at salinity ~29 and lower and at salinity > 32, even though its salinity range of the parameterisation covers the full salinity range of the measurements. All temperature measurements are below the temperature range of the GP89 parameterisation. Similar to GP89, MI02 results also underestimate fCO_2 relative to direct measurements at salinity ~29 and lower and at salinity > 32, but the salinity measurements are all below the salinity range of the parameterisation, which starts at 34. It generally overestimates fCO_2 between salinity 29 and 32. The temperature range of MI02 covers all temperature measurements, except most of the measurements made on the track back south, when the oceanic surface layer started cooling. SU20 results generally overestimate fCO_2 relative to direct measurements, but they compare well to the measured fCO_2 during the track south when the coldest sea surface temperatures are recorded. The salinity and temperature ranges of the SU20 parameterisation cover most measurements, except most of the salinities on the track north and most of the temperatures on the track south.

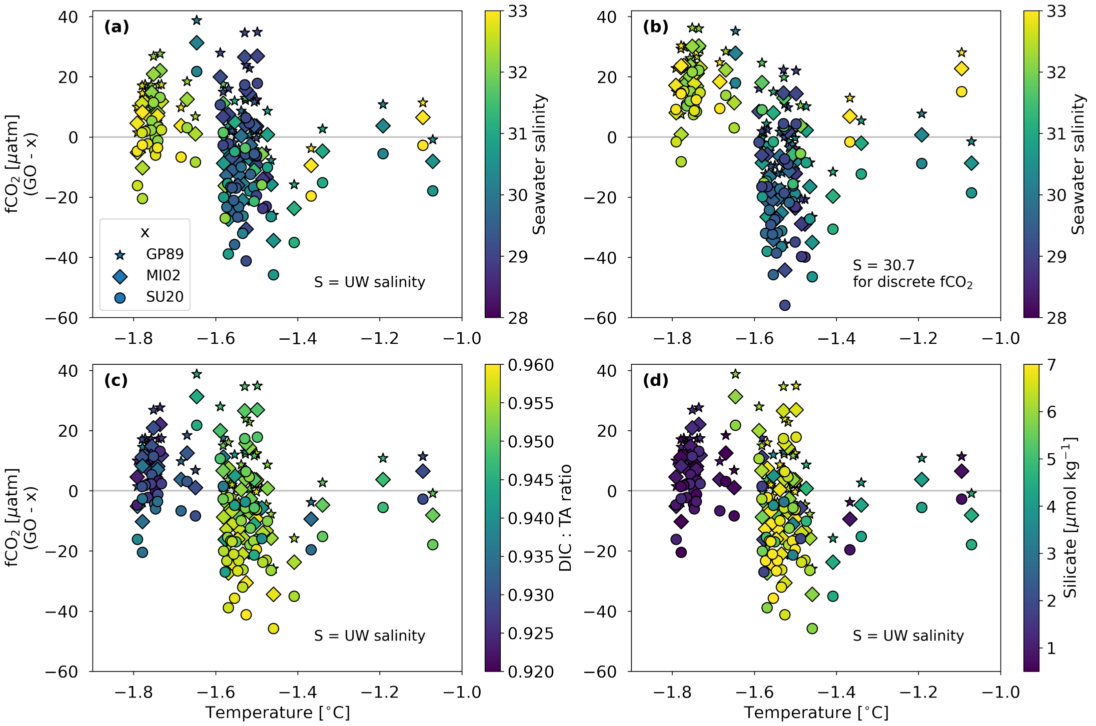

Figure 5.9: (a) The difference in measured and calculated fCO$_2$ for all underway seawater samples plotted against seawater temperature. The different markers indicate which formulation for the carbonic acid dissociation constants was used in the calculations. The salinity used in the fCO$_2$ calculation is the measured underway salinity. Markers are coloured according to the seawater salinity. (b) Same as (a), but fCO$_2$ for the discrete samples is calculated using a constant salinity value (instead of the seawater salinity values) of 30.7, which is the median of all underway samples. (c) Same as (a), but markers are coloured according to the DIC : TA ratio of the samples. (d) Same as (a), but markers are coloured according to the silicate content of the samples.

When plotting the discrepancies against seawater temperature, it appears that the most of the overestimation in fCO$_2$ for all three parameterisations occurs between -1.5 and -1.6 °C (Fig. 5.9a). Although the negative excursion in discrepancies coincides with low salinities, the discrepancies remain (and even become larger) when salinity values in the calculations for fCO$_2$ of the discrete samples are replaced by a constant value of 30.7 (Fig. 5.9b). The variability in the fCO$_2$ discrepancies over the measured seawater temperature range can therefore not be explained by the role of salinity in the parameterisations alone. The low salinities were measured during the track north, when the DIC : TA ratio and silicate content were also distinctly among the highest values measured during Leg 5 (Fig. 5.9c and d). These properties provide an explanation for higher seawater fCO$_2$ relative to, for example, samples with a lower DIC : TA ratio and colder waters. A higher fCO$_2$ is indeed also reflected in the GO fCO$_2$ (not shown here, but see e.g., Fig. 5.11b) However, it does not necessarily provide a straightforward explanation for why the fCO$_2$ from discrete samples is overestimated relative to the measured GO fCO_2.

In brief, the temperature and salinity ranges of the different K_1^* and K_2^* formulations do not offer a straightforward explanation for the fCO_2 discrepancies between measured and calculated values for the underway dataset of Leg 5. However, higher fCO_2 values determined for the low salinity seawater, associated with higher DIC : TA ratio and silicate content, seem to lead to the largest overestimations in fCO_2 relative to the GO fCO_2 for all three parameterisations (GP89, MI02, and SU20). Previous studies have found an apparent dependency of discrepancies between calculated and measured fCO_2 on the CO_2 concentration itself (e.g., Hoppe et al., 2012; Lee et al., 1996), with higher discrepancies at $fCO_2 > 500$ μatm (Lueker et al., 2000; Millero et al., 2002) and calculated fCO_2 values being lower than measured values. The extent and sign of the discrepancies can vary depending on the formulation used for the determination of K_1^* and K_2^* (Lueker et al., 2000). At $fCO_2 < 500$ μatm (i.e., within the range of the fCO_2 of contemporary surface oceans), no systematic discrepancy between measured and calculated values was found when using the LU00 or MI02 parameterisation (Millero et al., 2002), while some other parameterisations, such as GP89, did have an offset (Lueker et al., 2000). Hoppe et al. (2012) illustrated systematic underestimation (~30 %) between fCO_2 results calculated from TA and DIC, and those calculated from TA or DIC and pH in ocean acidification experiments, for fCO_2 values ranging between ~100 μatm to ~2000 μatm. In their study, they only used the DM87 formulation (i.e., Mehrbach et al. (1973) refitted by Dickson and Millero (1987)), and nutrient concentrations were estimated from literature and held constant per sub-dataset.

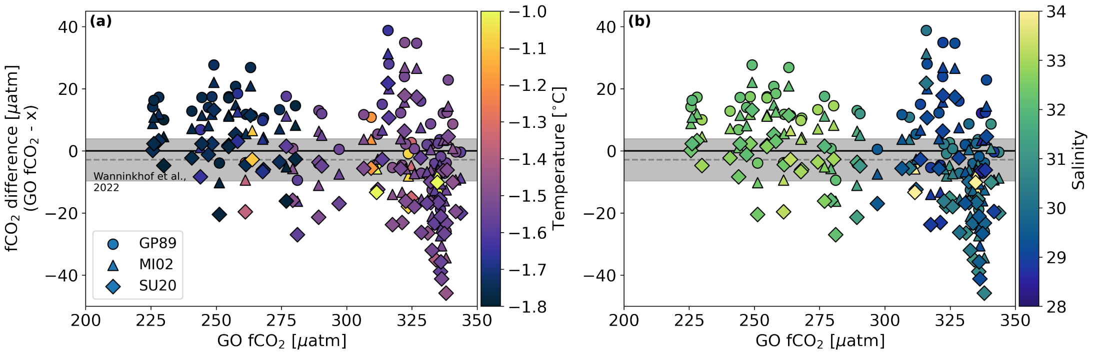

Figure 5.10: (a) The difference in measured fCO_2 and calculated fCO_2 for Leg 5 underway datapoints using different formulations for the carbonic acid dissociation constants (x = GP89, MI02, SU20), plotted against the measured underway fCO_2. Markers are coloured according to the seawater temperature. (b) Same as (a), but markers are coloured according to the seawater salinity.

The range of fCO_2 values in the Leg 5 underway dataset is relatively small and low ($<$ 400 μatm) compared to the ranges investigated by the studies mentioned above, which go up to at least 1500 μatm. The dependence of the discrepancy on CO_2 concentration is mostly relevant when $fCO_2 > 500$ μatm. Nevertheless, the Leg 5 underway results indicate a negative trend in the fCO_2 discrepancy for all parameterisations when the measured $fCO_2 > 300$ μatm (Fig. 5.10). The dependence of the fCO_2 discrepancy on CO_2 might be due to changes in chemical interactions at higher CO_2 concentration, thereby affecting the second dissociation constant of the carbonate system in seawater (K_2^*) (Lee et al., 1996), or due to changes in interactions between the borate and carbonate system at high CO_2, affecting both carbonic acid dissociation constants (Mojica Prieto and Millero, 2002).

Reason(s) for the underestimation of calculated fCO_2 in previous studies remain(s) unclear. However, if the measured underway fCO_2 data for Leg 5 of MOSAiC are assumed to be the closest to the true values, then the reasons for the underestimation outlined in most previous studies mentioned above are not necessarily the same as for the discrepancies observed here, because a) the latter are not systematic and b) the latter often overestimate the fCO_2 values rather than underestimate them.

Table 5.4: Mean, standard deviation, median, and range of differences between the measured underway GO fCO_2 and the calculated fCO_2 using discrete underway samples and different formulations for the carbonic acid dissociation constants. The discrepancy between measured and calculated fCO_2 values discussed in Wanninkhof et al. (2022), using the Lueker et al. (2000) formulation, is added for context. n = number of datapoints included in the statistics. See Table 5.3 for a summary of the labels for the parameterisation.

Parameterisation	**Mean ± 1 σ [μatm]**	**Median (min.-max.) [μatm]**	n
GP89	6.7 ± 13.3	8.7 (-25.9 to 38.7)	83
DM78	4.1 ± 13.1	5.8 (-28.9 to 35.9)	83
LU00	1.9 ± 13.3	3.4 (-31.5 to 33.7)	83
MI02	-0.4 ± 13.6	1.0 (-34.4 to 31.3)	83
SU20	-10.2 ± 14.1	-8.4 (-45.8 to 21.7)	83
Wanninkhof et al. (2022)	-2.9 ± 9.2	-	1617

Other factors to consider include the effects of dissolved organic matter and weak organic acids on TA (Fong and Dickson, 2019), proper characterisation of inorganic nutrient concentrations (Lueker et al., 2000), the accuracy of K_0 (McElligott et al., 1998), and the accuracy of K_2 (García-Ibáñez et al., 2022). The seawater collected for the DIC and TA samples in the current study flowed through the same underway system as the water that was analysed by the ship's GO fCO_2 system. However, the fCO_2 measurement is not made in *exactly* the same water as the DIC and TA samples. Uncertainties associated to this will have fed into differences between the measured and calculated results, which is expected to have introduced random variability into the discrepancies. In context of other studies, the discrepancies found for Leg 5 seem reasonable. For example, Millero et al. (2002) found a standard deviation of 22.7 μatm for the differences between measured and calculated fCO_2 values, which is larger than what is found for any of the parameterisations used in the current study (13 - 14 μatm). Moreover, the range of discrepancy values in Millero et al. (2002) where $fCO_2 < 500$ μatm is similar to the range in the current study, i.e., between -45 μatm and 40 μatm (Fig. 5.7). In recent work by Wanninkhof et al. (2022), the standard deviation of discrepancies for 1617 datapoints in the global ocean was found to be 9.2 μatm. The discrepancies found between measured and calculated underway fCO_2 values for MOSAiC Leg 5 (Table 5.4) are considered to be small enough for further scientific analysis.

The discussion on the effect of different K_1^* and K_2^* formulations on the calculated fCO_2 in the relatively extreme temperature and salinity conditions in the surface layer of the Central Arctic Ocean has highlighted that it would be beneficial for various studies on MOSAiC carbonate chemistry to agree on one of the parameterisations to allow for reliable inter-comparability. For the remainder of the analyses in the current study, we continue to use GP89 fCO_2 results to be consistent with the settings used in the fCO_2 calculations of the RaTS (Chapter 4).

5.3.2 Drivers of surface fCO_2 before and after freeze-up

The fCO_2 along the MOSAiC Leg 5 track varied considerably between ~200 μatm and 350 μatm (Fig. 5.11c), but remained lower than atmospheric CO_2. This indicates that the Central Arctic Ocean was a potential sink of CO_2 if air-sea gas exchange was not restricted by sea ice cover or by a thin surface meltwater layer with a different chemical composition than the seawater below. The relationship of fCO_2 to DIC varied along the track, depending on the ratio of DIC to TA. For example, DIC content decreased during most of the track northwards through the Amundsen Basin in search for an ice floe. However, fCO_2 remained relatively high, because the TA decreased to a similar degree as DIC (Fig. 5.11a). Prior to the start of the Leg 5 drift, fCO_2 suddenly decreased to 280 μatm and salinity increased to 32. During the drift northwards, the underway GO fCO_2 increased and stabilised around 310 μatm. Returning back south across the Amundsen and Nansen Basins after completion of the drift, fCO_2 decreased while DIC content increased, because TA increased more than DIC, increasing the buffering capacity of the seawater.

5.3.2.1 Changes in fCO_2 driven by spatial heterogeneity

The strong correlation between DIC and TA to salinity suggests that most of the variability in the carbonate system components was due to regional variability of surface layer properties, rather than biogeochemical processes. Specifically, the Leg 5 track and drift crossed a boundary between regions that are dominated by influences of either Atlantic Water (AW) typical for the Eurasian Basin or fresher surface water influenced by Pacific Water (PW) from the Canada basin. The summertime climatology of the regional salinity at 10 m depth gives an idea of the spatial heterogeneity of the isohalines (Fig. 5.12). AW entering along the eastern Fram Strait flows cyclonically, leading to higher salinity towards the east compared to salinities north of Greenland, which is where with lower salinity PW is found (Timmermans and Marshall, 2020) and where Polarstern sailed through in its transit north to find a new ice floe. After passing the North Pole, Leg 5 crossed a boundary transitioning from low salinity (PW) into higher salinity (AW) surface water where the Leg 5 ice floe was found. It then drifted back into the fresher PW. The transition from higher salinity, low fCO_2 water in the Amundsen Basin into lower salinity, higher fCO_2 water towards the Lomonosov Ridge is consis-

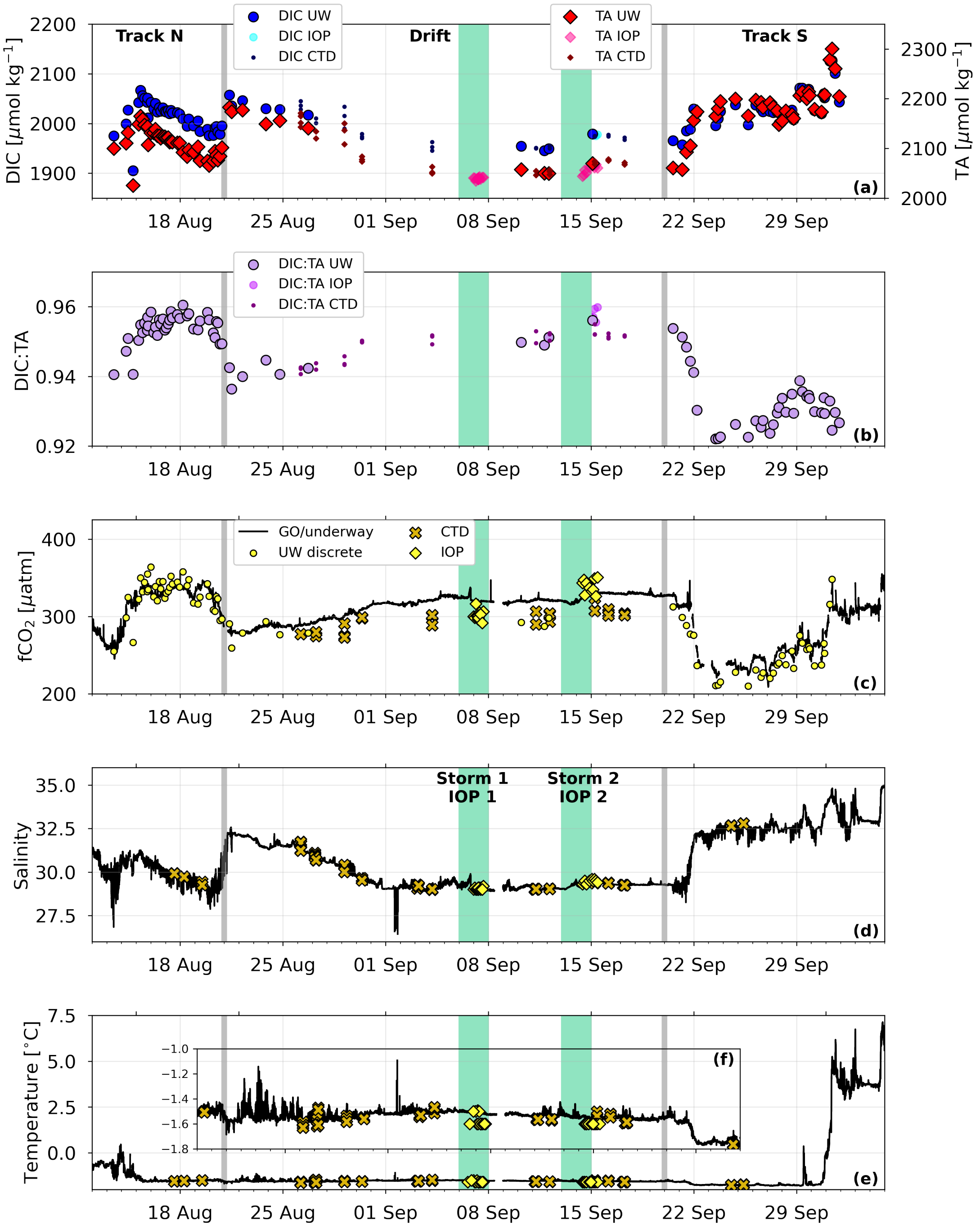

Figure 5.11: (a) DIC (circles) and TA (diamonds) content of underway discrete seawater samples, under-ice IOP samples, and CTD samples collected in the upper 20 m of the water column during Leg 5. (b) Same as (a), but for the DIC : TA ratio. (c) fCO$_2$ during Leg 5 as measured continuously by the GO system, and as calculated for the underway discrete seawater samples, the under-ice IOP samples, and the CTD samples collected in the upper 20 m of the water column (using the formulation by Goyet and Poisson (1989) for the carbonic acid dissociation constants). (d) Same as (b), but for salinity. The continuous underway salinity is measured at the underway seawater inlet at the keel of the ship. (e) Same as (d), but for seawater temperature. (f) Same as (e), but on a smaller temperature scale for the period between 19 August - 25 September 2020. Vertical grey bars in all subplots indicate the start and end of the Leg 5 drift period. Vertical green bars in all subplots indicate timing of two storms, during which IOPs took place.

tent with underway measurements in summer 2011 (Ulfsbo et al., 2014). Generally, the AW-influenced surface water (at the start of the drift) had a higher DIC and TA content and lower DIC:TA ratio than the PW-influenced surface water (most of the drift and end of the drift). After completion of the drifting period, the track south covered the latitudinal distance of the Leg 5 drift within less than 2 days, back into AW. The enhanced buffering capacity of the surface water further in the Amundsen Basin, combined with lower seawater temperatures (by then near freezing-point as the Central Arctic was freezing up), led to fCO_2 levels that were even lower than measured at the start of the drift in the same region a month earlier.

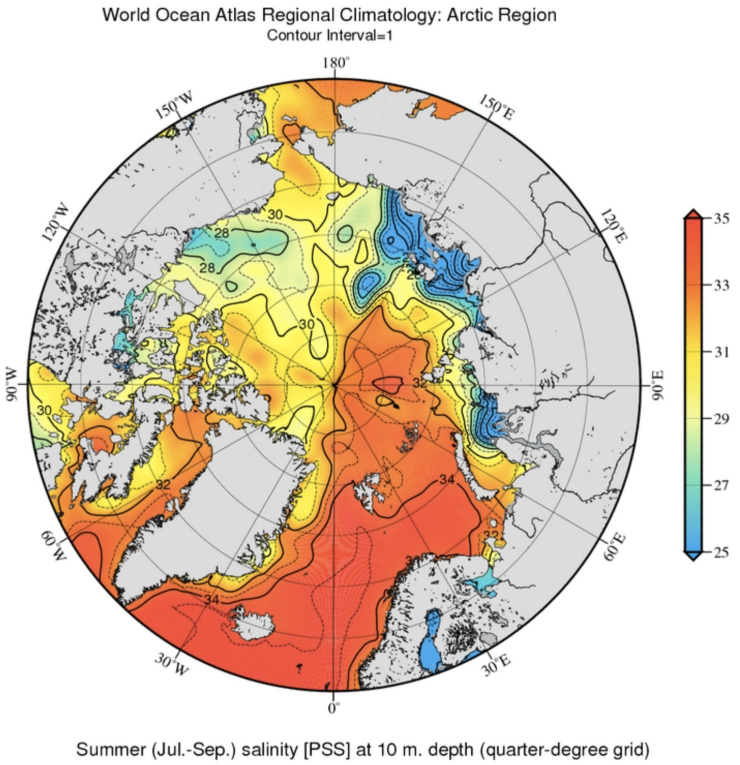

Figure 5.12: Regional summertime climatology of salinity at 10 m depth for the Arctic using all available data on NCEI until 2010 (https://www.ncei.noaa.gov/products/arctic-regional-climatology, last access 21 November 2022) (Boyer et al., 2015; Seidov et al., 2015).

With the MOSAiC data alone, it is challenging to disentangle variability caused by spatial heterogeneity in surface water properties and variability caused by time-dependent processes (on a timescale that can be captured by this dataset). Fortunately, three expeditions have been identified in the SOCAT (Surface Ocean CO_2 Atlas, version 2022) database that have tracks (or parts of their tracks) that pass near the MOSAiC Leg 5 track in a similar time of the year, namely, between August and October (Bakker et al., 2016). Details on the part of the expedition tracks used in this analysis are summarised in Table 5.5 and the parts of the tracks used here are shown in Fig. 5.13. The expeditions took place in the summer of 2012, 2014, and 2015 and are all undertaken on the *Polarstern*. This means that their fCO_2 measurements have been made on the same GO fCO_2 analyser and their results are analytically directly comparable to the MO-

SAiC results. For convenience, these expeditions will be referred to as Polarstern2012, Polarstern2014, and Polarstern2015 from now on. Note that any parts of the expedition tracks (and collected data) that were not near the MOSAiC Leg 5 track are not shown in any of the figures. Between 5 and 8 years have passed between these expeditions and the start of the MOSAiC expedition, and differences between the datasets are to be expected. However, similarities in the measurement results in time or space can help us more accurately explain the MOSAiC results. We here compare the SOCAT data to the Leg 5 tracks going north in search of a new ice floe and going south at the end of the expedition only, leaving aside the drifting period, which will be discussed subsequently.

Table 5.5: Information on the three expeditions that have SOCAT (version 2022) data near the MOSAiC Leg 5 track. Note that the table only contains the coordinates and dates for the portions of the track that are used in the current work to compare to the MOSAiC Leg 5 data. Source DOIs are given, but the data shown in this work are taken from the SOCAT (version 2022) database.

Expedition label	**Southernmost track coordinates**	**Northernmost track coordinates**	**Track dates**	**Source DOI**
Polarstern2012	5.9241°E, 70.1696°N	53.1743°E, 89.2878°N	20/09/2012-04/10/2012	10.3334/CDIAC/OTG.OA_VOS_POLARSTERN_2012
Polarstern2014	354.0783°E, 80.0646°N	25.4927°E, 89.9948°N	08/08/2014-27/08/2014	10.3334/CDIAC/OTG.OA_VOS_POLARSTERN_2014
Polarstern2015	30.8841°E, 82.5001°N	56.1719°E, 89.9996°N	23/08/2015-07/09/2015	10.3334/CDIAC/OTG.OA_VOS_POLARSTERN_2015

Polarstern2014 has a very similar track as most of the Leg 5 track north and they both took place in August (Fig. 5.13). Leg 5 fCO_2 during the journey north is lower than during Polarstern2014, except between 82-86°N (Fig. 5.14a), when Polarstern2014 sails much closer to the zero-meridian (east of Leg 5 track north), where surface waters are influenced by the AW entering the Arctic Ocean and have a higher salinity of ~33 (Fig. 5.15a) and lower DIC:TA ratio. Lower temperature and higher salinity towards the North Pole during Polarstern2014 may in part be due to AW influence, as the geographic location of the boundary between lower and higher salinity surface water may have been different in 2014 compared to 2020. Generally lower salinity values during Leg 5 compared to the overlapping Polarstern2014 track (e.g., 80-82°N and > 87°N) is due to enhanced sea ice melt in summer 2020, driven by higher air temperatures (Nicolaus et al., 2022; Shupe et al., 2022) compared to summer 2014. This is seen in the mean sea ice concentration (compare Fig. 5.17d and 5.17j), which was constantly higher than 90 % during Polarstern2014, while it was between 50-80 % for most of the Leg 5 Track North, and never exceeded 90 %. Surface DIC and TA content likely will have been diluted during Leg 5's track north, relative to summer 2014.

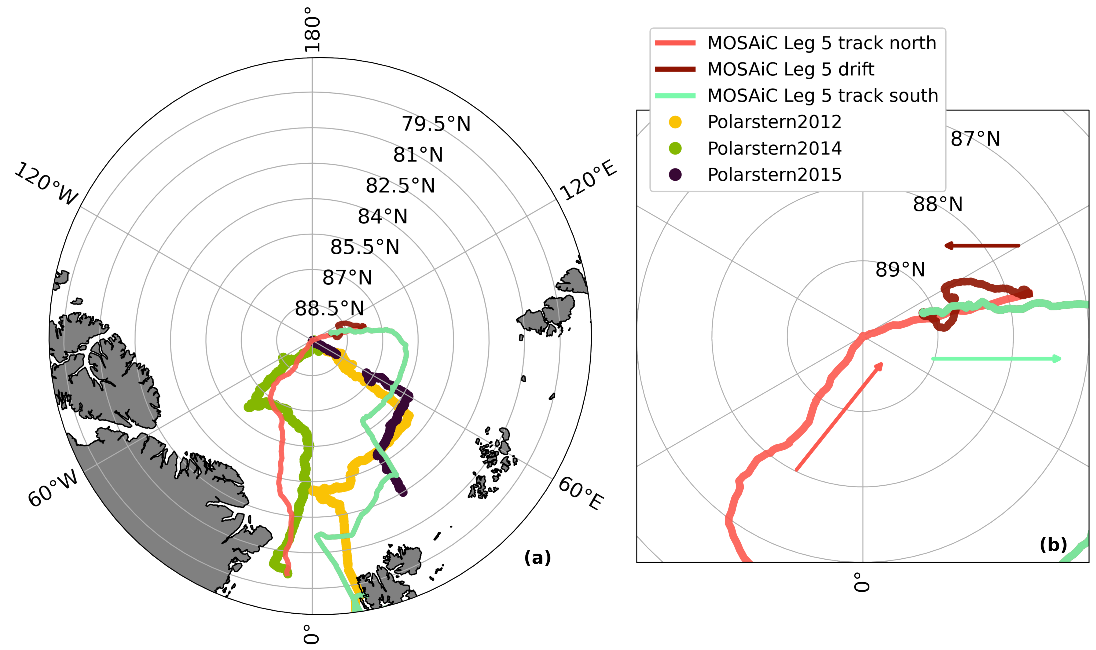

Figure 5.13: (a) Ship tracks for the track north, the drift, and the track south of Leg 5 of MOSAiC, as well as fractions of tracks of previous Arctic expeditions in close proximity to the MOSAiC Leg 5 tracks, as shown in SOCAT (version 2022). Colours of the tracks as shown here correspond to data collected along these tracks in subsequent figures. (b) Zoomed-in version of (a), north of 87°N, only for MOSAiC Leg 5 tracks. Arrows indicate the direction of the track sections.

The tracks of Polarstern2012 and Polarstern2015 are very similar to each other (Fig. 5.13), but the former took place in the transition from August into September and the latter from September into October, i.e., in a similar time of year as the Leg 5 track south after completion of the drift. The Leg 5 track south between 90-86°N does not overlap with the other tracks, as it is more towards the east. Despite the slightly different timings in the season, differences between the tracks, and different years, strong similarities exist among the fCO_2, salinity, and temperature results at latitudes $< 87°N$ (Figs. 5.14b, 5.15b, 5.16b). This indicates 1) that zonal variability in the surface ocean is not high within this relatively large region at this time of year, and 2) that processes affecting fCO_2, salinity, and temperature in this region did not greatly change between late August and early October. The extension of the sea ice melt season in 2020 by 1 month relative to most years previously (Rinke et al., 2021) may be a reason why the Leg 5 track data compares especially well with those from Polarsern2015, which took place a month earlier in the season, north of 87°N. In this region, the influence of AW increases from the North Pole towards 86°N. fCO_2 decreases southwards and finds a minimum between 83-86°N (Fig. 5.14b). This pattern, although less pronounced for Polarstern2012, matches a sharp increase in salinity to ∼33 and decrease in temperature to near seawater freezing point (Fig. 5.15b and 5.16b). Sea ice formation starts in this time of the year, but brine rejection is unlikely to have contributed much to the salinity increase of the surface layer, as no substantial concomitant increase in DIC content is observed in the Leg 5 data. Enhanced solubility driven by decreasing temperatures along the tracks can have contributed to decreasing fCO_2. Once near the ice edge, fCO_2, salinity, and temperature increase. This latitudinal gradient is expected, as solar radiation heats the surface water more where there is less sea ice cover and salinity is increased by mixing with subsurface water. The relationship between fCO_2 to salinity changes from negative to positive, which is most likely due to the positive relationship between salinity and temperature. Temperatures increase to > 5 °C, decreasing CO_2 solubility.

While the comparison to the SOCAT data suggests that the majority of variability in the carbonate system components, salinity, and temperature can be explained by spatial variability in dominant subsurface water mass properties, some of it is driven by interannual differences in sea ice cover and melt. The impact of the transition of the Central Arctic into freeze-up is discussed in the following section.

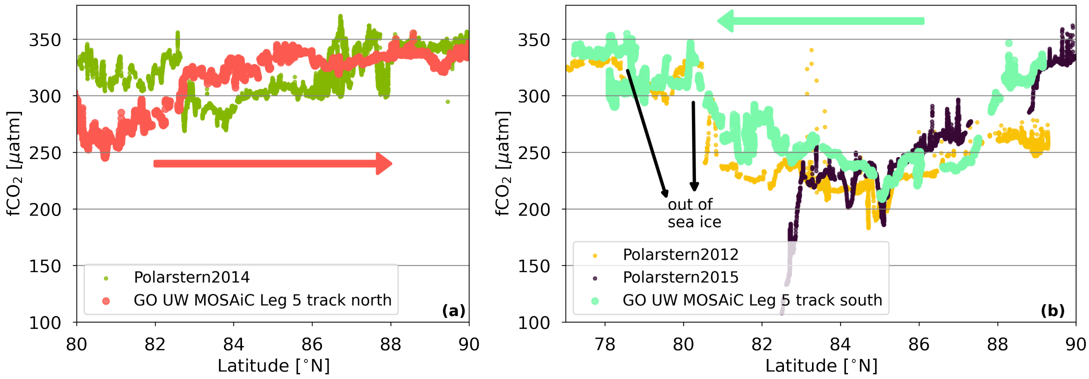

Figure 5.14: Underway fCO$_2$ measured continuously by the ship's GO system for (a) the Leg 5 track north and an expedition in summer 2014, and (b) for the Leg 5 track south and expeditions in summers 2012 and 2015. Arrows indicate the direction of the tracks for MOSAiC's Leg 5 only. In (b), the location where the ship sails out of the sea ice is annotated.

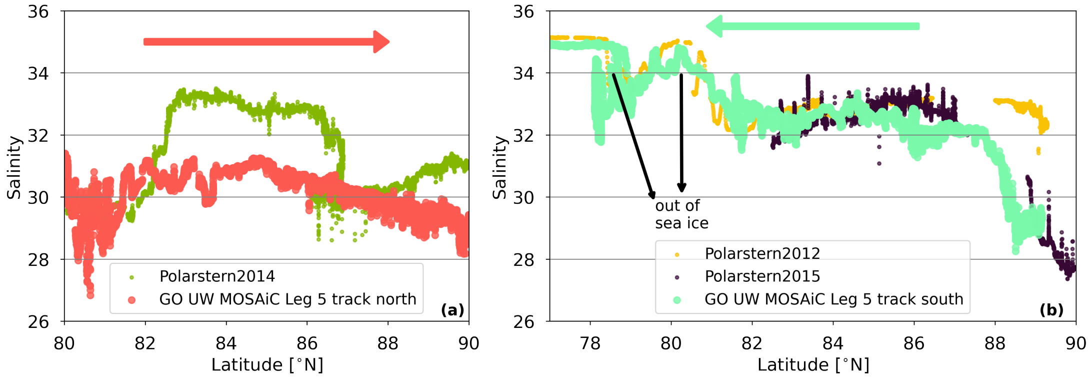

Figure 5.15: Same as Fig. 5.14, but for underway salinity.

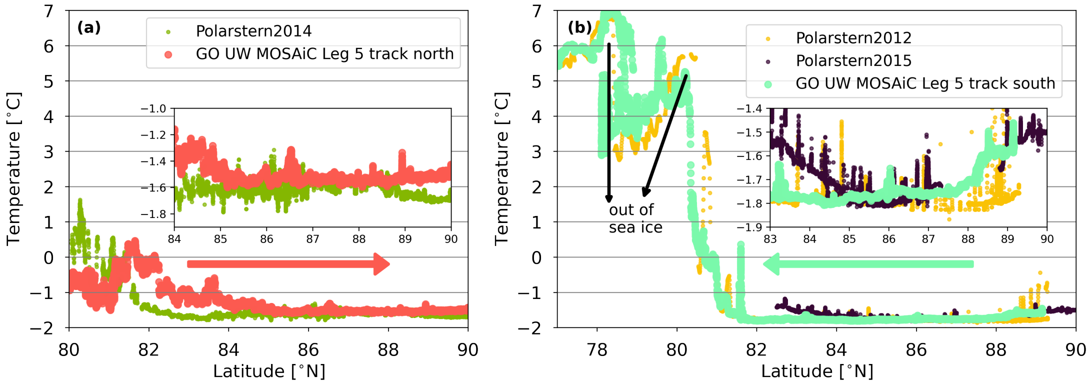

Figure 5.16: Same as Fig. 5.14, but for underway seawater temperature. Insets in subplots show seawater temperature measurements on a smaller temperature scale between 83 and 90°N.

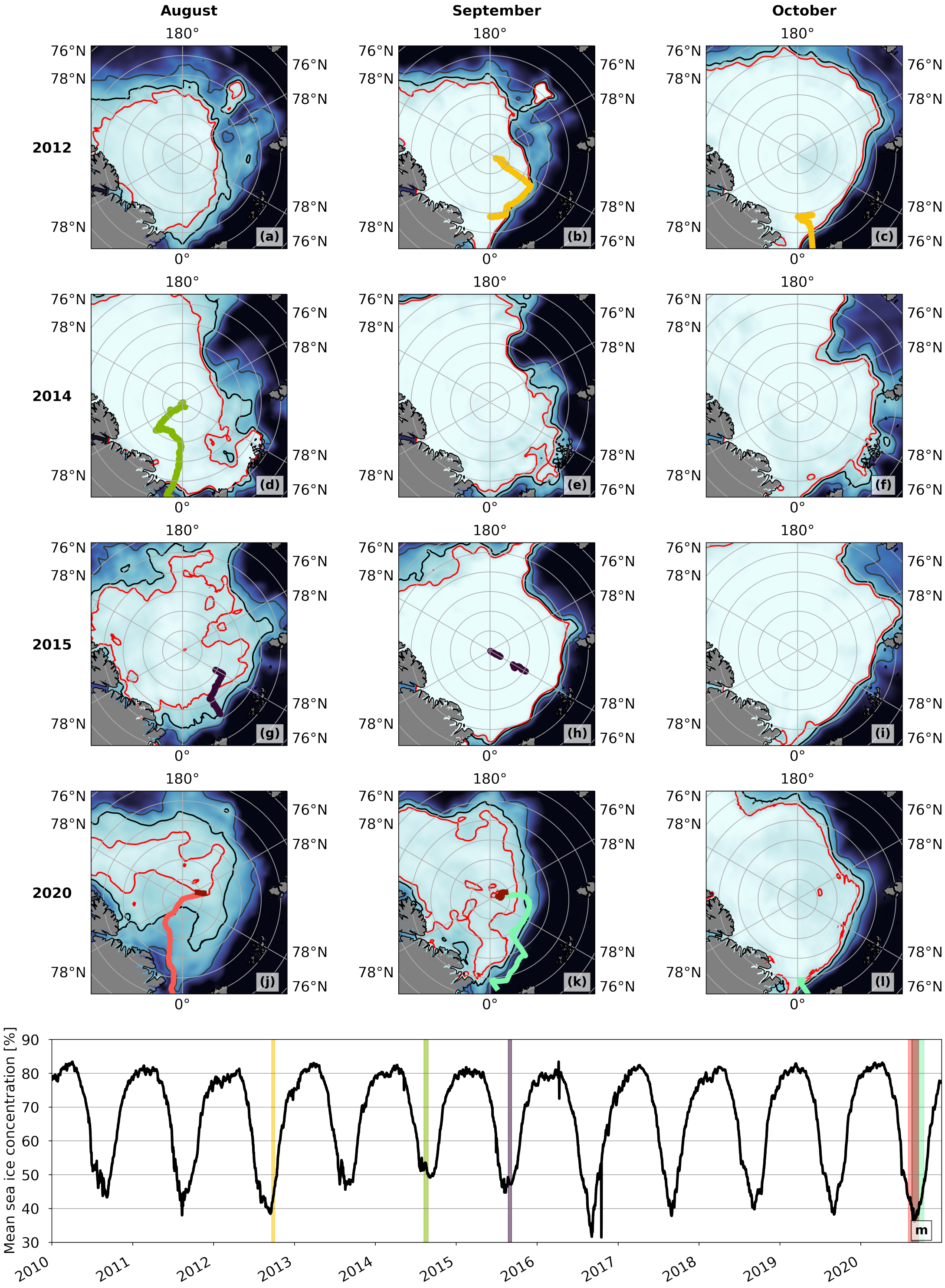

Figure 5.17: Monthly mean sea ice cover for August (left column), September (centre column), and October (right column) for 2012 (first row), 2014 (second row), 2015 (third row), and 2020 (fourth row), using OSTIA sea ice cover data (Good et al., 2020). Isolines at sea ice concentrations at 50 %, 80 %, and 90 % are indicated in each map with grey, black, and red lines, respectively. Subsets of tracks of Arctic expeditions for which underway measured fCO_2 data is available on SOCAT (version 2022) and which are in close vicinity to the MOSAiC Leg 5 track are shown in maps corresponding to the timing of the expedition. The Leg 5 track north, south, and the drift track are shown in (j), (k), and (l). (m) Arctic (> 60°N) regional mean sea ice concentration between 2010 and 2021. Vertical coloured bars indicate the time period when fCO_2 was measured during the different sections of Leg 5 and the other expeditions in 2012, 2014, and 2015.

5.3.2.2 Changes in fCO_2 driven by temporal variability

The MOSAiC Leg 5 drift is isolated from any other locations where underway fCO_2 measurements have previously been made in this time of year. I therefore defer from making many comparisons to any of the SOCAT data. Instead, I use the drift data to study the changes in the surface carbonate system driven by the seasonal transition into freeze-up. I do this by capitalising on the ship's journey to find the Leg 5 floe, and its journey south at the end of the drift. It so happens that the latitudinal range 89.10-87.75°N was crossed three times within a narrow longitudinal range (Fig. 5.13b):

1. Transect 1: As part of the transit, the ship crossed the North Pole to then find a floe at ∼87.75°N.
2. Transect 2: From here, the ship drifted with the floe in a zig-zag manner back to ∼89.1°N. This is the drift track.
3. Transect 3: Finally, from the end-point of the drift, the ship journeyed back south, passing ∼87.75°N at a similar longitude as on the track used to find the floe.

Unlike the tracks of the ship actively sailing in a single direction, the drift track is not a straight line. Strictly speaking, I therefore cannot speak of these three sections of the Leg 5 track as *transects*. However, as my comparisons to the SOCAT data in the previous section have shown that longitudinal gradients are not very strong in this small region, I will treat these three tracks as transects for the purpose of my analysis.

Fig. 5.18a shows the GO fCO_2 results for each of the transects and highlights the contrasting duration of each. Transect 1 and 3 only took 2 and 1 day(s), respectively. In the absence of any storms or significant sudden atmospheric events in the region affecting the water column at these times, their results can be considered as snapshots in time, i.e. the state of the system at the start and at the end of the Leg 5 drift. The duration of the drift (transect 2) was 31 days. Comparing the drift transect can give an indication of when certain changes in the surface water occurred due to time dependent or small-scale events, relative to transects 1 and 3.

The surface fCO_2 during the Leg 5 drift (i.e., transect 2) is higher by 10-20 μatm compared to transect 1 south of 88.75°N, except between 88.75-89°N where values remain around ∼320 μatm (Fig. 5.18a and 5.18b). Even though transect 1 lacks data south of ∼88°N, it is likely that the fCO_2 started increasing soon after the start of the drift. Similarities in the results of the latitudinal pattern for transect 3 (i.e., the transit back south) compared to the drift period indicate that most of the changes to the surface water carbonate system captured during the drift between 21 August and 20 September 2020 were representative for this region. Smaller changes occurred between the end of the drift and the timing of transect 3. For example, fCO_2 values between ∼88.25-88.75°N had decreased by the time the ship went back south relative to when it was last there during the drift. The transition from PW (salinity ∼29.25) back into the boundary region with AW (∼32) is evident around 88.25°N (Fig. 5.18c), where fCO_2 also decreases towards the south. Seawater temperature during the drift

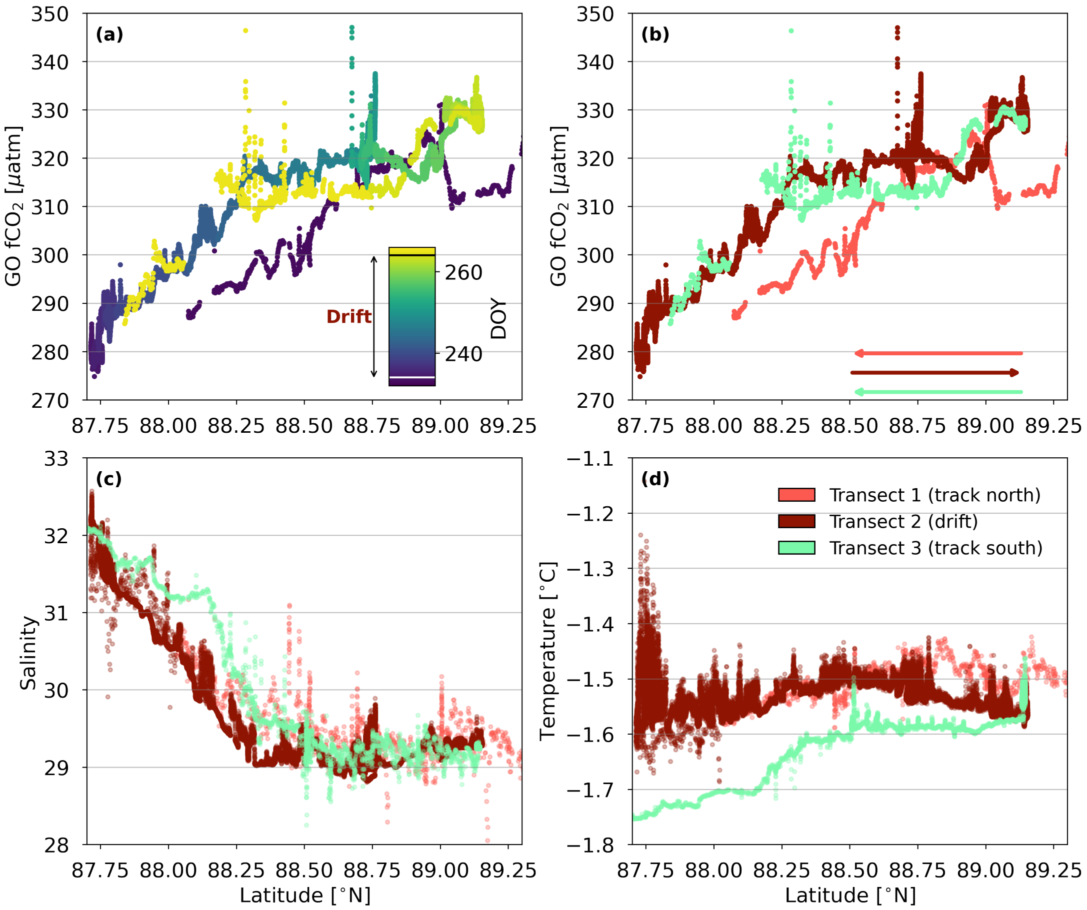

Figure 5.18: (a) Underway measured fCO$_2$ as measured by the GO system during Leg 5 between 87.75 and 89.25°N, including the final part of the track to find the Leg 5 floe, the Leg 5 drift, and the first part of the track going back south after abandoning the Leg 5 floe at the end of the expedition. Markers are coloured according to the day of the year (DOY). (b) Same as (a), but markers are coloured according to the different sections of the track, which are referred to as transects 1, 2, and 3 (see text for details). The arrows indicate the latitudinal direction (north- or southwards) of each transect, corresponding to the colour scheme. (c) Same as (b) but for salinity. (d) Same as (b) but for seawater temperature.

follow the same values back towards the North Pole, but start deviating towards colder temperatures around 88.5°N at the start of freeze-up (Fig. 5.18d). The much lower temperatures during transect 3 indicate a continuation of surface ocean cooling as the Arctic transitions into winter.

Differences based on latitudinally binned means show that the salinity decreased for the region in the middle of the drift period (Fig. 5.19c), coinciding with the peak fCO$_2$ increase (Fig. 5.19b). The freshening of the surface water is a continuation of the sea ice meltwater input, which ceases as the drift continues northwards and freeze-up begins. The negative correlation between the change in salinity and in fCO$_2$ during the drift relative to the start of the drift is a result of a decreased DIC:TA ratio (i.e. relatively higher TA content), which is likely associated to excess TA in sea ice meltwater (Rysgaard et al., 2011). South of 88.3°S, fCO$_2$ slightly increased between the drift at

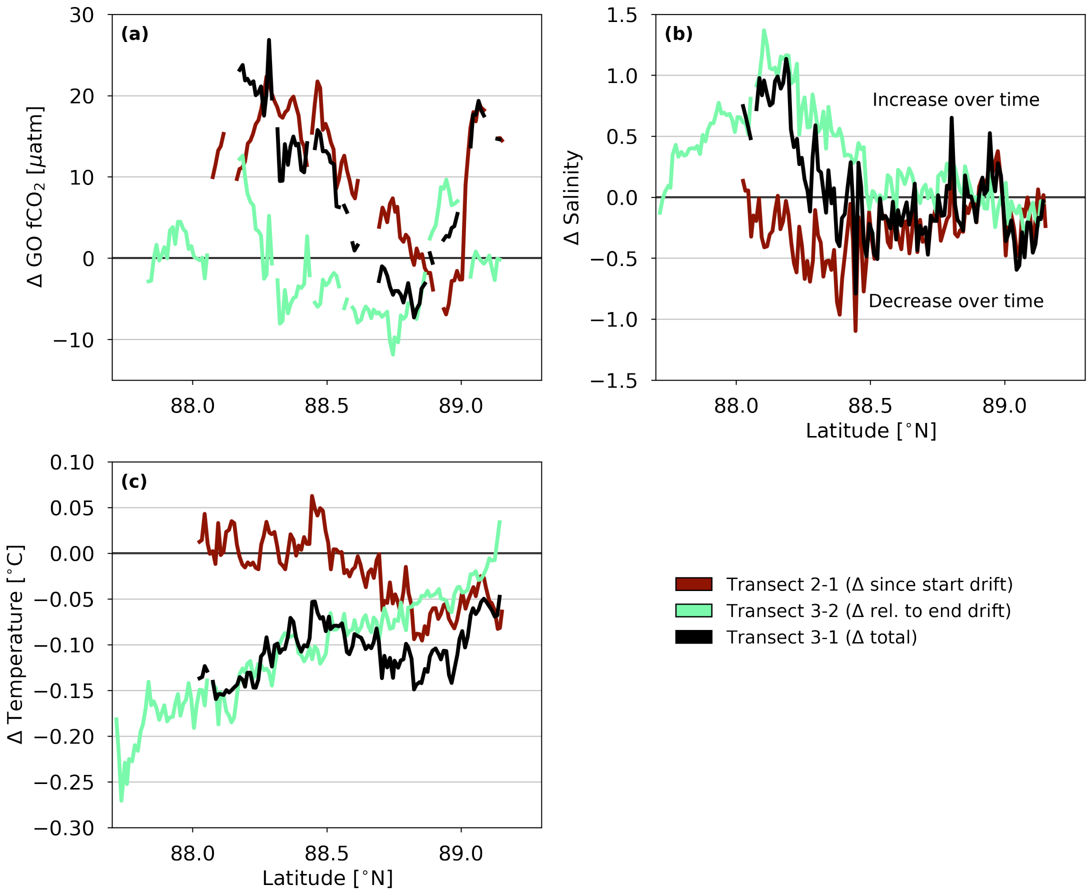

Figure 5.19: (a) Differences in the measured fCO$_2$ means within 0.01° latitude bins between transects. Lines indicate the difference between transects 2 and 1, 3 and 2, and 3 and 1. Markers are coloured according to the number of days between binned measurements. (b) Same as (a), but for salinity. (c) Same as (a), but for seawater temperature. Positive values indicate an increase over time, negative values indicate a decrease over time.

the end of August (transect 2) and transect 3 in late September. Although this is not obvious in Fig. 5.18b, it is seen more clearly in Fig. 5.19b. This increase over time coincides with an increase in salinity (Fig. 5.19c), such that the correlation between changes in salinity and fCO$_2$ between transects 2 and 3 become positive. It is possible that brine rejection contributed to seawater salinity and fCO$_2$ increase at this time of year, as sea ice started to grow. However, if brine rejection could solely explain the salinity increase between 0.5 and 1, then 0.3 and 0.7 m of sea ice would needed to have formed to bring about this change (assuming a decrease in sea ice salinity of 28, a mixed layer depth of 18.4 m (Kawaguchi et al., 2022), and mass conservation). As new sea ice formation was still in its infancy at this time of the year, brine rejection will likely only have made a small contribution to the seawater salinity increase and mixing processes are likely to have had a larger impact (see Section 5.3.3). Continuing decreasing seawater temperatures will have slightly offset any associated increases in fCO$_2$ due to increased CO$_2$ solubility (Weiss, 1974). Contributions of net remineralisation are not ruled out, but cannot be assessed for the different transects at this stage. To address this topic in the future, a similar analysis for these transects could be applied to data for biological oxygen consumption (e.g., remineralisation), derived from underway measurements by Membrane Inlet Mass Spectrometry during Leg 5, for oxygen isotopes, or for chlorophyll *a*.

In summary, the fCO_2 in the surface ocean in the region of the Leg 5 drift track initially increased along with freshening from sea ice meltwater input at the end of the summer season. Once meltwater input ceased following the onset of freeze-up, salinities stopped decreasing or even started increasing. This coincided with lower fCO_2 increase relative to the start of the drifting period. As seawater temperatures dropped and CO_2 solubility was enhanced, the fCO_2 decreased in much of the region. When the ship returned to the starting point of the drift track, salinity had increased since the start of the drift, likely due to mixing with subsurface water with possibly a small contribution of brine rejection. fCO_2 had also increased, but it is unclear why, as the ratio of DIC to TA did not change significantly and temperatures are much lower since the start of the drift (Fig. 5.11b, e).

5.3.3 Small-scale variability during the Leg 5 drift

As discussed above, meltwater input (and its decrease at the end of summer) was an important driver of the temporal changes in the marine carbonate system during Leg 5. Next, the thus-far mostly one-dimensional time line will be expanded to two dimensions by including the changes in the vertical profiles of the upper water column. Figures 5.20 and 5.21 show the physical properties and DIC and TA content in the upper 100 m of the water column, including data from a limited number of CTD casts during the transect going north and going south (start and end of drift period are indicated by vertical lines in the figures). The drift across a frontal region (Kawaguchi et al., 2022) as discussed for the underway data, is also clear in the vertical salinity profiles of the upper surface layer, coinciding with lower DIC and TA content. Below 20 m, salinity, DIC, and TA show relatively little variability during the drift and a temperature minimum layer is encountered at about 40-80 m.

The mixed layer is generally defined as the layer where mixing recently occurred and where vertical gradients of properties are relatively uniform. Its depth is defined as the depth at which the density increases above a certain threshold value (e.g., 0.03 kg m^{-3}) relative to a reference value near the surface (e.g., 10 m). The mixing layer is where strong mixing is actively occurring and its depth can be determined as the depth at which the turbulent kinetic energy drops below a certain threshold value (i.e., $\epsilon < 3\ 10^{-8}$ W kg^{-1}) (Kawaguchi et al., 2022). While the mixed layer depth during the Leg 5 drift did not significantly change from its mean value of 18.4 ± 3 m, the mixing layer depth was more variable around 17.8 m due to sea ice drift speed driven by wind (Kawaguchi et al., 2022). Within this oceanographic context, we here investigate small-scale processes that occurred in the upper ~50 m of the water column and directly underneath the sea ice during two storm events on 6 and 13 September 2020. High wind events can have a strong influence on surface mixed layer CO_2 on timescales of

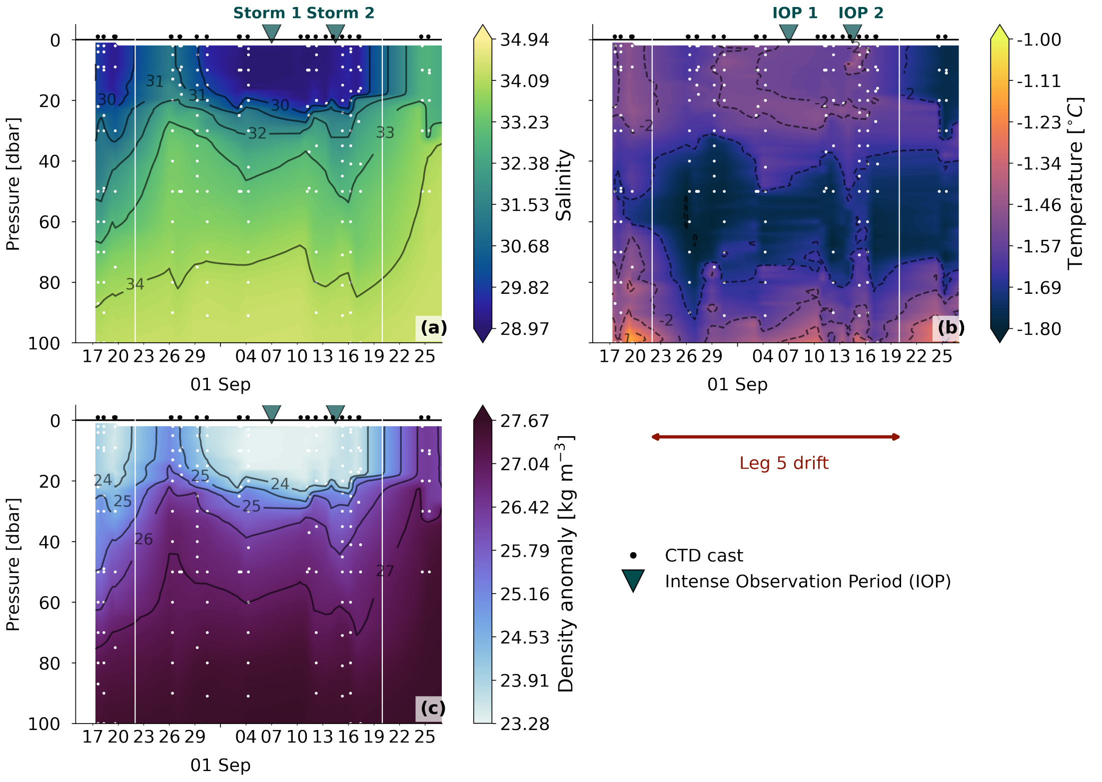

Figure 5.20: (a) Contour plot of salinity profiles measured by CTD casts during MOSAiC Leg 5 in the top 100 m of the water column. White lines indicate the beginning and end of the Leg 5 drift period, which is also indicated by the red arrow. White markers indicate the discrete sampling depths. Black markers at the surface indicate the timing of the CTD cast. Triangle markers indicate the timing of two storm events, during which IOPs were done. See Table 5.1 and text for details. (b) Same as (a), but for seawater temperature. (c) Same as (a), but for density.

1-10 days by exposing deeper carbon to the upper ocean through Ekman transport and entrainment (Mathis et al., 2012; Nicholson et al., 2022). Through shear stress, the upwelling effect due to wind also occurs underneath the ice, especially along shear zones in the ice (McPhee et al., 2005). Stratification in the summertime Arctic Ocean is strong and requires substantial kinetic energy input driven by wind-forcing to deepen the mixed layer. However, because Atlantic Water can be relatively close to the surface, its heat (and carbon) can be released to the ice-ocean interface during storm events (Meyer et al., 2017).

As mentioned in Section 5.2, MOSAiC teams working on the ice participated in high-frequency sampling and measurements during the two Leg 5 storms across platforms and disciplines to constrain rapid and small-scale processes: IOP 1 and IOP 2. The storms passed the ice floe location after the ship and ice floe had already drifted back across a boundary region from waters with higher salinity (AW) into a region with lower salinity, at the end of August/early September (Kawaguchi et al., 2022) (see Section 5.2). At the time of both storms, the water masses at the location of the ice floe should therefore be comparable. During these IOPs, a free-falling MSS was deployed at high frequency from a sampling site on the ice floe, away from the ship's influence (Schulz

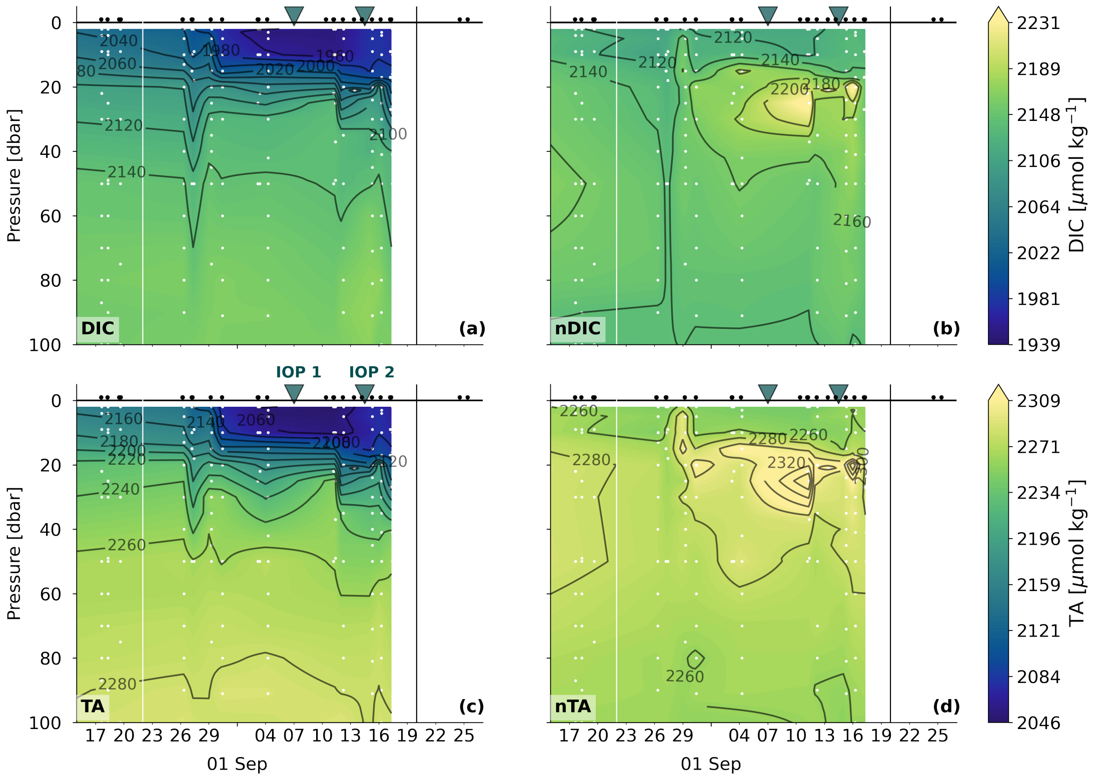

Figure 5.21: Same as Fig. 5.20 but for (a) DIC, (b) nDIC, (c) TA, and (d) nTA content in the upper 100 m during the Leg 5 drift of MOSAiC

et al., 2022). Its profiles of dissipation rates of turbulent kinetic energy (ϵ) indicate enhanced ocean turbulent mixing in the top 30 m during both storm events, but the mixing is more intense during the second storm on 13 September (Fig. C.5). The effect on the carbonate system in the surface layer was different for both storms due to differences in turbulent mixing and the amount of available meltwater input, as is discussed in the next sections.

5.3.3.1 Storm 6-7 September 2020 and IOP 1

Ocean dissipation rates show that the turbulence in the upper 30 m of the water column started increasing in the afternoon of 6 September and decreased in the afternoon of 7 September (Fig. C.5b) (Kawaguchi et al., 2022). Increasing dissipation rates matched increases in the underway salinity from ∼29.7 to 30, before it suddenly dropped to < 29 (Fig. 5.22e). The drop in salinity is consistent with salinity profiles from the MSS that show that the peak dissipation rates in the night of 6-7 September coincided with a plume of lower salinity water < 28.4 that was mixed down from the surface until about 13 m depth (Fig. 5.23b). Isohalines gradually deepened by ∼5 m by the end of the storm.

The source of the freshwater mixed into the upper water column was the freshwater stored within the meltwater lens in the top 1 m. The presence of the meltwater lens in leads before 6 September is indicated by strong salinity gradients between 0.4 and 0.7 m, and increasing salinity from < 10 at the surface to > 28 below the lens (Fig. C.7a, red

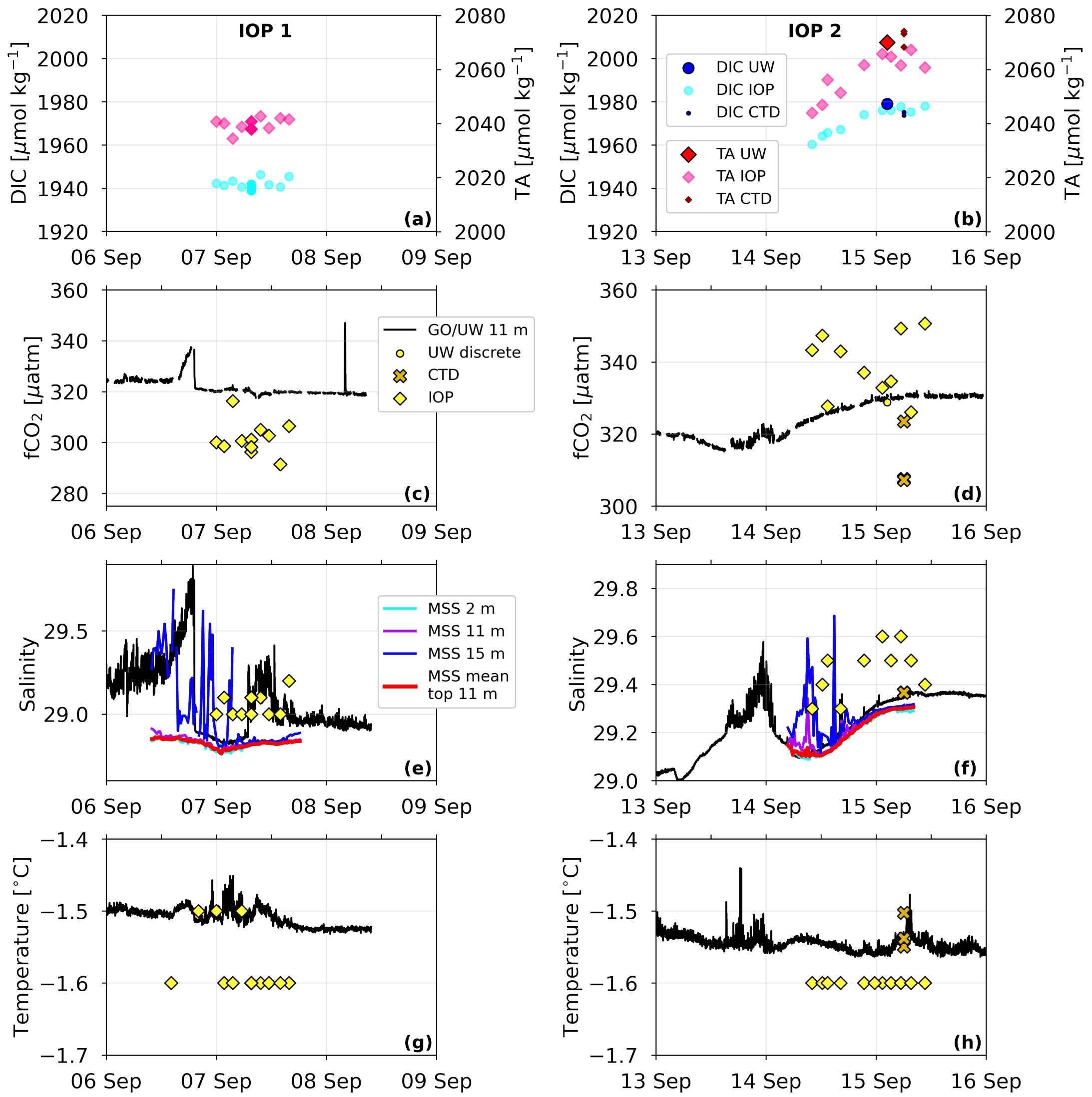

Figure 5.22: Measurements made during IOP 1 (left column) and IOP 2 (right column), each coinciding with a storm during Leg 5 of MOSAiC. Results are shown for DIC and TA content of under-ice water ((a), (b)), GO fCO_2 and fCO_2 determined for the underway discrete, CTD, and under-ice samples ((c), (d)), underway salinity and salinity measured by the MSS at various depths ((d), (f)), and temperature measured by the underway system and under the ice ((g), (h)).

colours). In the absence of sea ice formation, variability observed in the meltwater lens thickness was dependent on the width of the leads (Nomura et al., 2023). Ice started forming in leads from the beginning of September, which since then explained about 48 % of the change in the meltwater lens depth (Nomura et al., 2023). After the 6 September storm, the salinity gradient of the meltwater lens had weakened and the bottom of the meltwater lens shoaled to ~0.2 m (Fig. C.7, blue colours). A small part of the shoaling of the meltwater lens was attributed to brine rejection of newly formed ice in leads which drove density-driven mixing, causing active mixing of the meltwater and thereby counterintuitively resulting in a slightly lower salinity in the upper 5 m relative to the beginning of September (Fig. C.7a; Nomura et al., 2023). Most of the

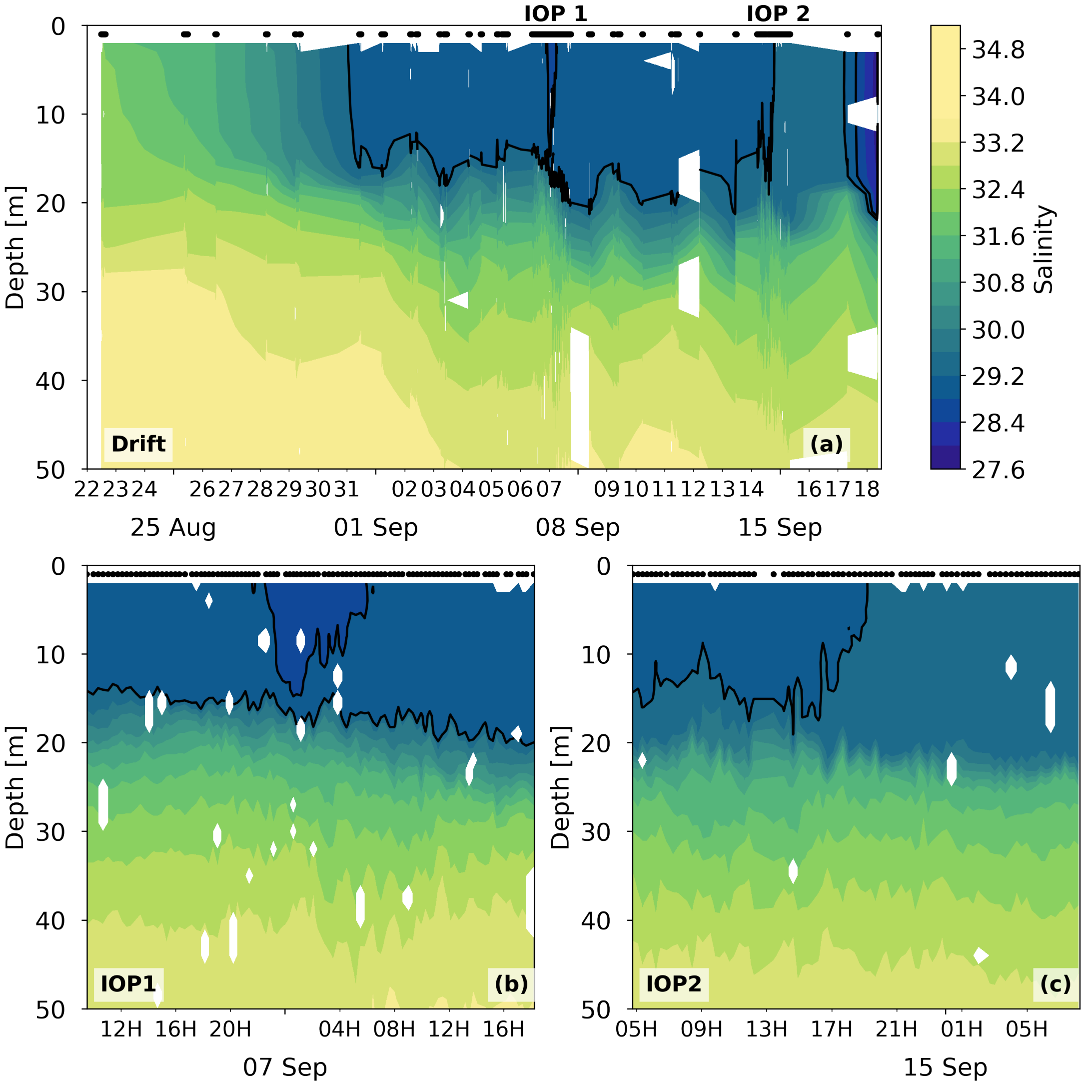

Figure 5.23: Salinity measured by the MSS in the top 100 m during Leg 5 (a), and during IOP 1 (b) and IOP 2 (c). Black isolines are plotted at 28.4 and 28.8 to emphasise mixing during the Leg 5 storms.

meltwater shoaling was likely due to wind-driven mixing (i.e., during the storm) and mixing due to turbulence caused by wind-driven motion of sea ice (Nomura et al., 2023).

DIC and TA samples underneath the ice were collected during the IOP 1, starting at the end of 6 September, when salinity had largely (but not completely) recovered from the meltwater input by continued mixing. At this stage, DIC and TA content underneath the sea ice were stable (Fig. 5.22a), even though underway fCO_2 dropped by about 5 μatm relative to the period before the storm. The calculated fCO_2 underneath the ice was lower than underway fCO_2 by 20 μatm and variable (Fig. 5.22c). The discrepancy in fCO_2 could either be due to the choice of formulation of the carbonic acid dissociation constants (see Section 5.3.1), or to a gradient between the sea ice and 11 m depth from which seawater is drawn for the underway GO fCO_2 analyser, or both.

The evolution of the under-ice salinity and temperature measurements do not resemble that from the MSS or the underway system, which is suggestive of lower variability over time at the base of the sea ice (Fig. 5.22e, g). However, it is also possible that the lower resolution of the under-ice salinity and temperature measurements fail to capture the subtle changes on these small timescales. As discrete measurements of DIC and TA prior to the storm are scarce, it is difficult to assess the impact of the storm on the carbonate system properties of the under-ice water. However, the continued mixing in the water column on 7 September does not seem to have greatly impacted the upper surface layer carbonate system. While the salinity measurements from the MSS do indicate that vertical interaction occurred within the mixed layer during this storm event, mixing seems to have been limited to the mixed layer depth and does not seem to have caused much entrainment of higher salinity, DIC, and TA water from below the mixed layer. The net effect of the 6 September storm was a slightly fresher, lower fCO_2, and colder mixed layer, which is contrasting to storm-associated fCO_2 peaks observed in other Arctic studies when storms effectively caused mixing with deeper water (Fransson et al., 2017).

5.3.3.2 Storm 13-14 September 2020 and IOP 2

A storm on 13-14 September 2020 briefly interrupted the onset of freeze-up by bringing in warm, humid air to the location of the Leg 5 floe (Kawaguchi et al., 2022; Shupe et al., 2022). This storm had a higher kinetic energy input and caused more turbulence in the upper 20 m than the storm on 6 September (Kawaguchi et al., 2022). Its onset can be seen in the increasing underway salinity (29.0 to 29.6) on 13 September (Fig. 5.22f). It is unclear whether the simultaneous subtle decrease in GO fCO_2 on 13 September ($\sim$3 μatm, Fig. 5.22d) was associated to these changes in salinity. Similar to the 6 September storm, the salinity suddenly decreases (to 29.1) in the transition from 13 to 14 September, before increasing again and stabilising between 29.3 and 29.4 on 15 September (Fig. 5.22f). MSS profiles (and IOP 2) only started on 14 September, but show consistent salinity results compared to those from the underway instrument (Fig. 5.22f), despite the distance between Ocean City on the ice and the ship where the measurements were respectively made. The temporary freshening during the 13 September storm is less than during the 6 September storm, as most of the meltwater lens at the surface had already been eroded and sea ice had started re-freezing again (Fig. C.7). Thus, there was less meltwater transferred into the mixed layer. The underway salinity increase preceding freshening during the storms is consistent between both storms, although they have different magnitudes (Fig. 5.22e and 5.22f). MSS salinity results at 15 m show similar salinity peaks during both storms. It is possible that the boundary of the mixed layer was closer to 11 m (= depth of underway measurements) at the onset of the storm and reached the sensors when turbulence increased. As the storm progressed, the isolines deepened slightly and the sensors measured the more homogeneous values representative for the mixed layer.

Mixing resulted in input of DIC and TA from below the mixed layer upwards, as shown by the enhanced DIC and TA content in the under-ice water after the storm relative to before the storm by $\sim$30 and $\sim$20 μmol kg^{-1}, respectively (Fig. 5.22b). If enhanced DIC and TA input reached the bottom of the sea ice, it likely also reached the air-sea interface in leads where it could affect CO_2 exchange. While mixing increased DIC and TA content in the upper 11 m, it diluted DIC and TA content at/below the mixed layer (Fig. 5.21a and 5.21c). The effects of storm-induced mixing reached depths until 100 m, as seen by a plume of enhanced silicate content between 13 and 17 September (Fig. C.4). No such plume is seen for nitrate or phosphate, because their vertical gradients in the upper 60 m are much smaller.

The increase of GO fCO_2 by 10 μatm during the storm event matches the increase in DIC and TA content measured in the under-ice water on 14-15 September (Fig. 5.22b and 5.22d). However, as opposed to the GO fCO_2 measurements and under-ice DIC and TA content, the calculated fCO_2 for the under-ice samples did not show a steady increase and were highly variable (Fig. 5.22d). This variability may in partly be due to the variability in the under-ice salinity measurements used in the calculations of fCO_2 (Fig. 5.22f), which affect the partitioning of the carbonate system when calculating fCO_2 from DIC and TA.

The turbulence caused by the storm eroded the remainder of the meltwater lens, which was no longer observed after the storm, as is illustrated by the lack in salinity gradients of the lead profiles (Fig. C.7). The combination of little meltwater input at the surface and mixing with subsurface water led to enhanced salinity in the mixed layer by almost 4 units and higher fCO_2 by 10 μatm by the end of the 13 September storm. While the step-wise fCO_2 increase during the 13 September storm was not large enough to result in outgassing to the atmosphere, it did have a lasting effect on CO_2 in the upper surface layer. These findings support the importance of the role of storms on polar surface water carbonate chemistry and CO_2 flux (Fransson et al., 2017; Nicholson et al., 2022).

5.3.4 The role of biogeochemical processes

At the end of August and beginning of September 2020, salinity normalised DIC (nDIC) and TA (nTA) show enhanced values between 15 m (the bottom of the mixed layer (Kawaguchi et al., 2022)) and 30 m depth (Fig. 5.21b and 5.21d). The timing of the change in these properties coincides with the onset of freeze-up (1 September) and drift back into surface waters with somewhat lower salinity. The ship and floe likely drifted into waters where nDIC and nTA below the mixed layer were enhanced. The stratification in the top 20 m may have isolated biogeochemical processes below the mixed layer from the mixed layer until wind-induced turbulence could break the buoyancy boundaries.

Datapoints with enhanced nTA and nDIC coincide with enhanced nutrient content (Fig. C.4) and net respiration, as indicated by preliminary biological oxygen supersaturation results based on discrete O2:Ar data (E. Chamberlain, personal communication). The combination of these findings suggest that respiration is the dominant process at the bottom of the mixed layer during most of the Leg 5 drift. However, net respiration would imply a slight decrease in nTA and therefore does not explain the nTA

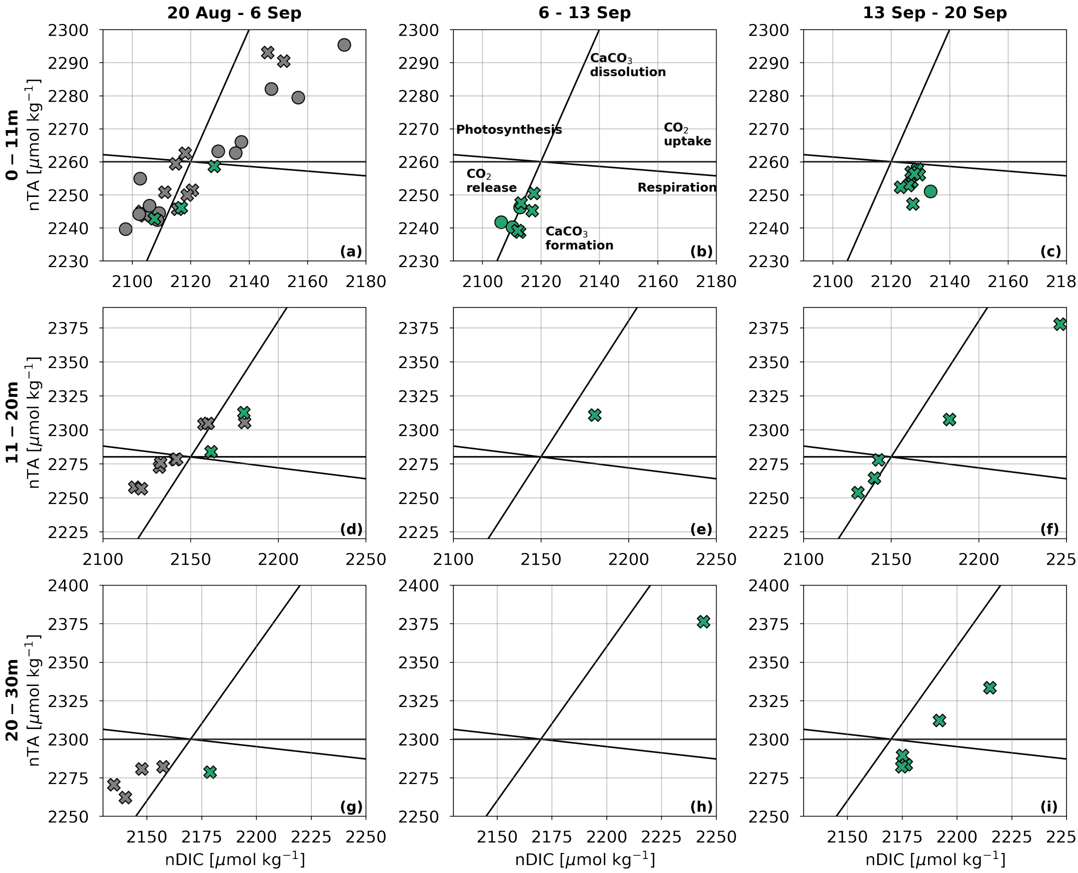

Figure 5.24: nTA plotted against nDIC for discrete samples collected from the underway system (circles) and CTD casts (crosses) for depths between 0-11 m (top row), 11-20 m (middle row), and 20-30 m (bottom row), for time between 20 August - 6 September (left column), 6-13 September (middle column), and 13-20 September (right column). Datapoints before 1 September have been plotted in grey, as the ice floe was drifting in surface waters with different properties than the surface waters later in September. Datapoints after 1 September are plotted in teal. Theoretical lines for the relative effect on net $CaCO_3$ dissolution/precipitation, CO_2 uptake/release, and photosynthesis/respiration are plotted in all panels (Zeebe and Wolf-Gladrow, 2001) and are annotated in (b). Axes are scaled differently per row.

enhancement. To investigate whether biogeochemical processes can explain the nTA and nDIC results, nTA and nDIC are plotted against each other for different depths ranges, namely, < 11 m, between 11 and 20 m, and between 20 and 30 m (Fig. 5.24). Datapoints are also separated according to the occurrence of the two storm events: before 6 September, between 6 and 13 September, and after 13 September. Theoretical lines are added to the figures as guidance to the relative direction of change over time if photosynthesis/respiration, $CaCO_3$ dissolution/formation, or CO_2 release/uptake were dominant processes (Zeebe and Wolf-Gladrow, 2001). In the top 11 m, nTA and nDIC contents are clustered together after the 6 September storm when mixing occurred within the mixed layer, but unlikely with water below the MLD. After the storm on 13 September, nTA and nDIC content in the top 11 m increase along the theoretical $CaCO_3$ dissolution line. Data below 11 m are scarce, but also seem to change along the

$CaCO_3$ dissolution line. The possible interpretation is as follows:

1. The onset of freezing at the beginning of September led to ikaite rejection from newly formed ice as also observed by Fransson et al. (2017) and Geilfus et al. (2016), which dissolved in the mixed layer and locally increased nTA (Geilfus et al., 2016) at the bottom of the mixed layer and to a lesser extent in the top 11 m.

2. Locally enhanced nDIC and nTA were mixed up to the surface during the storm on 13 September, which increased the nDIC and nTA at the surface, but caused a decrease at the bottom of - and below - the mixed layer.

3. Freezing resumed after the 13 September storm, rejecting ikaite to the surface water where it could dissolve, and thereby increasing nDIC and nTA again. Additionally, the storm brought in warm air, which briefly warmed the sea ice (Nicolaus et al., 2022; Shupe et al., 2022). Warmer temperatures may have increased the permeability of the ice and brine rejection (Cox and Weeks, 1982) and added more ikaite to the surface water.

As ikaite dissolution has been observed to occur directly underneath the sea ice (Fransson et al., 2017; Geilfus et al., 2016), it is unclear why the highest peaks in nDIC and nTA occurred deeper in the mixed layer during Leg 5, instead of nearer the ice-ocean interface. While the theoretical process lines in the nTA vs. nDIC plots of Fig. 5.24 can be useful to identify possible dominant biogeochemical processes, they cannot separate the relative influence of multiple simultaneous processes on the net outcome. For example, based on this approach there is no clear way to determine whether the increase in nTA and nDIC at depths shallower than 11 m is due to net $CaCO_3$ dissolution, net CO_2 uptake, net respiration, or a combination of processes. Whatever the cause of the enhanced nTA and nDIC below 11 m, the storm enhanced the connectivity between the surface and the subsurface layers, and thereby also allowed subsurface processes to affect the surface water.

5.4 Conclusion

Although marine CO_2-relevant processes associated to sea ice have been identified, we lack a sufficient mechanistic understanding of how sea ice changes the carbon sink of the Arctic Ocean on a seasonal time scale. The onset of freeze-up is a rapid transition in the year from an ocean that is melting to one that is freezing, characterised by shifts in physical and biogeochemical properties of the marine surface layer which exchanges carbon with the sea ice and atmosphere. Using data from the MOSAiC expedition, this study looked at the drivers of variability in the marine carbonate system prior, during, and after the onset of freeze-up in Central Arctic Ocean.

It first assessed the discrepancies between measured and calculated fCO_2 values depending on which formulation for the carbonic acid dissociation constants (K_1^* and K_2^*) is used. For the salinity and temperature values measured during Leg 5 of MOSAiC, all formulations for the different K_1^* and K_2^* required extrapolation beyond the salinity and temperature ranges within which they apply. Although the formulation by Millero et al. (2002) led to the lowest mean discrepancy, the formulation by Sulpis et al. (2020) led to better results for some parts of the track where the properties of the seawater were saltier and colder. This analysis showed that notable differences in fCO_2 results exist between various K_1^* and K_2^* formulations for low salinities and temperatures encountered in Arctic surface water. It also highlighted the need for consistent application of K_1^* and K_2^* formulations for studies in sea ice-covered regions. The latter is especially important to enhance comparability among MOSAiC studies on Arctic Ocean carbon cycling, and to improve carbon budget estimates.

Changes observed in the marine carbonate system during Leg 5 of MOSAiC (12 August - 12 October 2020) were due to a combination of spatial and temporal change during the drift. Comparisons to transects before and after the drift show that most of the observed fCO_2 increase was due to drift of the ice floe and ship into lower salinity surface waters with higher fCO_2 and different DIC and TA content. However, some of the increase was time-dependent, likely driven by CO_2 uptake before the onset of freeze-up. Two storms caused small scale variability in the surface mixed layer. The first storm caused temporary freshening in the upper 15 m, as it eroded and mixed the meltwater lens and there was unsubstantial mixing from the subsurface. The second storm caused mixing with the subsurface, where nDIC and nTA were biogeochemically enhanced and mixed into the surface layer, increasing DIC, TA, and fCO_2.

In a race against time while sea ice extent is diminishing, we need interdisciplinary collaboration to efficiently constrain important ocean-climate feedback processes, such as the Arctic Ocean CO_2 sink. Given the wealth of data acquired during MOSAiC, linkages between datasets have the potential to greatly improve our understanding of these mechanisms.

CHAPTER 6

Synthesis

Contents

6.1 Overview

The work of this PhD thesis covers different parts of polar regions (in the Southern Ocean and Arctic Ocean), systems (polynya, coastline, and open ocean), and sea ice regimes (seasonal and perennial), using different approaches (Eulerian or Lagrangian) to study the role of sea ice in the carbonate chemistry of the surface ocean (Table 6.1). The overarching theme that links the three research projects in this thesis together is the variability of the marine carbonate system in the surface ocean on different time scales.

Table 6.1: Overview of variety in regions, temporal time-scales, and approaches covered in this PhD research.

Chapter	Location	Temporal variability	Sea ice regime	Approach
Chapter 3	Weddell Sea coastal polynya	Semi-diurnal	Seasonal	Eulerian
Chapter 4	West Antarctic Peninsula coast	Seasonal and interannual	Seasonal	Eulerian
Chapter 5	Central Arctic Ocean	Seasonal and storm events	Perennial	Lagrangian

In Chapter 3, I discussed how tidal currents caused strong semi-diurnal variability in the carbonate chemistry of a coastal polynya in the south-eastern Weddell Sea during two case studies. The tides caused oscillation in vertical stratification by transporting water masses with diverging physical and biogeochemical properties across the sampling site. Surface water freshened by sea ice meltwater with low DIC and TA content was advected towards the south-west. Cold, sub-ice shelf water with higher DIC and TA content was observed at the bottom of the polynya during ebbing tide when water moved towards the north-east. The semi-diurnal variability in marine physico-chemical properties was very different between both case studies in different years, but showed that the resulting oscillation in fCO_2 can be high enough to bias CO_2 flux estimates if the timing of tides is not taken into account. Variability on such short time scales could be relevant for sampling efforts along other parts of the Antarctic coastline, such as the Rothera Time Series in Ryder Bay, at the WAP (Chapter 4). Ryder Bay is surrounded by glaciers with substantial glacial and sea ice meltwater input and is also subject to tides. Variability observed in summertime DIC and TA content in the time series is likely partly attributable to tidal currents.

For Chapter 4, I extended the Rothera Time Series for DIC and TA from 2014 to 2020 and used it to look into the drivers of interannual variability of the marine carbonate system. I studied how years differed from one another, as well as how seasons differed between years. A large part of Chapter 4 is dedicated to the wintertime data, as observations in this time of the year are scarce in polar regions. The time series showed that the mean wintertime fCO_2 depends on sea ice cover duration within the bay, as well as the input of glacial and sea ice meltwater from the previous melting season and how this meltwater is distributed throughout the water column. Sea ice cover has a stabilising effect on the water column by protecting it from wind-induced mixing (Venables and Meredith, 2014), but the timing of onset of freeze-up and melt is just as important. Early sea ice cover can restrict atmospheric CO_2 uptake and late melt can restrict CO_2 outgassing.

In Chapter 5, I had a closer look at the processes that occur at the onset of annual freeze-up while drifting along with an ice floe, but this time in the perennially sea ice-covered Central Arctic Ocean. Storm-induced mixing events caused a number of step-wise changes in the surface ocean carbonate system, affecting its transition into winter, such as first mixing the meltwater lens layer into the mixed layer and later entraining subsurface water into the mixed layer, thereby increasing surface water fCO_2. This work showed that events on short time scales from hours to days can have important impacts on the system during rapid seasonal transitions. While a Eulerian (stationary) sampling approach was used for the previous chapters, the observations for the Arctic Ocean were collected in a Lagrangian manner with reference to the flow of sea ice across the ocean. This approach was inherent to the design of the MOSAiC expedition, which had the higher-level objective to follow the life cycle of an ice floe. However, from an oceanographic perspective, the study would have benefited from stationary observations over time to be able to disentangle spatial from temporal changes in the data. This was partially overcome in Chapter 5 by using underway measurements during transit as transects to determine which changes occurred since the start of the drift.

Although *temporal variability* is the theme of this PhD research, in truth it is retrospective. With the exception of the RaTS work on interannual variability in the surface ocean carbonate chemistry, all results that I have presented are the product of unexpected and unforeseen opportunities that appeared since I started the PhD. The work on tidal influences on a coastal polynya only came about because our chief scientist during PS117 decided to make good use of a delay we experienced getting to Neumayer III Station by doing repeat casts in a coastal polynya. I collected samples in case they led to interesting findings, but gave them the lowest priority during laboratory analysis. The study became interesting for publication after approaching new collaborators about combining the data with a previous tidal study done in the same location some years earlier. Moreover, the original scope of my research was limited to the Southern Ocean. I changed "Southern Ocean" to "polar oceans" in my thesis title to be able to incorporate work in the Arctic as a result of being able to participate in the MOSAiC expedition. Besides the "core time series" of MOSAiC, which included weekly CTD casts, all sampling activities in the water column and on the sea ice were opportunistic and depended on resources available on board, weather conditions, and capacity of team members to complete the work.

6.2 Outlook

The ultimate value of understanding the role of sea ice in the marine carbonate system and polar ocean CO_2 flux is to improve modelling predictions of how changing global climate will affect marine biogeochemistry and climate-feedbacks. On large spatial and temporal scales, global ocean biogeochemical models (GOBMs) are able to produce satisfactory simulations of mean sea-air CO_2 fluxes (Hauck et al., 2020). Especially model ensembles produce low discrepancies to observation-based data products, as differences in the strength of the ocean overturning circulation among individual models are balanced out. However, on smaller spatial or temporal time scales, GOBMs struggle to estimate sea-air CO_2 fluxes relative to observations (Hauck et al., 2020). For example, observation-based CO_2 flux estimates show substantial multi-year to decadal variability in the Southern Ocean, with a decreasing trend in CO_2 uptake in the 1990s (Le Quéré et al., 2007) and a reinvigoration of the CO_2 sink after 2000 (Gregor et al., 2018; Landschützer et al., 2015; Munro et al., 2015). Suggestions for drivers of this multi-year variability in the Southern Ocean include variability in the SAM (Lenton and Matear, 2007; Lovenduski et al., 2007), ENSO (Landschützer et al., 2015), external forcing by volcanic eruptions (McKinley et al., 2020), and variability in marine biology and circulation (DeVries, 2022). Most biogeochemical models are unable to simulate the varying strength of the Southern Ocean CO_2 uptake over the length of a decade or less and its sensitivity to climate variability (Lenton et al., 2013). The fact that ocean models also struggle to reproduce seasonal variability of the Southern Ocean CO_2 flux (which is its dominant mode of variability (Gruber et al., 2019)) suggests that driving mechanisms are not sufficiently represented in ocean models (Gruber et al., 2019; Hauck et al., 2020). Process-based studies on small spatial and temporal scales are key to identifying these driving mechanisms (Swart et al., 2019).

Although the Arctic Ocean is included in some observation-based data products of ocean fCO_2 and CO_2 uptake (Landschützer et al., 2020; Rödenbeck et al., 2022), it is excluded in many others (e.g., see Rödenbeck et al., 2015), due to a lack of surface ocean fCO_2 data. As the Arctic Ocean is often not explicitly included in models, model-to-observation comparisons of global CO_2 flux estimates require gap filling techniques (e.g., Hauck et al., 2020). The seasonal and multi-year variability of the Arctic Ocean CO_2 sink has therefore not been evaluated to the same extent as the Southern Ocean (although see Schuster et al., 2013).

Given the paucity of *in situ* observations of ocean biogeochemistry in sea ice-covered regions, it is worth wondering how data acquired for the sea ice-covered Southern Ocean can help our understanding of changes in the Arctic Ocean, and vice versa. However, applying findings from one polar ocean to the other may not be straightforward, because the Southern Ocean and Arctic Ocean have very different oceanographic and cryospheric characters (see Section 2.6.1 and 2.6.2). For instance, a strong permanent halocline in the Arctic Ocean limits subsurface heat and nutrient input into the surface mixed layer, whereas the Southern Ocean has a much weaker stratification, allowing for more heat and nutrient input from deep waters. This deep water heat input restricts thick sea ice growth, which is why Southern Ocean sea ice is much thinner than Arctic sea ice, the latter being protected from bottom melting by the halocline. Antarctic sea ice is also thinner than Arctic sea ice because it occurs at lower latitudes (60-75°S compared to 70-90°N; Stammerjohn and Maksym, 2017).

The weaker stratification and higher nutrient content of the Southern Ocean also leads to a higher mean alkalinity than in the Arctic Ocean, resulting in a higher buffering capacity against decreasing pH due to CO_2 uptake (Shadwick et al., 2013). Despite its higher pH buffering capacity, regional pH observations in the Southern Ocean have been shown to have a higher seasonal amplitude than regional observations in the Arctic Ocean (Shadwick et al., 2013). This can be driven by low seasonal warming in some parts of the Southern Ocean, which enhances CO_2 solubility in the summertime relative to parts of the Arctic Ocean with the high seasonal warming. In case of the latter, summertime biological CO_2 uptake can thus be compromised by warmer surface seawater temperatures affecting CO_2 solubility (Shadwick et al., 2013). Such intercomparisons of observations from both polar oceans expose the complexity of the timing and interactions between physical and biogeochemical processes.

The seasonality of many marine biogeochemical variables is also affected by the different seasonality in the growth, melt, and extent of Arctic and Antarctic sea ice (Parkinson, 2014). Therefore, even if ocean circulation does not change in the future, the Southern and Arctic Ocean CO_2 uptake will respond differently to climate change. Nevertheless, there is a lot that scientists can learn from comparing Arctic and Antarctic studies to each other. For instance, Martinson and Steele (2001) have framed the Southern Ocean as an analogue to the possible future of the Arctic Ocean in terms of heat exchange with subsurface water and its effect on sea ice. A weaker shallow halocline in the Arctic Ocean as a result of lower sea ice extent increases the potential of warm Atlantic water to reach the surface during winter (Carmack et al., 2015; Polyakov et al., 2020), which - similarly to the Southern Ocean - would lead to thinner winter sea ice and potentially to an earlier sea ice retreat, thereby affecting the duration of a seasonally ice-free ocean. Extending this analogue to carbon, weaker stratification in the Arctic Ocean would also enhance entrainment of subsurface DIC, including CO_2, into the mixed layer, potentially creating a supply of CO_2 that can be released to the atmosphere through cracks and leads appearing in the thinned sea ice cover. The Arctic and Southern Ocean systems do not necessarily have to be comparable to gain insights from each other into the CO_2 uptake within each respective ocean. A well-studied, relatively constrained system, such as Ryder Bay, can be used as a reference for seasonality and succession of dominant drivers of the marine carbonate system. Long-term monitoring can reveal contrasts that can be just as insightful as similarities.

Maintenance of long-term monitoring programs, sustained funding for data synthesis, and expansion of spatial data coverage in sea ice-covered regions continue to be essential for polar science (Swart et al., 2019). Autonomous vehicles that are able to collect year-round data from remote parts of the ocean, such as Argo floats and saildrones, create immense opportunities to augment understanding of the marine carbon cycle in polar regions (e.g., Gray et al., 2018; Sutton et al., 2021). For example, the Southern Ocean Carbon and Climate (SOCCOM) program has been deploying biogeochemical floats in the Southern Ocean since 2014, and many of those deployed in the seasonal sea ice zone have collected pH data throughout the sea ice-covered winter (Bushinsky et al., 2019; Gray et al., 2018). These data could be used to study the interannual variability of fCO_2 in seasonally sea ice-covered open ocean regions or the entire Southern Ocean, including in the wintertime. While a comparison to a coastal time series, such as the RaTS, would be limited due to gradients in marine carbonate chemistry between shelf and open ocean regions, it can inform interpretations of processes that are relevant on a larger scale.

Our understanding of the role of sea ice in sea-air CO_2 flux needs advances from various angles. The autonomous vehicle community is improving pH sensor accuracy, and ideally needs to find a way to reduce uncertainties in their fCO_2 estimates, which are partly based on empirical relationships (Williams et al., 2016; Williams et al., 2017). An accurate fCO_2 sensor that can cope with high pressure at depth would be an additional major step forward. The modelling community is identifying discrepancies between model simulations and observation-based estimates of ocean CO_2 sinks, informing us of gaps in our knowledge and where there are still large uncertainties in our understanding (Hauck et al., 2020). In the meantime, the community working on seawater analyses of carbonate chemistry have plenty to get on with as well. Based on challenges that I repeatedly encountered during my own research and their impacts on my estimations for CO_2 flux in the Southern and Arctic Ocean, I have formulated three research topics for which I am excited to see progress in the near future (in no particular order):

Repeatedly-encountered scientific challenges

1. Resolving the **inconsistency among formulations of carbonic acid dissociation constants** for salinity and temperature conditions in polar surface waters, and move towards **consistent usage** among the polar research community.
2. Understanding the importance of **vertical gradients in carbonate system components** and variables that affect fCO_2, such as temperature, in the upper 15 m of the surface ocean.
3. Gaining a process-based understanding of **seasonal ocean-ice and ice-air CO_2 fluxes**, including for different sea ice types.

In Chapter 4, I showed that the net cumulative CO_2 uptake in Ryder Bay between 2011 and 2019 can differ by about 54 % depending on the choice of formulation for the carbonic acid dissociation constants used in deriving fCO_2 from DIC and TA. In Chapter 5, I explored a wider range of formulations that are derived for temperature and salinities similar to conditions in polar surface waters. I compared results to direct underway fCO_2 measurements. Discrepancies between calculated and measured values were lower for some formulations than others, but the best fit differed depending on the temperature and salinity of the seawater. Given the differences in TA and salinity, future work needs to explore whether there are differences in fCO_2 discrepancies between the Arctic Ocean and Southern Ocean. Currently, the formulation by Lueker et al. (2000) is recommended as best practice, especially for global ocean estimates (Dickson et al., 2007). However, application of the formulation by Lueker et al. (2000) to the conditions of polar surface oceans requires extrapolation beyond the salinity and temperature ranges for which the formulation is designed. No formulation for the carbonic acid dissociation constants currently exists that applies to the full range of salinity *and* temperature values recorded in the datasets that I analysed. Formulations that include low salinity and low temperature values (i.e. fresh and cold conditions common in sea ice-covered oceans) differ in their outcome to an extent that could be significant for carbon budgets. Moreover, within the polar science community, the choice of formulation is inconsistent. Having reached out among scientists working within marine carbonate chemistry in polar regions, I have noticed that there is an interest to address this topic. Sulpis et al. (2020) derived a formulation that applies to seawater temperature down to -1.67 °C and salinity down to 31.73 based on field data of DIC, TA, pH, fCO_2, temperature, and salinity, i.e. Global Ocean Data Analysis Project (GLODAP) and SOCAT, collected within 20 minutes of each other. However, the number of data points included for the Arctic and Southern Ocean were limited. I would like to see one or both of the following developments in the polar community:

- Reaching a consensus within the polar marine carbonate chemistry community on which formulation to use for the carbonic acid dissociation constants in studies specifically on sea ice-covered oceans (including seasonal sea ice).
- Developing a new parameterisation for the carbonic acid dissociation constants for a temperature and salinity range that includes the full range of temperature and salinity observed in sea ice-covered regions throughout the year, based on a combination of field data (e.g. using a similar approach to Sulpis et al. (2020)) and laboratory experiments using real sea water.

Even though these developments will improve global sea-air CO_2 flux estimates, they are perhaps not the source of highest uncertainty for the polar oceans. For instance, in recent years, errors in sea-air CO_2 flux estimates as a result of gradients in seawater properties in the upper meters of the ocean have received increasing attention (Miller et al., 2019; Watson et al., 2020; Woolf et al., 2016). It is common practice to collect samples and measurements between 5-15 m depth, often with the assumption that the carbonate system at those depths is representative for the surface. This is naturally not the case if a vertical gradient exists in the upper 10-20 m. On a global level, temperature corrections within the upper meters of the ocean (Dong et al., 2022) and corrections for the cool skin effect within the upper 1 mm have suggested significant adjustments to global CO_2 fluxes (Dong et al., 2022; Watson et al., 2020; Woolf et al., 2016). Estimates accounting for thermal gradients generally indicate higher ocean CO_2 uptake as the cooler skin temperature increases CO_2 solubility. A different salinity in the skin layer affects CO_2 flux as well, but is considered to have a much weaker effect than thermal gradients (Woolf et al., 2016). However, in regions with significant freshwater input, such as the Arctic Ocean in the melting season, salinity gradients in the upper surface layer can be substantial. This has two implications for CO_2 flux estimates in polar regions: 1) Like temperature, salinity affects the partitioning of the carbonate system (Woolf et al., 2016), 2) Freshwater input at the surface causes strong stratification, as density is driven by salinity in cold seawater. Stratification affects the vertical transport of DIC and TA, which means that fCO_2 at the depth of sampling could be different than in the molecular boundary layer (top 100 μm), where diffusion-controlled CO_2 exchange with the atmosphere occurs. In the Arctic, the shallow stratification could lead to an underestimation of CO_2 uptake up to 17 % (Dong et al., 2021). During the MOSAiC expedition, we observed a strong meltwater lens with a depth ranging from 0.2 to 2 m underneath the sea ice and in leads between ice floes. This ephemeral phenomenon and associated effects on fCO_2 and CO_2 flux estimates could be important at the onset of melt in the Southern Ocean, along Antarctic coastlines, or perennially sea ice covered regions, in addition to implications of gradients below this meltwater lens. From anecdotes, I have learnt that a meltwater lens has also been observed in Ryder Bay at the beginning of spring (e.g., in 2016/2017). Being too shallow to be fully recorded in CTD casts, corrections cannot yet reliably be made for the carbonate chemistry time series. Moving forward, sampling activities for the RaTS will add more frequent seawater sampling for DIC, TA, and nutrients within the top 2 m of the ocean (collected with small boat and Niskin bottle) so that future studies can compare flux estimates to those determined from data at the standard 15 m depth.

Direct sea-air CO_2 flux measurements, e.g. eddy covariance, are valuable to determine the accuracy of flux estimates and associated gradient corrections based on bulk seawater measurements of fCO_2 or fCO_2 derived from other carbonate system components (e.g., Dong et al., 2021). Moreover, direct gas flux measurements will play an important role in developing an understanding of how processes within sea ice modulate the sea-air flux (i.e. third point in the box above), because they give estimates on the *total* gas flux, i.e. the sea-air flux *plus* the ice-air flux. In this work, the presence of sea ice was accounted for in CO_2 flux estimates by scaling the gas transfer velocity with the fraction of open water. Using this simple method for gas flux estimates, as well as more sophisticated methods that consider shear and convection (Loose et al., 2014), we are only accounting for the direct flux between the ocean and the atmosphere where there is open water. In other words, we are not incorporating the CO_2 flux between the sea ice and the atmosphere in our total CO_2 flux estimate. At 100 % sea ice cover, we keep the contribution of the gas transfer velocity at 1 % (instead of reducing it to 0 %) of its original value calculated for open ocean conditions, with the intention to simulate sea-ice-air gas fluxes that occur in winter (see Section 4.2). However, this implicitly assumes that the ice-air flux depends on the fCO_2 of the underlying seawater, which in reality it does not and instead depends on the fCO_2 in the brine and the porosity of the sea ice. Combining direct CO_2 flux measurements above sea ice and fCO_2 measurements in under-ice seawater at different stages of sea ice growth will lead to better constraints on the direct role of sea ice in the CO_2 flux in polar regions.

Datasets generated by the MOSAiC community provide opportunities to explore solutions to the above challenges, some of which are already under way. For example, concurrent measurements of seawater fCO_2 and CO_2 flux can constrain sea-ice-air fluxes. Additional vertical profiles of DIC and TA content in ice cores and in the seawater below can further explain the carbonate chemistry driving changes in inorganic carbon fluxes, as well as upper ocean gradients. Findings can feed into refined conceptual models that can be applied to Antarctic sea ice, as well, stimulating dialogue between the polar regions.

6.3 Concluding remarks

During my expeditions at sea, I have stood mesmerised by the view of the ocean and the sea ice. My mind would initially be racing with scientific curiosity, but inspired by the epic scenery, it always seemed to eventually wander towards more reflective thoughts. I would like to conclude my PhD research with these.

The most challenging moments have been those when uncertainties seemed too high to be able to complete my scientific endeavours. In these moments, it helped me to be reminded that the irony in this is that the scientific method is rooted in the belief that all we have is uncertainty, that we have the ability to reduce uncertainty, and that we cannot reach complete certainty. To be able to embrace uncertainty creates resilience and freedom, and makes science a much more enjoyable (and productive) experience. And as in science, as in life.

After having completed my PhD research, I continue to see the ocean as a big blue mystery, and the sea ice as an enigma. The only difference is that, now, I have many more questions than I did before. I may never *truly* know the answers to these, but I have learnt ways to try to reduce the uncertainty about why this icy world is so fascinating to me.

APPENDIX A

Appendix to Chapter 3

I Sentinel images of Ekström polynya

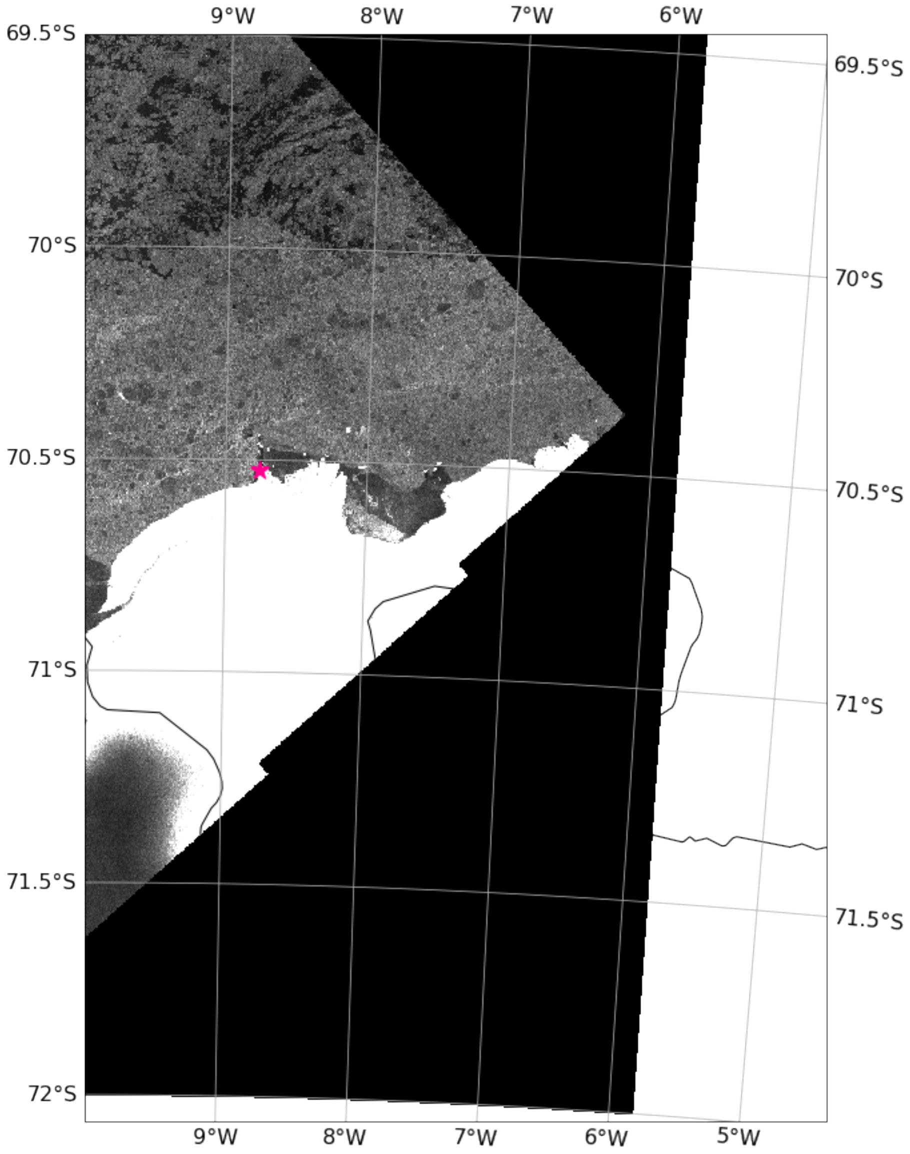

Figure A.1: Sentinel-1 SAR image of the Ekström Ice Shelf and polynya on 12.01.2015 (PS89) (ESA, 2021). The pink star indicates the sampling location for the PS89 tidal observation.

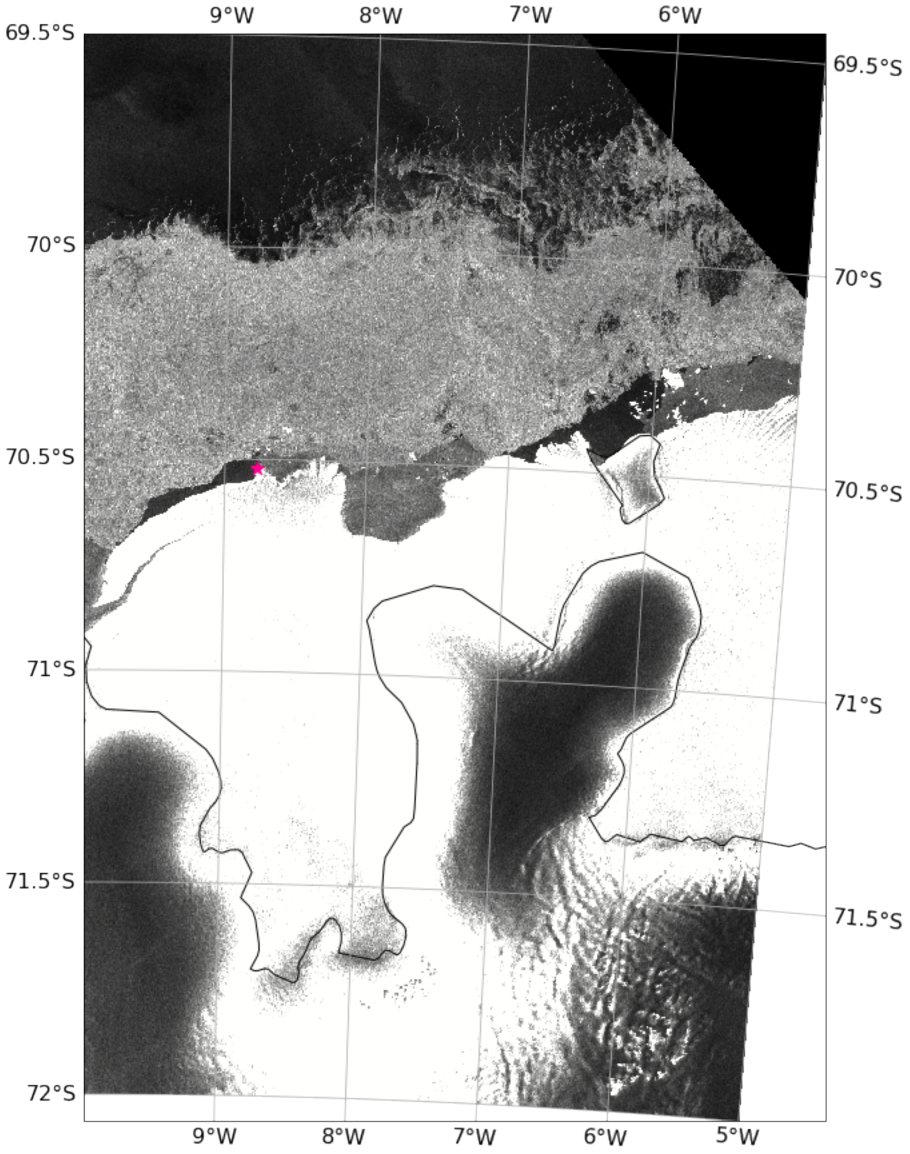

Figure A.2: Sentinel-1 SAR image of the Ekström Ice Shelf and polynya on 10.01.2019 (PS117) (ESA, 2021). The pink star indicates the sampling location for the PS117 tidal observation.

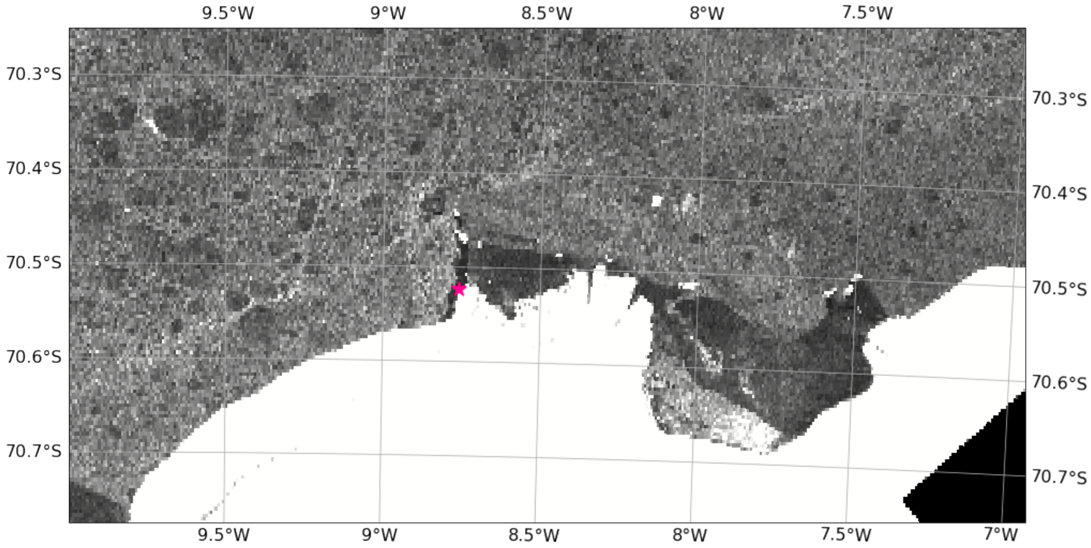

Figure A.3: Sentinel-1 SAR image of the Ekström Ice Shelf and polynya on 12.01.2015 (PS89), zoomed in (ESA, 2021). The pink star indicates the sampling location for the PS89 tidal observation.

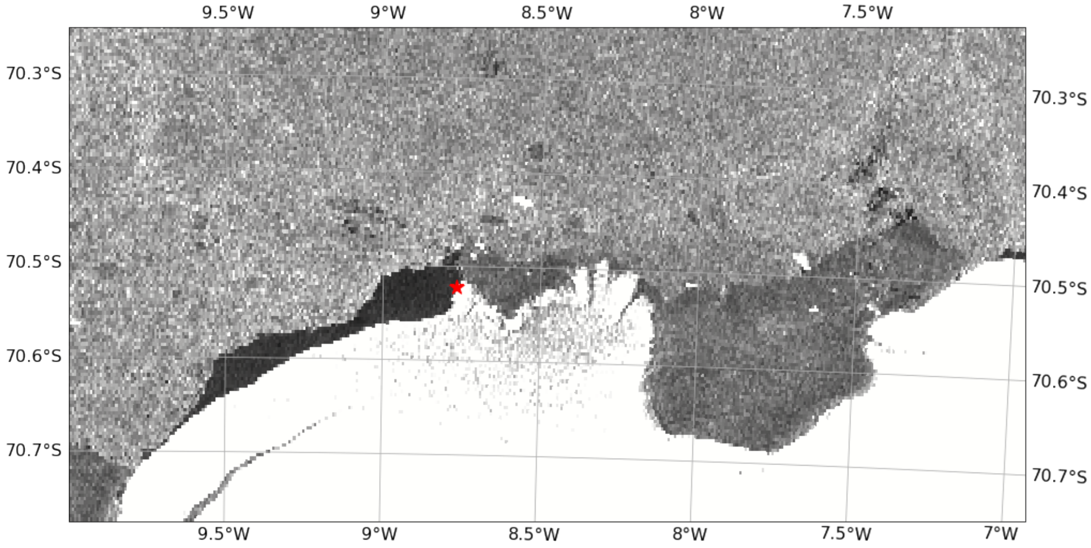

Figure A.4: Sentinel-1 SAR image of the Ekström Ice Shelf and polynya on 10.01.2019 (PS117), zoomed in (ESA, 2021). The pink star indicates the sampling location for the PS117 tidal observation.

II Data references

Table A.1: References to all supporting data and data sources used in this work.

Data type	**Data source**	**Reference**
PS89 and PS117 DIC/TA data	Pangaea	(González-Dávila et al., 2022)
PS89 physical oceanographic data AWI CTD (continuous)	Pangaea	(Rohardt and Boebel, 2015a)
PS117 physical oceanographic data AWI CTD (continuous)	Pangaea	(Rohardt and Boebel, 2020)
PS89 CTD bottle data, incl. nutrient data (discrete)	Pangaea	(Rohardt and Boebel, 2015b)
PS117 CTD bottle data, incl. nutrient data (discrete)	Pangaea	(Rohardt et al., 2020)
PS89 ADCP	Pangaea	(Witte and Boebel, 2018)
PS117 ADCP	Pangaea	(Boebel and Tippenhauer, 2019)
PS89 wind speed	Pangaea	(König-Langlo, 2015)
PS117 wind speed	Pangaea	(Schmithüsen, 2020)
xCO$_2$ Syowa	ESRL NOAA	(Dlugokencky et al., 2019)
Antarctica boundaries	SCAR ADD	(Gerrish et al., 2020)
Ekström CTD data	Pangaea	(Smith et al., 2020b)
Sentinel 1 - SAR	European Space Agency	(ESA, 2021)
Southern Ocean Bathymetry	IBSCO Version 1.0, Pangaea	(Arndt et al., 2013)

III Sampling at study site

Table A.2: CTD sensor precisions.

Variable	Sensor or method	Expedition	Precision	Reference
Conductivity	SBE4c	PS89, manufacturer specification	0.003 mSc m^{-1} [a]	(Driemel et al., 2017)
Salinity	SBE4c	PS117	0.0004[b]	(Rohardt and Tippenhauer, 2020)
Temperature	SBE3plus	PS89, manufacturer specification	0.001 °C [a]	(Driemel et al., 2017)
Temperature	SBE3plus	PS117	0.00000 °C [a]	(Rohardt and Tippenhauer, 2020)
Pressure	Digiquartz with TC	PS89, manufacturer specification	0.015 % full scale	(Driemel et al., 2017)
Fluorescence	Wetlabs EcoFLR	PS89 and PS117	-	(Rohardt and Tippenhauer, 2020)
Dissolved O_2	SBE43	PS89	0.43[c] ml L^{-1}	(Boebel, 2015)
Dissolved O_2	SBE43	PS117	0.42[d] ml L^{-1}	(Rohardt and Tippenhauer, 2020)

[a] Average of the residual of post-calibration by Sea-Bird Scientific. [b] Standard deviation of the residual of the difference between the sensor measurements and the Optimare Precision Salinometer samples analysed on board. [c] Standard deviation of the difference in dissolved oxygen Winkler samples analysed on a potentiometric detection system and on a photometric end-point system on board. [d] Standard deviation of the residual of the difference between the sensor measurements and Winkler titration samples.

Table A.3: Analytical uncertainty of the DIC and TA analyses using the variability of the CRM measurements per CRM batch. n refers to the number of CRMs that were run to obtain the measured values. Values listed for CRMs are certified values by Prof. Andrew Dickson's laboratory at the Scripps Institution of Oceanography of the University of California, San Diego (https://www.ncei.noaa.gov/access/ocean-carbon-acidification-data-system/oceans/Dickson_CRM/batches.html, last access: 14 March 2022). Net coulometer counts were calibrated against the certified DIC values of the reference material, which was run before and after the sample runs per analysis day. This gave a value for counts per μmol, for each CRM run. These were averaged and used (along with density and volume) to obtain the concentration of DIC per sample in μmol kg^{-1}.

Dataset	CRM batch no.	n	DIC [μmol kg^{-1}]		TA [μmol kg^{-1}]	
			CRM	Measured	CRM	Measured
PS89	137	25	2031.90 ± 0.62	2031.90 ± 1.22	2231.59 ± 0.32	2231.71 ± 1.09
PS117	176	133	2024.22 ± 0.82	2024.22 ± 3.32	2226.38 ± 0.53	2226.30 ± 3.18
PS117	185	17	2029.88 ± 0.62	2029.88 ± 2.88	2220.67 ± 0.58	2221.09 ± 0.85

Table A.4: Analytical precisions for nutrient concentrations.

Dataset	NO_3^- [μmol kg^{-1}]	PO_4^{3-} [μmol kg^{-1}]	SiO_4 [μmol kg^{-1}]
PS89[a]	0.15	0.02	1.0
PS117[b]	0.041	0.008	0.057

[a] $\pm 1\ \sigma$ of replicate samples for PS89. [b] $\pm 1\ \sigma$ of repeat measurements of working standard at similar concentrations as average values for the tidal observation period of PS117: 30, 2, 60 μmol kg^{-1} for NO_3^-, PO_4^{3-}, and SiO_4, respectively.

IV Underway measurements

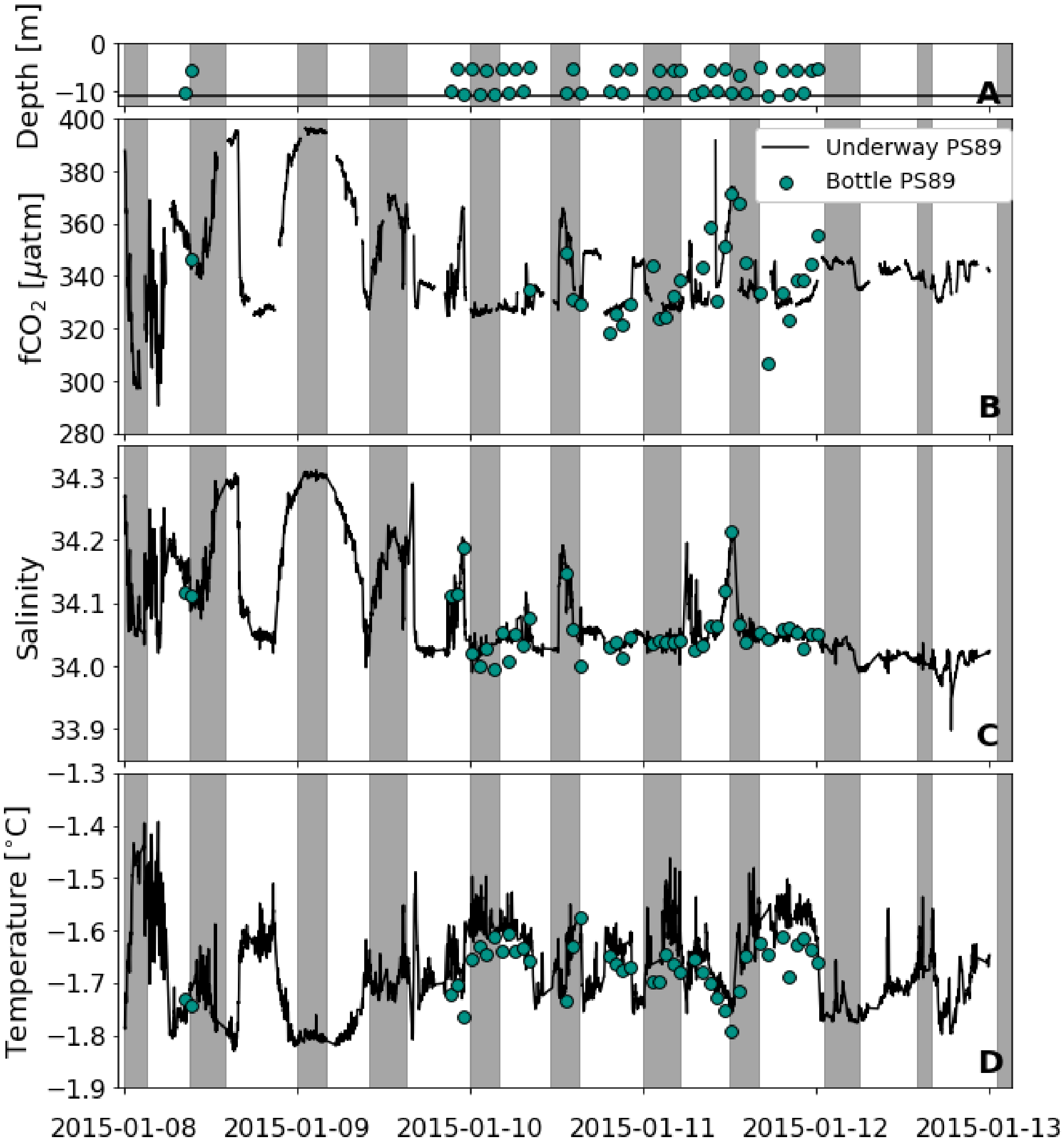

Figure A.5: A comparison of measurements between the continuous measurements from the on-board underway system and the discrete samples of the surface seawater for PS89. (a) Depth at which the surface discrete samples were collected during the tidal observation. The horizontal black line indicates depth at 11 m, which is the depth of the intake for the continuous $f\mathrm{CO}_2$ measurements. (b) The $f\mathrm{CO}_2$ continuous measurements from the on-board underway system (black line) and the calculated $f\mathrm{CO}_2$ from the discrete surface samples (circles). (c) Same as (b), but for salinity. (d) Same as (b), but for temperature. The grey areas indicate periods of ebbing tide (where the u and v components of the modelled tidal currents are both positive).

V Continuous profile vs. discrete bottle density measurements

To study the tidal cycle, profile measurements from the CTD casts are interpolated over time and depth. The high vertical resolution profile measurements for salinity and temperature are collected at a 1 dbar resolution on the down-cast, which is higher than the resolution of the discrete bottle samples and measurements that are collected on the up-cast. Difference in resolution and natural variability in the water column result in a slight difference between the high vertical resolution profile (down-cast) and discrete (low vertical resolution) bottle measurements (up-cast) at equal depth. To ensure that the bottle data with the lower vertical resolution is sufficiently representative, we compare the time and depth-interpolated bottle data to the high vertical profile measurements interpolated over time for the physical variables. As an example, we show the comparison for density (Fig. A.6). It shows that the resolution of the bottle data sufficiently captures the same features in the water column as seen in the high resolution profile data. The bottle measurements are therefore reliable for interpretation of the chemical variables. As the higher vertical resolution profile measurements capture more detail of the features in the water column, these are used for the time series interpolations wherever applicable.

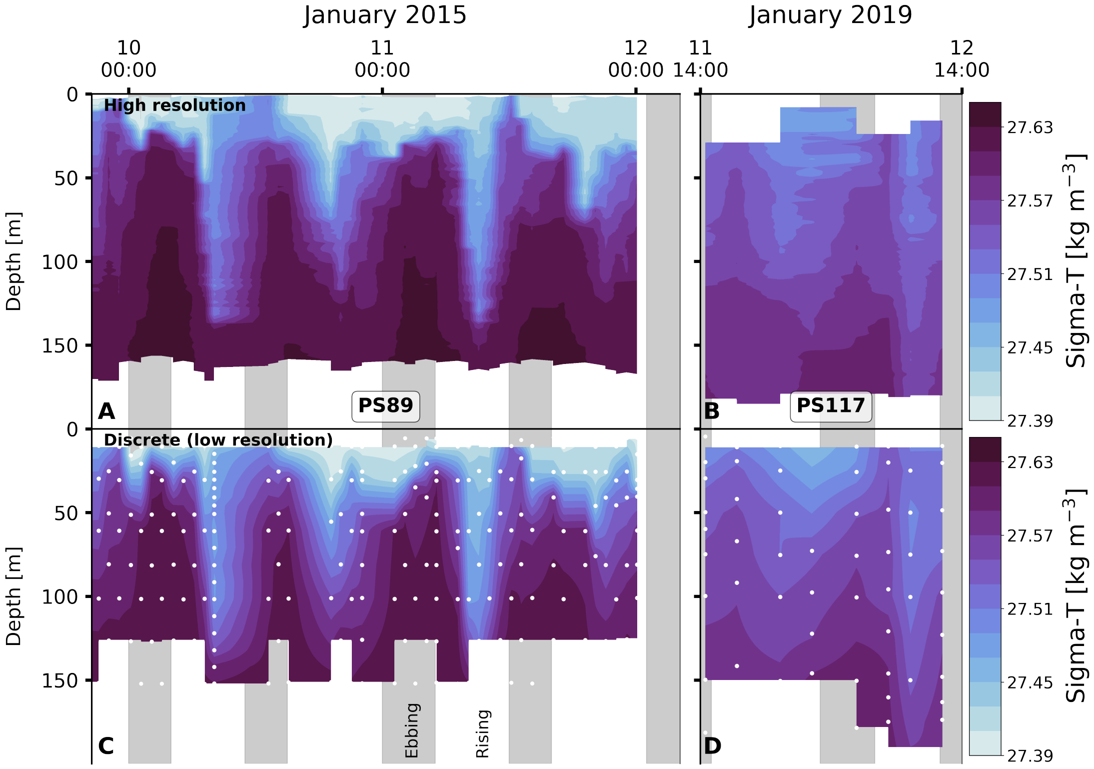

Figure A.6: (a) High vertical resolution profile of sigma-t for PS89. (b) High vertical resolution profile of sigma-t for PS117. (c) Discrete (low vertical resolution) profile measurements at bottle sampling depth for PS89. (d) Discrete (low vertical resolution) profile measurements at bottle sampling depth for PS117. Sampling depths are shown in white markers in C and D.

VI Currents

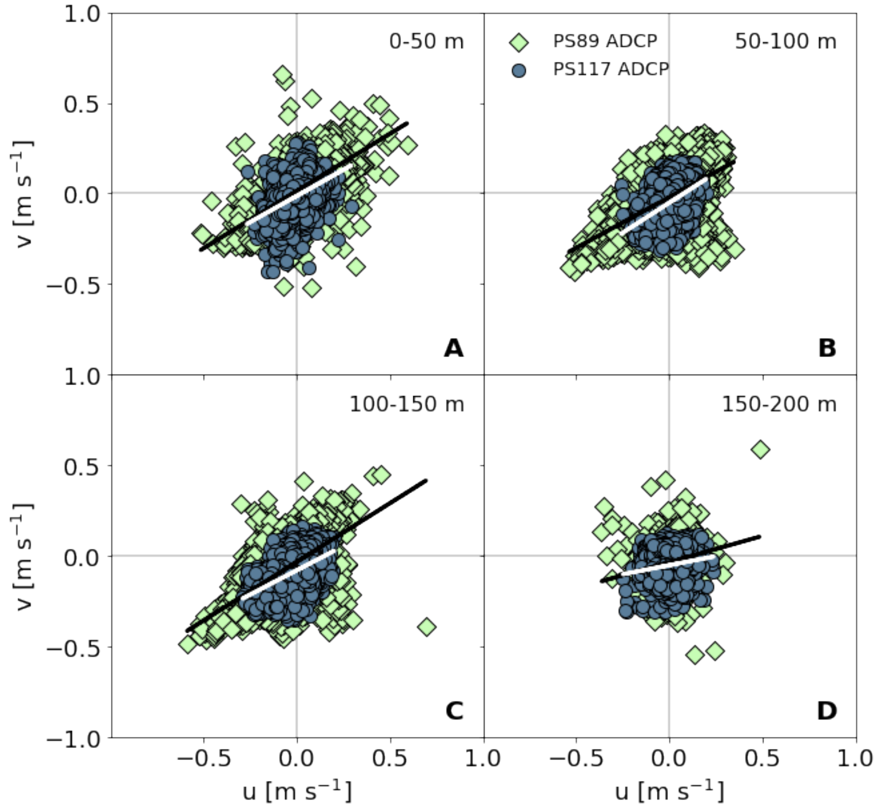

Figure A.7: Correlations of the u and v components of the ADCP data for the tidal observations during PS89 (green diamonds) and PS117 (blue circles) between 0 - 50 m ((a), 50 - 100 m (b), 100 - 150 m (c), and 150 - 200 m (d). All correlations are significant (p-value < 0.05) and positive, as shown with the black (PS89) and white (PS117) linear regression lines. (a) $v = 0.63 \times u + 0.014$ (PS89); $v = 0.58 \times u$ - 0.01 (PS117). (b) $v = 0.56 \times u$ - 0.02 (PS89); $v = 0.66 \times u$ - 0.05 (PS117). (c) $v = 0.65 \times u$ - 0.03 (PS89); $v = 0.54 \times u$ - 0.08 (PS117). (d) $v = 0.29 \times u$ - 0.034 (PS89); $v = 0.20 \times u$ - 0.05 (PS117).

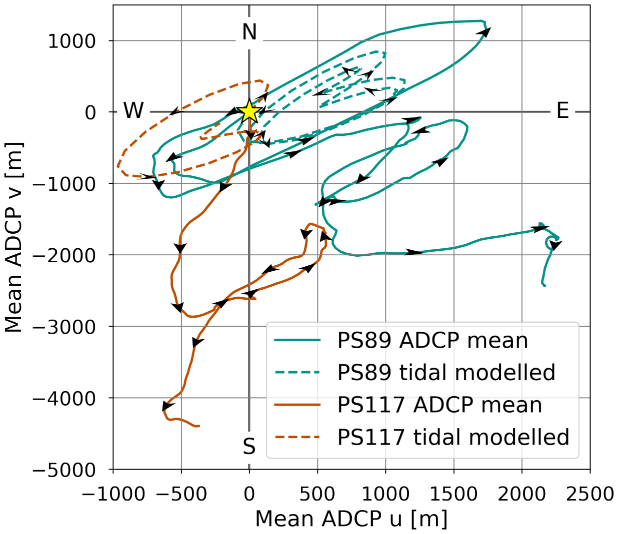

Figure A.8: The hypothetical distance that a water parcel could have travelled relative to a starting point at the ship's position (indicated by the yellow star) at the starting time of sampling during the PS89 (green) and PS117 (orange) tidal observations. Full lines show the distance travelled using the water column mean ADCP current data. Dashed values show the distance travelled using the modelled water column mean tidal current data. Black arrows indicate the direction of the currents. These calculations assume that the mean currents apply to the larger shelf and polynya region, disregards topographic influences, and ignores the presence of the ice shelf, which is located directly south of the sampling site.

VII Tidal variability

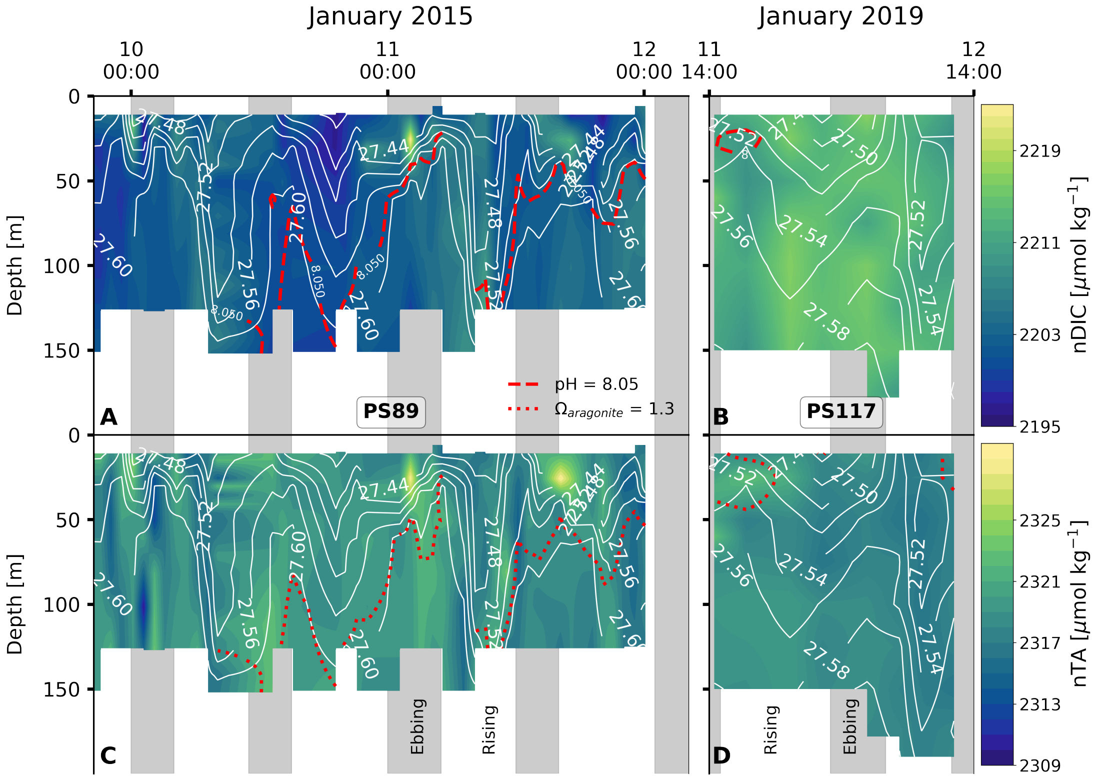

Figure A.9: Salinity-normalised DIC content at the sampling site during the PS89 (a) and PS117 (b) tidal observations, as well as salinity-normalised TA content for the PS89 (c) and PS117 (d) observations. White contour lines indicate sigma-t in kg m^{-3}. Vertical grey shaded areas indicate periods of ebbing tide, as defined in the text. Dashed red lines in A and B indicate the depth at which the pH = 8.05. Dotted red lines in C and D indicate the depth at which the calcite saturation state (Ω_{ca}) = 2.05. These are arbitrary values, used to illustrate the variability in the water column. pH ranged between 8.02-8.12 and 8.02-8.06 for PS89 and PS117, respectively. Ω_{ca} ranged between 1.95-2.43 and 1.92-2.13 for PS89 and PS117, respectively.

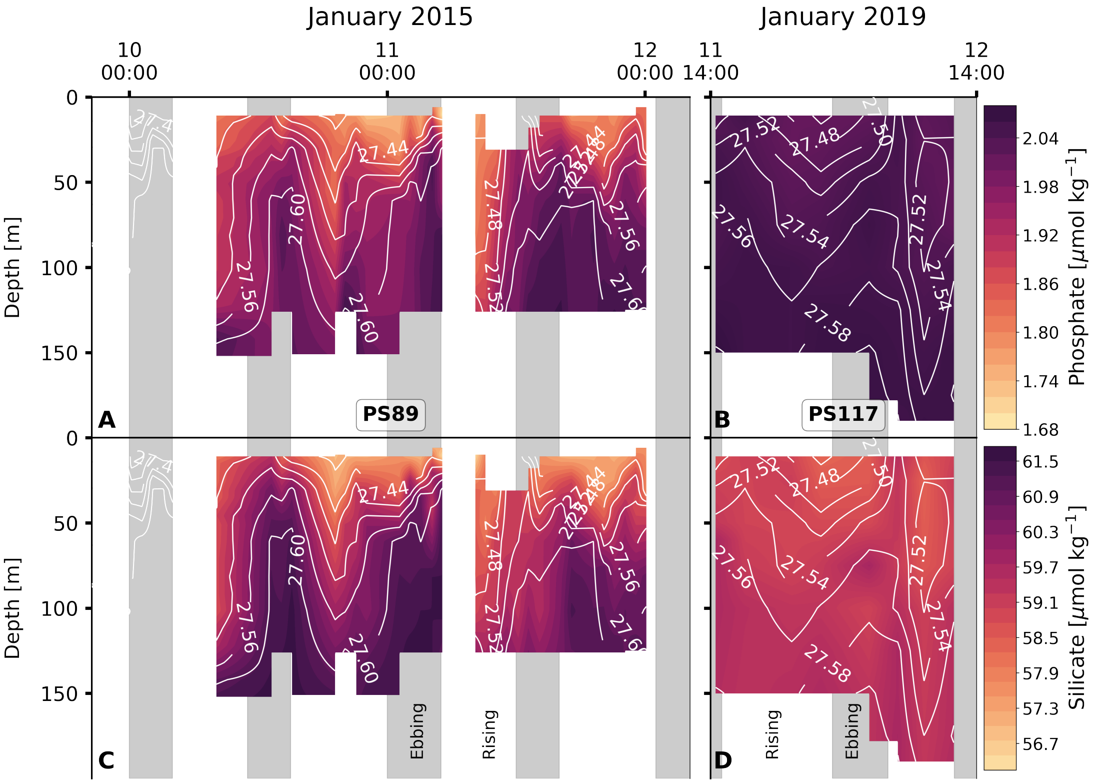

Figure A.10: As for Fig. A.9, but instead for phosphate and silicate content and not including the pH and calcite saturation contours that are shown in Fig. A.9.

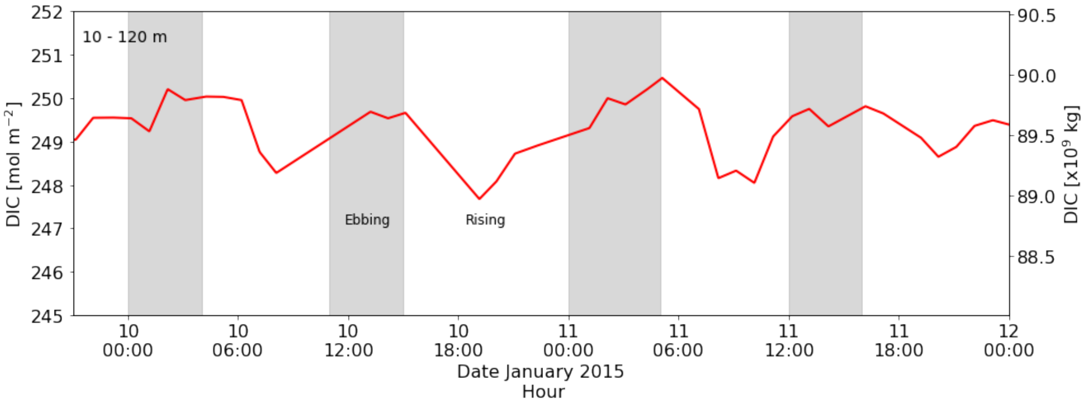

Figure A.11: Left y axis: total water column DIC content between 10 and 120 m during the PS89 tidal observation. Right y axis: total DIC content between 10 and 120 m for the entire PS89 polynya, using the estimated dimensions in the text and assuming an ellipsoidal area.

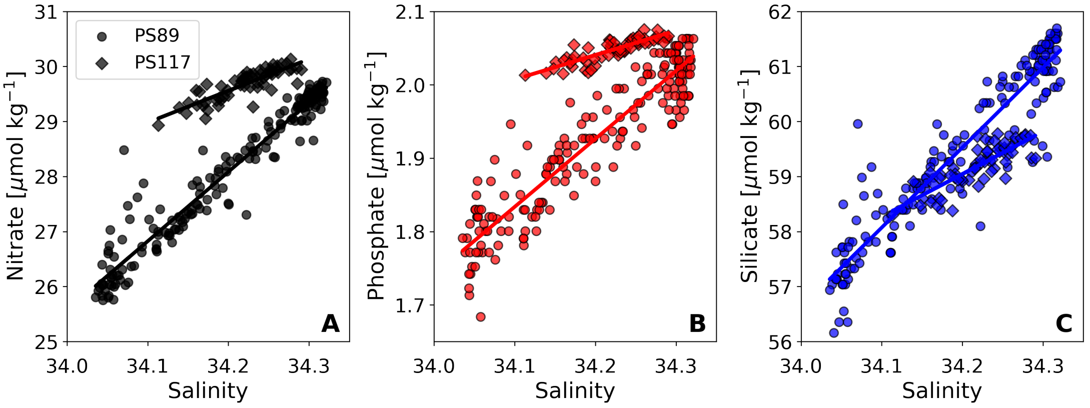

Figure A.12: Nitrate (A, black), phosphate (B, red), and silicate (C, blue) content plotted against salinity for the PS89 (circles) and PS117 (diamonds) tidal observations, including linear regression lines.

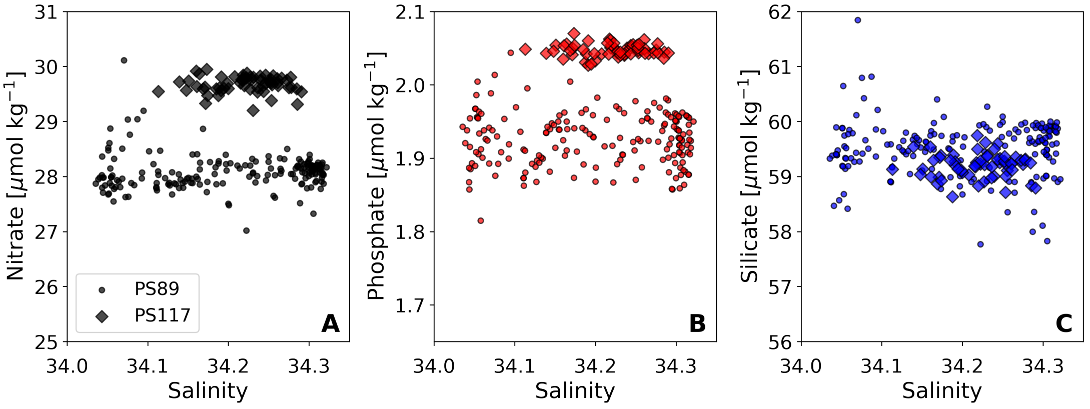

Figure A.13: Salinity-normalised (following Friis et al. (2003)) nitrate (A, black), phosphate (B, red), and silicate (C, blue) content plotted against salinity for the PS89 (circles) and PS117 (diamonds) tidal observations.

VIII Wind

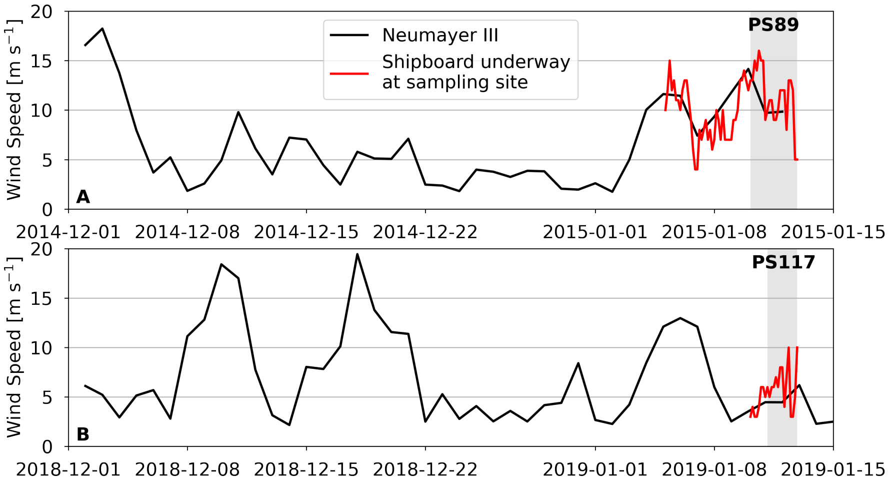

Figure A.14: (a) Wind speed measured at Neumayer III Research Station (black) in the time prior and during the PS89 tidal observation, as well as the ship-board wind speed measurements during the PS89 tidal observation (red). (b) Wind speed measured at Neumayer III Research Station in the time prior and during the PS117 tidal observation (black), as well as the ship-board wind speed measurements during the PS117 tidal observation (red). Grey areas indicate the duration of the tidal observations.

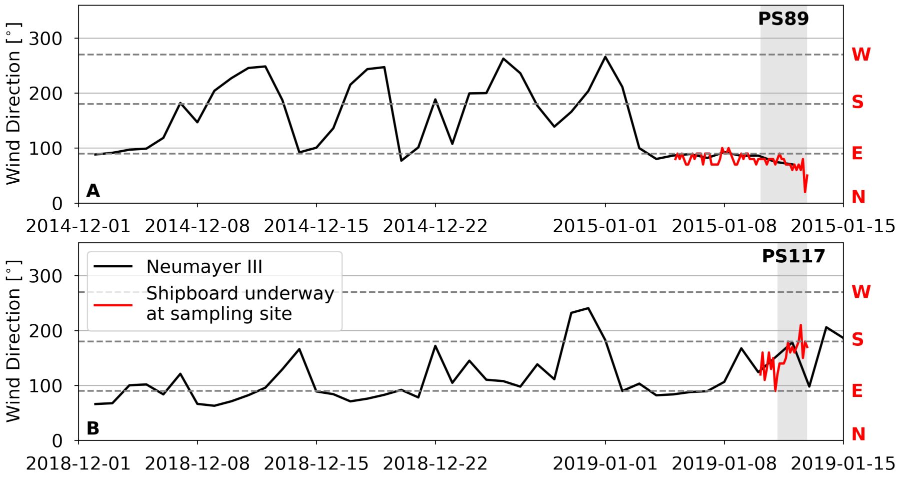

Figure A.15: Same as Fig. A.14, but for wind direction. Horizontal dashed lines indicate 90°, 180°, and 270°. North, East, South, and West directions are indicated by the red initials at the right side of the plots.

APPENDIX B |

Appendix to Chapter 4

I CTD sensors

Table B.1: Sensors on RaTS CTD and precisions.

Variable	Sensor	Precision [unit]	Reference
Salinity	Chelsea Instruments Aquapak CTD (until end 2002), SeaBird 19+ (from 2003 onwards)	0.005	(Venables et al., 2013; Venables and Meredith, 2014)
Temperature	Chelsea Instruments Aquapak CTD (until end 2002), SeaBird 19+ (from 2003 onwards)	0.002 °C	(Venables et al., 2013; Venables and Meredith, 2014)
Chlorophyll *a* derived from fluorescence sensor data, calibrated with chlorophyll *a* samples at 15 m depth	Fluorometer on Chelsea Instruments Aquapak CTD (until end 2002), WetLabs inline fluorometer (from 2003 onwards)		(Clarke et al., 2008; Venables et al., 2013)

II Analytical uncertainties for DIC and TA

Table B.2: Analytical uncertainties for DIC and TA analysed for the RaTS, analysed at either the University of East Anglia (UEA), Norwich, UK, or the Institute for Marine Research (IMR), Tromsø, Norway.

CRM batch	Number of CRM runs	Field season	DIC precision $[\mu\text{mol kg}^{-1}]$	TA precision $[\mu\text{mol kg}^{-1}]$	Location of analysis	Reference
107		2011-2014	< 2.2	< 2.2	UEA	(Legge et al., 2017)
130	47	2013-2014	1.6	1.0	NIOZ	(Jones et al., 2017b)
130	54/45	2014-2015	1.7	1.5	NIOZ	(Jones et al., 2017b)
130	21/19	2015-2016	1.2	0.6	NIOZ	(Jones et al., 2017b)
133	55	2016-2017	5.29	5.41	UEA	This work.
182	96	2017-2019	1.4	2.71	UEA	This work.
185	16	2019-2020	0.77	1.73	UEA	This work.

III Determination of marine carbonate system components

Table B.3: Settings used for the determination of fCO_2 using PyCO2SYS (Humphreys et al., 2022). Temperature and pressure at which the seawater samples were analysed were set at 25 °C and 0 dbar (default).

Function input	**Input meaning**	**Setting**	**Setting meaning**	**Reference**	**Comment**
Opt_pH_scale	pH scale for any pH entries	1	Total pH scale. $pH = -\log_{10}(H^+ + [HSO_4^-])$	(Zeebe and Wolf-Gladrow, 2001)	Best practice according to Orr et al. (2015)
Opt_k_carbonic	Set of equilibrium constant parameterisations for carbonic acid dissociation	10	$2 < T < 35$ °C, $19 < S < 43$, total pH scale, real seawater	(Lueker et al., 2000)	Recommended by Orr et al. (2015) as best practice
		16	$-1.67 < T < 31.80$ °C, $30.73 < S < 37.57$, total scale, field measurements	(Sulpis et al., 2020)	Based on field data, including in the polar regions
		2	$-1 < T < 40$ °C, $10 < S < 50$, seawater scale, artificial seawater	(Goyet and Poisson, 1989)	Used by Legge et al. (2015) and Legge et al. (2017)
Opt_k_bisulfate	Equilibrium constant parameterisation for bisulfate ion dissociation	1		(Dickson, 1990)	Recommended by Orr et al. (2015) as best practice
Opt_total_borate	Boron:salinity relationship to estimate total borate	1		(Uppström, 1974)	Recommended by Orr et al. (2015) as best practice
Opt_k _fluoride	Equilibrium constant parameterisation for hydrogen fluoride dissociation	1	Automatic differentiation, accounting for equilibrating solutes effects	(Dickson and Riley, 1979)	Recommended by Dickson et al. (2007) and Orr et al. (2015) as best practice
Opt_buffers_mode	Calculation for buffer factors	1			Recommended by Humphreys et al. (2022) for the most accurate calculations.
Opt_gas_constant	Gas constant (R) value	3	8.314 462 618... J mol^{-1} K^{-1}		

IV Datasets used in this work

Table B.4: References and URLs for additional datasets used in this work.

Dataset	**Reference**	**URL or DOI**
RaTS DIC / TA for 2010-2014	(Legge et al., 2015)	
Mean sea level pressure	(Connolley, 2004)	https://legacy.bas.ac.uk/met/metlog/
Wind speed	(Connolley, 2004)	https://legacy.bas.ac.uk/met/metlog/
Atmospheric xCO2	(Dlugokencky et al., 2019)	
IBSCO bathymetry	(Arndt et al., 2013)	https://doi.org/10.1594/PANGAEA.805736
GEBCO bathymetry	(GEBCO, 2022)	10.5285/e0f0bb80-ab44-2739-e053-6c86abc0289c
SAM index	(Marshall, 2023; Marshall, 2003)	legacy.bas.ac.uk/met/gjma/sam.html
SOI index	(CPC, 2023)	https://www.cpc.ncep.noaa.gov/data/indices/

V Season definitions

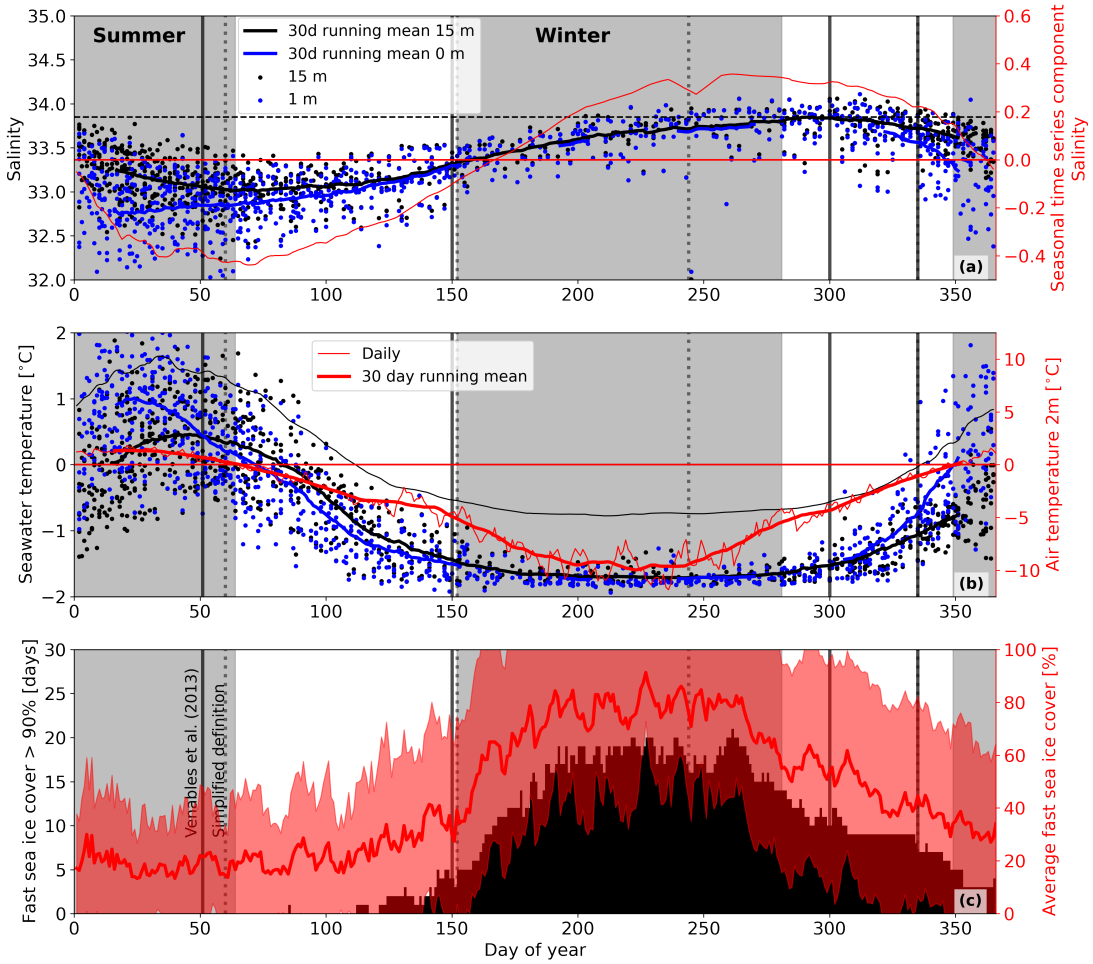

Figure B.1: (Top) Salinity at 1 and 15 m depth (left y-axis) and the de-seasonalised salinity at 15 m depth in Ryder Bay between 1998 and 2020 (right y-axis). Dashed black line indicates maximum salinity at the surface based on the 30-day running mean. (Middle) Seawater temperature at 1 and 15 m depth (left y-axis). The de-seasonalised seawater temperature at 15 m is shown by a thin black line. Daily mean air temperature is shown on the right y-axis. (Bottom) Histogram for number of days in RaTS (1998-2020) when fast sea ice cover was higher than 90 % (left y-axis). The average fast sea ice cover for the time series is plotted on the right y-axis. Vertical black lines indicate the seasons as defined by Venables et al. (2013). Dotted grey vertical lines indicate the seasons according to DJF, MAM, JJA, and SON. The shaded areas indicate the seasons as defined in this work. See text in Chapter 4 for details.

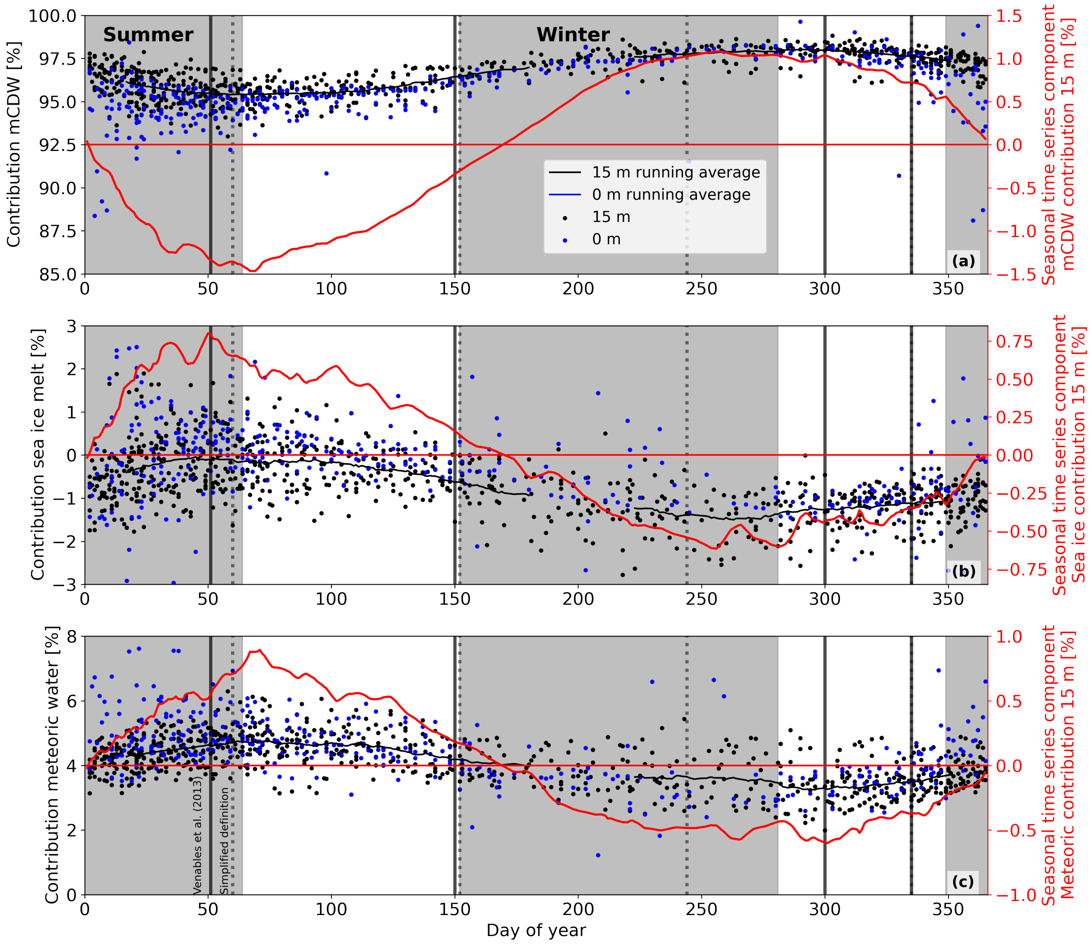

Figure B.2: (Top) Contribution of mCDW at 1 and 15 m depth (left y-axis) and the de-seasonalised mCDW contribution at 15 m depth (right y-axis) in Ryder Bay between 2002 and 2020. (Middle) Same as top, but for the contribution of sea ice meltwater. (Bottom) Same as top, but for meteoric water. Vertical black lines indicate the seasons as defined by Venables et al. (2013). Dotted grey vertical lines indicate the seasons according to DJF, MAM, JJA, and SON. The shaded areas indicate the seasons as defined in this work. See text in Chapter 4 for details.

VI De-seasonalised annual plots for high and low stratification years

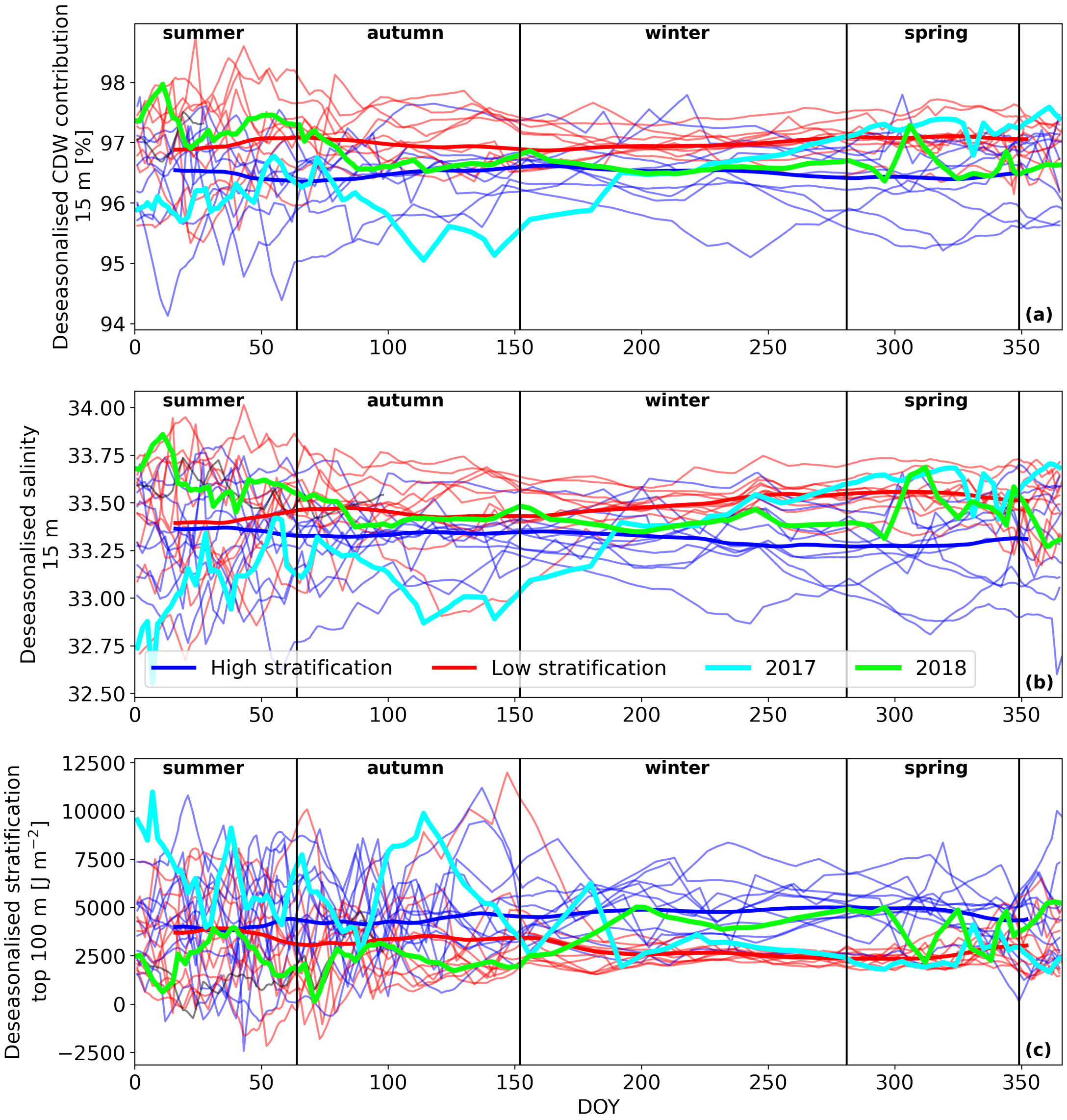

Figure B.3: De-seasonalised CDW contribution at 15 m (a), salinity at 15 m (b), and stratification in the top 100 m (c) for each year of the RaTS, coloured according to "high stratification" or "low stratification" winter. The results for 2017 and 2018 are highlighted in cyan and neon green, respectively.

VII Relationships to chlorophyll *a* in springtime

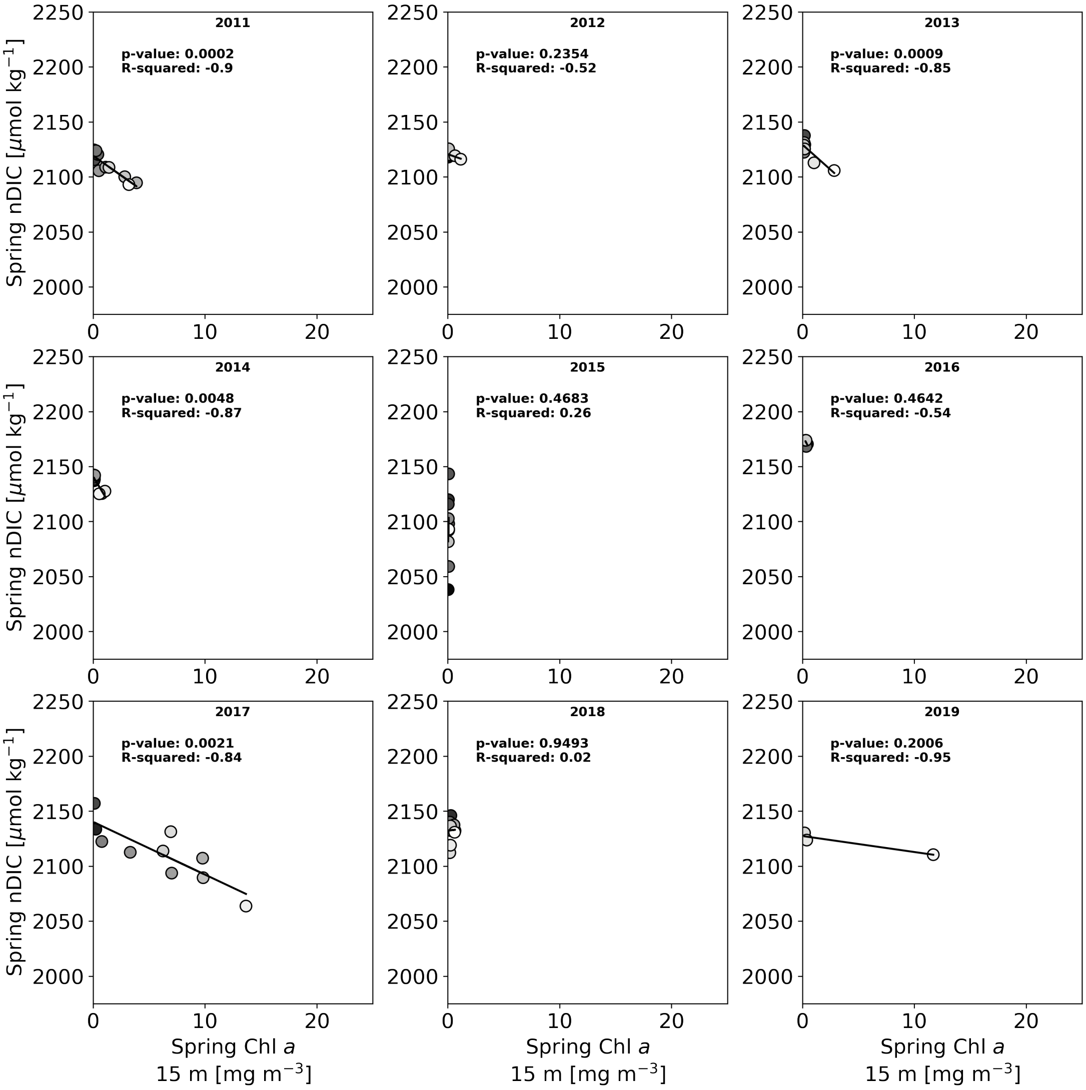

Figure B.4: Linear regression between springtime nDIC content and chlorophyll *a* concentrations at 15 m depth for RaTS 2011-2019. Markers are coloured according to the gradient representing time between the start of spring (black) and the end of spring (white).

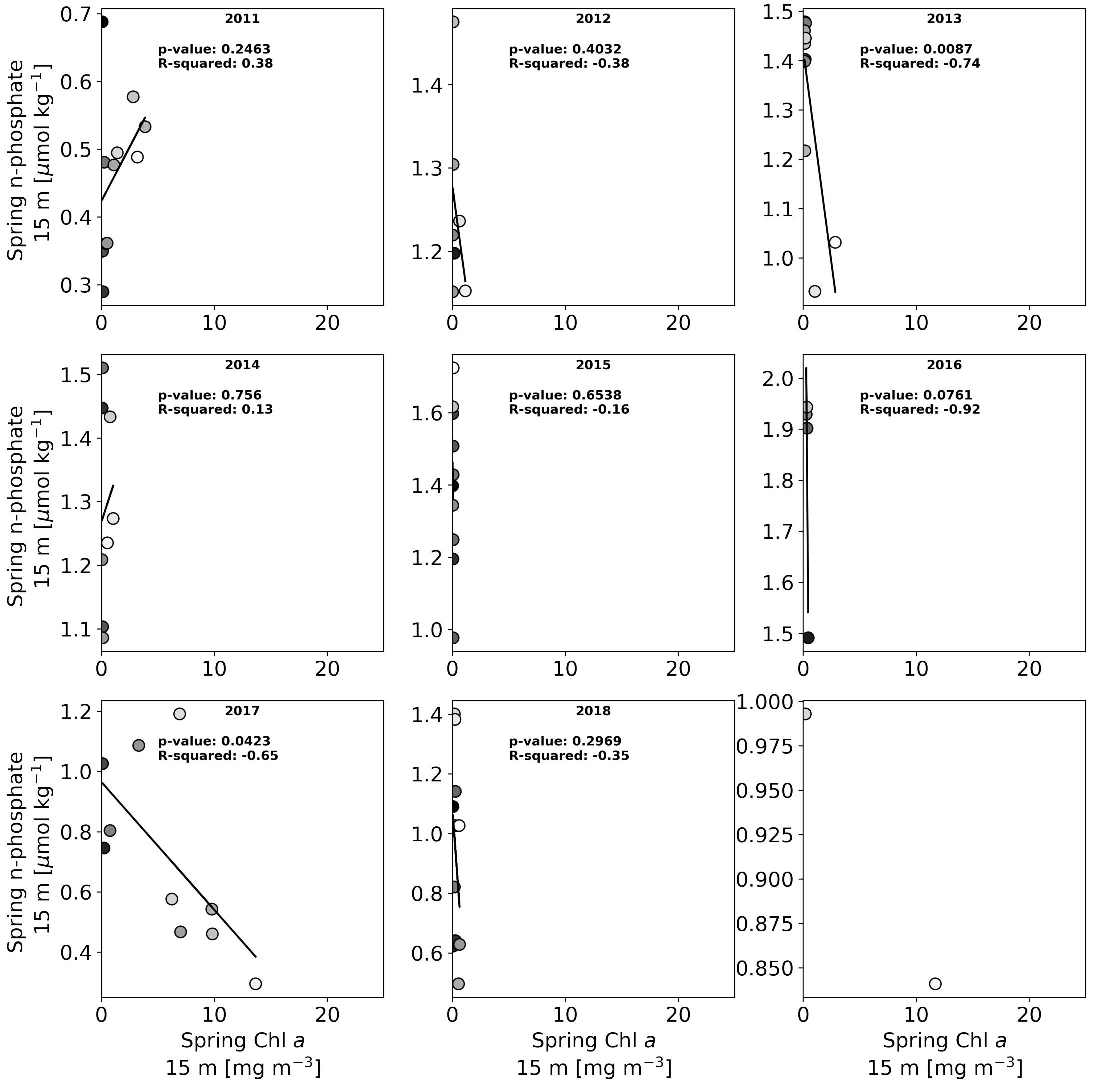

Figure B.5: Linear regression between springtime n-phosphate content and chlorophyll a concentrations at 15 m depth for RaTS 2011-2019. Markers are coloured according to the gradient representing time between the start of spring (black) and the end of spring (white).

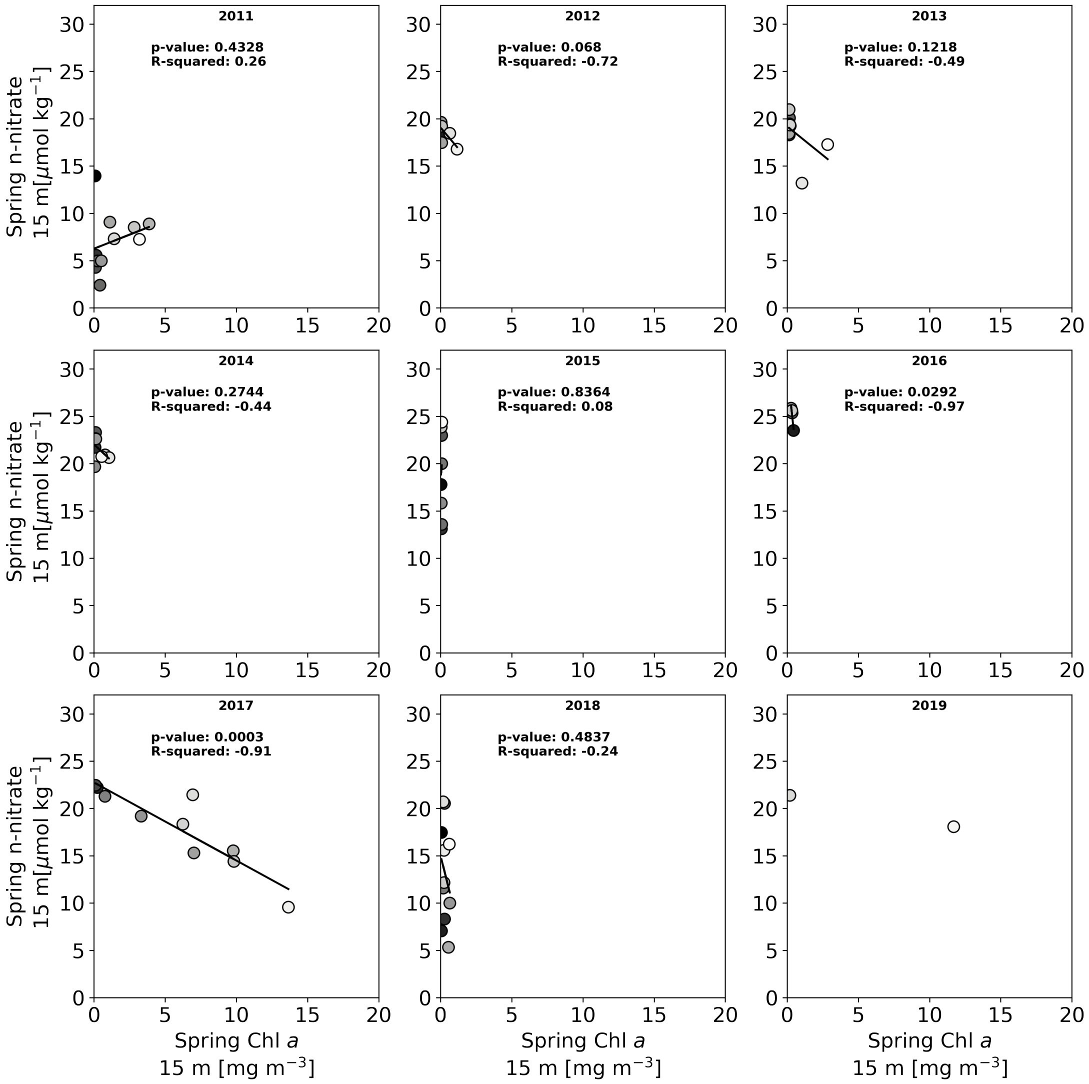

Figure B.6: Linear regression between springtime n-nitrate content and chlorophyll *a* concentrations at 15 m depth for RaTS 2011-2019. Markers are coloured according to the gradient representing time between the start of spring (black) and the end of spring (white).

VIII Vertical gradients in POC in top 30 m

Particulate organic carbon (POC) was determined based on the relationship found by Legendre and Michaud (1999) with chlorophyll *a*:

$$log(POC) = 2.21 + 0.51 log(Chla) \qquad \text{(Eq. B.1)}$$

Result are shown in Fig. B.7. To compare the differences in vertical gradients of DIC to POC, the units for the latter were converted from mg m^{-3} to μmol kg^{-1}, using 12.001 g mol^{-1} as the molar mass of carbon and the density based on salinity and temperature. Fig B.8. Vertical gradients were calculated by subtracting the values for the 15 m samples from the respective shallower samples either at 0, 2, or 5 m depth. Vertical gradients for DIC cannot be explained by the vertical gradients in POC, except for the data points of the summer of 2017 / 2018, where a positive relationship shows that lower DIC content at the surface was associated to lower POC content.

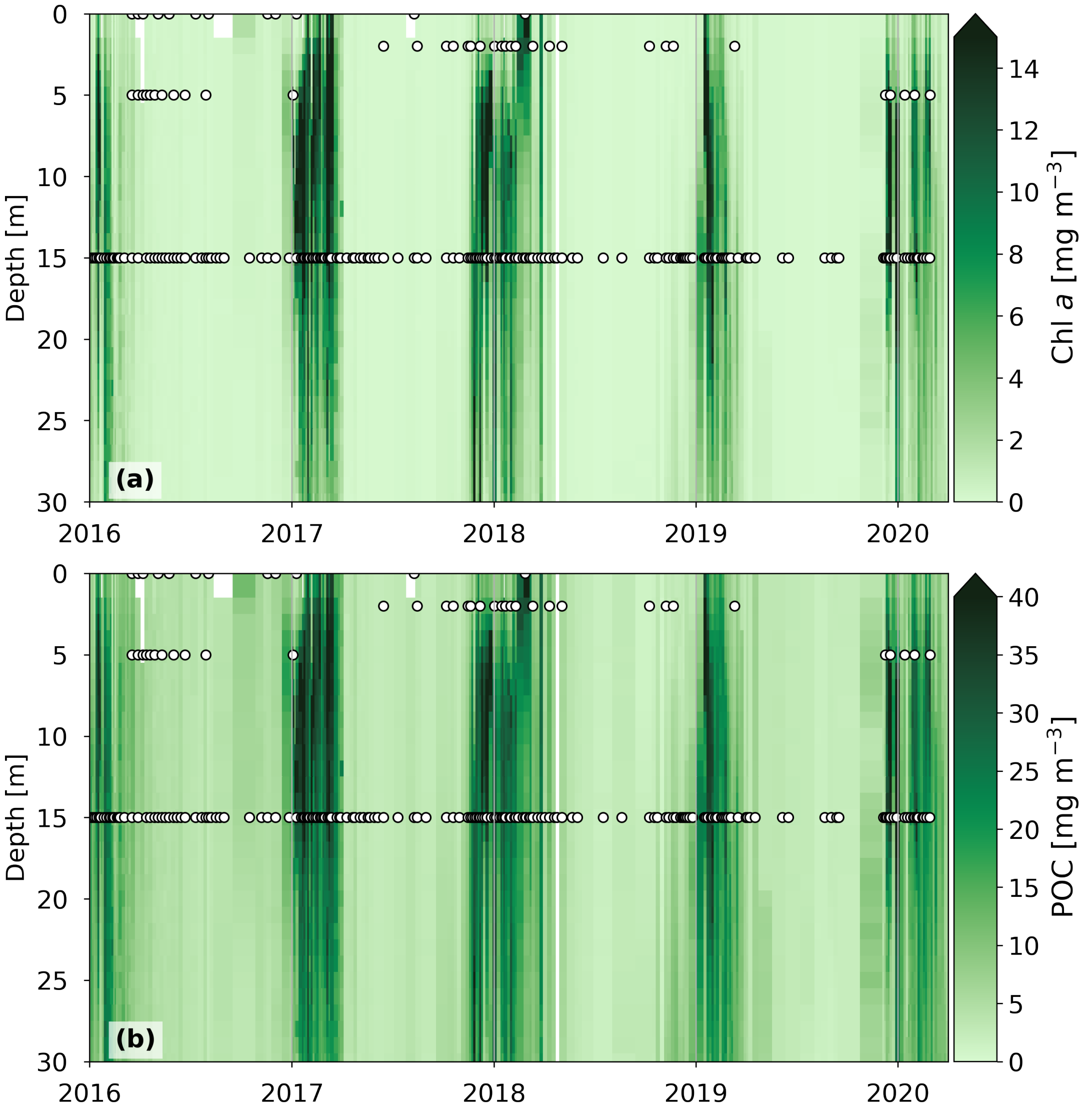

Figure B.7: (a) Chlorophyll *a* in the top 30 m of the RaTS between 2016 and 2020, when occasionally samples shallower than 15 m were collected. White markers indicate the date and depth at which seawater samples were collected. (b) Same as (a), but for POC, which was determined according to Legendre and Michaud (1999).

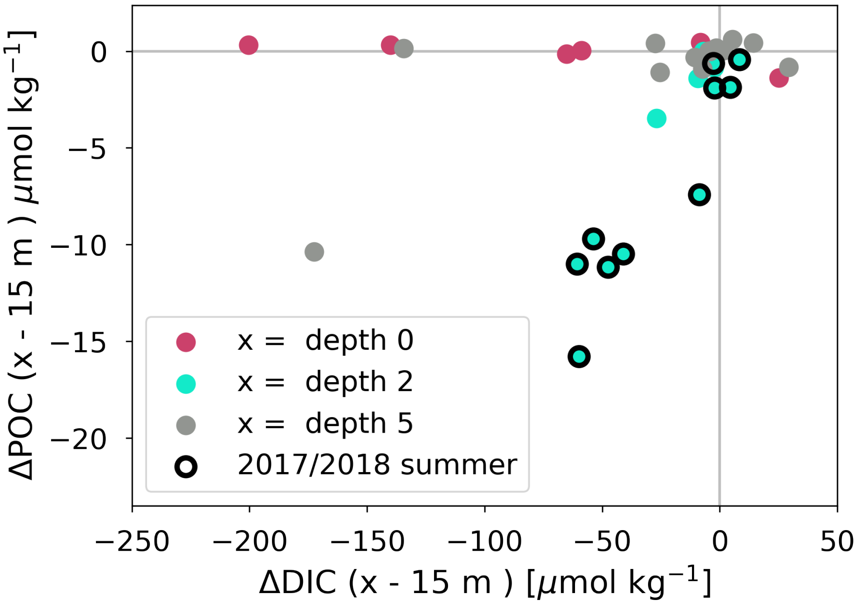

Figure B.8: The differences between the surface samples (at 0, 2, or 5 m depth) and the sample collected at the same station at 15 m depth for POC and DIC. Data points for the summer of 2017 / 2018 are marked with a thick black line.

APPENDIX C

Appendix to Chapter 5

I Data

Table C.1: References for auxiliary and other datasets used in this work.

Data	Database	DOI	Reference
Ship underway seawater fCO_2	SOCAT v2022	https://doi.org/10.25921/1h9f-nb73	(Bakker et al., 2016)
Global Ocean OSTIA Sea Surface Temperature and Sea Ice Reprocessed	OSTIA	https://doi.org/10.48670/moi-00168	(Good et al., 2020)
Under ice MSS profiles	PANGAEA	https://doi.org/10.1594/PANGAEA.939816	(Schulz et al., 2022)
Bathymetry	GEBCO	https://doi.org/10.5285/e0f0bb80-ab44-2739-e053-6c86abc0289c	(GEBCO, 2022)
DIC / TA content MOSAiC	PANGAEA	https://doi.org/10.1594/PANGAEA.954969	

II Changes during and after Leg 5 drift

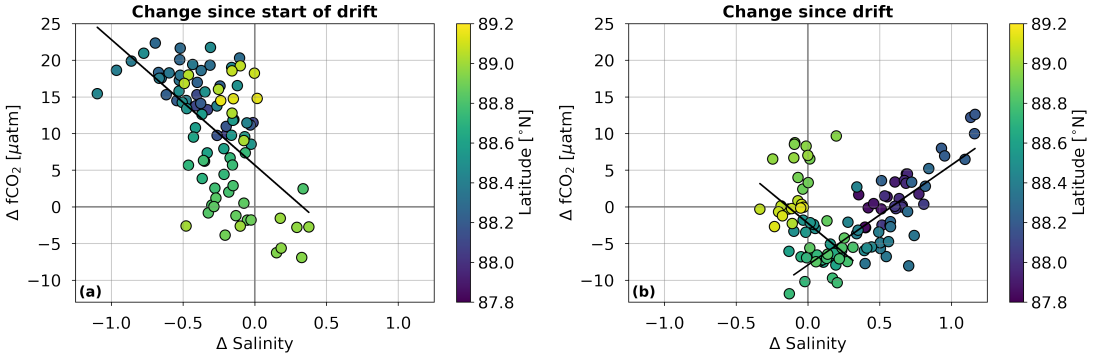

Figure C.1: (a) Differences between the drift (transect 2) and transect 1 (see text in Chapter 5) in mean fCO_2 and salinity per latitudinal bin. Markers are coloured according to latitude. Black line indicates the linear regression. Expression of the linear regression is -17.1 x + 5.7 (p-value < 0.001). (b) Same as (a) but for differences between transect 3 and the drift track (transect 2). Two regression lines are plotted for data north and south of 88.5°N. Expressions of the linear regression are -16.2 x − 2.3 (p-value < 0.001) and 13.64 x − 7.9 (p-value < 0.001).

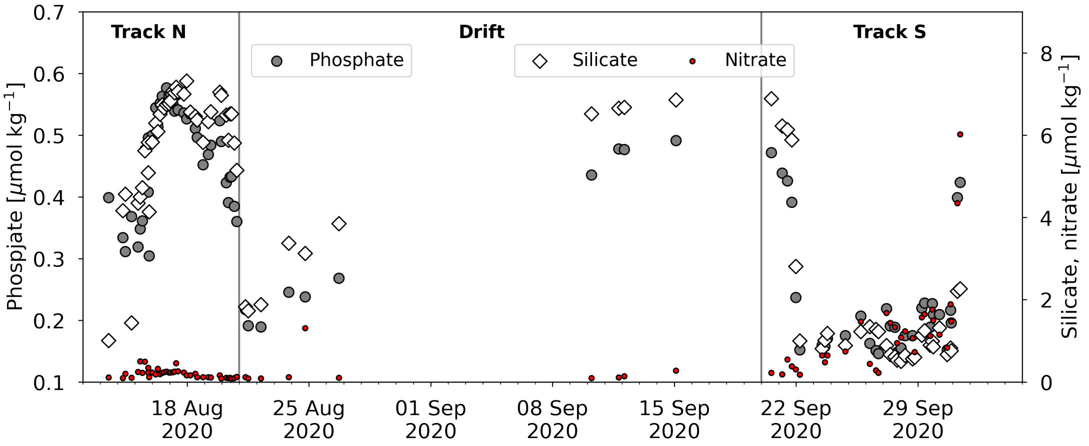

Figure C.2: Phosphate, nitrate, and silicate content from the underway discrete seawater samples collected during Leg 5. Vertical grey lines indicate the start and end of the Leg 5 drift period.

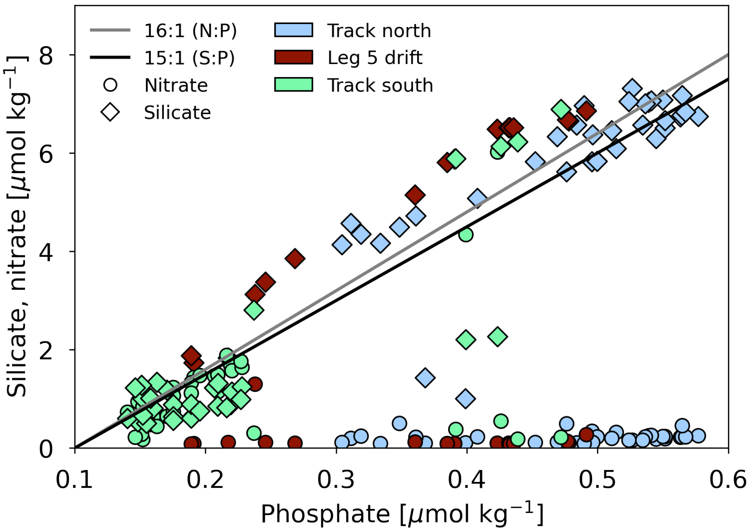

Figure C.3: Silicate (diamonds) and nitrate (circles) content plotted against phosphate content for all underway discrete seawater samples collected during Leg 5. Markers are coloured according to the two transit tracks and the drift track.

III Upper 100 m during Leg 5

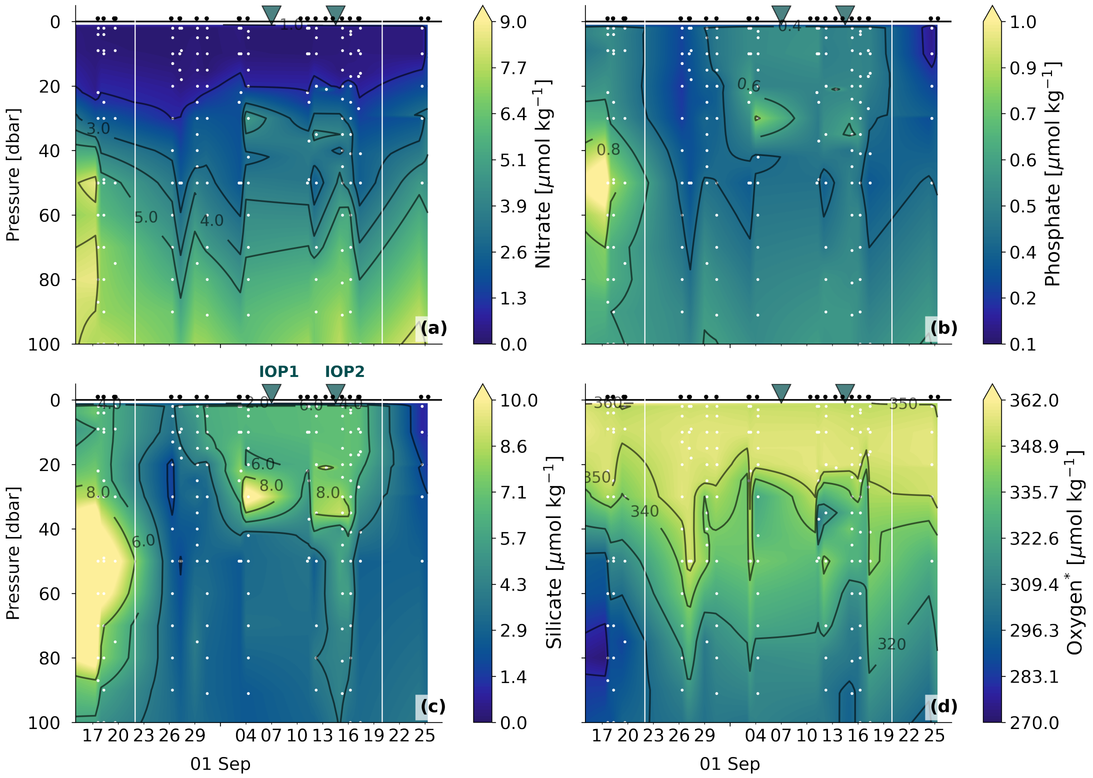

Figure C.4: Contour plots of (a) nitrate, (b) phosphate, (c) silicate, and (d) dissolved oxygen profiles measured by CTD casts during MOSAiC Leg 5 in the top 100 m of the water column. White lines indicate the beginning and end of the Leg 5 drift period. White markers indicate the discrete sampling depths. Black markers at the surface indicate the timing of the CTD cast. Triangle markers indicate the timing of two storm events during Leg 5 of MOSAiC, during which IOPs were done. See Table 5.1 and text for details. *Dissolved oxygen values are preliminary, as the CTD oxygen measurements still need to be officially calibrated at the time of writing. The dissolved oxygen values shown here have been temporarily manually calibrated by Adam Ulfsbo.

IV IOPs during Leg 5

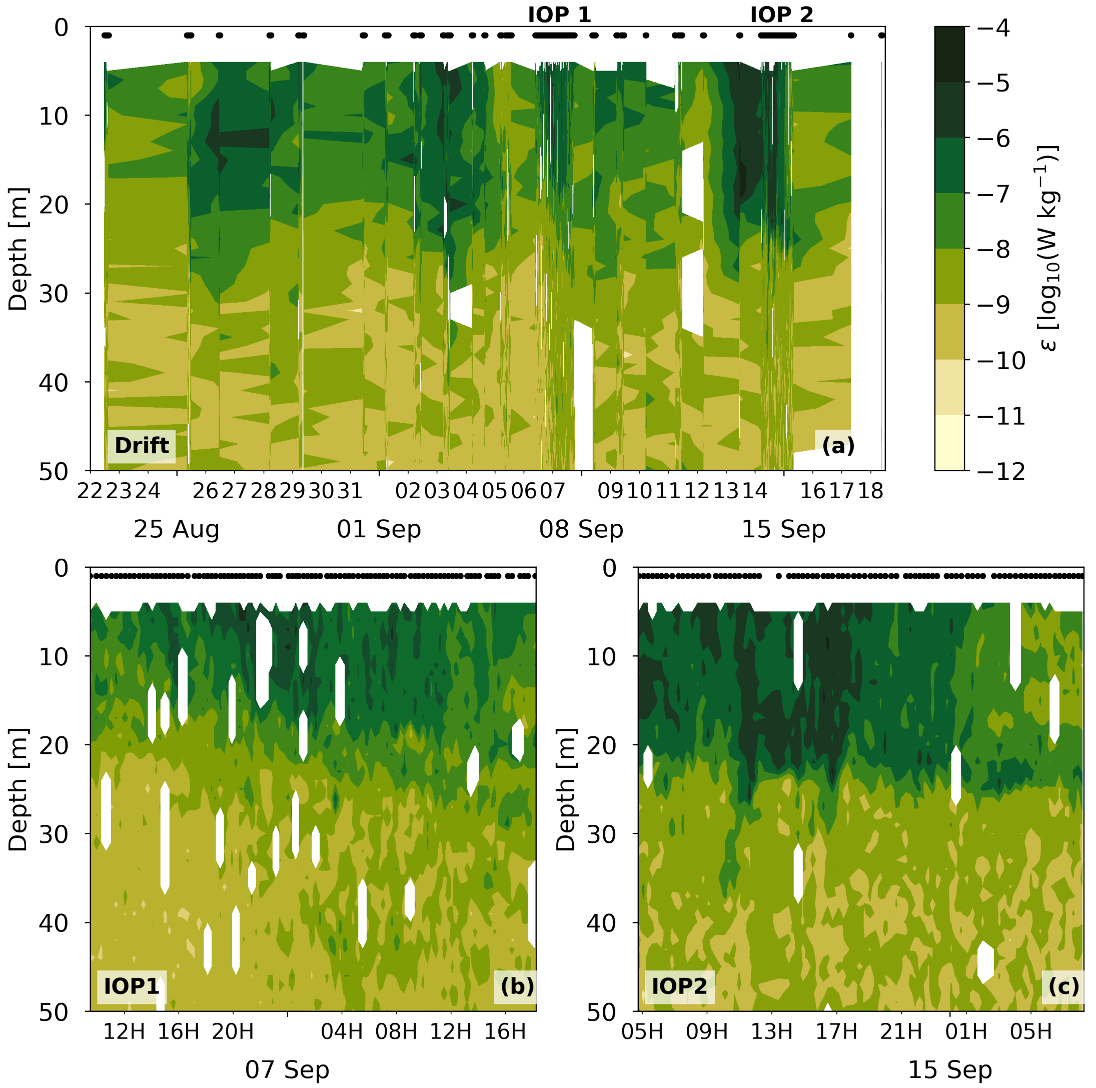

Figure C.5: Logarithmic turbulent kinetic energy dissipation rate measured by the MSS during Leg 5 (a) and during IOP 1 (b) and IOP 2 (c).

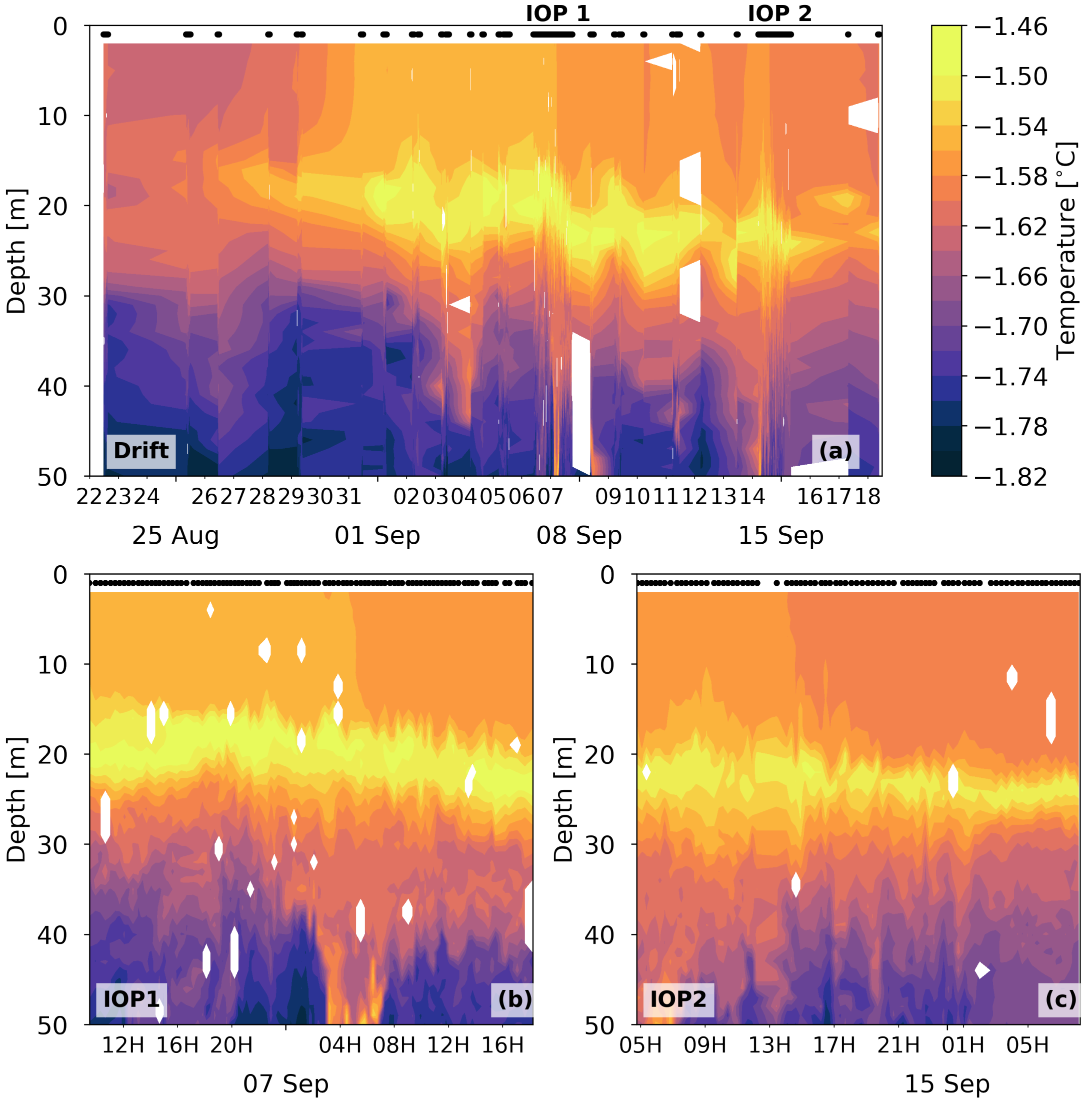

Figure C.6: Same as Fig. C.5, but for temperature measured by the MSS.

V Salinity and temperature profiles in leads and underneath sea ice during Leg 5

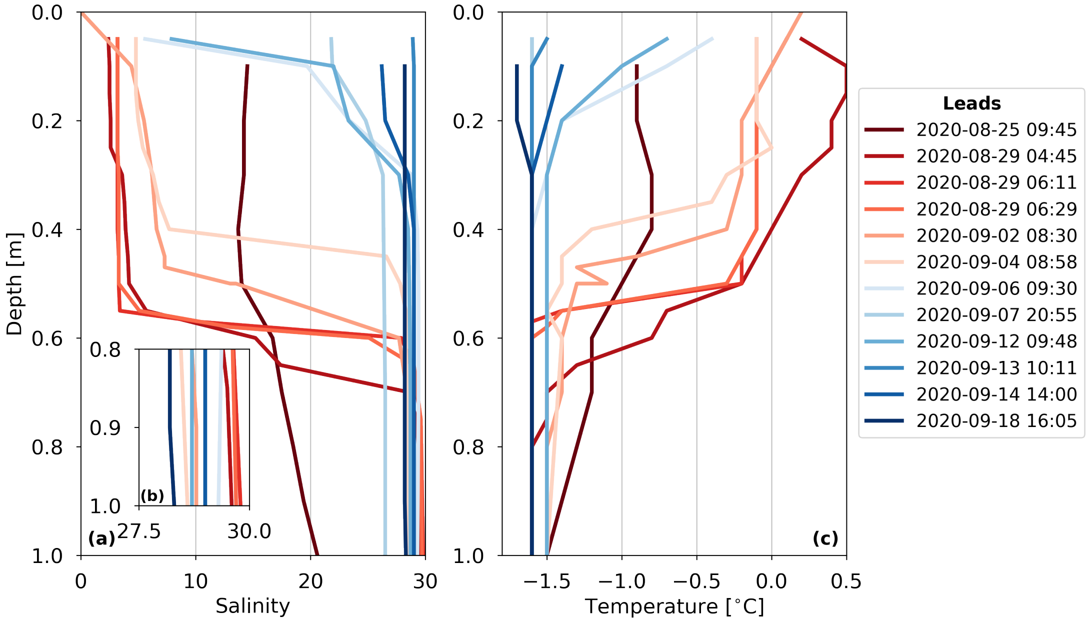

Figure C.7: Salinity (a) and temperature (b) profiles in the top meter of leads around the Leg 5 MOSAiC floe during the drift. Profiles collected before the first storm on 6 September are coloured in red hues. Profiles collected after 6 September are coloured in blue hues.

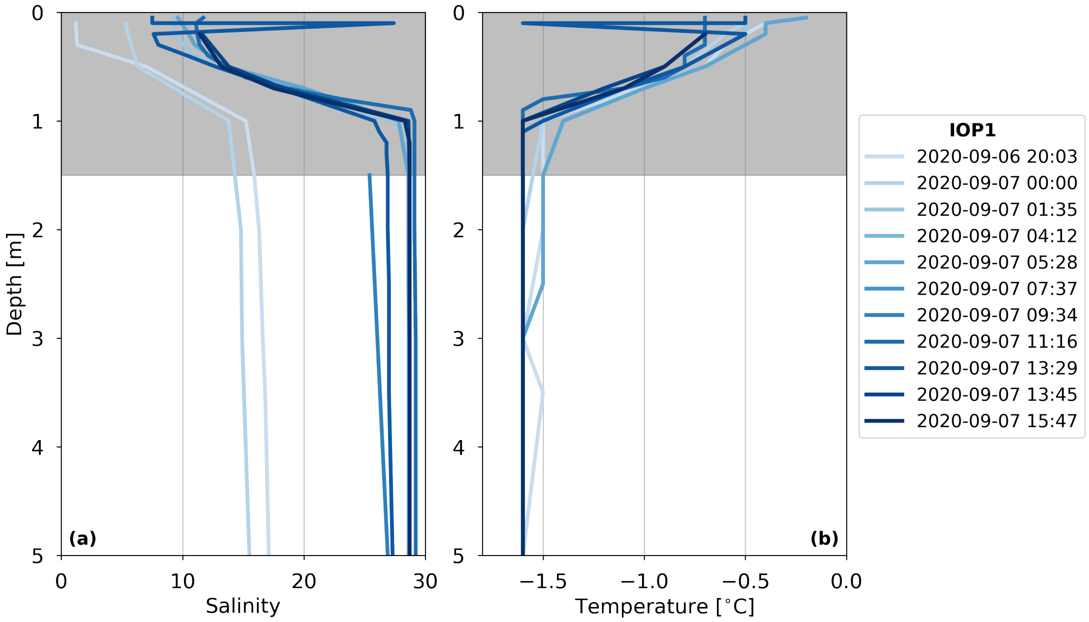

Figure C.8: Salinity (a) and temperature (b) profiles in the top 5 m at EcoLodge, measured through a hole in the sea ice during IOP 1 (6-7 September 2020). The grey area in the plots indicates the sea ice thickness.

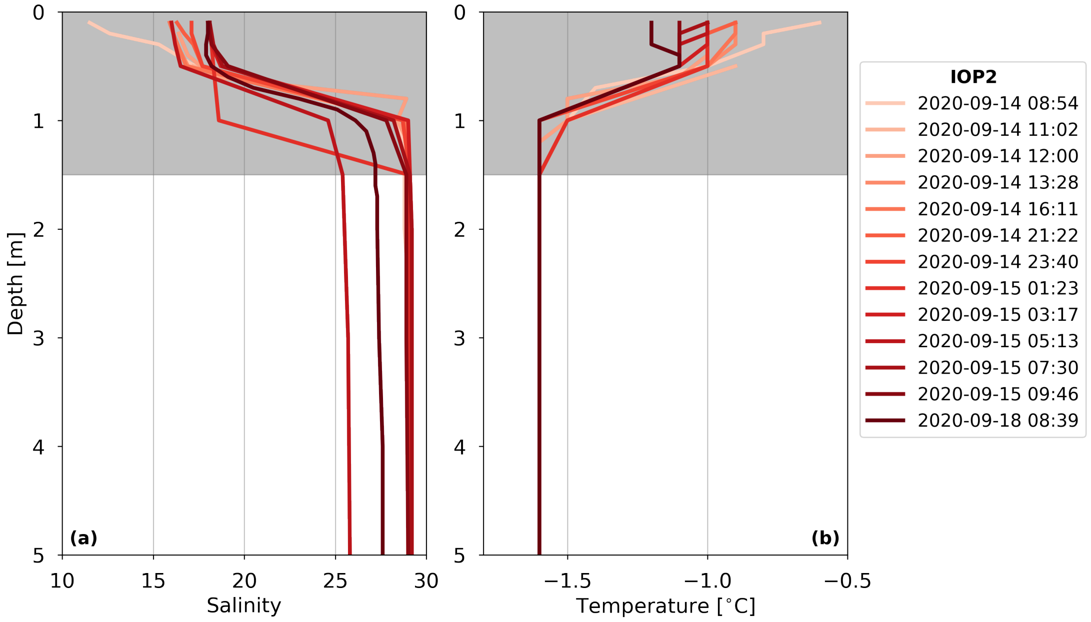

Figure C.9: Same as Fig. C.8, but measured during IOP 2 (14-15 September 2020, with an additional profile on 18 September 2020).

REFERENCE LIST

Aagaard, K. and E. C. Carmack (1989). "The role of sea ice and other fresh water in the Arctic circulation". *Journal of Geophysical Research* 94.C10, pp. 14485–14498. ISSN: 0148-0227. DOI: 10.1029/jc094ic10p14485.

Aagaard, Knut, L. K. Coachman, and Eddy Carmack (1981). "On the halocline of the Arctic Ocean". *Deep Sea Research Part A, Oceanographic Research Papers* 28.6, pp. 529–545. ISSN: 01980149. DOI: 10.1016/0198-0149(81)90115-1.

Abernathey, Ryan P. et al. (2016). "Water-mass transformation by sea ice in the upper branch of the Southern Ocean overturning". *Nature Geoscience* 9, pp. 596–601. ISSN: 17520908. DOI: 10.1038/ngeo2749.

Alderkamp, Anne Carlijn et al. (2012). "Iron from melting glaciers fuels phytoplankton blooms in the Amundsen Sea (Southern Ocean): Phytoplankton characteristics and productivity". *Deep-Sea Research Part II: Topical Studies in Oceanography* 71-76, pp. 32–48. ISSN: 09670645. DOI: 10.1016/j.dsr2.2012.03.005.

Anderson, L. G. et al. (1991). "The transport of anthropogenic carbon dioxide into the Weddell Sea". *Journal of Geophysical Research* 96.C9. ISSN: 01480227. DOI: 10.1029/91jc01785.

Anderson, Leif G. and Staffan Kaltin (2001). "Carbon fluxes in the Arctic Ocean-potential impact by climate change". *Polar Research* 20.2, pp. 225–232. DOI: 10.3402/polar.v20i2.6521.

Andersson, A. J. and F. T. MacKenzie (2012). "Revisiting four scientific debates in ocean acidification research". *Biogeosciences* 9.3, pp. 893–905. ISSN: 17264170. DOI: 10.5194/bg-9-893-2012.

Arndt, Jan Erik et al. (2013). *The International Bathymetric Chart of the Southern Ocean (IBCSO) Version 1.0.* data set. Supplement to: Arndt, JE et al. (2013): The International Bathymetric Chart of the Southern Ocean Version 1.0 – A new bathymetric compilation covering circum-Antarctic waters. Geophysical Research Letters, 40(9), 1-7, https://doi.org/10.1002/grl.50413. DOI: 10.1594/PANGAEA.805736. URL: https://doi.org/10.1594/PANGAEA.805736.

Arrigo, Kevin R. and Gert L. van Dijken (2003). "Phytoplankton dynamics within 37 Antarctic coastal polynya systems". *Journal of Geophysical Research: Oceans* 108.8. ISSN: 21699291. DOI: 10.1029/2002jc001739.

Arrigo, Kevin R., Gert L. van Dijken, and Aaron L. Strong (2015). "Environmental controls of marine productivity hot spots around Antarctica". *Journal of Geophysical Research: Oceans* 120, pp. 5545–5565. ISSN: 21699313. DOI: 10.1002/2015JC010888. arXiv: arXiv:1402.6991v1.

Arrigo, Kevin R., Gert van Dijken, and Matthew Long (2008a). “Coastal Southern Ocean: A strong anthropogenic CO_2 sink”. *Geophysical Research Letters* 35.21, pp. 1–6. ISSN: 00948276. DOI: 10.1029/2008GL035624.

Arrigo, Kevin R., Gert van Dijken, and Sudeshna Pabi (2008b). “Impact of a shrinking Arctic ice cover on marine primary production”. *Geophysical Research Letters* 35.L19603, pp. 1–6. ISSN: 00948276. DOI: 10.1029/2008GL035028.

Arroyo, M. C., E. H. Shadwick, and B. Tilbrook (2019). “Summer carbonate chemistry in the Dalton Polynya, East Antarctica”. *Journal of Geophysical Research: Oceans* 124.8, pp. 5634–5653. ISSN: 21699291. DOI: 10.1029/2018JC014882. URL: https://doi.org/10.1029/2018JC014882.

Bakker, D. C.E. et al. (2008). “A rapid transition from ice covered CO_2-rich waters to a biologically mediated CO_2 sink in the eastern Weddell Gyre”. *Biogeosciences* 5.5, pp. 1373–1386. ISSN: 17264189. DOI: 10.5194/bg-5-1373-2008.

Bakker, Dorothee C.E. et al. (2016). “A multi-decade record of high-quality fCO_2 data in version 3 of the Surface Ocean CO_2 Atlas (SOCAT)”. *Earth System Science Data* 8, pp. 383–413. ISSN: 18663516. DOI: 10.5194/essd-8-383-2016.

Barber, D. G. and R. A. Massom (2007). “Chapter 1 The Role of Sea Ice in Arctic and Antarctic Polynyas”. *Elsevier Oceanography Series*. Ed. by W. O. Smith and D. G. Barber. Vol. 74. 06. Chap. 1, pp. 1–54. ISBN: 9780444529527. DOI: 10.1016/S0422-9894(06)74001-6.

Barber, David G. et al. (2015). “Selected physical, biological and biogeochemical implications of a rapidly changing Arctic Marginal Ice Zone”. *Progress in Oceanography* 139, pp. 122–150. ISSN: 00796611. DOI: 10.1016/j.pocean.2015.09.003. URL: http://dx.doi.org/10.1016/j.pocean.2015.09.003.

Bates, N. R. and J. T. Mathis (2009). “The Arctic Ocean marine carbon cycle: Evaluation of air-sea CO_2 exchanges, ocean acidification impacts and potential feedbacks”. *Biogeosciences* 6.11, pp. 2433–2459. ISSN: 17264189. DOI: 10.5194/bg-6-2433-2009.

Bates, Nicholas R. et al. (2006). “An increasing CO_2 sink in the Arctic Ocean due to sea-ice loss”. *Geophysical Research Letters* 33.L23609, pp. 1–7. ISSN: 00948276. DOI: 10.1029/2006GL027028.

Beardsley, Robert C., Richard Limeburner, and W. Brechner Owens (2004). “Drifter measurements of surface currents near Marguerite Bay on the western Antarctic Peninsula shelf during austral summer and fall, 2001 and 2002”. *Deep-Sea Research Part II: Topical Studies in Oceanography* 51.17-19, pp. 1947–1964. ISSN: 09670645. DOI: 10.1016/j.dsr2.2004.07.031.

Beaufort, L. et al. (2011). “Sensitivity of coccolithophores to carbonate chemistry and ocean acidification”. *Nature* 476.7358, pp. 80–83. ISSN: 00280836. DOI: 10.1038/nature10295.

Beszczynska-Möller, Agnieszka et al. (2012). “Variability in Atlantic water temperature and transport at the entrance to the Arctic Ocean, 1997-2010”. *ICES Journal of Marine Science* 69.5, pp. 852–863. DOI: 10.1093/icesjms/fss056.

Boebel, Olaf (2015). “The expedition PS89 of the research vessel POLARSTERN to the Weddell Sea in 2014/2015”. *Berichte zur Polar-und Meeresforschung= Reports on polar and marine research* 689. DOI: 10.2312/BzPM_0689_2015.

— (2019). “The Expedition PS117 of the Research Vessel POLARSTERN to the Weddell Sea in 2018/2019”. *Berichte zur Polar-und Meeresforschung= Reports on polar and marine research* 732. DOI: 10.2312/BzPM_0732_2019.

Boebel, Olaf and Sandra Tippenhauer (2019). *Raw data of continuous VM-ADCP (vessel-mounted Acoustic Doppler Current Profiler) profile during POLARSTERN cruise PS117.* data set. Alfred Wegener Institute, Helmholtz Centre for Polar and Marine Research, Bremerhaven. DOI: 10.1594/PANGAEA.902725. URL: https://doi.org/10.1594/PANGAEA.902725.

Boetius, Antje et al. (2015). “Microbial ecology of the cryosphere: Sea ice and glacial habitats”. *Nature Reviews Microbiology* 13, pp. 677–690. ISSN: 17401534. DOI: 10.1038/nrmicro3522.

Bowman, Jeff S. (2015). “The relationship between sea ice bacterial community structure and biogeochemistry: A synthesis of current knowledge and known unknowns”. *Elementa* 3, pp. 1–20. ISSN: 23251026. DOI: 10.12952/journal.elementa.000072.

Bown, Johann et al. (2017). “Bioactive trace metal time series during Austral summer in Ryder Bay, Western Antarctic Peninsula”. *Deep-Sea Research Part II* 139, pp. 103–119. ISSN: 0967-0645. DOI: 10.1016/j.dsr2.2016.07.004. URL: http://dx.doi.org/10.1016/j.dsr2.2016.07.004.

Boyer, T.P. et al. (2015). “Arctic Ocean Regional Climatology (NCEI Accession 0115771) [Arctic summertime 10 m depth salinity climatology]”. *NOAA National Centers for Environmental Information.* DOI: 10.7289/V5QC01J0.

Brewer, Peter G. and Joel C. Goldman (1976). “Alkalinity changes generated by phytoplankton growth”. *Limnology and Oceanography* 21.1, pp. 108–117. ISSN: 19395590. DOI: 10.4319/lo.1976.21.1.0108.

Brown, Peter J. et al. (2015). “Carbon dynamics of the Weddell Gyre, Southern Ocean”. *Global Biogeochemical Cycles* 29, pp. 288–306. DOI: 10.1002/2014GB005006.

Buitenhuis, Erik T. et al. (2019). “Large Contribution of Pteropods to Shallow CaCO3 Export”. *Global Biogeochemical Cycles* 33.3, pp. 458–468. ISSN: 19449224. DOI: 10.1029/2018GB006110.

Bushinsky, Seth M. et al. (2019). “Reassessing Southern Ocean air-sea CO_2 flux estimates with the addition of biogeochemical float observations”. *Global Biogeochemical Cycles* 33.11, pp. 1370–1388. ISSN: 19449224. DOI: 10.1029/2019GB006176.

Cai, Wei-Jun et al. (2010). “Decrease in the CO_2 uptake capacity in an ice-free Arctic Ocean Basin”. *Science* 329.5991, pp. 556–560. DOI: 10.1126/science.1189338.

Carmack, Eddy C. (1974). “A quantitative characterization of water masses in the Weddell Sea during summer”. *Deep-Sea Research and Oceanographic Abstracts* 21.6, pp. 431–443. ISSN: 00117471. DOI: 10.1016/0011-7471(74)90092-8.

Carmack, E. et al. (2015). “Toward quantifying the increasing role of oceanic heat in sea ice loss in the new arctic”. *Bulletin of the American Meteorological Society* 96.12, pp. 2079–2105. ISSN: 00030007. DOI: 10.1175/BAMS-D-13-00177.1.

Carrillo, Christopher J. and David M Karl (1999). “Dissolved inorganic carbon pool dynamics in northern Gerlache Strait, Antarctica”. 104.C7, pp. 15873–15884.

Carrillo, Christopher J., Raymond C. Smith, and David M. Karl (2004). “Processes regulating oxygen and carbon dioxide in surface waters west of the Antarctic Peninsula”. *Marine Chemistry* 84, pp. 161–179. ISSN: 03044203. DOI: 10.1016/j.marchem.2003.07.004.

Cavalieri, D. J. and C. L. Parkinson (2012). “Arctic sea ice variability and trends, 1979-2010”. *The Cryosphere* 6, pp. 881–889. ISSN: 19940416. DOI: 10.5194/tc-6-881-2012.

Chapman, Christopher C. et al. (2020). “Defining Southern Ocean fronts and their influence on biological and physical processes in a changing climate”. *Nature Climate Change* 10.3, pp. 209–219. ISSN: 17586798. DOI: 10.1038/s41558-020-0705-4. URL: http://dx.doi.org/10.1038/s41558-020-0705-4.

Chapman, Christopher and Jean Baptiste Sallée (2017). “Isopycnal mixing suppression by the Antarctic Circumpolar Current and the Southern Ocean meridional overturning circulation”. *Journal of Physical Oceanography* 47.8, pp. 2023–2045. ISSN: 15200485. DOI: 10.1175/JPO-D-16-0263.1.

Chelton, Dudley B. et al. (1990). “Geosat altimeter observations of the surface circulation of the Southern Ocean”. *Journal of Geophical Research* 95.C10, pp. 17877–17903. DOI: 10.1029/JC095iC10p17877.

Chierici, M and A Fransson (2009). “Calcium carbonate saturation in the surface water of the Arctic Ocean: undersaturation in freshwater influenced shelves”. *Biogeosciences* 6, pp. 2421–2432.

Clarke, Andrew et al. (2008). “Seasonal and interannual variability in temperature, chlorophyll and macronutrients in northern Marguerite Bay, Antarctica”. *Deep-Sea Research Part II: Topical Studies in Oceanography* 55.18-19, pp. 1988–2006. ISSN: 09670645. DOI: 10.1016/j.dsr2.2008.04.035.

Clem, Kyle R. and Ryan L. Fogt (2013). “Varying roles of ENSO and SAM on the Antarctic Peninsula climate in austral spring”. *Journal of Geophysical Research Atmospheres* 118.20, pp. 11, 481–11, 492. ISSN: 21698996. DOI: 10.1002/jgrd.50860.

Clem, Kyle R et al. (2016). “The relative influence of ENSO and SAM on Antarctic Peninsula climate”. *Journal of Geophysical Research: Atmospheres* 121, pp. 9324–9341. DOI: 10.1002/2016JD025305.

Connolley, William (2004). *Antarctic Meteorology Online BAS*. URL: https://legacy.bas.ac.uk/met/metlog/ (visited on 01/20/2021).

Cox, Gordon F.N. and Wilford F. Weeks (1982). “Equations for determining the gas and brine volumes in sea ice samples”. *CRREL Report (US Army Cold Regions Research and Engineering Laboratory)* 29.102, pp. 306–316. ISSN: 0022-1430. DOI: 10.3189/s0022143000008364.

CPC (2023). *Monthly atmospheric and SST indices.* Climate Prediction Centre, NOAA. URL: https://www.cpc.ncep.noaa.gov/data/indices/ (visited on 03/14/2022).

Cyronak, Tyler, Kai G. Schulz, and Paul L. Jokiel (2016). "The Omega myth: what really drives lower calcification rates in an acidifying ocean Tyler". *ICES Journal of Marine Science* 73.3, pp. 558–562. DOI: 10.1093/icesjms/fsv075.

Dai, Aiguo et al. (2019). "Arctic amplification is caused by sea-ice loss under increasing CO_2". *Nature Communications* 10, pp. 1–13. ISSN: 20411723. DOI: 10.1038/s41467-018-07954-9. URL: http://dx.doi.org/10.1038/s41467-018-07954-9.

de Boyer Montégut, Clément et al. (2004). "Mixed layer depth over the global ocean: An examination of profile data and a profile-based climatology". *Journal of Geophysical Research: Oceans* 109.12, pp. 1–20. ISSN: 21699291. DOI: 10.1029/2004JC002378.

Deacon, G. E.R. (1979). "The Weddell Gyre". *Deep Sea Research Part A, Oceanographic Research Papers* 26.9, pp. 981–995. ISSN: 01980149. DOI: 10.1016/0198-0149(79)90044-X.

Delille, Bruno et al. (2014). "Southern Ocean CO_2 sink: The contribution of the sea ice". *Journal of Geophysical Research: Oceans* 119, pp. 3868–3882. DOI: 10.1002/2014JC009941.Received. URL: http://onlinelibrary.wiley.com/doi/10.1002/jgrc.20353/abstract.

DeVries, Tim (2014). "The oceanic anthropogenic CO_2 sink: Storage, air-sea fluxes, and transports over the industrial era". *Global Biogeochemical Cycles* 28.7, pp. 631–647. ISSN: 19449224. DOI: 10.1002/2013GB004739.

— (2022). "Atmospheric CO_2 and sea surface temperature variability cannot explain recent decadal variability of the ocean CO_2 sink". *Geophysical Research Letters* 49.7, pp. 1–12. ISSN: 19448007. DOI: 10.1029/2021GL096018.

Dickson, A. G. (1981). "An exact definition of total alkalinity and a procedure for the estimation of alkalinity and total inorganic carbon from titration data". *Deep Sea Research Part A, Oceanographic Research Papers* 28.6, pp. 609–623. ISSN: 01980149. DOI: 10.1016/0198-0149(81)90121-7.

— (1990). "Standard potential of the reaction: AgCl(s) + 1 2H2(g) = Ag(s) + HCl(aq), and and the standard acidity constant of the ion HSO4- in synthetic sea water from 273.15 to 318.15 K". *The Journal of Chemical Thermodynamics* 22.2, pp. 113–127. ISSN: 10963626. DOI: 10.1016/0021-9614(90)90074-Z.

Dickson, A. G. and F. J. Millero (1987). "A comparison of the equilibrium constants for the dissociation of carbonic acid in seawater media". *Deep Sea Research Part A, Oceanographic Research Papers* 34.10, pp. 1733–1743. ISSN: 01980149. DOI: 10.1016/0198-0149(87)90021-5.

Dickson, A. G., C. L. Sabine, and J. R. Christian (2007). *Guide to Best Practices for Ocean CO_2 Measurements.* Ed. by A. G. Dickson, C. L. Sabine, and J. R. Christian. North Pacific Marine Science Organization, p. 191. ISBN: 1897176074. DOI: 10.25607/OBP-1342. URL: www.pices.int.

Dickson, A.G. and J.P. Riley (1979). "The estimation of acid dissociation constants in sea-water media from potentiometric titrations with strong base". 7, pp. 101–

109. DOI: 10.1016/0304-4203(79)90002-1. URL: https://doi.org/10.1016/0304-4203(79)90002-1.

Dieckmann, Gerhard S. et al. (2008). “Calcium carbonate as ikaite crystals in Antarctic sea ice”. *Geophysical Research Letters* 35.8, pp. 35–37. ISSN: 00948276. DOI: 10.1029/2008GL033540.

Dlugokencky, E.J. et al. (2019). *Atmospheric Carbon Dioxide Dry Air Mole Fractions from the NOAA ESRL Carbon Cycle Cooperative Global Air Sampling Network, 1968-2018*. data set. Version: 2019–07. DOI: https://doi.org/10.15138/wkgj-f215.

Dmitrenko, Igor A. et al. (2012). “Tide-induced vertical mixing in the Laptev Sea coastal polynya”. *Journal of Geophysical Research: Oceans* 117.5, pp. 1–19. ISSN: 21699291. DOI: 10.1029/2011JC006966.

Doney, Scott C. et al. (2009). “Ocean acidification: The other CO_2 problem”. *Annual Review of Marine Science* 1, pp. 169–192. ISSN: 19411405. DOI: 10.1146/annurev.marine.010908.163834.

Dong, Yuanxu et al. (2021). “Near-surface stratification due to ice melt biases Arctic air-sea CO_2 flux estimates”. *Geophysical Research Letters* 48.22, pp. 1–10. ISSN: 19448007. DOI: 10.1029/2021GL095266.

Dong, Yuanxu et al. (2022). “Update on the temperature corrections of global air-sea CO_2 flux estimates”. *Global Biogeochemical Cycles* 36.9, pp. 1–13. ISSN: 19449224. DOI: 10.1029/2022GB007360.

Driemel, Amelie et al. (2017). “From pole to pole: 33 years of physical oceanography onboard R/V Polarstern”. *Earth System Science Data* 9.1, pp. 211–220. ISSN: 18663516. DOI: 10.5194/essd-9-211-2017.

Droste, Elise S. et al. (2022). “The influence of tides on the marine carbonate chemistry of a coastal polynya in the south-eastern Weddell Sea”. *Ocean Science* 18.5, pp. 1293–1320. DOI: 10.5194/os-18-1293-2022.

Ducklow, Hugh W. et al. (2013). “West Antarctic peninsula: An ice-dependent coastal marine ecosystem in transition”. *Oceanography* 26.3, pp. 190–203. ISSN: 10428275. DOI: 10.5670/oceanog.2013.62.

Eayrs, Clare et al. (2021). “Rapid decline in Antarctic sea ice in recent years hints at future change”. *Nature Geoscience* 14, pp. 460–464. ISSN: 17520908. DOI: 10.1038/s41561-021-00768-3. URL: http://dx.doi.org/10.1038/s41561-021-00768-3.

Eicken, Hajo and Manfred A. Lange (1989). “Development and properties of sea ice in the coastal regime of the southeastern Weddell Sea”. *Journal of Geophysical Research: Oceans: Oceans* 94.C6, pp. 8193–8206. DOI: 10.1029/JC094iC06p08193.

Else, Brent G.T. et al. (2013). “Further observations of a decreasing atmospheric CO_2 uptake capacity in the Canada Basin (Arctic Ocean) due to sea ice loss”. *Geophysical Research Letters* 40.6, pp. 1132–1137. ISSN: 00948276. DOI: 10.1002/grl.50268.

ESA (2021). *Sentinel 1 SAR Dataset*. European Space Agency. Data retrieved from Copernicus Open Access Hub: https://scihub.copernicus.eu/.

Fahrbach, E. et al. (1994). “Suppression of bottom water formation in the southeastern Weddell sea”. *Deep-Sea Research Part I* 41.2, pp. 389–411. ISSN: 09670637. DOI: 10.1016/0967-0637(94)90010-8.

Fairall, C. W. et al. (2011). “Implementation of the coupled ocean-atmosphere response experiment flux algorithm with CO_2, dimethyl sulfide, and O3”. *Journal of Geophysical Research: Oceans* 116.C00F09, pp. 1–15. ISSN: 21699291. DOI: 10.1029/2010JC006884.

Feely, Richard A. et al. (2004). “Impact of anthropogenic CO_2 on the CaCO3 system in the oceans”. *Science* 305, pp. 362–366. DOI: 10.2134/jae1985.0003.

Fer, Ilker et al. (2022). “Upper-ocean turbulence structure and ocean-ice drag coefficient estimates using an ascending microstructure profiler during the MOSAiC Drift”. *Journal of Geophysical Research: Oceans* 127.9, pp. 1–23. ISSN: 2169-9275. DOI: 10.1029/2022jc018751.

Fogt, Ryan L, David H Bromwich, and Keith M Hines (2011). “Understanding the SAM influence on the South Pacific ENSO teleconnection”. *Climate Dynamics* 36, pp. 1555–1576. DOI: 10.1007/s00382-010-0905-0.

Fong, Michael B. and Andrew G. Dickson (2019). “Insights from GO-SHIP hydrography data into the thermodynamic consistency of CO_2 system measurements in seawater”. *Marine Chemistry* 211.September 2018, pp. 52–63. ISSN: 03044203. DOI: 10.1016/j.marchem.2019.03.006. URL: https://doi.org/10.1016/j.marchem.2019.03.006.

Foster, Theodore D. and Eddy C. Carmack (1976). “Temperature and salinity structure in the Weddell Sea”. *Journal of Physical Oceanography* 6, pp. 36–44.

Fransson, Agneta, Melissa Chierici, and Yukihiro Nojiri (2009). “New insights into the spatial variability of the surface water carbon dioxide in varying sea ice conditions in the Arctic Ocean”. *Continental Shelf Research* 29.10, pp. 1317–1328. ISSN: 02784343. DOI: 10.1016/j.csr.2009.03.008.

Fransson, Agneta et al. (2011). “Antarctic sea ice carbon dioxide system and controls”. *Journal of Geophysical Research: Oceans* 116.12, pp. 1–18. ISSN: 21699291. DOI: 10.1029/2010JC006844.

Fransson, Agneta et al. (2013). “Impact of sea-ice processes on the carbonate system and ocean acidification at the ice-water interface of the Amundsen Gulf, Arctic Ocean”. *Journal of Geophysical Research: Oceans* 118.12, pp. 7001–7023. ISSN: 21699291. DOI: 10.1002/2013JC009164.

Fransson, Agneta et al. (2017). “Effects of sea-ice and biogeochemical processes and storms on under-ice water fCO_2 during the winter-spring transition in the high Arctic Ocean: Implications for sea-air CO_2 fluxes”. *Journal of Geophysical Research: Oceans* 122.7, pp. 5566–5587. DOI: 10.1002/2016JC012478.

Fransson, A et al. (2001). “The importance of shelf processes for the modification of chemical constituents in the waters of the Eurasian Arctic Ocean: implication for carbon fluxes”. *Continental Shelf Research* 21, pp. 225–242.

Friedlingstein, Pierre et al. (2022). “Global Carbon Budget 2022”. *Earth System Science Data* 14.11, pp. 4811–4900. DOI: 10.5194/essd-14-4811-2022.

Friis, K., A. Körtzinger, and D. W.R. Wallace (2003). "The salinity normalization of marine inorganic carbon chemistry data". *Geophysical Research Letters* 30.2, pp. 1–4. ISSN: 00948276. DOI: 10.1029/2002GL015898.

Frölicher, Thomas L. et al. (2015). "Dominance of the Southern Ocean in anthropogenic carbon and heat uptake in CMIP5 models". *Journal of Climate* 28.2, pp. 862–886. ISSN: 08948755. DOI: 10.1175/JCLI-D-14-00117.1.

García-Ibáñez, Maribel I. et al. (2022). "Gaining insights into the seawater carbonate system using discrete fCO_2 measurements". *Marine Chemistry* 245.104150, pp. 1–10. ISSN: 03044203. DOI: 10.1016/j.marchem.2022.104150.

GEBCO (2022). *GEBCO 2022 Grid*. DOI: 10.5285/e0f0bb80-ab44-2739-e053-6c86abc0289c. URL: https://www.gebco.net/data%7B%5C_%7Dand%7B%5C_%7Dproducts/gridded%7B%5C_%7Dbathymetry%7B%5C_%7Ddata/ (visited on 01/11/2023).

Geilfus, N. X. et al. (2012). "Dynamics of pCO_2 and related air-ice CO_2 fluxes in the Arctic coastal zone (Amundsen Gulf, Beaufort Sea)". *Journal of Geophysical Research: Oceans* 117.C00G10, pp. 1–15. ISSN: 21699291. DOI: 10.1029/2011JC007118.

Geilfus, N. X. et al. (2013). "First estimates of the contribution of CaCO3 precipitation to the release of CO_2 to the atmosphere during young sea ice growth". *Journal of Geophysical Research: Oceans* 118, pp. 244–255. ISSN: 21699291. DOI: 10.1029/2012JC007980.

Geilfus, Nicolas Xavier et al. (2016). "Estimates of ikaite export from sea ice to the underlying seawater in a sea ice-seawater mesocosm". *The Cryosphere* 10, pp. 2173–2189. ISSN: 19940424. DOI: 10.5194/tc-10-2173-2016.

Gerland, Sebastian et al. (2019). "Essential gaps and uncertainties in the understanding of the roles and functions of Arctic sea ice". *Environmental Research Letters* 14.043002, pp. 1–13. ISSN: 17489326. DOI: 10.1088/1748-9326/ab09b3. URL: http://dx.doi.org/10.1088/1748-9326/ab09b3.

Gerringa, Loes J.A. et al. (2012). "Iron from melting glaciers fuels the phytoplankton blooms in Amundsen Sea (Southern Ocean): Iron biogeochemistry". *Deep-Sea Research Part II: Topical Studies in Oceanography* 71-76, pp. 16–31. ISSN: 09670645. DOI: 10.1016/j.dsr2.2012.03.007.

Gerrish, L., P. Fretwell, and P. Cooper (2020). *High resolution vector polygons of the Antarctic coastline (7.3) [Data set].* data set. DOI: 10.5285/0a6d85d7-fc9c-4d68-a58d-e792f68ae9f4.

Gleitz, Markus, Ulrich V. Bathmann, and Karin Lochte (1994). "Build-up and decline of summer phytoplankton biomass in the eastern Weddell Sea, Antarctica". *Polar Biology* 14.6, pp. 413–422. ISSN: 07224060. DOI: 10.1007/BF00240262.

Golden, K. M., S. F. Ackley, and V. I. Lytle (1998). "The percolation phase transition in sea ice". *Science* 282.5397, pp. 2238–2241. ISSN: 00368075. DOI: 10.1126/science.282.5397.2238.

Goldman, Joel C. and Peter G. Brewer (1980). "Effect of nitrogen source and growth rate on phytoplankton-mediated changes in alkalinity". *Limnology and Oceanography* 25.2, pp. 352–357. DOI: 10.4319/lo.1980.25.2.0352.

González-Dávila, Melchor et al. (2022). *Dissolved inorganic carbon and total alkalinity of seawater samples from a Weddell Sea coastal polynya during two tidal observation case studies for RV POLARSTERN expeditions PS89 and PS117.* data set. DOI: 10.1594/PANGAEA.946363. URL: https://doi.org/10.1594/PANGAEA.946363.

Good, Simon et al. (2020). "The current configuration of the OSTIA system for operational production of foundation sea surface temperature and ice concentration analyses". *Remote Sensing* 12.4, pp. 1–20. ISSN: 20724292. DOI: 10.3390/rs12040720.

Goyet, Catherine and Alain Poisson (1989). "New determination of carbonic acid dissociation constants in seawater as a function of temperature and salinity". *Deep Sea Research* 30.11, pp. 1635–1654. DOI: 10.1016/0198-0149(89)90064-2. URL: https://doi.org/10.1016/0198-0149(89)90064-2.

Gray, Alison R. et al. (2018). "Autonomous Biogeochemical Floats Detect Significant Carbon Dioxide Outgassing in the High-Latitude Southern Ocean". *Geophysical Research Letters* 45.17, pp. 9049–9057. ISSN: 19448007. DOI: 10.1029/2018GL078013.

Greene, Charles, Thomas M. Cronin, and A. J. Pershing (2008). "Arctic climate change and its impacts on the ecology of the North Atlantic". *Ecology* 89.11, S24–S38. DOI: 10.1890/07-0550.1.

Gregor, Luke, Schalk Kok, and Pedro M.S. Monteiro (2018). "Interannual drivers of the seasonal cycle of CO_2 in the Southern Ocean". *Biogeosciences* 15.8, pp. 2361–2378. ISSN: 17264189. DOI: 10.5194/bg-15-2361-2018.

Gruber, Nicolas, Peter Landschützer, and Nicole S. Lovenduski (2019). "The variable Southern Ocean carbon sink". *Annual Review of Marine Science* 11, pp. 159–86. DOI: 10.1146/annurev-marine-121916-063407.

Gruber, Nicolas et al. (2009). "Oceanic sources, sinks, and transport of atmospheric CO_2". *Global Biogeochemical Cycles* 23.GB1005, pp. 1–21. ISSN: 08866236. DOI: 10.1029/2008GB003349.

Hauck, Judith et al. (2020). "Consistency and challenges in the ocean carbon wink estimate for the Global Carbon Budget". *Frontiers in Marine Science* 7, pp. 1–22. ISSN: 22967745. DOI: 10.3389/fmars.2020.571720.

Haumann, F. Alexander, Nicolas Gruber, and Matthias Münnich (2020). "Sea ice induced Southern Ocean subsurface warming and surface cooling in a warming climate". *AGU Advances* 1.e2019AV000132, pp. 1–22. ISSN: 2576-604X. DOI: 10.1029/2019av000132.

Hauri, C. et al. (2015). "Two decades of inorganic carbon dynamics along the West Antarctic Peninsula". *Biogeosciences* 12.22, pp. 6761–6779. ISSN: 17264189. DOI: 10.5194/bg-12-6761-2015.

Henley, Sian F. et al. (2017). "Macronutrient supply, uptake and recycling in the coastal ocean of the west Antarctic Peninsula". *Deep-Sea Research Part II: Topical Studies in Oceanography* 139, pp. 58–76. ISSN: 09670645. DOI: 10.1016/j.dsr2.2016.10.003. URL: http://dx.doi.org/10.1016/j.dsr2.2016.10.003.

Henley, Sian F. et al. (2018). "Macronutrient and carbon supply, uptake and cycling across the Antarctic Peninsula shelf during summer". *Philosophical Transactions of* *the Royal Society A: Mathematical, Physical and Engineering Sciences* 376.2122, pp. 1–28. ISSN: 1364503X. DOI: 10.1098/rsta.2017.0168.

Heywood, Karen J et al. (1998). "Transport and water masses of the Antarctic slope front system in the eastern Weddell Sea". *Ocean, ice, and atmosphere: Interactions at the Antarctic continental margin, Antarctic Research Series* 75, pp. 203–214.

Ho, David T. et al. (2006). "Measurements of air-sea gas exchange at high wind speeds in the Southern Ocean: Implications for global parameterizations". *Geophysical Research Letters* 33.16, p. L16611. ISSN: 00948276. DOI: 10.1029/2006GL026817.

Holmes, Robert Max et al. (2012). "Seasonal and annual fluxes of nutrients and organic matter from large rivers to the Arctic Ocean and surrounding seas". *Estuaries and Coasts* 35, pp. 369–382. ISSN: 15592723. DOI: 10.1007/s12237-011-9386-6.

Hoppe, C. J.M. et al. (2012). "Implications of observed inconsistencies in carbonate chemistry measurements for ocean acidification studies". *Biogeosciences* 9.7, pp. 2401–2405. ISSN: 17264170. DOI: 10.5194/bg-9-2401-2012.

Hoppema, M. and L. G. Anderson (2007). "Chapter 6 Biogeochemistry of Polynyas and Their Role in Sequestration of Anthropogenic Constituents". *Elsevier Oceanography Series*. Ed. by W. O. Smith and D. G. Barber. Vol. 74. 06. Chap. 6, pp. 193–221. ISBN: 9780444529527. DOI: 10.1016/S0422-9894(06)74006-5.

Hoppema, Mario (2004). "Weddell Sea is a globally significant contributor to deep-sea sequestration of natural carbon dioxide". *Deep-Sea Research Part I: Oceanographic Research Papers* 51.9, pp. 1169–1177. ISSN: 09670637. DOI: 10.1016/j.dsr.2004.02.011.

Hoppema, Mario et al. (1999). "Annual uptake of atmospheric CO_2 by the Weddell sea derived from a surface layer balance, including estimations of entrainment and new production". *Journal of Marine Systems* 19.4, pp. 219–233. ISSN: 09247963. DOI: 10.1016/S0924-7963(98)00091-8.

Hoppema, Mario et al. (2002). "Renewal time and transport of unventilated Central intermediate water of the Weddell Sea derived from biogeochemical properties". *Journal of Marine Research* 60.5, pp. 677–697. ISSN: 00222402. DOI: 10.1357/002224002762688696.

Hoppmann, Mario et al. (2015). "Ice platelets below Weddell Sea landfast sea ice". *Annals of Glaciology* 56.69, pp. 175–190. ISSN: 02603055. DOI: 10.3189/2015AoG69A678.

Huhn, Oliver et al. (2013). "Decline of deep and bottom water ventilation and slowing down of anthropogenic carbon storage in the Weddell Sea, 1984-2011". *Deep-Sea Research Part I: Oceanographic Research Papers* 76, pp. 66–84. ISSN: 09670637. DOI: 10.1016/j.dsr.2013.01.005. URL: http://dx.doi.org/10.1016/j.dsr.2013.01.005.

Humphreys, M. P. and R. S. Matthews (2022). "Calkulate: total alkalinity from titration data in Python". *Zenedo*. DOI: 10.5281/zenodo.2634304. URL: https://mphumphreys.wordpress.com/projects/software/calkulate/.

Humphreys, Matthew P. et al. (2022). "PyCO_2SYS v1.8: Marine carbonate system calculations in Python". *Geoscientific Model Development* 15.1, pp. 15–43. ISSN: 19919603. DOI: 10.5194/gmd-15-15-2022.

Huot, Pierre Vincent et al. (2021). “Influence of ocean tides and ice shelves on ocean-ice interactions and dense shelf water formation in the D’Urville Sea, Antarctica”. *Ocean Modelling* 162.March 2020, p. 101794. ISSN: 14635003. DOI: 10.1016/j.ocemod.2021.101794. URL: https://doi.org/10.1016/j.ocemod.2021.101794.

Ivanov, V. V. et al. (2004). “Cascades of dense water around the world ocean”. *Progress in Oceanography* 60, pp. 47–98. ISSN: 00796611. DOI: 10.1016/j.pocean.2003.12.002.

Jähne, Bernd (2019). “Air-sea gas exchange”. *Encyclopedia of Ocean Sciences*. Ed. by J. Kirk Cochran, Henry Bokuniewicz, and Patricia Yager. 3rd ed. Academic Press. Chap. 6, pp. 1–13. ISBN: 9780124095489. DOI: 10.1016/B978-0-12-409548-9.11613-6.

Janout, Markus A. et al. (2016). “Sea-ice retreat controls timing of summer plankton blooms in the Eastern Arctic Ocean”. *Geophysical Research Letters* 43.24, pp. 12, 493–12, 501. ISSN: 19448007. DOI: 10.1002/2016GL071232.

Jiang, Li Qing et al. (2019). “Surface ocean pH and buffer capacity: past, present and future”. *Scientific Reports* 9.18924, pp. 1–11. ISSN: 20452322. DOI: 10.1038/s41598-019-55039-4. URL: http://dx.doi.org/10.1038/s41598-019-55039-4.

Johnson, K. M. (1992). *Operator’s Manual: Single-Operator Multiparameter Metabolic Analyzer (SOMMA) for Total Carbon Dioxide (CT) with Coulometric Detection*. Tech. rep. New York: Brookhaven National Lab. Upton, NY. DOI: 10.2172/10194787. URL: https://doi.org/10.2172/10194787.

Johnson, Kenneth M., Arthur E. King, and John McN. Sieburth (1985). “Coulometric TCO_2 analyses for marine studies: An introduction”. *Marine Chemistry* 16.1, pp. 61–82. ISSN: 03044203. DOI: 10.1016/0304-4203(85)90028-3.

Jones, E. P., B. Rudels, and L. G. Anderson (1995). “Deep waters of the Arctic Ocean: origins and circulation”. *Deep-Sea Research Part I* 42.5, pp. 737–760. ISSN: 09670637. DOI: 10.1016/0967-0637(95)00013-V.

Jones, Elizabeth M. et al. (2017a). “Mesoscale features create hotspots of carbon uptake in the Antarctic Circumpolar Current”. *Deep-Sea Research Part II: Topical Studies in Oceanography* 138, pp. 39–51. ISSN: 09670645. DOI: 10.1016/j.dsr2.2015.10.006. URL: http://dx.doi.org/10.1016/j.dsr2.2015.10.006.

Jones, Elizabeth M. et al. (2017b). “Ocean acidification and calcium carbonate saturation states in the coastal zone of the West Antarctic Peninsula”. *Deep-Sea Research Part II: Topical Studies in Oceanography* 139, pp. 181–194. ISSN: 09670645. DOI: 10.1016/j.dsr2.2017.01.007. URL: http://dx.doi.org/10.1016/j.dsr2.2017.01.007.

Jones, Elizabeth M. et al. (2021). “Calcium carbonate saturation states along the West Antarctic Peninsula”. *Antarctic Science* 21, pp. 1–21. ISSN: 13652079. DOI: 10.1017/S0954102021000456.

Jones, Elizabeth M. et al. (2022). “Carbon and nutrient cycling in Antarctic landfast sea ice from winter to summer”. *Limnology and Oceanography*, pp. 1–24. ISSN: 0024-3590. DOI: 10.1002/lno.12260.

Kawaguchi, Yusuke et al. (2022). “Turbulent mixing during late summer in the ice-ocean boundary layer in the Central Arctic Ocean: Results from the MOSAiC Expedition”.

Journal of Geophysical Research: Oceans 127.8, pp. 1–30. ISSN: 21699291. DOI: 10.1029/2021JC017975.

Khatiwala, S., F. Primeau, and T. Hall (2009). "Reconstruction of the history of anthropogenic CO_2 concentrations in the ocean". *Nature* 462.7271, pp. 346–349. ISSN: 00280836. DOI: 10.1038/nature08526. URL: http://dx.doi.org/10.1038/nature08526.

Kirillov, Sergey A. et al. (2013). "The penetrative mixing in the Laptev Sea coastal polynya pycnocline layer". *Continental Shelf Research* 63.March 2008, pp. 34–42. ISSN: 02784343. DOI: 10.1016/j.csr.2013.04.040. URL: http://dx.doi.org/10.1016/j.csr.2013.04.040.

König-Langlo, Gert (2015). *Meteorological observations during POLARSTERN cruise PS89 (ANT-XXX/2).* data set. Alfred Wegener Institute, Helmholtz Centre for Polar and Marine Research, Bremerhaven. DOI: 10.1594/PANGAEA.844571. URL: https://doi.org/10.1594/PANGAEA.844571.

Kotovitch, Marie et al. (2016). "Air-ice carbon pathways inferred from a sea ice tank experiment". *Elementa* 4.000112, pp. 1–15. ISSN: 23251026. DOI: 10.12952/journal.elementa.000112.

Krumpen, Thomas et al. (2021). "MOSAiC drift expedition from October 2019 to July 2020: Sea ice conditions from space and comparison with previous years". *Cryosphere* 15.8, pp. 3897–3920. ISSN: 19940424. DOI: 10.5194/tc-15-3897-2021.

Kwok, R (2018). "Arctic sea ice thickness , volume , and multiyear ice coverage: losses and coupled variability (1958 - 2018)". *Environmental Research Letters* 13.105005, pp. 1–9. DOI: 10.1088/1748-9326/aae3ec.

Kwok, R and D A Rothrock (2009). "Decline in Arctic sea ice thickness from submarine and ICESat records : 1958 - 2008". *Geophysical Research Letters* 36.L15501, pp. 1–5. DOI: 10.1029/2009GL039035.

Lake, R. A. and E. L. Lewis (1970). "Salt rejection by sea ice during growth". *Journal of Geophysical Research* 75.3, pp. 583–597. DOI: 10.1029/jc075i003p00583.

Landschützer, Peter, Nicolas Gruber, and Dorothee C.E. Bakker (2016). "Decadal variations and trends of the global ocean carbon sink". *Global Biogeochemical Cycles* 30.10, pp. 1396–1417. ISSN: 19449224. DOI: 10.1002/2015GB005359.

Landschützer, Peter et al. (2014). "Recent variability of the global ocean carbon sink". *Global biogeochemical cycles* 28, pp. 927–949. DOI: 10.1002/2014GB004853.

Landschützer, Peter et al. (2015). "The reinvigoration of the Southern Ocean carbon sink". *Science* 349.6253, pp. 1221–1224. DOI: 10.1126/science.aab2620.

Landschützer, Peter et al. (2020). "A uniform pCO_2 climatology combining open and coastal oceans". *Earth System Science Data Discussions* 12, pp. 2536–2553. DOI: 10.5194/essd-12-2537-2020.

Lannuzel, Delphine et al. (2020). "The future of Arctic sea-ice biogeochemistry and ice-associated ecosystems". *Nature Climate Change* 10.11, pp. 983–992. ISSN: 17586798. DOI: 10.1038/s41558-020-00940-4. URL: http://dx.doi.org/10.1038/s41558-020-00940-4.

Le Quéré, Corinne et al. (2007). "Saturation of the southern ocean CO_2 sink due to recent climate change". *Science* 316.5832, pp. 1735–1738. ISSN: 00368075. DOI: 10.1126/science.1136188.

Lee, Kitack, Frank J. Millero, and Douglas M. Campbell (1996). "The reliability of the thermodynamic constants for the dissociation of carbonic acid in seawater". *Marine Chemistry* 55.3-4, pp. 233–245. ISSN: 03044203. DOI: 10.1016/S0304-4203(96)00064-3.

Legendre, L. and J. Michaud (1999). "Chlorophyll a to estimate the particulate organic carbon available as food to large zooplankton in the euphotic zone of oceans". *Journal of Plankton Research* 21.11, pp. 2067–2083. ISSN: 01427873. DOI: 10.1093/plankt/21.11.2067.

Legge, Oliver J. et al. (2015). "The seasonal cycle of ocean-atmosphere CO_2 flux in Ryder Bay, west Antarctic Peninsula". *Geophysical Research Letters* 42.8, pp. 2934–2942. ISSN: 19448007. DOI: 10.1002/2015GL063796.

Legge, Oliver J. et al. (2017). "The seasonal cycle of carbonate system processes in Ryder Bay, West Antarctic Peninsula". *Deep-Sea Research Part II: Topical Studies in Oceanography* 139, pp. 167–180. ISSN: 09670645. DOI: 10.1016/j.dsr2.2016.11.006. URL: http://dx.doi.org/10.1016/j.dsr2.2016.11.006.

Legrésy, Benoît et al. (2004). "Influence of tides and tidal current on Mertz Glacier, Antarctica". *Journal of Glaciology* 50.170, pp. 427–435. ISSN: 00221430. DOI: 10.3189/172756504781829828.

Lencina-Avila, Jannine M. et al. (2018). "Past and future evolution of the marine carbonate system in a coastal zone of the Northern Antarctic Peninsula". *Deep-Sea Research Part II: Topical Studies in Oceanography* 149, pp. 193–205. ISSN: 09670645. DOI: 10.1016/j.dsr2.2017.10.018. URL: https://doi.org/10.1016/j.dsr2.2017.10.018.

Lenton, Andrew and Richard J. Matear (2007). "Role of the Southern Annular Mode (SAM) in Southern Ocean CO_2 uptake". *Global Biogeochemical Cycles* 21.2, pp. 1–17. ISSN: 08866236. DOI: 10.1029/2006GB002714.

Lenton, Andrew, Richard J. Matear, and Bronte Tilbrook (2006). "Design of an observational strategy for quantifying the Southern Ocean uptake of CO_2". *Global Biogeochemical Cycles* 20.4, pp. 1–11. ISSN: 08866236. DOI: 10.1029/2005GB002620.

Lenton, Andrew et al. (2013). "Sea-air CO_2 fluxes in the Southern Ocean for the period 1990-2009". *Biogeosciences Discussions* 10.1, pp. 285–333. ISSN: 1810-6277. DOI: 10.5194/bgd-10-285-2013.

Lewis, E and D Wallace (1998). *Program Developed for CO_2 System Calculations*. Carbon Dioxide Information Analysis Center, pp. 1–29.

Llanillo, P. J. et al. (2019). "Oceanographic Variability induced by Tides, the Intraseasonal Cycle and Warm Subsurface Water intrusions in Maxwell Bay, King George Island (West-Antarctica)". *Scientific Reports* 9.1, pp. 1–17. ISSN: 20452322. DOI: 10.1038/s41598-019-54875-8.

Loose, Brice and Peter Schlosser (2011). “Sea ice and its effect on CO_2 flux between the atmosphere and the Southern Ocean interior”. *Journal of Geophysical Research: Oceans* 116.C11019, pp. 1–15. ISSN: 21699291. DOI: 10.1029/2010JC006509.

Loose, Brice et al. (2014). “A parameter model of gas exchange for the seasonal sea ice zone”. *Ocean Science Discussions* 10.1, pp. 17–28. DOI: 10.5194/os-10-17-2014.

Lovenduski, Nicole S. et al. (2007). “Enhanced CO_2 outgassing in the Southern Ocean from a positive phase of the Southern Annular Mode”. *Global Biogeochemical Cycles* 21.2, pp. 1–14. ISSN: 08866236. DOI: 10.1029/2006GB002900.

Lueker, Timothy J., Andrew G. Dickson, and Charles D. Keeling (2000). “Ocean pCO_2 calculated from dissolved inorganic carbon, alkalinity, and equations for K1 and K2: Validation based on laboratory measurements of CO_2 in gas and seawater at equilibrium”. *Marine Chemistry* 70.1-3, pp. 105–119. ISSN: 03044203. DOI: 10.1016/S0304-4203(00)00022-0.

Makinson, Keith et al. (2011). “Influence of tides on melting and freezing beneath Filchner-Ronne Ice Shelf, Antarctica”. *Geophysical Research Letters* 38.6, pp. 4–9. ISSN: 00948276. DOI: 10.1029/2010GL046462.

Markus, Thorsten, Julienne C. Stroeve, and Jeffrey Miller (2009). “Recent changes in Arctic sea ice melt onset, freezeup, and melt season length”. *Journal of Geophysical Research: Oceans* 114.C12024, pp. 1–14. ISSN: 21699291. DOI: 10.1029/2009JC005436.

Marshall, Gareth (2023). *An observation-based Southern Hemisphere Annular Mode Index.* URL: legacy.bas.ac.uk/met/gjma/sam.html (visited on 01/07/2022).

Marshall, Gareth J. (2003). “Trends in the Southern Annular Mode from observations and reanalyses”. *Journal of Climate* 16.24, pp. 4134–4143. ISSN: 08948755. DOI: 10.1175/1520-0442(2003)016<4134:TITSAM>2.0.CO;2.

Martinson, D. G. and D. C. McKee (2012). “Transport of warm upper circumpolar deep water onto the Western Antarctic Peninsula Continental Shelf”. *Ocean Science* 8.4, pp. 433–442. ISSN: 18120784. DOI: 10.5194/os-8-433-2012.

Martinson, Douglas G. and Richard A. Iannuzzi (1998). “Antarctic Ocean-Ice Interaction: Implications from Ocean Bulk Property Distributions in the Weddell Gyre”. *Antarctic sea ice: Physical processes, Interactions and variability* 74, pp. 243–271. DOI: 10.1029/ar074p0243.

Martinson, Douglas G. and Michael Steele (2001). “Future of the Arctic sea ice cover: Implications of an Antarctic analog”. *Geophysical Research Letters* 28.2, pp. 307–310. ISSN: 00948276. DOI: 10.1029/2000gl011549.

Mathis, Jeremy T. et al. (2012). “Storm-induced upwelling of high pCO_2 waters onto the continental shelf of the western Arctic Ocean and implications for carbonate mineral saturation states”. *Geophysical Research Letters* 39.L07606, pp. 1–6. ISSN: 00948276. DOI: 10.1029/2012GL051574.

McElligott, S. et al. (1998). “Discrete water column measurements of CO_2 fugacity and pH(T) in seawater: A comparison of direct measurements and thermodynamic calculations”. *Marine Chemistry* 60.1-2, pp. 63–73. ISSN: 03044203. DOI: 10.1016/S0304-4203(97)00080-7.

McKinley, Galen A. et al. (2020). “External forcing explains recent decadal variability of the ocean carbon sink”. *AGU Advances* 1.2, pp. 1–10. ISSN: 2576-604X. DOI: 10.1029/2019av000149.

McPhee, M. G. et al. (2005). “Upwelling of Arctic pycnocline associated with shear motion of sea ice”. *Geophysical Research Letters* 32.L10616, pp. 1–4. ISSN: 00948276. DOI: 10.1029/2004GL021819.

Mehrbach, C. et al. (1973). “Measurement of the Apparent Dissociation Constants of Carbonic Acid in Seawater At Atmospheric Pressure”. *Limnology and Oceanography* 18.6, pp. 897–907. ISSN: 19395590. DOI: 10.4319/lo.1973.18.6.0897.

Meredith, Michael P. et al. (2008). “Variability in the freshwater balance of northern Marguerite Bay, Antarctic Peninsula: Results from δ18O”. *Deep-Sea Research Part II: Topical Studies in Oceanography* 55.3-4, pp. 309–322. ISSN: 09670645. DOI: 10.1016/j.dsr2.2007.11.005.

Meredith, Michael P. et al. (2010). “Changes in the freshwater composition of the upper ocean west of the Antarctic Peninsula during the first decade of the 21st century”. *Progress in Oceanography* 87.1-4, pp. 127–143. ISSN: 00796611. DOI: 10.1016/j.pocean.2010.09.019. URL: http://dx.doi.org/10.1016/j.pocean.2010.09.019.

Meredith, Michael P. et al. (2013). “The freshwater system west of the antarctic peninsula: Spatial and temporal changes”. *Journal of Climate* 26.5, pp. 1669–1684. ISSN: 08948755. DOI: 10.1175/JCLI-D-12-00246.1.

Meredith, Michael P. et al. (2017). “Changing distributions of sea ice melt and meteoric water west of the Antarctic Peninsula”. *Deep-Sea Research Part II: Topical Studies in Oceanography* 139, pp. 40–57. ISSN: 09670645. DOI: 10.1016/j.dsr2.2016.04.019. URL: http://dx.doi.org/10.1016/j.dsr2.2016.04.019.

Meredith, Michael P. et al. (2021). “Local- and large-scale drivers of variability in the coastal freshwater budget of the Western Antarctic Peninsula”. *Journal of Geophysical Research: Oceans* 126.6, pp. 1–22. ISSN: 21699291. DOI: 10.1029/2021JC017172.

Metzl, Nicolas (2019). “A canary in the Southern Ocean”. *Nature Climate Change* 9, pp. 651–652. ISSN: 17586798. DOI: 10.1038/s41558-019-0562-1.

Meyer, Amelie et al. (2017). “Mixing rates and vertical heat fluxes north of Svalbard from Arctic winter to spring”. *Journal of Geophysical Research: Oceans* 122, pp. 4569–4586. DOI: 10.1002/2016JC012441.

Middelburg, Jack J., Karline Soetaert, and Mathilde Hagens (2020). “Ocean alkalinity, buffering and biogeochemical processes”. *Reviews of Geophysics* 58.3, pp. 1–28. ISSN: 19449208. DOI: 10.1029/2019RG000681.

Mikis, Anna et al. (2019). “Temporal variability in foraminiferal morphology and geochemistry at the West Antarctic Peninsula: a sediment trap study”. *Biogeosciences* 16, pp. 3267–3282. DOI: 10.5194/bg-16-3267-2019.

Miller, Lisa A. et al. (2011). “Carbon dynamics in sea ice: A winter flux time series”. *Journal of Geophysical Research: Oceans* 116.2, pp. 1–20. ISSN: 21699291. DOI: 10.1029/2009JC006058.

Miller, Lisa A. et al. (2019). “Air-sea CO_2 flux estimates in stratified Arctic coastal waters: How wrong can we be?” *Geophysical Research Letters* 46, pp. 235–243. ISSN: 19448007. DOI: 10.1029/2018GL080099.

Millero, Frank J. et al. (2002). “Dissociation constants for carbonic acid determined from field measurements”. *Deep-Sea Research Part I: Oceanographic Research Papers* 49.10, pp. 1705–1723. ISSN: 09670637. DOI: 10.1016/S0967-0637(02)00093-6.

Mintrop, Ludger (2003). *VINDTA Manual for Versions 3S and 3C*. Tech. rep. Kiel, pp. 1–136.

— (2016). *VINDTA 3C Manual*. Manual downloaded from https://www.marianda.com/. URL: https://www.marianda.com/.

Mo, Ahra et al. (2022). “Impact of Sea Ice Melting on Summer Air-Sea CO_2 Exchange in the East Siberian Sea”. *Frontiers in Marine Science* 9.February, pp. 1–12. ISSN: 22967745. DOI: 10.3389/fmars.2022.766810.

Moffat, C. and M. Meredith (2018). “Shelf-ocean exchange and hydrography west of the Antarctic Peninsula: A review”. *Philosophical Transactions of the Royal Society A: Mathematical, Physical and Engineering Sciences* 376.2122, pp. 1–17. ISSN: 1364503X. DOI: 10.1098/rsta.2017.0164.

Moffat, Carlos, B. Owens, and R. C. Beardsley (2009). “On the characteristics of Circumpolar Deep Water intrusions to the west Antarctic Peninsula Continental Shelf”. *Journal of Geophysical Research: Oceans* 114.5, pp. 1–16. ISSN: 21699291. DOI: 10.1029/2008JC004955.

Moffat, Carlos et al. (2008). “A first description of the Antarctic Peninsula Coastal Current”. *Deep-Sea Research Part II: Topical Studies in Oceanography* 55.3-4, pp. 277–293. ISSN: 09670645. DOI: 10.1016/j.dsr2.2007.10.003.

Mojica Prieto, Francisco Javier and Frank J. Millero (2002). “The values of pK1 + pK2 for the dissociation of carbonic acid in seawater”. *Geochimica et Cosmochimica Acta* 66.14, pp. 2529–2540. DOI: 10.1016/S0016-7037(02)00855-4.

Monteiro, Thiago, Rodrigo Kerr, and Eunice da Costa Machado (2020). “Seasonal variability of net sea-air CO_2 fluxes in a coastal region of the northern Antarctic Peninsula”. *Scientific Reports* 10.1, pp. 1–15. ISSN: 20452322. DOI: 10.1038/s41598-020-71814-0. URL: https://doi.org/10.1038/s41598-020-71814-0.

Morrison, Adele K., Thomas L. Frölicher, and Jorge L. Sarmiento (2015). “Upwelling in the Southern Ocean”. *Physics Today* 68.1, pp. 27–32. ISSN: 00319228. DOI: 10.1063/PT.3.2654.

Mucci, Alfonso et al. (2010). “CO_2 fluxes across the air-sea interface in the southeastern Beaufort Sea: Ice-free period”. *Journal of Geophysical Research: Oceans* 115.4, pp. 1–14. ISSN: 21699291. DOI: 10.1029/2009JC005330.

Mueller, Rachael D. et al. (2018). “Tidal influences on a future evolution of the Filchner-Ronne Ice Shelf cavity in the Weddell Sea, Antarctica”. *Cryosphere* 12.2, pp. 453–476. ISSN: 19940424. DOI: 10.5194/tc-12-453-2018.

Münchow, Andreas, Humfrey Melling, and Kelly K. Falkner (2006). “An observational estimate of volume and freshwater flux leaving the Arctic Ocean through Nares Strait”. *Journal of Physical Oceanography* 36.11, pp. 2025–2041. ISSN: 00223670. DOI: 10.1175/JPO2962.1.

Munro, David R. et al. (2015). “Estimates of net community production in the Southern Ocean determined from time series observations (2002-2011) of nutrients, dissolved inorganic carbon, and surface ocean pCO_2 in Drake Passage”. *Deep-Sea Research Part II: Topical Studies in Oceanography* 114, pp. 49–63. ISSN: 09670645. DOI: 10.1016/j.dsr2.2014.12.014. URL: http://dx.doi.org/10.1016/j.dsr2.2014.12.014.

Nansen, Fritjof (1897). *Farthest North, Volumes I and II.* New York: Harper and Brothers Publishers.

Naveira Garabato, A. C., R. Ferrari, and K. L. Polzin (2011). “Eddy stirring in the Southern Ocean”. *Journal of Geophysical Research: Oceans* 116.C09019, pp. 1–29. ISSN: 21699291. DOI: 10.1029/2010JC006818.

Negrete-García, Gabriela et al. (2019). “Sudden emergence of a shallow aragonite saturation horizon in the Southern Ocean”. *Nature Climate Change* 9.4, pp. 313–317. ISSN: 17586798. DOI: 10.1038/s41558-019-0418-8. URL: http://dx.doi.org/10.1038/s41558-019-0418-8.

Nicholls, Keith W. et al. (2009). “Ice-ocean processes over the continental shelf of the Southern Weddell Sea, Antarctica: A review”. *Reviews of Geophysics* 47.3, pp. 1–23. ISSN: 87551209. DOI: 10.1029/2007RG000250.

Nicholson, Sarah-anne et al. (2022). “Storms drive outgassing of CO_2 in the subpolar Southern Ocean”. *Nature Communications* 13.158, pp. 1–12. DOI: 10.1038/s41467-021-27780-w.

Nicolaus, Marcel et al. (2022). “Overview of the MOSAiC expedition: Snow and sea ice”. *Elementa* 10.1. ISSN: 23251026. DOI: 10.1525/elementa.2021.000046.

Nixdorf, Uwe; et al. (2021). “MOSAiC Extended Acknowledgement”. *Zenodo.* DOI: 10.5281/zenodo.5541624.. URL: http://dx.doi.org/10.5281/%7B%5C%%7D0Dzenodo.5541624..

Nomura, Daiki, Hisayuki Yoshikawa-Inoue, and Takenobu Toyota (2006). “The effect of sea-ice growth on air-sea CO_2 flux in a tank experiment”. *Tellus, Series B: Chemical and Physical Meteorology* 58.5, pp. 418–426. ISSN: 02806509. DOI: 10.1111/j.1600-0889.2006.00204.x.

Nomura, Daiki et al. (2013a). “Arctic and Antarctic sea ice acts as a sink for atmospheric CO_2 during periods of snowmelt and surface flooding”. *Journal of Geophysical Research: Oceans* 118.12, pp. 6511–6524. ISSN: 21699291. DOI: 10.1002/2013JC009048.

Nomura, Daiki et al. (2013b). “Characterization of ikaite ($CaCO3 \cdot 6H2O$) crystals in first-year Arctic sea ice north of Svalbard”. *Annals of Glaciology* 54.62, pp. 125–131. ISSN: 02603055. DOI: 10.3189/2013AoG62A034.

Nomura, Daiki et al. (2018). “CO_2 flux over young and snow-covered Arctic pack ice in winter and spring”. *Biogeosciences* 15.11, pp. 3331–3343. ISSN: 17264189. DOI: 10.5194/bg-15-3331-2018.

Nomura, D. et al. (2023). “Meltwater layer dynamics in a central Arctic lead: Effects of lead width, re-freezing, and mixing during late summer”. *Elementa: Science of the Anthropocene* 11, pp. 1–18. DOI: 10.1525/elementa.2022.00102.

Notz, Dirk and Julienne Stroeve (2016). “Observed Arctic sea-ice loss directly follows anthropogenic CO_2 emission”. *Science* 354.6313, pp. 747–750. ISSN: 10959203. DOI: 10.1126/science.aag2345.

Olbers, Dirk and Hartmut Hellmer (2010). “A box model of circulation and melting in ice shelf caverns”. *Ocean Dynamics* 60.1, pp. 141–153. ISSN: 16167341. DOI: 10.1007/s10236-009-0252-z.

Orr, A. et al. (2004). “A ’low-level’ explanation for the recent large warming trend over the western Antarctic Peninsula involving blocked winds and changes in zonal circulation”. *Geophysical Research Letters* 31.6, pp. 4–7. ISSN: 00948276. DOI: 10.1029/2003gl019160.

Orr, J. C., J. M. Epitalon, and J. P. Gattuso (2015). “Comparison of ten packages that compute ocean carbonate chemistry”. *Biogeosciences* 12.5, pp. 1483–1510. ISSN: 17264189. DOI: 10.5194/bg-12-1483-2015.

Orr, James C. et al. (2005). “Anthropogenic ocean acidification over the twenty-first century and its impact on calcifying organisms”. *Nature* 437.7059, pp. 681–686. ISSN: 00280836. DOI: 10.1038/nature04095.

Orsi, A. H., G. C. Johnson, and J. L. Bullister (1999). “Circulation, mixing, and production of Antarctic Bottom Water”. *Progress in Oceanography* 43.1, pp. 55–109. ISSN: 00796611. DOI: 10.1016/S0079-6611(99)00004-X.

Orsi, Alejandro H., Worth D. Jr Nowlin, and Thomas Whitworth III (1993). “On the circulation and stratification of the Weddell Gyre”. *Deep Sea Research I* 40.1, pp. 169–203.

Orsi, Alejandro H., William M. Smethie, and John L. Bullister (2002). “On the total input of Antarctic waters to the deep ocean: A preliminary estimate from chlorofluorocarbon measurements”. *Journal of Geophysical Research: Oceans* 107.8. ISSN: 21699291. DOI: 10.1029/2001jc000976.

Orsi, Alejandro H., Thomas Whitworth, and Worth D. Nowlin (1995). “On the meridional extent and fronts of the Antarctic Circumpolar Current”. *Deep-Sea Research Part I* 42.5, pp. 641–673. ISSN: 09670637. DOI: 10.1016/0967-0637(95)00021-W.

Overland, James E and Muyin Wang (2013). “When will the summer Arctic be nearly sea ice free?” *Geophysical Research Letters* 40, pp. 2097–2101. DOI: 10.1002/grl.50316.

Padman, Laurie, Matthew R. Siegfried, and Helen A. Fricker (2018). “Ocean Tide Influences on the Antarctic and Greenland Ice Sheets”. *Reviews of Geophysics* 56.1, pp. 142–184. ISSN: 19449208. DOI: 10.1002/2016RG000546.

Padman, Laurie et al. (2002). "A new tide model for the Antarctic ice shelves and seas". *Annals of Glaciology* 34, pp. 247–254. ISSN: 02603055. DOI: 10.3189/172756402781817752.

Padman, Laurie et al. (2009). "Tides of the northwestern Ross Sea and their impact on dense outflows of Antarctic Bottom Water". *Deep-Sea Research Part II: Topical Studies in Oceanography* 56.13-14, pp. 818–834. ISSN: 09670645. DOI: 10.1016/j.dsr2.2008.10.026. URL: http://dx.doi.org/10.1016/j.dsr2.2008.10.026.

Papadimitriou, S. et al. (2003). "Experimental evidence for carbonate precipitation and CO_2 degassing during sea ice formation". *Geochimica et Cosmochimica Acta* 68.8, pp. 1749–1761. ISSN: 00167037. DOI: 10.1016/j.gca.2003.07.004.

Papadimitriou, S. et al. (2012). "The effect of biological activity, CaCO3 mineral dynamics, and CO_2 degassing in the inorganic carbon cycle in sea ice in late winter-early spring in the Weddell Sea, Antarctica". *Journal of Geophysical Research: Oceans* 117.C08011, pp. 1–12. ISSN: 21699291. DOI: 10.1029/2012JC008058.

Parkinson, C. L. and D. J. Cavalieri (2012). "Antarctic sea ice variability and trends, 1979-2010". *The Cryosphere* 6, pp. 871–880. ISSN: 19940416. DOI: 10.5194/tc-6-871-2012.

Parkinson, Claire L. (2014). "Global sea ice coverage from satellite data: Annual cycle and 35-yr trends". *Journal of Climate* 27, pp. 9377–9382. DOI: 10.1175/JCLI-D-14-00605.1.

Parmentier, Frans Jan W. et al. (2013). "The impact of lower sea-ice extent on Arctic greenhouse-gas exchange". *Nature Climate Change* 3, pp. 195–202. ISSN: 1758678X. DOI: 10.1038/nclimate1784.

Petty, A. A. et al. (2021). "Assessment of ICESat-2 sea ice surface classification with Sentinel-2 Imagery: Implications for rreeboard and mew estimates of lead and floe geometry". *Earth and Space Science* 8.3, pp. 1–17. ISSN: 23335084. DOI: 10.1029/2020EA001491.

Pfeil, B. et al. (2013). "A uniform, quality controlled Surface Ocean CO_2 Atlas (SOCAT)". *Earth System Science Data* 5.1, pp. 125–143. ISSN: 18663508. DOI: 10.5194/essd-5-125-2013.

Polyakov, Igor V. et al. (2020). "Weakening of cold halocline layer exposes sea ice to oceanic heat in the eastern Arctic Ocean". *Journal of Climate* 33.18, pp. 8107–8123. ISSN: 08948755. DOI: 10.1175/JCLI-D-19-0976.1.

Prezelin, B. B. et al. (2000). "The linkage between Upper Circumpolar Deep Water (UCDW) and phytoplankton assemblages on the west Antarctic Peninsula continental shelf". *Journal of Marine Research* 58.2, pp. 165–202. ISSN: 00222402. DOI: 10.1357/002224000321511133.

Rabe, Benjamin et al. (2022). "Overview of the MOSAiC expedition: Physical oceanography". *Elementa Science of the Anthropocene* 10.1, pp. 1–31.

Rantanen, Mika et al. (2022). "The Arctic has warmed nearly four times faster than the globe since 1979". *Communications Earth & Environment* 3.168, pp. 1–10. DOI: 10.1038/s43247-022-00498-3.

Reiser, Fabian, Sascha Willmes, and Günther Heinemann (2020). "A new algorithm for daily sea ice lead identification in the arctic and antarctic winter from thermal-infrared satellite imagery". *Remote Sensing* 12.1957, pp. 1–16. ISSN: 20724292. DOI: 10.3390/rs12121957.

Renfrew, Ian A. (2002). "Coastal polynyas in the southern Weddell Sea: Variability of the surface energy budget". *Journal of Geophysical Research* 107.C6. ISSN: 0148-0227. DOI: 10.1029/2000jc000720.

Riebesell, Ulf et al. (2000). "Reduced calcification of marine plankton in response to increased atmospheric CO_2". *Nature* 407.6802, pp. 364–366. ISSN: 00280836. DOI: 10.1038/35030078.

Rignot, E. et al. (2013). "Ice-shelf melting around Antarctica". *Science* 341.6143, pp. 266–270. ISSN: 10959203. DOI: 10.1126/science.1235798.

Rinke, Annette et al. (2021). "Meteorological conditions during the MOSAiC expedition: Normal or anomalous?" *Elementa* 9.1, pp. 1–17. ISSN: 23251026. DOI: 10.1525/elementa.2021.00023.

Rintoul, Stephen R. (2018). "The global influence of localized dynamics in the Southern Ocean". *Nature* 558.7709, pp. 209–218. ISSN: 14764687. DOI: 10.1038/s41586-018-0182-3.

Rodehacke, C. B. et al. (2007). "Formation and spreading of Antarctic deep and bottom waters inferred from a chlorofluorocarbon (CFC) simulation". *Journal of Geophysical Research: Oceans* 112.C09001, pp. 1–17. ISSN: 21699291. DOI: 10.1029/2006JC003884.

Roden, Nicholas P. et al. (2013). "Annual cycle of carbonate chemistry and decadal change in coastal Prydz Bay, East Antarctica". *Marine Chemistry* 155, pp. 135–147. ISSN: 03044203. DOI: 10.1016/j.marchem.2013.06.006. URL: http://dx.doi.org/10.1016/j.marchem.2013.06.006.

Rödenbeck, Christian et al. (2022). "Data-based estimates of interannual sea-Air CO_2 flux variations 1957-2020 and their relation to environmental drivers". *Biogeosciences* 19.10, pp. 2627–2652. ISSN: 17264189. DOI: 10.5194/bg-19-2627-2022.

Rödenbeck, C. et al. (2014). "Interannual sea-air CO_2 flux variability from an observation-driven ocean mixed-layer scheme". *Biogeosciences* 11.17, pp. 4599–4613. ISSN: 17264189. DOI: 10.5194/bg-11-4599-2014.

Rödenbeck, C. et al. (2015). "Data-based estimates of the ocean carbon sink variability - First results of the Surface Ocean pCO_2 Mapping intercomparison (SOCOM)". *Biogeosciences* 12.23, pp. 7251–7278. ISSN: 17264189. DOI: 10.5194/bg-12-7251-2015.

Rogachev, Konstantin A. et al. (2001). "Lunar fortnightly modulation of tidal mixing near Kashevarov Bank, Sea of Okhotsk, and its impacts on biota and sea ice". *Progress in Oceanography* 49.1-4, pp. 373–390. ISSN: 00796611. DOI: 10.1016/S0079-6611(01)00031-3.

Rogge, Andreas et al. (2023). “Carbon dioxide sink in the Arctic Ocean from cross-shelf transport of dense Barents Sea water”. *Nature Geoscience* 16.1, pp. 82–88. ISSN: 17520908. DOI: 10.1038/s41561-022-01069-z.

Rohardt, Gerd and Olaf Boebel (2015a). *Physical oceanography during POLARSTERN cruise PS89 (ANT-XXX/2)*. data set. Alfred Wegener Institute, Helmholtz Centre for Polar and Marine Research, Bremerhaven. DOI: 10.1594/PANGAEA.846701. URL: https://doi.org/10.1594/PANGAEA.846701.

— (2015b). *Physical oceanography measured on water bottle samples during POLARSTERN cruise PS89 (ANT-XXX/2)*. data set. Alfred Wegener Institute, Helmholtz Centre for Polar and Marine Research, Bremerhaven. DOI: 10.1594/PANGAEA.846773. URL: https://doi.org/10.1594/PANGAEA.846773.

— (2020). *Physical oceanography during POLARSTERN cruise PS117*. data set. Alfred Wegener Institute, Helmholtz Centre for Polar and Marine Research, Bremerhaven. DOI: 10.1594/PANGAEA.910663. URL: https://doi.org/10.1594/PANGAEA.910663.

Rohardt, Gerd and Sandra Tippenhauer (2020). *CTD Data Processing Report RV POLARSTERN Cruise PS117*. DOI: 10.1594/PANGAEA.910663.

Rohardt, Gerd et al. (2020). *Physical oceanography measured on water bottle samples during POLARSTERN cruise PS117*. data set. Alfred Wegener Institute, Helmholtz Centre for Polar and Marine Research, Bremerhaven. DOI: 10.1594/PANGAEA.910673. URL: https://doi.org/10.1594/PANGAEA.910673.

Rozema, P. D. et al. (2017). “Interannual variability in phytoplankton biomass and species composition in northern Marguerite Bay (West Antarctic Peninsula) is governed by both winter sea ice cover and summer stratification”. *Limnology and Oceanography* 62, pp. 235–252. ISSN: 19395590. DOI: 10.1002/lno.10391.

Rudels, B., L. G. Anderson, and E. P. Jones (1996). “Formation and evolution of the surface mixed layer and halocline of the Arctic Ocean”. *Journal of Geophysical Research C: Oceans* 101.C4, pp. 8807–8821. ISSN: 01480227. DOI: 10.1029/96JC00143.

Ryan, Svenja et al. (2020). “Exceptionally Warm and Prolonged Flow of Warm Deep Water Toward the Filchner-Ronne Ice Shelf in 2017”. *Geophysical Research Letters* 47.13. ISSN: 19448007. DOI: 10.1029/2020GL088119.

Rysgaard, S. et al. (2007). “Inorganic carbon transport during sea ice growth and decay: A carbon pump in polar seas”. *Journal of Geophysical Research: Oceans* 112.C03016, pp. 1–8. ISSN: 21699291. DOI: 10.1029/2006JC003572.

Rysgaard, S. et al. (2009). “Increased CO_2 uptake due to sea ice growth and decay in the Nordic Seas”. *Journal of Geophysical Research: Oceans* 114.9, pp. 1–9. ISSN: 21699291. DOI: 10.1029/2008JC005088.

Rysgaard, S. et al. (2011). “Sea ice contribution to the air-sea CO_2 exchange in the Arctic and Southern Oceans”. *Tellus, Series B: Chemical and Physical Meteorology* 63.5, pp. 823–830. ISSN: 02806509. DOI: 10.1111/j.1600-0889.2011.00571.x.

Rysgaard, S. et al. (2012). “Ikaite crystals in melting sea ice - Implications for pCO_2 and pH levels in Arctic surface waters”. *Cryosphere* 6.4, pp. 901–908. ISSN: 19940416. DOI: 10.5194/tc-6-901-2012.

Rysgaard, S. et al. (2013). “Ikaite crystal distribution in winter sea ice and implications for CO_2 system dynamics”. *The Cryosphere* 7, pp. 707–718. DOI: 10.5194/tc-7-707-2013.

Saba, Grace K. et al. (2014). “Winter and spring controls on the summer food web of the coastal West Antarctic Peninsula”. *Nature Communications* 5.4318, pp. 1–8. ISSN: 20411723. DOI: 10.1038/ncomms5318.

Sarmiento, Jorge L. and Nicolas Gruber (2013). *Ocean Biogeochemical Dynamics.* Princeton University Press. ISBN: 9781400849079. DOI: 10.1515/9781400849079. URL: https://doi.org/10.1515/9781400849079.

Savidge, Dana K. and Julie A. Amft (2009). “Circulation on the West Antarctic Peninsula derived from 6 years of shipboard ADCP transects”. *Deep-Sea Research Part I: Oceanographic Research Papers* 56.10, pp. 1633–1655. ISSN: 09670637. DOI: 10.1016/j.dsr.2009.05.011.

Schanke, Nicole L. et al. (2021). “Biogeochemical and ecological variability during the late summer-early autumn transition at an ice-floe drift station in the Central Arctic Ocean”. *Limnology and Oceanography* 66.S1, S363–S382. ISSN: 19395590. DOI: 10.1002/lno.11676.

Schmithüsen, Holger (2020). *Meteorological observations during POLARSTERN cruise PS117.* data set. Alfred Wegener Institute, Helmholtz Centre for Polar and Marine Research, Bremerhaven. DOI: 10.1594/PANGAEA.913632. URL: https://doi.org/10.1594/PANGAEA.913632.

Schulz, Kirstin et al. (2022). “A full year of turbulence measurements from a drift campaign in the Arctic Ocean 2019-2020”. *Scientific Data* 9.1, pp. 1–11. ISSN: 20524463. DOI: 10.1038/s41597-022-01574-1.

Schuster, U. et al. (2013). “An assessment of the Atlantic and Arctic sea-air CO_2 fluxes, 1990-2009”. *Biogeosciences* 10.1, pp. 607–627. DOI: 10.5194/bg-10-607-2013.

Seidov, D. et al. (2015). “Oceanography north of 60°N from World Ocean Database”. *Progress in Oceanography* 132, pp. 153–173. ISSN: 00796611. DOI: 10.1016/j.pocean.2014.02.003. URL: http://dx.doi.org/10.1016/j.pocean.2014.02.003.

Semiletov, Igor et al. (2004). “Atmospheric CO_2 balance: The role of Arctic sea ice”. *Geophysical Research Letters* 31.5, pp. 2–5. ISSN: 00948276. DOI: 10.1029/2003gl017996.

Shadwick, E. H. et al. (2011). “Export of Pacific carbon through the Arctic Archipelago to the North Atlantic”. *Continental Shelf Research* 31, pp. 806–816. ISSN: 02784343. DOI: 10.1016/j.csr.2011.01.014. URL: http://dx.doi.org/10.1016/j.csr.2011.01.014.

Shadwick, E. H. et al. (2013). “Vulnerability of polar oceans to anthropogenic acidification: Comparison of Arctic and Antarctic seasonal cycles”. *Scientific Reports* 3.2339, pp. 1–7. ISSN: 20452322. DOI: 10.1038/srep02339.

Shupe, Matthew D et al. (2022). "Overview of the MOSAiC expedition-Atmosphere". *Elementa Science of the Anthropocene* 10.1, pp. 1–54. DOI: 10.1525/elementa.2021.00060.

Simpson, J. H., C. M. Allen, and N. C. G. Morris (1978). "Fronts on the continental shelf". *Journal of Geophysical Research* 83.C9, pp. 4607–4614. DOI: 10.1029/JC083iC09p04607.

Sims, Richard Peter et al. (2022). "Tidal mixing of estuarine and coastal waters in the Western English Channel controls spatial and temporal variability in seawater CO_2". *Biogeosciences Discussions* 19, pp. 1657–1674. ISSN: 1810-6277. DOI: 10.5194/bg-19-1657-2022.

Skogseth, Ragnheid et al. (2013). "Creation and tidal advection of a cold salinity front in Storfjorden: 1. Polynya dynamics". *Journal of Geophysical Research: Oceans* 118.7, pp. 3278–3291. ISSN: 21699291. DOI: 10.1002/jgrc.20231.

Smith, Emma Clare et al. (2020b). *CTD profiles from beneath Ekstroem Ice Shelf and Atka Bay.* data set. DOI: 10.1594/PANGAEA.914478. URL: https://doi.org/10.1594/PANGAEA.914478.

Smith, Emma C. et al. (2020). "Detailed Seismic Bathymetry Beneath Ekström Ice Shelf, Antarctica: Implications for Glacial History and Ice-Ocean Interaction". *Geophysical Research Letters* 47.10. ISSN: 19448007. DOI: 10.1029/2019GL086187.

Stammerjohn, Sharon E. et al. (2008a). "Sea ice in the western Antarctic Peninsula region: Spatio-temporal variability from ecological and climate change perspectives". *Deep-Sea Research Part II: Topical Studies in Oceanography* 55.18-19, pp. 2041–2058. ISSN: 09670645. DOI: 10.1016/j.dsr2.2008.04.026.

Stammerjohn, Sharon E. et al. (2008b). "Trends in Antarctic annual sea ice retreat and advance and their relation to El Niño-Southern Oscillation and Southern Annular Mode variability". *Journal of Geophysical Research: Oceans* 113.3, pp. 1–20. ISSN: 21699291. DOI: 10.1029/2007jc004269.

Stammerjohn, Sharon and Ted Maksym (2017). "Gaining (and losing) Antarctic sea ice: variability, trends and mechanisms". *Sea ice.* Ed. by David N. Thomas. Third Edit. John Wiley & Sons, Ltd. Chap. 10, pp. 261–289. ISBN: 9781118778388.

Stammerjohn, Sharon et al. (2012). "Regions of rapid sea ice change: An inter-hemispheric seasonal comparison". *Geophysical Research Letters* 39.L06501, pp. 1–8. ISSN: 00948276. DOI: 10.1029/2012GL050874.

Stroeve, Julienne and Dirk Notz (2018). "Changing state of Arctic sea ice across all seasons". *Environmental Research Letters* 13.103001, pp. 1–23. ISSN: 17489326. DOI: 10.1088/1748-9326/aade56.

Stukel, Michael R. et al. (2017). "Mesoscale ocean fronts enhance carbon export due to gravitational sinking and subduction". *Proceedings of the National Academy of Sciences of the United States of America* 114.6, pp. 1252–1257. ISSN: 10916490. DOI: 10.1073/pnas.1609435114.

Sulpis, Olivier, Siv K. Lauvset, and Mathilde Hagens (2020). "Current estimates of K_1^* and K_2^* appear inconsistent with measured CO_2 system parameters in cold oceanic regions". *Ocean Science* 16.4, pp. 847–862. ISSN: 18120792. DOI: 10.5194/os-16-847-2020.

Sulpis, Olivier et al. (2021). "Calcium carbonate dissolution patterns in the ocean". *Nature Geoscience* 14.6, pp. 423–428. ISSN: 17520908. DOI: 10.1038/s41561-021-00743-y. URL: http://dx.doi.org/10.1038/s41561-021-00743-y.

Sutton, A. J., N. L. Williams, and B. Tilbrook (2021). "Constraining Southern Ocean CO_2 flux uncertainty using uncrewed surface vehicle observations". *Geophysical Research Letters* 48.3, pp. 1–9. ISSN: 19448007. DOI: 10.1029/2020GL091748.

Swart, Sebastiaan et al. (2019). "Constraining Southern ocean air-sea-ice fluxes through enhanced observations". *Frontiers in Marine Science* 6.421, pp. 1–10. ISSN: 22967745. DOI: 10.3389/fmars.2019.00421.

Takahashi, T (2002). "Global air-sea flux of CO_2 based on surface ocean pCO_2, and seasonal biological and temperature effects". *Deep-Sea Research Part II* 49, pp. 1601–1622. URL: papers2://publication/uuid/438F305C-9B5A-493D-B7A6-7EAA86F98C00.

Takahashi, Taro et al. (2009). "Climatological mean and decadal change in surface ocean pCO_2, and net sea-air CO_2 flux over the global oceans". *Deep-Sea Research Part II: Topical Studies in Oceanography* 56, pp. 554–577. ISSN: 09670645. DOI: 10.1016/j.dsr2.2008.12.009.

Tanhua, Toste et al. (2009). "Ventilation of the Arctic Ocean: Mean ages and inventories of anthropogenic CO_2 and CFC-11". *Journal of Geophysical Research: Oceans* 114.C01002, pp. 1–11. ISSN: 21699291. DOI: 10.1029/2008JC004868.

Tank, Suzanne E. et al. (2012). "A land-to-ocean perspective on the magnitude, source and implication of DIC flux from major Arctic rivers to the Arctic Ocean". *Global Biogeochemical Cycles* 26.4, pp. 1–15. ISSN: 08866236. DOI: 10.1029/2011GB004192.

Thompson, Andrew F. and Jean Baptiste Sallée (2012). "Jets and Topography: Jet transitions and the impact on transport in the Antarctic Circumpolar Current". *Journal of Physical Oceanography* 42, pp. 956–972. ISSN: 00223670. DOI: 10.1175/JPO-D-11-0135.1.

Thompson, Andrew F. et al. (2018). "The Antarctic Slope Current in a Changing Climate". *Reviews of Geophysics* 56.4, pp. 741–770. ISSN: 19449208. DOI: 10.1029/2018RG000624.

Timmermann, R., Q. Wang, and H. H. Hellmer (2012). "Ice-shelf basal melting in a global finite-element sea-ice/ice-shelf/ocean model". *Annals of Glaciology* 53.60, pp. 303–314. ISSN: 02603055. DOI: 10.3189/2012AoG60A156.

Timmermans, Mary Louise and John Marshall (2020). "Understanding Arctic Ocean Circulation: A Review of Ocean Dynamics in a Changing Climate". *Journal of Geophysical Research: Oceans* 125.4, pp. 1–35. ISSN: 21699291. DOI: 10.1029/2018JC014378. URL: https://doi.org/10.1029/2018JC014378.

Tortell, Philippe D et al. (2014). "Geophysical Research Letters". *Geophysical Research Letters* 41, pp. 6803–6810. DOI: 10.1002/2014GL061266.

Tremblay, Jean Eric et al. (2002). "Climatic and oceanic forcing of new, net, and diatom production in the North Water". *Deep-Sea Research Part II: Topical Studies* *in Oceanography* 49.22-23, pp. 4927–4946. ISSN: 09670645. DOI: 10.1016/S0967-0645(02)00171-6.

Turner, John et al. (2015). "Recent changes in Antarctic sea ice". *Philosophical Transaction of The Royal Society A* 373.20140163, pp. 1–12. DOI: 10.1098/rsta.2014.0163.

Turner, John et al. (2017). "Unprecedented springtime retreat of Antarctic sea ice in 2016". *Geophysical Research Letters* 44.13, pp. 6868–6875. ISSN: 19448007. DOI: 10.1002/2017GL073656.

Ulfsbo, Adam et al. (2014). "Late summer net community production in the central Arctic Ocean using multiple approaches". *Global biogeochemical cycles* 28, pp. 1129–1148. DOI: 10.1002/2014GB004833.

Uppström, Leif R. (1974). "The boron/chlorinity ratio of deep-sea water from the Pacific Ocean". *Deep-Sea Research and Oceanographic Abstracts* 21.2, pp. 161–162. ISSN: 00117471. DOI: 10.1016/0011-7471(74)90074-6.

Våge, Kjetil et al. (2018). "Ocean convection linked to the recent ice edge retreat along east Greenland". *Nature Communications* 9.1287, pp. 1–8. ISSN: 20411723. DOI: 10.1038/s41467-018-03468-6. URL: http://dx.doi.org/10.1038/s41467-018-03468-6.

Van Leeuwe, Maria A. et al. (2018). "Microalgal community structure and primary production in Arctic and Antarctic sea ice: A synthesis". *Elementa Science of the Anthropocene* 6.4, pp. 1–25. ISSN: 23251026. DOI: 10.1525/elementa.267.

Van Leeuwe, Maria A. et al. (2022). "On the phenology and seeding potential of sea-ice microalgal species". *Elementa* 10.1, pp. 1–19. ISSN: 23251026. DOI: 10.1525/elementa.2021.00029.

Venables, Hugh J., Andrew Clarke, and Michael P. Meredith (2013). "Wintertime controls on summer stratification and productivity at the western Antarctic Peninsula". *Limnology and Oceanography* 58.3, pp. 1035–1047. ISSN: 00243590. DOI: 10.4319/lo.2013.58.3.1035.

Venables, Hugh J. and Michael P. Meredith (2014). "Feedbacks between ice cover, ocean stratification, and heat content in Ryder Bay, western Antarctic Peninsula". *Journal of Geophysical Research: Oceans* 119, pp. 3868–3882. DOI: 10.1002/2013JC009669. URL: http://onlinelibrary.wiley.com/doi/10.1002/jgrc.20353/abstract.

Venables, Hugh J., Michael P. Meredith, and J. Alexander Brearley (2017). "Modification of deep waters in Marguerite Bay, western Antarctic Peninsula, caused by topographic overflows". *Deep-Sea Research Part II: Topical Studies in Oceanography* 139, pp. 9–17. ISSN: 09670645. DOI: 10.1016/j.dsr2.2016.09.005.

Vernet, M. et al. (2019). "The Weddell Gyre, Southern Ocean: Present knowledge and future challenges". *Reviews of Geophysics* 57.3, pp. 623–708. ISSN: 19449208. DOI: 10.1029/2018RG000604. URL: https://doi.org/10.1029/2018RG000604.

Wallace, Margaret I. et al. (2008). "On the characteristics of internal tides and coastal upwelling behaviour in Marguerite Bay, west Antarctic Peninsula". *Deep-Sea Research Part II: Topical Studies in Oceanography* 55, pp. 2023–2040. ISSN: 09670645. DOI: 10.1016/j.dsr2.2008.04.033.

Wang, Chunzai and Paul C Fiedler (2006). “Progress in Oceanography ENSO variability and the eastern tropical Pacific: A review”. *Progress in Oceanography* 69, pp. 239–266. DOI: 10.1016/j.pocean.2006.03.004.

Wang, Qiang and Sergey Danilov (2022). “A Synthesis of the Upper Arctic Ocean Circulation During 2000-2019: Understanding the Roles of Wind Forcing and Sea Ice Decline”. *Frontiers in Marine Science* 9.863204, pp. 1–24. DOI: 10.3389/fmars.2022.863204.

Wang, Xiaomeng et al. (2010). “Late autumn to spring changes in the inorganic and organic carbon dissolved in the water column at Scholaert Channel, West Antarctica”. *Antarctic Science* 22.2, pp. 145–156. ISSN: 09541020. DOI: 10.1017/S0954102009990666.

Wanninkhof, R. (1992). “Relationship between wind speed and gas exchange over the ocean”. *Journal of Geophysical Research* 97.C5, pp. 7373–7382. ISSN: 01480227. DOI: 10.1029/92JC00188.

Wanninkhof, Rik (2014). “Relationship between wind speed and gas exchange over the ocean revisited”. *Limnology and Oceanography: Methods* 12.JUN, pp. 351–362. ISSN: 15415856. DOI: 10.4319/lom.2014.12.351.

Wanninkhof, Rik et al. (2022). “Comparison of discrete and underway CO_2 measurements: Inferences on the temperature dependence of the fugacity of CO_2 in seawater”. *Marine Chemistry* 247.104178, pp. 1–9. ISSN: 03044203. DOI: 10.1016/j.marchem.2022.104178. URL: https://doi.org/10.1016/j.marchem.2022.104178.

Watson, Andrew J. et al. (2020). “Revised estimates of ocean-atmosphere CO_2 flux are consistent with ocean carbon inventory”. *Nature Communications* 11.4422, pp. 1–6. ISSN: 20411723. DOI: 10.1038/s41467-020-18203-3. URL: http://dx.doi.org/10.1038/s41467-020-18203-3.

Weiss, R. F. (1974). “Carbon dioxide in water and seawater: The solubility of a non-ideal gas”. *Marine Chemistry* 2, pp. 203–215.

Weiss, R. F. and B. A. Price (1980). “Nitrous oxide solubility in water and seawater”. *Marine Chemistry* 8, pp. 347–359. ISSN: 0308521X.

Williams, N. L. et al. (2016). “Empirical algorithms to estimate water column pH in the Southern Ocean”. *Geophysical Research Letters* 43.7, pp. 3415–3422. DOI: 10.1002/2016GL068539.

Williams, N. L. et al. (2017). “Calculating surface ocean pCO_2 from biogeochemical Argo floats equipped with pH: An uncertainty analysis”. *Global Biogeochemical Cycles* 31.3, pp. 591–604. ISSN: 19449224. DOI: 10.1002/2016GB005541.

Witte, Hannelore and Olaf Boebel (2018). *Processed 2 minutes-averaged continuous VM-ADCP (vessel-mounted Acoustic Doppler Current Profiler) profiles during POLARSTERN cruise PS89.* data set. Alfred Wegener Institute, Helmholtz Centre for Polar and Marine Research, Bremerhaven. DOI: 10.1594/PANGAEA.885934. URL: https://doi.org/10.1594/PANGAEA.885934.

Wolf-Gladrow, Dieter A. et al. (2007). “Total alkalinity: The explicit conservative expression and its application to biogeochemical processes”. *Marine Chemistry* 106.1-2 SPEC. ISS. Pp. 287–300. ISSN: 03044203. DOI: 10.1016/j.marchem.2007.01.006.

Woodgate, Rebecca A. and Knut Aagaard (2005). “Revising the Bering Strait freshwater flux into the Arctic Ocean”. *Geophysical Research Letters* 32.L02602, pp. 1–4. ISSN: 00948276. DOI: 10.1029/2004GL021747.

Woodgate, Rebecca A., Eberhard Fahrbach, and Gerd Rohardt (1999). “Structure and transports of the East Greenland Current at 75°N from moored current meters”. *Journal of Geophysical Research: Oceans* 104.C8, pp. 18059–18072. ISSN: 21699291. DOI: 10.1029/1999jc900146.

Woodgate, Rebecca A., Thomas J. Weingartner, and Ron Lindsay (2012). “Observed increases in Bering Strait oceanic fluxes from the Pacific to the Arctic from 2001 to 2011 and their impacts on the Arctic Ocean water column”. *Geophysical Research Letters* 39.24, pp. 1–6. ISSN: 19448007. DOI: 10.1029/2012GL054092.

Woolf, D. K. et al. (2016). “On the calculation of air-sea fluxess of CO_2 in the presence of temperature and salinity gradients”. *Journal of Geophysical Research: Oceans* 121, pp. 3010–3028. ISSN: 21699291. DOI: 10.1002/2015JC011427.

Wu, Yingxu et al. (2019). “What drives the latitudinal gradient in open-ocean surface dissolved inorganic carbon concentration?” *Biogeosciences* 16.13, pp. 2661–2681. ISSN: 17264189. DOI: 10.5194/bg-16-2661-2019.

Yager, P. L. et al. (1995). “The Northeast Water Polynya as an atmospheric CO_2 sink: a seasonal rectification hypothesis”. *Journal of Geophysical Research* 100.C3, pp. 4389–4398. ISSN: 01480227. DOI: 10.1029/94JC01962.

Yamamoto-Kawai, Michiyo et al. (2009). “Aragonite undersaturation in the Arctic: Effects of ocean acidification and sea ice melt”. *Science* 326, pp. 1098–1100. URL: http://www.ncbi.nlm.nih.gov/pubmed/19965425.

Yasunaka, Sayaka et al. (2018). “Arctic Ocean CO_2 uptake: An improved multiyear estimate of the air-sea CO_2 flux incorporating chlorophyll a concentrations”. *Biogeosciences* 15.6, pp. 1643–1661. ISSN: 17264189. DOI: 10.5194/bg-15-1643-2018.

You, Qinglong et al. (2021). “Warming amplification over the Arctic Pole and Third Pole: Trends , mechanisms and consequences”. *Earth-Science Reviews* 217.103625, pp. 1–25. ISSN: 0012-8252. DOI: 10.1016/j.earscirev.2021.103625. URL: https://doi.org/10.1016/j.earscirev.2021.103625.

Zeebe, Richard E. and Dieter Wolf-Gladrow (2001). *CO_2 in seawater: equilibrium, kinetics, isotopes.* Ed. by D. Halpern. Amsterdam, The Netherlands: Elsevier Oceanography Series 65, Elsevier B.V. ISBN: 0444505792.

Zemmelink, H. J. et al. (2006). “CO_2 deposition over the multi-year ice of the western Weddell Sea”. *Geophysical Research Letters* 33.L13606, pp. 1–4. ISSN: 00948276. DOI: 10.1029/2006GL026320.

Zhou, Q. et al. (2014). “Wind-driven spreading of fresh surface water beneath ice shelves in the eastern Weddell Sea”. *Journal of Geophysical Research: Oceans* 119.6, pp. 3818–3833. DOI: 10.1002/2013JC009556.Received.